Heat and mass transfers in curved cooling channels of rocket engines

Yohann Torres

To cite this version:

Yohann Torres. Heat and mass transfers in curved cooling channels of rocket engines. Mechanics [physics]. Université de Valenciennes et du Hainaut-Cambrésis, 2008. English. NNT : 2008VALE0021 . tel-03009976

HAL Id: tel-03009976
https://uphf.hal.science/tel-03009976
Submitted on 17 Nov 2020

HAL is a multi-disciplinary open access archive for the deposit and dissemination of scientific research documents, whether they are published or not. The documents may come from teaching and research institutions in France or abroad, or from public or private research centers.

L'archive ouverte pluridisciplinaire **HAL**, est destinée au dépôt et à la diffusion de documents scientifiques de niveau recherche, publiés ou non, émanant des établissements d'enseignement et de recherche français ou étrangers, des laboratoires publics ou privés.

THÈSE

Présentée à

L´Université de Valenciennes et du Hainaut Cambrésis

Ecole Doctorale ED72 – Sciences pour l´ingénieur

Pour obtenir le grade de

DOCTEUR

Option : MÉCANIQUE-ÉNERGÉTIQUE

Par

YOHANN TORRES

le 09.10.2008

Transferts énergétiques dans les canaux de refroidissement courbes de moteurs fusées

Jury

Rapporteurs:	T. Arts	Professeur, Université Catholique de Louvain, Institute von Karman
	B. Weigand	Professeur, Université de Stuttgart, Institute of Aerospace Thermodynamics
Examinateurs:	G. Bois	Professeur, ENSAM Lille
	B. Desmet	Professeur, Université de Valenciennes, Laboratoire de Mécanique Énergétique, Directeur de Thèse
	O. Haidn	Docteur, DLR Lampoldshausen
	M. Oschwald	Docteur, DLR Lampoldshausen
	D. Suslov	Docteur, DLR Lampoldshausen

▪ KEYWORDS :

Heat transfer, Flow transfer, Curved flows, Dean vortices, “Edges” vortices, Cooling channel, Nusselt, Rocket engine, Secondary motions, Hydrogen, Methane, CFD, Reynolds Stress Model (RSM), Fluid experiments, Temperatures measurement, Cryogenic, DLR

Acknowledgements

I would like to express my deep and sincere gratitude to my supervisor, Dr. Dmitry Suslov, Technology Department of the German Institute of Space Propulsion, DLR, Lampoldshausen, Germany. His wide knowledge and his logical way of thinking have been of great value for me. His understanding, encouraging and personal guidance have provided a good basis for the present thesis.

I am deeply grateful to my university supervisor, Professor Bernard Desmet, Head of the Laboratoire de Mécanique Énergétique, Valenciennes, France, for his detailed and constructive comments, and for his important support throughout this work. I wish to express my warm and sincere thanks to Alain Lecocq who introduced me to the DLR of Lampoldshausen.

I owe my most sincere gratitude to Dr. Oskar Haidn, Head of the Technology Department of the DLR of Lampoldshausen and to Dr. Michael Oschwald, Head of the Heat Transfer Department who gave me the opportunity and financial support to work with them and to manage all experimental and numerical investigations of the project.

I express my gratitude to the department FLTCY of the company SNECMA, located in Vernon in France, having allowed me to participate in the VIA research program with the DLR and for having supported the first year of this PhD. My particular thanks are due to Francoise Perrel and Laure-Sophie Ballester, who gave me precious information and solid supervision.

My warm thanks are due to Lucas Stefanini. His expertise in the use of software and his brilliant ideas have been of great value in this study. He received a Diploma degree (Diplôme de Recherche Technologique) with honors for his work. I warmly thank Marco De Rosa and Dirk Greuel, for their valuable advice and friendly help. I am grateful to Anouar Ben Ezzedine, Fabien Francke, Sylvain Giupponni and Thomas Maugé for their very serious student work. I wish to thank Artur Walz-Steinbach and Michael Zepmeisel for their very precious mechanical and electrical work, i.e. to have built a robust test bench and for their permanent good temper, whatever happened!

My sincere thanks are due to the official referees, Prof. Tony Arts, Prof. Bernhard Weigand and Prof. Gérard Bois for their reviews.

My special gratitude is due to my brothers and my parents for their loving support. I owe particular thanks to Krikri, who always believed in me and encouraged me to finish this work. She helped me to persist in the realisation of this PhD.

CONTENTS

NOTATION

- Greek Symbols

α_θ	Angular Blending Function	[-]
β_d	Thermal Dilatation	[K^{-1}]
δ_w	Dynamical Boundary Layer Thickness	[m]
λ	Thermal Conductivity	[$W\ m^{-1}\ K^{-1}$]
$\lambda_{Gö}$	Wavelength of Görtler rolls	[m]
κ	Curvature Coefficient	[-]
ε	Turbulent Eddy Dissipation	[$m^2\ s^{-3}$]
ρ	Density	[$kg\ m^{-3}$]
φ	Angular Coordinate in Cylindrical Coordinate System	[-]
μ	Dynamic Viscosity	[Pa·s]
μ_t	Turbulent Dynamic Viscosity	[Pa s]
υ	Kinematic Viscosity	[$m^2\ s^{-1}$]
ξ	Friction Factor	[-]
θ	Turning angle	[rad]
ω	Turbulent Eddy Frequency	[s^{-1}]
ψ_c	Curvature Coefficient for Heat Transfer	[-]
τ_{ij}	Reynolds Stress Tensor	[Pa]
τ_w	Wall Shear Stress	[Pa]

- Latin Symbols

a	Parameter for Measurement Accuracy	[K^2]
A	Cross-section area	[m^2]
b	Parameter for Measurement Accuracy	[-]
b	Parameter in the Niino empirical correlation	[-]
c_P	Specific Heat Capacity	[$J\ kg^{-1}\ K^{-1}$]
d_t	Distance between Thermal Contact and "Hot" Thermocouple Junction	[m]
D	Pipe Diameter	[m]
De	Dean Number (common reference)	[-]
De_1	Dean Number (Dean, 1928)	[-]
D_h	Hydraulic Diameter	[m]
$E_{(i-j)}$	Estimated fractional error	[-]
F_{cent}	Volume Centrifugal Force	[$N\ m^{-3}$]
g	Gravitational Acceleration	[$m\ s^{-2}$]
Gö	Görtler Number	[-]
h	Convective Heat Transfer Coefficient	[$W\ m^{-2}\ K^{-1}$]
h	Specific Enthalpy	[$J\ kg^{-1}$]
h_c	Channel (or Fin) Height	[m]
I_{SP}	Specific Impulse on Earth	[s]
k	Turbulent Kinetic Energy	[$m^2\ s^{-2}$]
k_{rel}	Relative Roughness Factor	[-]
k_s	Averaged Roughness	[m]
k_s^+	Reduced Roughness Factor	[-]
L(r)	Turbulent Length Scale	[m]
L_{tot}	Length of a Duct	[m]
L_{max}	Required Length to Choke a Flow by Frictional Effects	[m]
L_{base}	Typical Length of the Copper Alloy Base	[m]
Lc	Length of a Curvature	[m]
M	Molar Mass	[$kg\ mol^{-1}$]

m	Mass	[kg]
$\dot{m}$	Mass Flow Rate	[kg s^{-1}]
Ma	Mach Number	[-]
Nu	Nusselt Number	[-]
p	Pressure	[Pa], [bar]
P	Perimeter	[m]
Pr	Prandtl Number	[-]
P_w	Wetted Perimeter	[m]
P_{ij}	Production Tensor of Tensor Stress	[kg m^{-1} s^{-3}]
$\dot{q}$	Heat Flux Density	[W m^{-2}]
Q	Heat	[J]
$\dot{Q}$	Heat Flux	[W]
$\dot{Q}_i$	Heat Flux by Ideal Fin	[W]
$\dot{Q}_a$	Heat Flux through Real Fin	[W]
r	Radial Coordinate in Cylindrical System	[m]
r′	Reduced Radial Coordinate	[-]
R_0	Gas Constant	[J mol^{-1} K^{-1}]
R_{ww}	Streamwise Turbulent Correlation (Along Axis z)	[-]
R_{uu}	Streamwise Turbulent Correlation (Along Axis x)	[-]
R_{vv}	Streamwise Turbulent Correlation (Along Axis y)	[-]
R_c	Curvature Radius	[m]
Re	Reynolds Number	[-]
Re_δ	Reynolds Number (based on Boundary Layer Thickness)	[-]
S	Area of a Channel Section	[m^2]
S_h	Heated Surface of the Channel	[m^2]
s	Curvilinear Coordinate Along the Cooling Channel Wall	[m]
t	Thickness of the Fin; Time	[m]; [s]
T	Temperature	[K]

u	x-Velocity Component	$[\mathrm{m\ s^{-1}}]$
U_i	Velocity along *i*-Axis	$[\mathrm{m\ s^{-1}}]$
U_τ	Friction Velocity of Main Flow Velocity Component, chapter 3	$[\mathrm{m\ s^{-1}}]$
u_r	Radial Velocity Component	$[\mathrm{m\ s^{-1}}]$
u_φ	Velocity Component on Angular Cylindrical Axis	$[\mathrm{m\ s^{-1}}]$
v	y-Velocity Component	$[\mathrm{m\ s^{-1}}]$
V	Voltage	[V]
V_m	Mole Volume	$[\mathrm{m^3\ mol^{-1}}]$
W_τ	z-Axis Friction Velocity	$[\mathrm{m\ s^{-1}}]$
w	z-Velocity Component	$[\mathrm{m\ s^{-1}}]$
w_0	Maximal z-Velocity Component	[m]
$w_{heaters}$	Width of the Thermal Nozzle	[m]
w_{throat}	With of the Copper Block	[m]
X	Shapping Parameter for the Nozzle	[-]
x	First Cartesian Coordinate	[m]
x_c	Curvilinear Abscissa	[m]
y	Second Cartesian Coordinate	[m]
y^+	Dimensionless y-Ordinate	[-]
z	Third Cartesian Coordinate	[m]

- Subscripts

a	"Real" Case (for a Fin Study)
c	Curved
cont	Containment
ch	Channel
b	Bulk
crit	Critical Value
eff	Efficiency
f - fin	Thermal Fin
i	Ideal Case (for a Fin Study)

in	Inlet
mani	Manifold
meas	Measured
out	Outlet
P	Precision
R	Resolution
Root	Root of the fin
s	Straight
th	Thermocouple
θ	Reference to an Angle
w	Wall

- Abbreviation

SSME	Space Shuttle Main Engine
AR	Aspect Ratio
BC	Boundary Conditions
CFD	Computational Fluid Dynamic
DLR	Deutsches Zentrum für Luft- und Raumfahrt German Institute of Space Propulsion
DNS	Direct Numerical Simulation
EH3C	Electrically Heated Curved Cooling Channels
GCI	Grid Convergence Index
HARCC	High Aspect Ratio Cooling Channel
LDV	Laser Doppler Velocimetry
LES	Large Eddy Simulation
LOx	Liquid Oxygen
LH2 or LH_2	Liquid Hydrogen
M3 – P4 - P5 - P8	Test Benches at the DLR of Lampoldshausen
NASA	National Aeronautics and Space Administration
PIV	Particle Image Velocimetry
TBC	Thermal Barrier Coating

1. Introduction

1.1. Motivation and Presentation of the Problem

1.1.1. Space Propulsion

Chemical rocket engines still represent the only rocket propulsion system which is able to transport payload into earth orbit. Competition in the space transport area of the world market has grown drastically during the last ten years, with increasing commercial activities in Europe, Russia and USA. Moreover, the entrance of new countries to this commercial market area (Japan, China, India, Brazil...) means enhanced requirements for the reliability, performance and costs of rocket systems. To preserve the role of Europe in this domain, the European countries have developed new powerful rocket systems in the successful Ariane family, shown in Figure 1. From Ariane 1 (left) to Ariane 5 (ECA version, right), an increased payload capacity and corresponding reduction of the launch costs have been achieved.

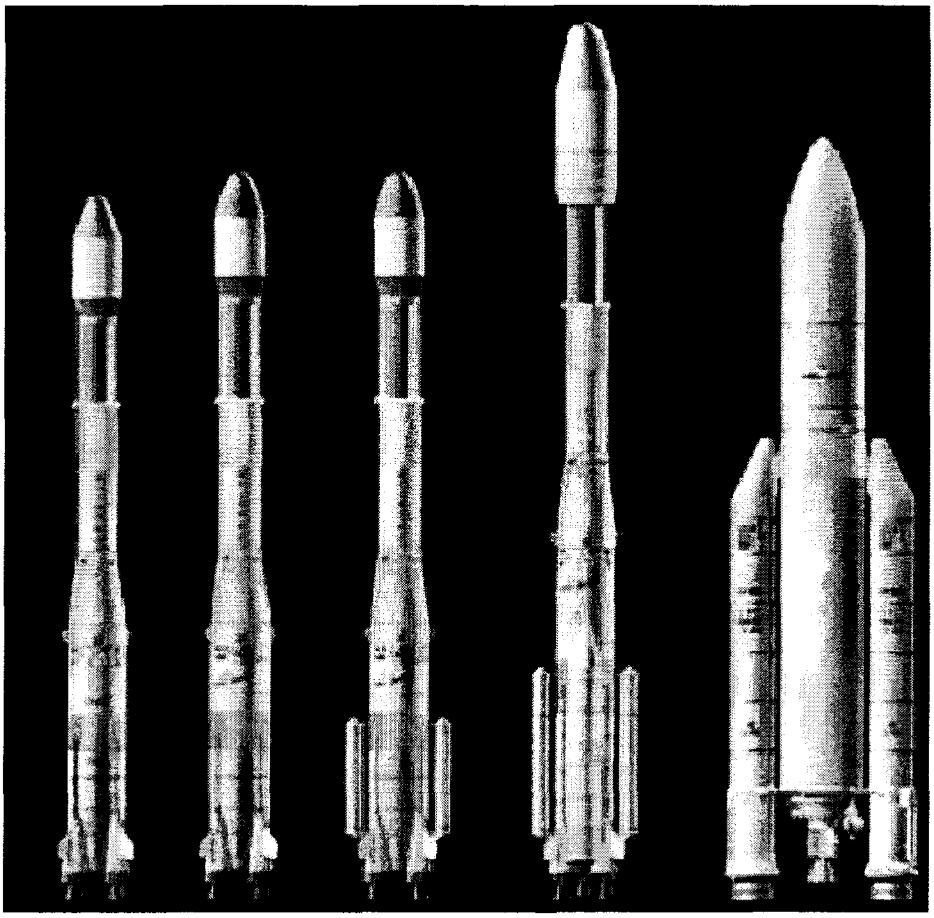

Figure 1 : European Rockets Ariane family from Ariane 1 (left) to Ariane 5 (right).

The European Space Agency ESA and the National Space Agencies of European countries Centre National de Recherches Spatiales CNES in France and Deutsches Zentrum für Luftund Raumfahrt DLR in Germany manage the research on the cryogenic rocket engines. The first stage of the Ariane 5 (Vulcain 2 engine) has a thrust of *1355 kN*. The new cryogenic upper stage engine for the Ariane 5 launcher with *185 kN* of thrust VINCI was tested at DLR Lampoldshausen in 2007 under vacuum conditions, at the test bench P4 within a demonstration programme. The specific impulse (I_{sp}) is the parameter most referred to for evaluating propulsion engine efficiency [Esch, 2003]. It is defined as momentum changes per unit mass of propellant. The specific impulse of the Vulcain second generation reaches *434* seconds in vacuum, compared to *453* for the American Space Shuttle Main Engine (SSME).

The use of high energy cryogenic propellants is still the main international tendency (American Space Shuttles with the SSME engine, European launchers with the Vulcain2 engine, Russian Space Shuttle Energia with the RD-0120). This technology allows an essential enhancement of engine performance. The combination of liquid oxygen (LOX) and liquid hydrogen (LH_2) delivers high calorific enthalpy: $13.4\ kJ\ kg^{-1}$ [Loh, 1968]. The hot gas temperatures resulting from the propellants combustion reach up to *3700 K*, whereas the coolants mostly are below cryogenic temperatures. Considerable thermal gradients are thus observed through the combustion chamber walls.

The materials of the combustion chamber wall have to withstand extreme thermal and mechanical loads which are controlled by efficient cooling. For optimal design of the cooling system, with minimal hydrodynamic loss, precise knowledge of the heat transfer is required. Therefore, the investigations on heat transfer processes are performed at DLR to optimise rocket engine cooling systems, durability and service life.

1.1.2. Cooling Systems

The increase in life and reliability of the combustion chamber is the dominant technical challenge to obtain high performance for the next generation of liquid propulsion engines. Therefore, the prediction of heat transfer characteristics in a cryogenic high performance combustion chamber is one of the most important tasks in the design work of a rocket engine. The material of the chamber must withstand extreme thermal and pressure load. A precise determination of the heat transfer from the hot gas to the external jacket is required. A temperature increase of *40 K* at the chamber walls can reduce a rocket engine's service life by *50%* [Fröhlich, 1993, Immich, 1997].

The heat transfer mechanism through combustion chamber walls needs to be well understood to prepare the next rocket engine generation development. It can be proposed to enumerate the major cooling methods, used in the last *40* years which can be classified in four groups: Film cooling, transpiration cooling, ablation cooling and convective cooling. The cooling systems of real rocket engines usually apply several of these methods simultaneously. For example, the Vulcain *2* uses a film cooling system, a regenerative convective cooling system and an insulation coating (TBC Thermal Barrier Coating).

1.1.2.1. Different technical solutions

- Film cooling

The film cooling method allows the formation of a low temperature gas layer near the internal combustion chamber wall. The coolant fluid is injected through the walls via specially profiled holes or slots. The propellants or the exhaust gas (after the gas generator) are typically used as a cooling medium. Despite the high thermal efficiency of this method, the existence of a relatively cold boundary layer results in a loss of specific impulse foe the engine. A compromise between thermal reliability and engine effectiveness has to be reached. Dynamical and thermal instabilities on the internal walls of the combustion chamber are often investigated to guarantee optimal conditions of the film layer development and its interaction with hot gas main flow. The typical mass flow rate for the coolant reaches up to *3%* of the mass flow rate of the propellant (here hydrogen).

- Transpiration/effusion cooling

With transpiration/effusion cooling, the wall of the combustion chamber is manufactured from porous material (sinter metal, porous ceramic, carbon fiber reinforced in carbon ...). The cooling medium flows through the pores into the combustion chamber and dissipates the thermal energy from the wall material. The main advantage of this method is to considerably reduce the required mass flow and pressure drop (less than *1%* of the total mass flow rate in the combustion chamber used as coolant) that discharge the turbo-pumps and by the way minimize the loss of specific impulse due to the cooling system. Moreover, in a protected atmosphere, the combustion chamber wall can reach very high temperatures without destruction (up to *2900 K*), by applying C/C as combustion chamber material. In spite of these advantages, it is rarely used to design real rocket engines because of the difficulties in manufacturing and the imprecise control of heat and mass transfer through porous materials.

- Ablation cooling

Ablative cooling involves the use of wall materials which undergo endothermic thermal degradation (chemical and physical changes) and consequent mass removal but leave enough material to preserve structural geometry and integrity. The ablation method is based on a thermal protection material fixed on the internal combustion chamber walls. The ablative material is sublimated and a mixture layer is created on the wall, protecting the walls from high temperatures. During this transformation, the sublimation forms a thin layer which dissipates the thermal energy from the wall to the combustion chamber, subsequently reducing wall temperature. In operating conditions the thickness of the ablative layer decreases due to the sublimation process. A special profile must be designed with a variation of the ablative material thickness along the chamber axis, to preserve a permanent optimal profile of the internal walls thus ensuring efficient combustion.

- Convective cooling

The convective cooling method is still the most frequently used cooling method for all kinds of rocket engines. In the next paragraph (1.1.2.2), this method will be described, as well as the use of the regenerative process.

1.1.2.2. The regenerative convective cooling

The convective cooling system is based on transfer of the thermal energy, due to the convective heat transfer process from the combustion chamber to the coolant flowing in cooling channels. Most of the combustion chamber walls are built from a copper alloy with high thermal conductivity to decrease the wall temperature, allowing a high radial heat flux. The determination of the material properties is a challenge of the first order, especially for fatigue resistance. The material used to build the combustion chamber of the Vulcain 2 is the Narloy-Z (*Cu 96.5%, Ag 3%, Zr 0.5%*). The percentages are calculated with global weight rate. The copper alloy Elbrodur G (Cu *99.25%, Cr 0.65%, Zr 0.1%*) is also a good compromise between high conductivity and mechanical strength and is used at DLR Lampoldshausen to build combustion chambers for technology development tests. The coolant fluid flows through the cooling channels in the combustion chamber walls in a double jacket structure. The cooling channel geometry around the combustion chamber must adopt the optimal jacket structure to obtain higher thermal efficiency, small pressure drop (limiting the turbo-pumps loads) and manufacturing feasibility (precise milling of the combustion chamber walls). Figure 2 shows some typical cooling channel designs used successfully in rocket combustion chambers.

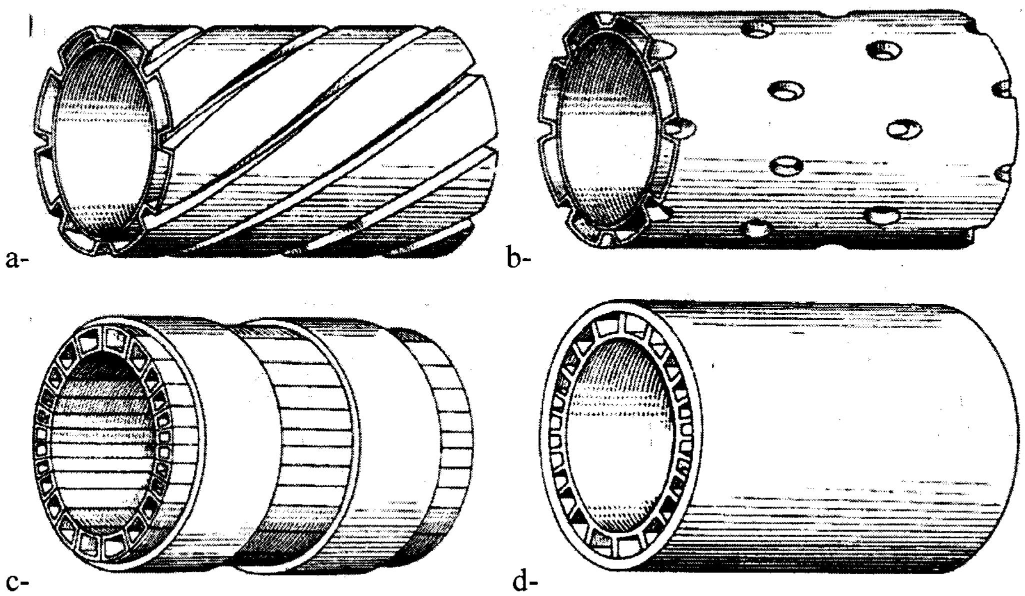

Figure 2 : Different cooling channel geometries [Kudrazwek, 1993]

a- spiralled cooling channels

b- Cooling flows in double walls

c- Welded channels

d- Straight milled channels.

The main challenge to select the adequate cooling channel design is the compromise between thermal efficiency, reduced pressure drop along the channels and acceptable range of mechanical loads (increasing service life). A combination of different cooling channels design is often used. For exemple, the Vulcain 2 nozzle is built with two different types of cooling channels. The upper part of the nozzle is built with machined rectangular cooling channels, directly milled in the chamber walls. The extension of the nozzle uses spiralled welded cooling channels, as shown in Figure 3. In the design of such a system, the method of machining the cooling channels must first be considered, in terms of production, feasibility and costs. To evaluate the efficiency of the convective heat transfer process, parameters such as coolant mass flow, fluid and material properties, geometry and surface roughness must all be taken into account.

To improve the global energy balance, fuel flows through the cooling channels before being injected in the combustion chamber. This is called the regenerative cooling method. Regenerative cooling improves the overall efficiency of the system due to the improved combustion characteristics of higher fuel temperatures at injection imposing greater combustion enthalpy and stability. Moreover, the enthalpy gain of the coolant following passage through the cooling channels may be used to drive the turbo-pumps. This corresponds to a specific engine class: the expander cycles (like the Vinci Engine).

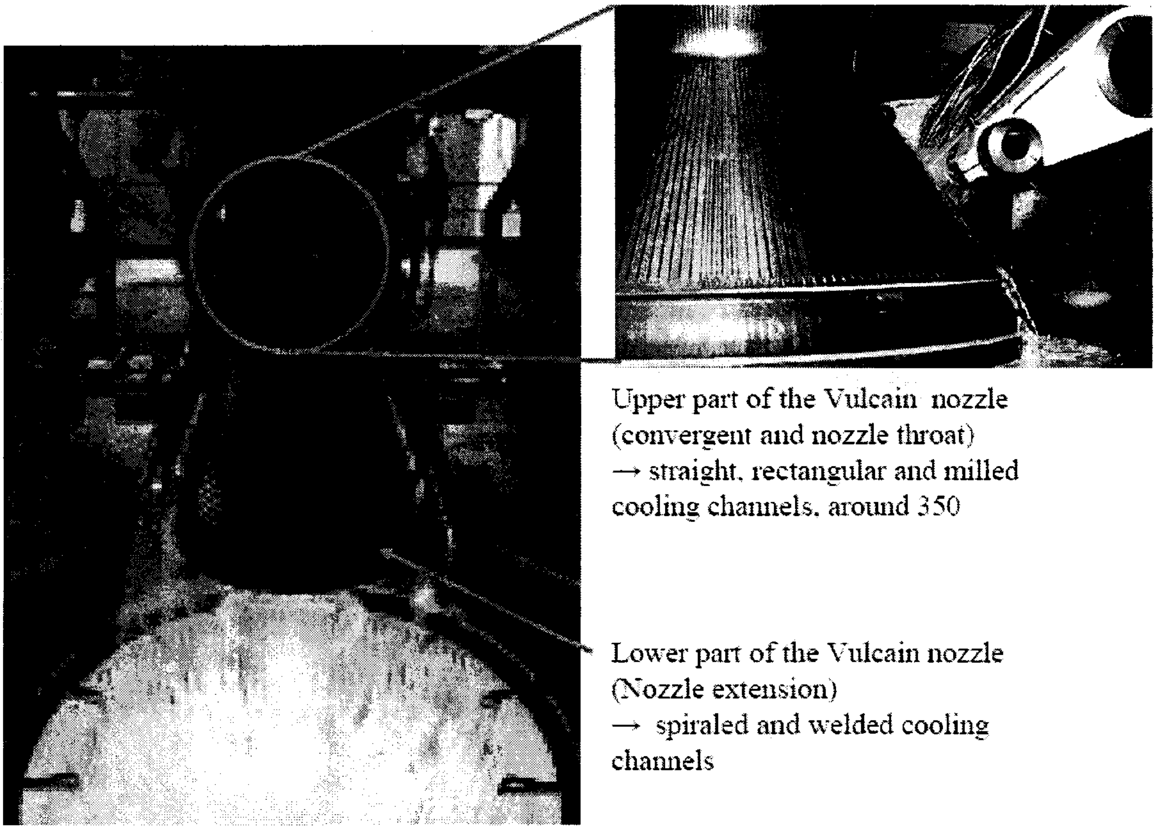

Upper part of the Vulcain nozzle (convergent and nozzle throat)
→ straight, rectangular and milled cooling channels, around 350

Lower part of the Vulcain nozzle (Nozzle extension)
→ spiraled and welded cooling channels

Figure 3 : left: Vulcain 1 at the P5 test bench in the DLR of Lampoldshausen, Right: Upper part of the Vulcain 2 nozzle Straight and machined cooling channels (EADS and DLR pictures).

At the entrance of the channels into the combustion chamber walls of the Vulcain engine, hydrogen has a very low temperature (about $35\ K$), just at the exit of the cryogenic turbo-pump. Along the length of the channel, the hydrogen is warmed up, injected and burned in the combustion chamber. The pressure in the combustion chamber is one important factor influencing the heat flux densities through the chamber walls. The Vulcain 2 engine operates at an internal combustion chamber pressure of $11.5\ MPa$, whereas the SSME (Space Shuttle Main Engine) has an optimal chamber pressure of $20.5\ MPa$. The corresponding heat flux densities reach up to $80\ MW\ m^{-2}$ through the nozzle throat walls of the Vulcain 2 engine. Figure 4 shows a typical heat flux density profile from experimental work on the SSME [Dexter, 2004].

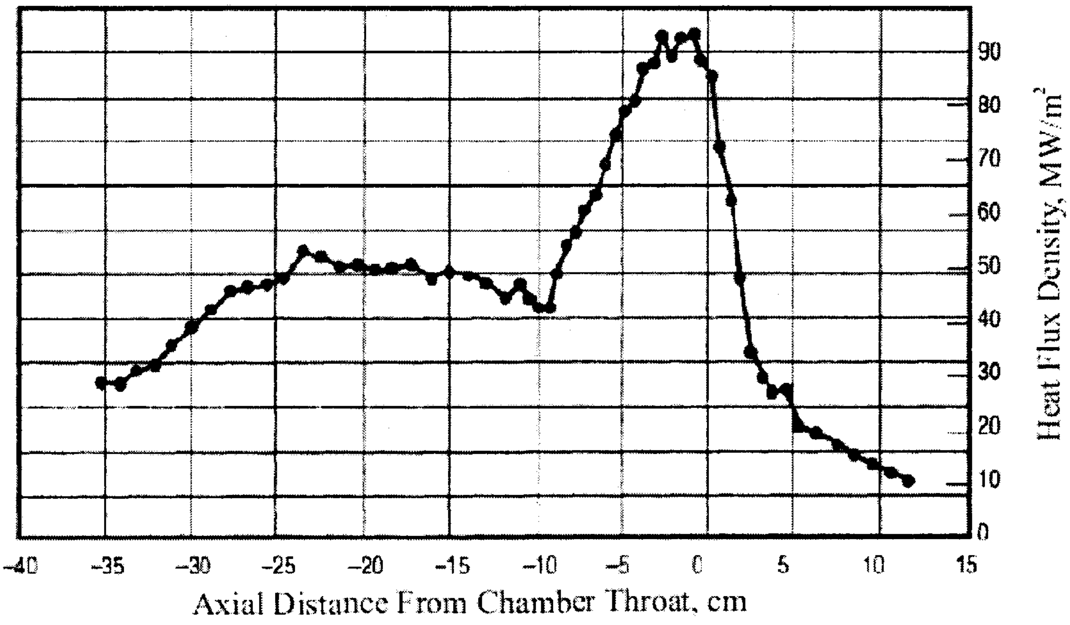

Figure 4 : Measured Heat Flux Density along Chamber Axis of SSME under particular experimental conditions [Dexter, 2004].

The fuel turbo-pump feeds the fluid into the cooling channels and the pressure of the fuel must be high enough to ensure positive backflow margin at the end of the channel. Figure 5 describes the path of the fuel in the regenerative cooling system of a rocket engine (here Vulcain 2). By the way of illustration, several estimations of hydrogen pressure and temperature values along a cooling system of a cryogenic rocket engine are given here [Herbetz, 2001, Fröhlich, 1991]:

- Hydrogen (LH_2) properties at the exit of turbo-pumps and entrance of cooling channels: $T_0 \sim 35\ K, p_0 \sim 160\ bar$
- LH_2 after the passage in cooling channels: $T_1 \sim 110\ K, p_1 \sim 130\ bar$
- Combustion gases after the injectors, in the combustion chamber: $T_2 \sim 3500\mathrm{K}$, $p_2 \sim 115\ bar$

The state of hydrogen in a cooling channel of a rocket engine is shown in an enthalpy-entropy diagram (see Figure 5- c).

A basic calculation of the heat transfer in the cooling channels can be applied to the Vulcain 2 configuration. The heat flux density through the chamber walls is about $40\ MW\ m^{-2}$ for the sections located before the nozzle. An estimation of the chamber area ($\sim 1\ m^2$) gives us the global radial heat flux through the chamber walls: $\sim 40\ MW$. The hydrogen coolant mass flow rate reaches $38\ kg\ s^{-1}$ [Herbertz, 2001] and the heat capacity of the hydrogen at $150\ bar$ does not vary much between $35\ K$ and $300\ K$ (between 12500 and $14500\ J\ kg^{-1}\ K^{-1}$). This gives an estimation of the temperature difference along the cooling channels of the Vulcain 2 engine. The conservation of heat gives a temperature difference of $75\ K$ which has to be evaluated carefully due to wide approximations: averaged heat capacity values along the channel, simplified geometry parameters of the chamber, simplified radial heat flux profile along the chamber walls.

$$\dot{Q}_{radial} = \dot{m}_{channels}\, c_p \Delta T \tag{1.1}$$

Nevertheless, these approximations have been illustrated in Figure 5 a).

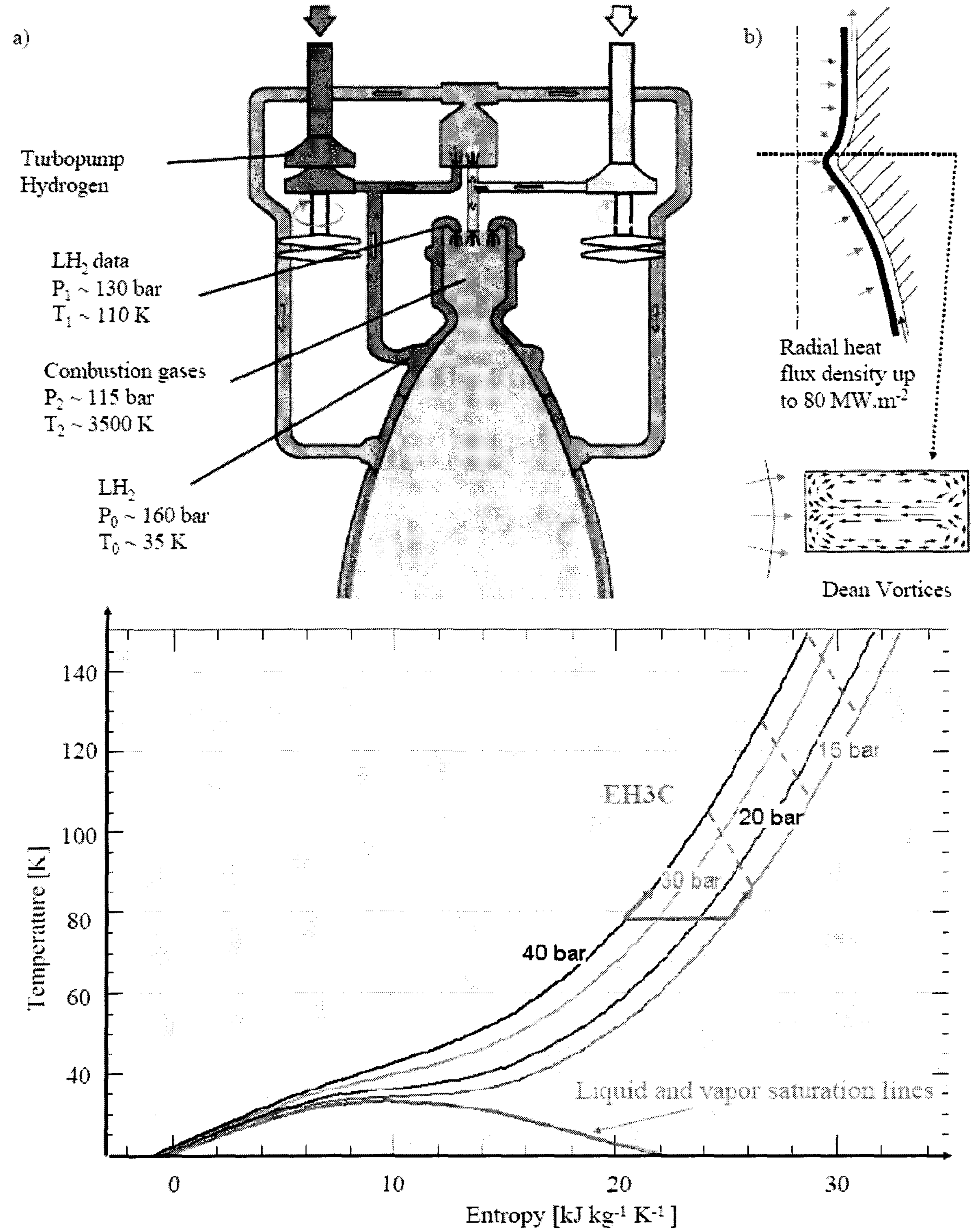

Figure 5 a) Simplified flow diagram of the Vulcain 2 engine, [www.snecma.com] b) Induced secondary motions (Dean Vortexes) in a cross-section of a curved channel c) Hydrogen properties.

The fuel is injected after being forced into the cooling channels. This method allows a high heat flux through the combustion chamber walls (conductive cooling method) and a drastic reduction of temperature walls (down to *800 K*). The pressure loss due to the coolant flow in the micro channels is partially compensated by the regenerative cooling system. Indeed, the energy loss from the turbo-pumps to force the fuel into the cooling channels will be partially compensed by the gain of enthalpy energy, re-introduced in the combustion chamber. A major advantage of this cooling method is the relatively well-known technology of manufacturing the regenerative cooling channels. After turning the chamber in copper alloy, the cooling channels are milled in the chamber (see Figure 3- right). The channel enclosure is ensured by an electro-deposition process with galvanised copper and thus with galvanised nickel for the extern jacket. Particular geometries are applied to elaborate the cooling channels: they receive high aspect ratio geometry, presenting a higher thermal efficiency due to high fin disposition. The dimensions of a HARCC (High aspect ratio cooling channel) vary along the chamber axis, in order to adapt the channel geometry to the local temperature, heat flux and mechanical strength of the chamber wall. For the Vulcain 2 combustor, the cooling channels adopt a high aspect ratio from *5:1* to *9:1*, the height being perpendicular to the chamber axis [Fröhlich, 1991]. At the entrance of the hydrogen collector, the cooling channels present an aspect ratio of *4.6* (*2.6 mm* width to *12 mm* height). At the throat section, the heat flux through the chamber walls can be twice as high as the heat flux at another position in the combustor (*60-80* $MW\ m^{-2}$ through the throat walls instead of *30-40* $MW\ m^{-2}$ for a straight section). Use of a HARCC at the throat section allows better thermal efficiency. The dimensions of the HARCC at the throat section of the Vulcain 2 engine are *1.3 mm* width to *11 mm* height; that gives an aspect ratio of *8.46*.

1.1.3. Curved channels

For an optimal design of the cooling system, precise knowledge of the heat transfer processes and of the hydrodynamic losses in the combustion chamber and in the cooling channels is necessary. More particularly, the effect of curvature in the cooling channels needs to be better analysed numerically and experimentally. The combustion chamber profile imposes some curvatures to the cooling channel, because they follow the nozzle profile of the combustion chamber. These curvatures create secondary flows inside the channel which modify heat flux characteristics through the chamber walls. It is an important industrial goal to estimate the flow distortion due to the channel bends, and to compare the local and global enthalpy gains in comparison to straight channel configurations. Figure 5b illustrates the curved passages and their cross-sections where secondary motions appear (Dean vortices). These secondary motions are pushing fluid from the middle of the channel to the concave wall (see Figure 6). Heat transfer is thus enhanced at the concave wall and reduced at the convex wall. In the case of real rocket engine cooling channels, only one side of the cooling channel, the concave or the convex, is heated as illustrated in Figure 6.

The main advantage of Computational Fluid Dynamics (CFD) is the universal character of the simulation and the extended analyses for obtaining rich data bases. This facilitates comprehension of physical phenomena. One simulation can be easily extended by varying the numerical parameters (geometry, boundary conditions …). It helps to quickly find an optimal technical solution for mechanical and thermal analyses of a system. Recent simulations in Large Eddy Simulations (LES) of asymmetrically heated curved channels [Münch, 2005, Lopes, 2003, Vasquez, 2002] have improved the knowledge of mechanisms inside the channels in terms of fluid dynamics and heat transfer.

Despite recent substantial progress in the numerical simulation of heat transfer processes, an essential requirement is the existence of experimental data. Concerning numerical simulations of rocket engines using Reynolds-averaged Navier-Stokes equations (RANS), a typical reliability of the results can be evaluated at *+/- 20%*. Experimental test cases are always necessary to validate numerical models. Moreover, in the domain of curved channels under high asymmetrical heat flux, reliable experimental results are rare. The curved channels of rocket engines can be described by the following operating points:

- Small channel geometry (less than *1 mm* for the hydraulic diameter)
- Particular curvature (dimension of rocket engine channels)
- Extreme heat transfer density values
- Asymmetrical heating, concerning the concave or the convex channel side
- Real engine typical coolants (Hydrogen, Methane, etc) below supercritical state
- Particular dynamic conditions (Reynolds number up to 5×10^6, Dean number up to 5×10^5).

Configuration	Concave heated wall 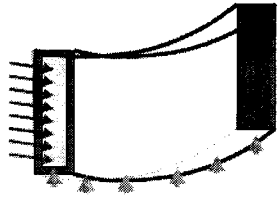		Convex heated wall 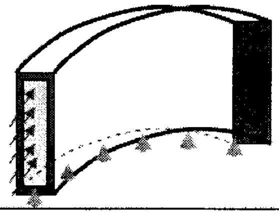	
Heat transfer enhancement	From *+15%* to *+35%*		From *-15%* to *+20%*	
Dean's vortices	Dynamical	Thermal	Dynamical	Thermal
$De = \mathrm{Re}\sqrt{\frac{D_h}{2R_c}}$	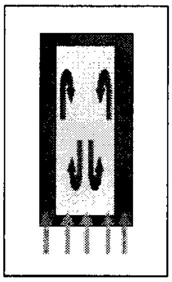	+ bulk flow displaced on hot wall. reduction of fin effect by identical heat flux density	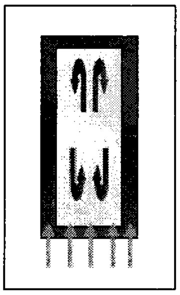	- Bulk flow pushed to the cold concave wall. Enhancement of the fin effect

Figure 6 : Configurations of asymmetrically heated curved channels

Once all these particular operating conditions are obtained, an adequate measurement system must be reliable enough to extract the phenomenon of interest. In a real combustion chamber, where all these operating points are given, it is quite impossible to collect reliable experimental data, due to inaccessibility of sensors in the combustion chamber walls. In all the experiments on real combustion chambers, experimental data reliability is quite low because of spatial resolution problems with sensor implementation. Furthermore, precision of temperature sensor is inversely dependent on the level of heat flux. In real engine experiments, the orientation of thermocouples perpendicular to the iso temperature lines brings about additional systematic temperature errors which are difficult to evaluate. For exemple, the positioning of a temperature sensor in the Vulcain 2 combustion chamber walls generated a temperature field modification in the structure during experiments [Fröhlich, 1993]. A 100 Kelvin deviation was thus applied to the measured temperature after the tests to account for the perturbation effect of the implementation of sensors.

A number of experimental tests were carried out directly on combustion chambers in the Japanese National Space Laboratory in order to identify the role of the curvature on the heat transfer [Niino, 1982, Kumakawa, 1986]. These quality of the results from these tests illustrate the advantage of recreation of all operating conditions (geometry, heat transfer value, coolant, etc). The determination of the heat flux enhancement was deduced from an inverse method, using one thermocouple per cross-section. From these experiments, empirical correlations were developed.

Several other experimental test cases were realised at laboratory scale, in order to better identify the role of channel curvature in heat transfer with better instrumentation than is possible in a real combustion chamber. The drawback of this approach is the difficulty in reaching all representative operating conditions of real engine.

The NASA Lewis research Centre developed a research programme with laboratory scale experimental [Meyer, 1997, Wadel, 1996] and numerical investigations [Wenneberg, 2005] in cooperation with American Universities (Purdue University). In Meyer's experiments, nitrogen was used to cool an electrically heated curved channel. Thermocouples were implemented in the channel wall to locally determine the heat transfer and the modification of the temperature field due to concave and convex curvature. Nitrogen was used at ambient temperature and the heat flux reached ($1\ MW\ m^{-2}$) and the dynamical characteristics (Re up to 1×10^{6}) were relatively small in comparison to real operating conditions. Although the channel geometry was quite similar to rocket engine cooling channels, the heat flux was symmetrically distributed along the convex and the concave sides which does not correspond to reality. A similar experiment was designed at the University of Purdue with concave heating. The results better reflected reality due to the asymmetry of the heating. Nevertheless, this experiment [Sturgis, 1998] does not fulfil all representative operating conditions of a real curved cooling channel of a rocket engine. The dynamic and thermal conditions are under-scaled in comparison to reality (Re up to 1.3×10^{5}, asymmetrical heat flux density up to $0.5\ MW\ m^{-2}$).

The University of Dresden [Neuner, 1998] provided similar experiments with air through a scaled-up, asymmetrically heated channel. The large dimensions of the channel allowed direct access inside the channel to measure the secondary velocity field using hot wire technology. Thermocouples were also mounted in the channel wall to determine the temperature field and the heat transfer characteristics. However, the applicability of the results to real engines is limited due to the scaled nature of experiment in terms of geometry ($D_h=56\ mm$), dynamical (Re up to 4×10^{5}) and thermal (asymmetrical heat flux up to $0.06\ MW\ m^{-2}$) characteristics.

All the preceding experimental investigations have shown heat flux modifications in curved channels in comparison to the straight configuration. Table 1 in paragraph 1.2 summarises the corresponding experimental results. Concerning the case of the cooling channel with its concave side heated, the different results present an enhancement of the heat flux at the concave side between *5* and *40%.* Further experimental and numerical investigations are thus needed to improve knowledge of the range of heat flux enhancement in the particular case of the curved cooling channels of rocket engines.

1.2. Outline of the thesis

Existing empirical correlations produce reasonably accurate results for a limited operational range. Indeed, the correlations can be applied to cooling channels operated under similar experimental conditions in terms of heat flux and temperature range, dynamic and thermal parameters such as(Reynolds number, Prandtl number, Dean number, geometric analogies. However, variation in the considered experimental conditions outside the applicable range of the correlations usually results in loss of reliability. Empirical correlations are generally defined for a limited range of experimental conditions and they are not available for extrapolated conditions. The main goal of experimental test cases is to associate measurement accuracy and representative experimental conditions (near Vulcain 2 cooling channels characteristics).

At the nozzle throat section of the Vulcain 2 engine, hydrogen in the curved cooling channels has a pressure of approximately *140 bar* with a bulk temperature of *70 K*. The corresponding mass flow rate is $100\ g\ s^{-1}$ for a channel with width $w=1.3\ mm$ and height $h_c=11\ mm$, [Fröhlich, 1991]. Thus, the following Re, Pr and De are calculated to have an estimation of the Vulcain 2 engine conditions:

$$\mathrm{Re}_{vulcain} = \frac{\rho_{Vulcain}\, u_{vulcain}\, D_{h\,vulcain}}{\mu_{vulcain}} = 2.7\times10^{6} \tag{1.2}$$

$$\mathrm{Pr}_{vulcain} = \frac{\mu_{vulcain}\, c_{p\,vulcain}}{\lambda_{vulcain}} = 0.81 \tag{1.3}$$

$$De_{vulcain} = \mathrm{Re}_{vulcain}\sqrt{\kappa_{vulcain}} = 2.7\times10^{6}\sqrt{\frac{2.33\times10^{-3}}{2\times0.7}} = 1.1\times10^{5} \tag{1.4}$$

where R_c is the curvature radius and $\kappa = \dfrac{D_h}{2\cdot R_c}$ the curvature coefficient. **(1.5)**

Experimental results are needed to extend the range of applicability of the existing empirical correlations and to check the numerical resolutions. However, reliable experimental data are difficult to obtain under extreme thermal, mechanical and dynamic conditions such as those found in the cooling channels of rocket engines. Data precision and reliability are one of the most important challenges in rocket engine development when considering the high development costs and safety requirements. In the throat section of the combustion chamber, experimental data are difficult to collect, because of difficult accessibility and high thermo-mechanical loads. This means that existing empirical correlations and numerical simulations need to be checked by means of reliable experimental measurements.

The project EH3C (Electrically Heated Curved Cooling Channels) was sponsored by the German Space Propulsion Institute (DLR) within the scope of this PhD work. Two test specimens were designed, built and tested at the DLR Lampoldshausen. These 2 test specimens consist of 2 asymmetrically heated cooling channels each, one straight and one curved. Numerical simulations were provided in order to reproduce the EH3C experimental conditions within the scope of this PhD. This work is supervised by the University of Valenciennes and the Hainault Cambresis.

The EH3C experimental work uses a set of temperature and pressure sensors (*98* thermocouples, *3* pressure sensors) in order to identify the role of the curvature in the asymmetrical heat transfer. The advantage of having an electrically heated channel means better accessibility to the channel neglecting all sources of imprecision from combustion. Indeed, in real engine tests, it is quite difficult to determine the hot gas side heat flux characteristics.

Moreover, the EH3C experiment reaches a very high level of asymmetrical heat flux density ($\sim 17\ MW\ m^{-2}$) in comparison to all other experiments with electrically heated channels. The role of asymmetry in terms of heat flux is an important factor (refer to Paragraph 2.2.2). The EH3C experiments use real coolant in electrically heated channels, like hydrogen and methane.

The Table 1 summarises the experimental conditions of the different test cases, already presented in Paragraph 1.1.3. Colours have been added in order to characterise the operating points of the experiments. In blue the operational range of flow and heat transfer in a real cooling channel of rocket engine is described (Vulcain 2 cooling channels). green respresents good experimental reliability as to real engine configuration, yellow indicates relatively unrepresentative conditions and orange indicates a different range of experimental data in comparison to the real case.

Exp.	Re	De	Coolant	Pr	Heat Flux Density	AR	Instrumentation & Precision
	[-] (10^5)	[-] (10^5)		[-]	[$MW\ m^{-2}$]	[-]	
Vulcain 2*	*27*	*1.1*	H_2	*0.81*	Asym. *80*	*4.6* to *8.46*	
Taylor*, 1968					Sym.		
Niino* - Kumakawa* 1982, 1986			H_2		Asym. *30*	*5* to *8*	*1* time ~*7* TCs
Meyer$^+$ 1997	*10*	*2*	N_2	~ *0.7*	Sym. *1.7*	*1* and *10*	TC
Neuner$^+$ 1998	*4*	*0.7*	Air	~ *0.7*	Asym. *0.06*	*8*	~*8* times *6* TC + Hot wire
Sturgis$^+$ 1999	*1.3*	*0.3*	FC-72	~*10*	Asym. ~*0.5*	*2*	*3* times *5* TCs
Torres$^+$ 2008 (EH3C)	*3.3*	*0.22*	H_2	*0.75*	Asym. *17*	*9.2*	*98* TCs → 7% measurement error
	2.3	*0.156*	CH_4	*0.8*	Asym. *2*	*9.2*	
					Asym./Sym.	AR	
$^+$electrically heated *Real engine					Asymmetrical/ Symmetrical	Aspect Ratio	TC Thermocouple

Table 1 : Test cases and experimental conditions for heated curved cooling channels.

The thesis can be divided into four main chapters.

Firstly, an detailed review of empirical correlations and numerical simulations of fluid flow and heat transfer in curved cooling channels is presented. All particularities of a channel of a rocket engine are taken into account.

Secondly, the design of the EH3C test specimens is presented, as well as the fluid dynamical and heat flux operating conditions achieved. The measurement error and an inverse method are defined to analyse the experimental results.

Chapters three and four respectively deal with the numerical simulation work conducted, and the presentation of the experimental results. The data are thus analysed, compared and interpreted.

2. Heat and Fluid Flow Transfers in Cooling Channels

During the last 100 years, the heat and fluid flow transfers in pipes have been largely investigated, theoretically and experimentally. Concerning the cooling channels of rocket engines, a special configuration of heat transfer, mass transfer and channel geometry has to be taken into account:

- Small channel dimension ($D_h \sim 1\ mm$)
- Rectangular cross-section
- High Aspect Ratio Cooling Channel, HARCC, up to *15*
- Curved channel, $R_c \sim 100\ mm$
- High heat flux density (up to $80\ MW\ m^{-2}$)
- Asymmetrical heat flux through concave or convex side (smaller side)
- High Reynolds number ($\sim 3 \times 10^6$), high Dean number ($\sim 10^5$)
- Fluid in supercritical state

A review of several empirical correlations and experiments is presented in this chapter, analysing the different particularities of the cooling channels of rocket engines.

2.1. Flow in pipes

2.1.1. Theory and Empirical Correlations

The energy cost of pumping a fluid through a pipe has always played a critical role in industrial research. In the case of space propulsion, the rocket is an independent energy system which has to deliver reliable propulsion conditions. The turbo-pumps have to deliver special conditions of pressure and temperature of the propellants at the entrance of the injector head and along the cooling systems. Liquid hydrogen and oxygen are filled into pressurized tanks (up to *5 bar*). The turbo-pumps must afterwards increase the pressure (up to *300 bar*) to reach the operating points of the combustion chamber and of the cooling systems. In order to gain an overview of pressure drop relations through cooling channels, empirical and theoretical correlations of the friction factor and of pressure losses are investigated.

- *Classical correlations of pressure losses*

In circular pipes, the pressure losses and the friction factors have been very often investigated and checked experimentally [Idelchik, 2005, Moody, 1944, Schlichting, 1968].

The circular pipe has a diameter D ($D > 1\ mm$) and a length l_{tot}. The fluid along the channel flows with an axial velocity w and has the following thermodynamic parameters: density ρ, pressure p, temperature T (averaged temperature over a pipe cross-section), kinematic viscosity ν, dynamic viscosity μ, specific heat capacity (at constant pressure) c_p

and thermal conductivity λ. The fluid properties are supposed to be constant over a pipe cross section in this paragraph.

From these notations, the non-dimensional Reynolds number can be defined, based on the main flow:

$$\mathrm{Re} = \frac{\rho w D}{\mu} \tag{2.1}$$

The Reynolds number corresponds to the ratio of the inertial forces to viscous forces.

The most common definition of the friction factor ξ is linked to the wall shear stress τ_w, [Schichtling, 1968].

$$\Delta p = \xi \frac{l_{tot}}{D_h} \frac{1}{2} \rho w^2 \tag{2.2}$$

$$\text{where } \xi = \frac{\tau_w}{\frac{1}{8} \rho w^2} \tag{2.3}$$

For circular pipes and for isentropic flows, several empirical correlations have been defined, for different ranges of *Re*.

The laminar friction factor, with $\mathrm{Re} < 2300$, was theoretically analysed by Blasius, [Blasius, 1911] giving the basic relation:

$$\xi = \frac{64}{\mathrm{Re}} \tag{2.4}$$

The turbulent flows in circular smooth tubes, with $2300 < \mathrm{Re} < 10^5$, have been experimentally investigated and the most used correlation was defined by Blasius [Schlichting, 1968] too:

$$\xi = 0.3164 \times \mathrm{Re}^{-0.25} \tag{2.5}$$

For higher Reynolds numbers in circular smooth pipes, $\mathrm{Re} > 10^6$, the classic e of Prandtl and von Karman [Schlichting, 1968] can be applied, taking the velocity defect ratio laws as reference:

$$\sqrt{\frac{1}{\xi}} = -0.8 + 2\log_{10}\left(\mathrm{Re}\sqrt{\xi}\right) \tag{2.6}$$

Another empirical correlation was proposed by [McAdams, 1932] presenting good reliability (*+/-5%*) with experiments [Scaggs, 1988]:

$$\xi = 0.0056 + \frac{0.5}{\mathrm{Re}^{0.32}} \tag{2.7}$$

- *Influence of roughness*

Noting k_s^+ the reduced roughness factor and $k_{rel} = \frac{k_s}{D_h}$ the relative one:

$k_s^+ = \frac{k_s W_\tau}{\upsilon}$, where k_s is the averaged roughness (so called *Ra*) and W_τ the main flow friction velocity $W_\tau = \sqrt{\frac{|\tau_w|}{\rho}}$

A pipe is considered as smooth for a reduced roughness k_s^+ lower than *5*. Indeed, $k_s^+ < 5$ indicates that the roughness height is contained in the viscous sub layer $y^+ = \frac{y w_\tau}{\upsilon} < 5$ and has no influence on the rest of the turbulent flow.

Considering the influence of roughness in terms of flow resistance and friction enhancement, two classic empirical correlations (Colebrook, Miller) are commonly applied for rough pipes with $5 < k^+ < 60$, [Gersten, 1983]:

$$\sqrt{\frac{1}{\xi}} = 1.74 - 2\log_{10}\left(\frac{2k_s}{d} + \frac{18.7}{\mathrm{Re}\sqrt{\xi}}\right) \tag{2.8}$$

$$\xi = \frac{0.25}{\left[\log_{10}\left(\frac{k}{3.7d}\right) + \frac{5.74}{\mathrm{Re}^{0.9}}\right]^2} \tag{2.9}$$

For a fully rough surface ($k^+ > 70$), the classic of von Karman can be used:

$$\sqrt{\frac{1}{\xi}} = 1.74 - 2\log_{10}\left(\frac{2k_s}{d}\right) \tag{2.10}$$

- *Capillary flows*

Capillary tubes have been experimentally investigated to determine the friction factors [Choi, 1991]. When the hydraulic diameter reaches the dimension of the Kolmogorov scale, the radial turbulent dissipation is minimised, inducing a reduction of friction stresses. For rectangular hydraulic diameter under *0.08 mm*, with a Reynolds number up to $2{\cdot}10^4$, the classic empirical correlation of Blasius was modified:

$$\xi = 0.14 \times \mathrm{Re}^{-0.182} \tag{2.11}$$

- *Rectangular channels*

All the preceding correlations have thus to be modified to take into account the rectangular geometry of the pipes, inducing shear stress asymmetries and modifications of classic pressure loss laws [Schlichting, 1968].

The determination of the friction factor for turbulent flow in a rectangular duct is much more complex than in circular pipes. First of all, an equivalent diameter (hydraulic diameter) is defined to adapt correlations and theory from circular ducts to noncircular ones.

$$D_h = \frac{4S}{P_w} \tag{2.12}$$

where P_w is the wetted perimeter of the S-surface cross-section.

Moreover, geometrical asymmetries (due to wall corners) cause secondary flows that move fluid from low to high shear stress regions inside the flow. The fluid moves from the centre of the channel to the corner, creating secondary flows, see Figure 7.

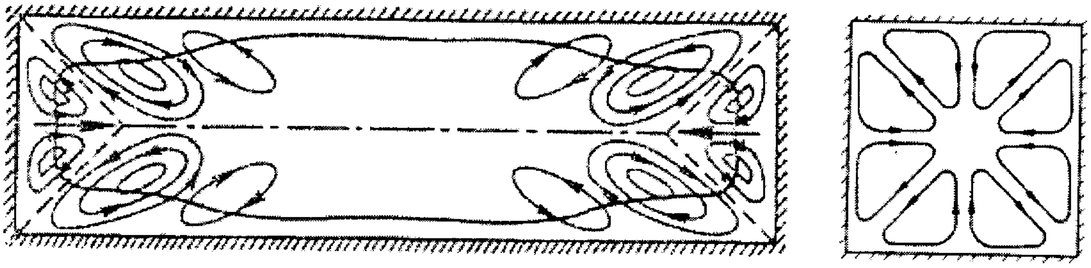

Figure 7 : Secondary flows in noncircular pipe section [Gersten, 1983].

The displacement of the iso-velocity lines can be observed in Figure 8. The influence of edges by turbulent flows on the main velocity profile over a cross-section of the rectangular channels is evident.

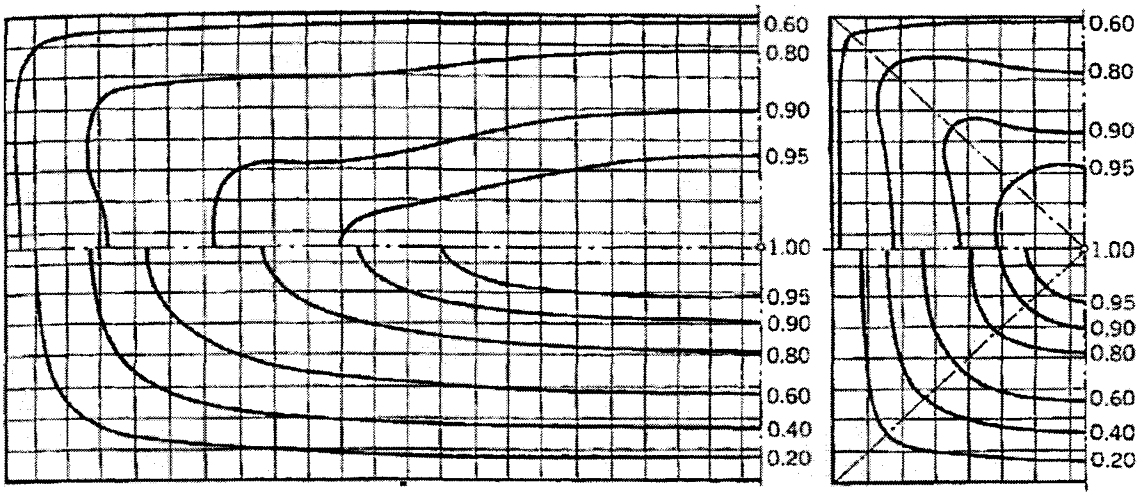

Figure 8 : Iso-velocity profile (scale is the relative axial velocity w referred to the maximal main velocity w_0) in rectangular (left) and square channel (right) for laminar (down) and turbulent (up) flows [Leutheusser, 1963].

For laminar flows, the friction factor through a non-circular pipe differs from a circular pipe configuration. It has been experimentally proven that the aspect ratio (height over width ratio), noted *AR*, plays a major role too.

For a square pipe, the following friction factor was determined [Gersten, 1983]:

$$\xi = \frac{56.9}{\mathrm{Re}} \tag{2.13}$$

and for a rectangular channel, with an aspect ratio of *5* [Gersten, 1983]:

$$\xi = \frac{76.3}{\mathrm{Re}} \tag{2.14}$$

For higher aspect ratio channels, $7 < AR < 169$, Dean proposed the following expression of the friction factor for laminar flows, [Dean, 1978]:

$$\xi = \frac{48}{\text{Re}} \tag{2.15}$$

In the case of turbulent flows, due to geometrical asymmetries, the turbulence repartition is neither homogeneous (varying turbulence intensities in space) nor isotropic (different turbulence contributions according to x, y and z directions). These secondary flow velocities reach a maximum of *1-2%* of the axial velocity [Gersten, 1983] and significantly modifie the global pressure losses. In reference to the main velocity, this secondary flow intensity decreases with increasing Reynolds number of the main flow [Gessner, 1965]. That means that the influence of these secondary velocities is restricted in highly turbulent flows.

Moreover, it was observed, too, that the friction factor does not have any dependence on aspect ratio when $AR > 7$, for laminar or turbulent flows [Gessner, 1965]. This can be explained by the fact that with high aspect ratio, the opposite corners are closer and the "edges" vortices join together. The secondary velocity pattern does not change anymore for $AR > 7$ channels.

The classic Prandtl for a turbulent flow through a circular pipe was applied by Leutheusser, [Leutheusser, 1963] to rectangular ducts. The experimental results for an $AR=3$ are overestimated by *3%* by the classic Prandtl . These experimental results were numerically simulated by Naot et al. using a Reynolds stress turbulence model which is a non-isotropic turbulence model [Naot, 1974]. Good accordance has been found for high Reynolds number flows (up to 1.5×10^5).

Hartnett compiled many experimental results [Hartnett, 1962] and deduced that the role of aspect ratio of the rectangular geometry can be neglected. The Prandtl expression for a circular tube confirms more than 10 different experimental results of turbulent flows (Re up to 2×10^5) through rectangular channels (AR up to 169) with an accuracy of *+/-20%*. For empirical correlations, applied to a set of experimental results, it is common to obtain this kind of inaccuracy.

With a larger set of experimental data, including those from Hartnett, Jones proposed a modified Prandtl equation, taking into account a modified expression of the Reynolds number, Re^* [Jones, 1976]. He pointed out that the use of hydraulic diameter was not appropriate to high aspect ratio channels. The Re^* expression comes from laminar investigations, to corroborate the classic friction factor correlation of Blasius in rectangular channels:

$$\xi = \frac{64}{\text{Re}^*} \tag{2.16}$$

It has been found that:

$$\text{Re}^* = \text{Re}\left(\frac{2}{3} + \frac{11}{24}\frac{1}{AR}\left(2 - \frac{1}{AR}\right)\right) \tag{2.17}$$

Including this expression of Re^* in the classic correlation of Prandtl to determine friction factors in rectangular channels with turbulent flows, Jones obtained a good approximation (under *5%*) of friction factors.

The same experimental data collection was studied by Dean, [Dean, 1979].

These data concern turbulent flows (*Re* up to 10^4) with high aspect ratio rectangular channel ($7 < AR < 169$). Two correlations expressing the friction factor have been established. They both characterise all different experimental results with an accuracy of *+/-15%*. The first correlation refers to the Blasius law and the second one adapts the velocity defect law of Nikuradse [Schlichting, 1968] for high aspect ratio channels:

$$\xi = 0.292 \times \mathrm{Re}^{-0.25} \qquad \textbf{(2.18)}$$

and $$\sqrt{\frac{1}{\xi}} = 0.96 + 1.16\log_{10}\left(\mathrm{Re}\sqrt{\xi}\right) \qquad \textbf{(2.19)}$$

From all the preceding results, it can be summarised that for turbulent flows, the friction factor depends on aspect ratio. For an $AR=3$ channel, the pressure loss is *3%* lower than for circular pipes. The pressure losses through rectangular channels become independent from aspect ratio for higher aspect ratios than *7*. Figure 9 shows the variation of the friction factor depending on the aspect ratio, taking into account the experimental results of Leutheusser [Leutheusser, 1963] and the investigations of Dean [Dean, 1979].

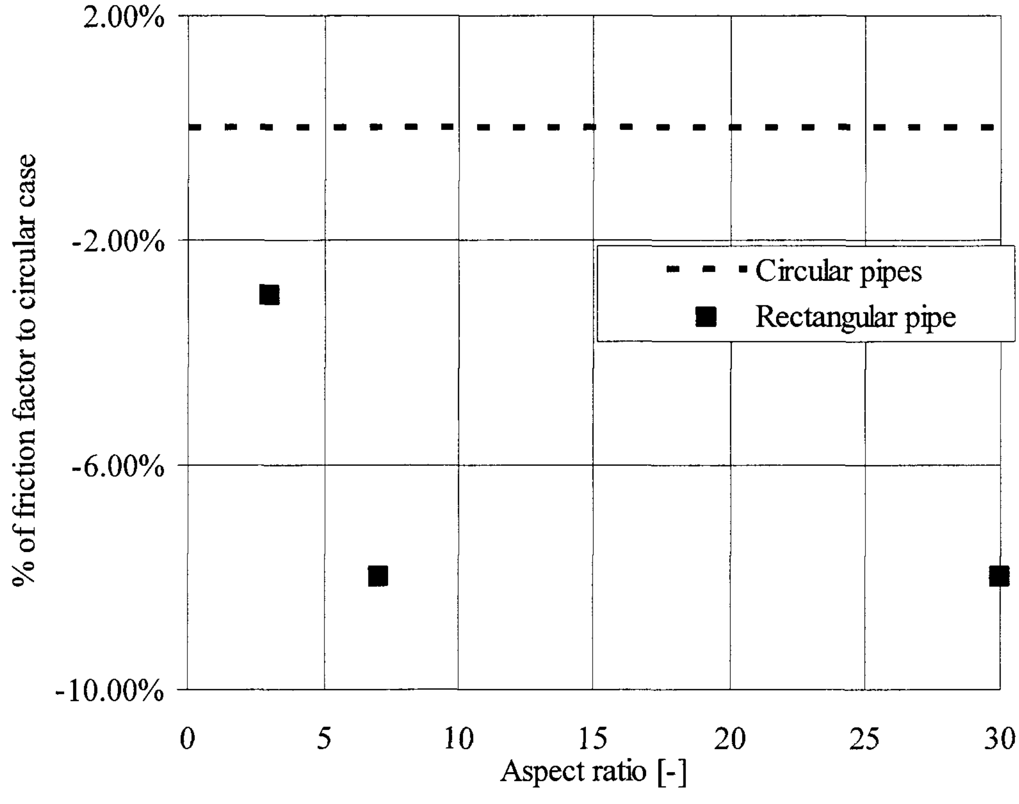

Figure 9 : Friction factor dependence with aspect ratio of rectangular channels, [Leutheusser, 1963, Dean, 1979].

- *Fanno flows*

For adiabatic, one dimensional and steady state flows, through a constant area pipe, the friction forces can be considered and this brings irreversible flows in comparison to isentropic flows. The Fanno flow approach takes into account the compressibility of the fluid. The classic relation of the pressure loss cannot be easily used in the case of compressible flow because of the change of the flow density along the pipe. The Fanno flow model [Zucrow, 1976] defines the maximum length of a duct, L_{max} which corresponds to the longer subsonic length of the channel by subsonic inlet conditions and by considering frictional effects. The friction factor is supposed to be constant along the length of the channel. By isothermal flow, this assumption is validated because of constant Reynolds number all over the channel length (constant mass flow rate and constant viscosity). The Mach number M is the fluid to sound velocity ratio.

$$\frac{\bar{\xi} L_{\max}}{D_h} = \frac{1-M^2}{M^2} + \frac{\gamma-1}{\gamma}\ln\left(\frac{\frac{\gamma+1}{2}M^2}{1+\frac{\gamma-1}{2}M^2}\right) \tag{2.20}$$

Applying this relation for two subsonic points along a pipe with constant area, for an adiabatic and isothermal flow, it is possible to connect the inlet and outlet Mach numbers:

$$\left(\frac{\bar{\xi} L_{\max}}{D_h}\right)_{in\rightarrow sonic} = \left(\frac{\bar{\xi} L_{\max}}{D_h}\right)_{outlet\rightarrow sonic} + \left(\frac{\bar{\xi} L_{tot}}{D_h}\right)_{in\rightarrow outlet} \tag{2.21}$$

Assuming the perfect gas model for the fluid, it is possible to link the static pressure ratio to the Mach number ratio:

$$\frac{p_{out}}{p_{in}} = \frac{M_{in}}{M_{out}}\left(\frac{1+\frac{\gamma-1}{2}M_{in}^2}{1+\frac{\gamma-1}{2}M_{out}^2}\right)^{1/2} \tag{2.22}$$

- *Curved channels*

When flow is turned, pressure and velocity distributions change. The centrifugal force is applied on unit volume fluid elements:

$$F_{cent} = \rho\frac{w^2}{R_c} \tag{2.23}$$

R_c being the streamline curvature radius of the considered fluid element. The concave side is the outside of the curve seen from the inside of the pipe. A schema describes the force balance on a fluid element between two curved plates in a 2-dimension flow, see Figure 10.

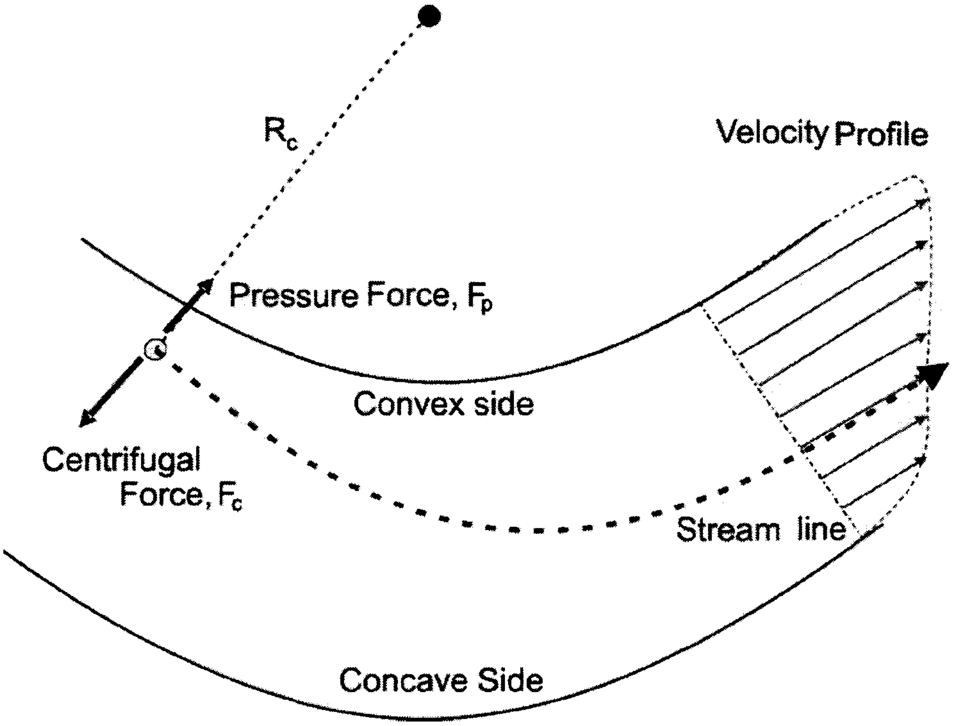

Figure 10 : Typical forces balance in curved channel.

In the curved pipes, the stationary flows present a radial pressure gradient, created by reaction of the wall to the centrifugal forces. This ratio of forces can be unstable in certain zones of the pipe, like concave boundary layers, or near lateral walls. In extreme cases, if the convex curvature and the main velocity are strong enough, local separation of the flow on the convex side can be observed. Some recirculation zones or highly unstable flow zones can appear. All these structural modifications due to the curvature induce variation of the flow stratification and of its global pressure loss along a pipe. These influences were investigated, and some empirical correlations can be used to characterise the curvature effects on the friction factor.

The flow structures in curved pipes are always characterised by the Reynolds number and by the curvature coefficient κ.

$\kappa = \dfrac{D_h}{2R_c}$, where R_c is the curvature radius. **(2.24)**

Laminar flows are perturbed by curvature and the friction factor enhancement was investigated by Adler, [Adler, 1934]

$$\left(\frac{\xi_c}{\xi_s}\right)_{laminar} = 0.106 \times \left[\frac{1}{2}\mathrm{Re}\,\kappa^{0.5}\right]^{0.5} \qquad \textbf{(2.25)}$$

and by Prandtl [Prandtl, 1949, quoted by Gersten, 1983]

$$\left(\frac{\xi_c}{\xi_s}\right)_{laminar} = 0.37 \times \left[\frac{1}{2}\mathrm{Re}\,\kappa^{0.5}\right]^{0.36} \qquad \textbf{(2.26)}$$

The transition from a laminar flow to a turbulent one does not operate at the same conditions as in a straight pipe configuration. Assuming that the transition Reynolds number for a straight circular pipe is *2400*, the corresponding transition Re for a curved duct is proposed here [Gersten, 1983]:

$$\mathrm{Re}_{trans} = 2400 \times \left[1 + 8.6\kappa^{0.45}\right]^{0.45} \qquad \textbf{(2.27)}$$

Indeed, the presence of secondary flows in the bend tends to stabilize the flow. A velocity fluctuation is damped by the centrifugal forces and the transversal pressure gradient. By the way, the transition from laminar to turbulent flow appears at higher Reynolds number.

Within a range of $0.034 < \mathrm{Re}\cdot\kappa^2 < 300$, for fully turbulent flows, the following empirical correlation was developed by Ito to define the friction factor [Ito, 1959]:

$$\xi\sqrt{\frac{1}{\kappa}} = 0.029 + 0.304\left[\mathrm{Re}\,\kappa^2\right]^{-0.25} \qquad \textbf{(2.28)}$$

Over this range, it means for $\mathrm{Re}\cdot\kappa^2 > 300$, Ito proposes two empirical correlations, the first one taking into account the friction factor in a straight pipe defined by Blasius for turbulent flows:

$$\frac{\xi_c}{\xi_s} = \left[\mathrm{Re}\,\kappa^2\right]^{1/20} \qquad \textbf{(2.29)}$$

where $\xi_s = 0.3164 \cdot \mathrm{Re}^{-0.25}$ and the second one based on the velocity-distribution law:

$$\sqrt{\frac{1}{\xi_c}} = 2.11 \times \log_{10}\left(\mathrm{Re}\sqrt{\frac{1}{\kappa}}\xi_c^{3/2}\right) - 0.23 \qquad \textbf{(2.30)}$$

These two empirical correlations were checked and validated by analytical investigations [Mori, 1967]. Over the application range $0.034 < \mathrm{Re}\cdot\kappa^2 < 300$, the proposed analytical expression by Mori corroborates very well the empirical results of Ito. Nevertheless, the authors calculated *7* to *8%* errors for the second Ito correlation. Several empirical correlations were respectively proposed by White [White, 1929]

$$\frac{\xi_c}{\xi_s} = 1 + 0.075 \times \left[\mathrm{Re}\,\kappa^2\right]^{0.25} \qquad \textbf{(2.31)}$$

and by Gnielinski[Gnielinski, 1976]

$$\xi_c = \frac{0.3164}{\mathrm{Re}^{0.25}} + 0.04 \times \kappa^{0.5} \qquad \textbf{(2.32)}$$

All the preceding empirical correlations assume that the curvatures are long enough to develop the centrifugal instabilities and imply consequent differences with straight channels. By considering ducts with small curvature angles (less than *20°* as turning angle for example) it is not possible anymore to consider all the preceding correlations (they only calculate the "curved" friction factor with the pipe dimensions, flow characteristics and the curvature radii but not with the length of the curvatures). Nevertheless, an additional loss coefficient has been introduced to take into account additional pressure losses due to "length" of the curvature (turning angle θ). Indeed, by longer curvature the pressure loss will be higher and not linear to the tube length. To the classic friction factor in a straight pipe ξ_s, a component directly linked to the turning angle ξ_θ can be added [Gersten, 1983].

$$\xi_c = \xi_{c,White} + \xi_\theta \frac{D_h}{l_{tot}} \qquad \textbf{(2.33)}$$

For $\mathrm{Re}\,\kappa^2 < 91$,

$$\xi_\theta = 0.00873 \times \alpha_\theta \kappa \xi_c \qquad \textbf{(2.34)}$$

where α_θ is a blending function: $\begin{array}{l} \alpha_{\theta=45^\circ} = 1 + 14.2 \times \kappa^{-1.47} \\ \alpha_{\theta=90^\circ} = 0.95 + 17.2 \times \kappa^{-1.96} \end{array}$

For $\mathrm{Re}\,\kappa^2 > 91$,

$$\xi_\theta = 0.0024 \times \alpha_\theta \kappa^{0.84} \mathrm{Re}^{-0.17} \qquad \textbf{(2.35)}$$

Figure 11 illustrates the three main correlations [Gnielinski, White and Ito] and the correction of Gersten with White's correlation for a constant Reynolds number of 5×10^4 of the flow in a circular pipe with constant diameter ($D_h=0.01\ m$) by changing the curvature radius.

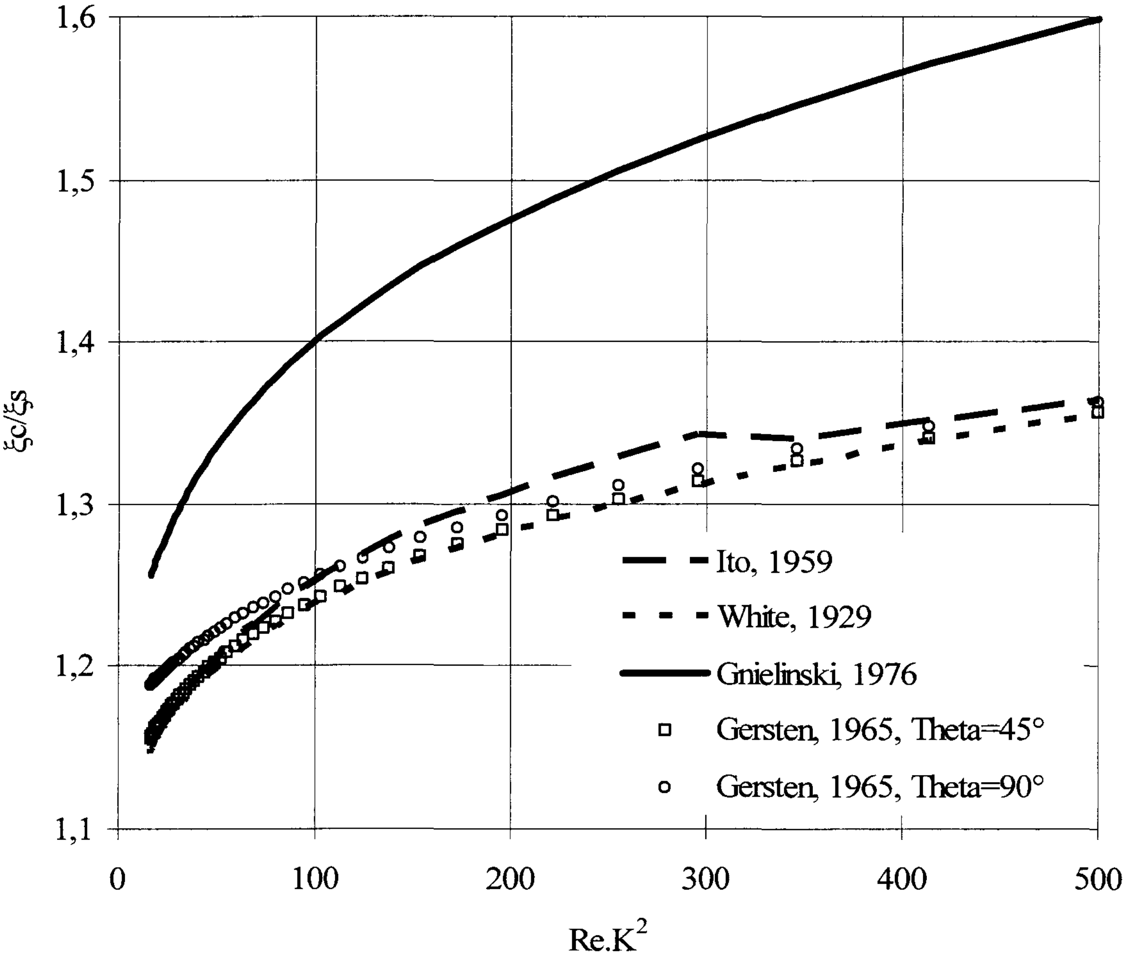

Figure 11 : Curved to straight friction factor ratio for turbulent flows (*Re* = *5·10⁴*) in curved pipe (*0.018<K<0.1*).

The internal 3 dimensional structure of the instabilities in curvatures need to be classified and analysed. The two most famous instabilities and secondary motions due to curvature were described and analysed by Görtler and by Dean, [Görtler, 1940, Dean, 1927-1928]. In all this work, the Taylor instabilities are not studied (when walls are rotating or moving).

2.1.2. Görtler Vortices

For flows on concave surfaces, the boundary layer thickness and turbulent fluctuations are submitted to centrifugal instabilities. Characterised by the Rayleigh criteria [Petitjeans, 1995, Jeschke, 1998], these instabilities introduce secondary flows. For turbulent flows, these centrifugal instabilities on concave surfaces have been characterised by Görtler [Görtler, 1940].

Under particular conditions, the fluid adopts a "mushrooms configuration" on concave walls, in high velocity variation zones, typically within the boundary layer thickness. The appearance of these instabilities can be correlated with a non-dimensional number: the "Görtler" number [Görtler, 1940].

$$G\ddot{o} = \mathrm{Re}_{\delta}\sqrt{\frac{\delta}{R_c}} \qquad \textbf{(2.36)}$$

δ being the boundary layer thickness and Re_{δ} the corresponding Reynolds number.

In the laminar domain, the concave side has a stabilising role (increasing the critical transition Reynolds number from laminar to turbulent). Indeed, the convex side presents a lower critical Reynolds number than the concave side, to characterize the laminar-turbulent transition. This means that the flow separation or the first appearance of turbulence appears at the convex side. On the contrary, in the turbulent regime, it has been observed (numerically and experimentally) that the concave side enhances turbulent mixing and destabilises the main flow, whereas the convex side is stabilizing the main turbulent flow [Tani, 1962, So, 1973]. Figure 12 describes a typical main velocity profile in which Görtler rolls appear on the concave side. The Rayleigh criterion delimits the appearance zone of centrifugal instabilities which strongly modify the boundary layer thickness [Petitjeans, 1995].

Directly at the concave side, the main velocity profile exhibits local variations (see Figure 12), named Görtler rolls. The turbulent boundary layer thickness is bigger on the concave side than on the convex one, when a flow between two plates is considered. Outside the boundary layer, the fluid goes faster near the convex side. The typical accelerated profile on the convex side numerically (two dimensional numerical simulation) and experimentally (flows on a curved plate or through very low aspect ratio channels) observed [Lopes, 2003]. In 3D investigations, the aspect ratio of a channel must be low enough (large concave width) to let the flow develop along the concave side and to neglect the influence of lateral walls.

Görtler analysed these centrifugal instabilities with first order simplifications of Navier Stokes equations. First and second order simplifications were described and analysed for different laminar flows on concave plate [Jeschke, 1998]:

- Forced convection with constant wall temperature
- Mixed convection with constant wall temperature
- Natural convection with constant wall temperature
- Natural convection with constant wall heat flux

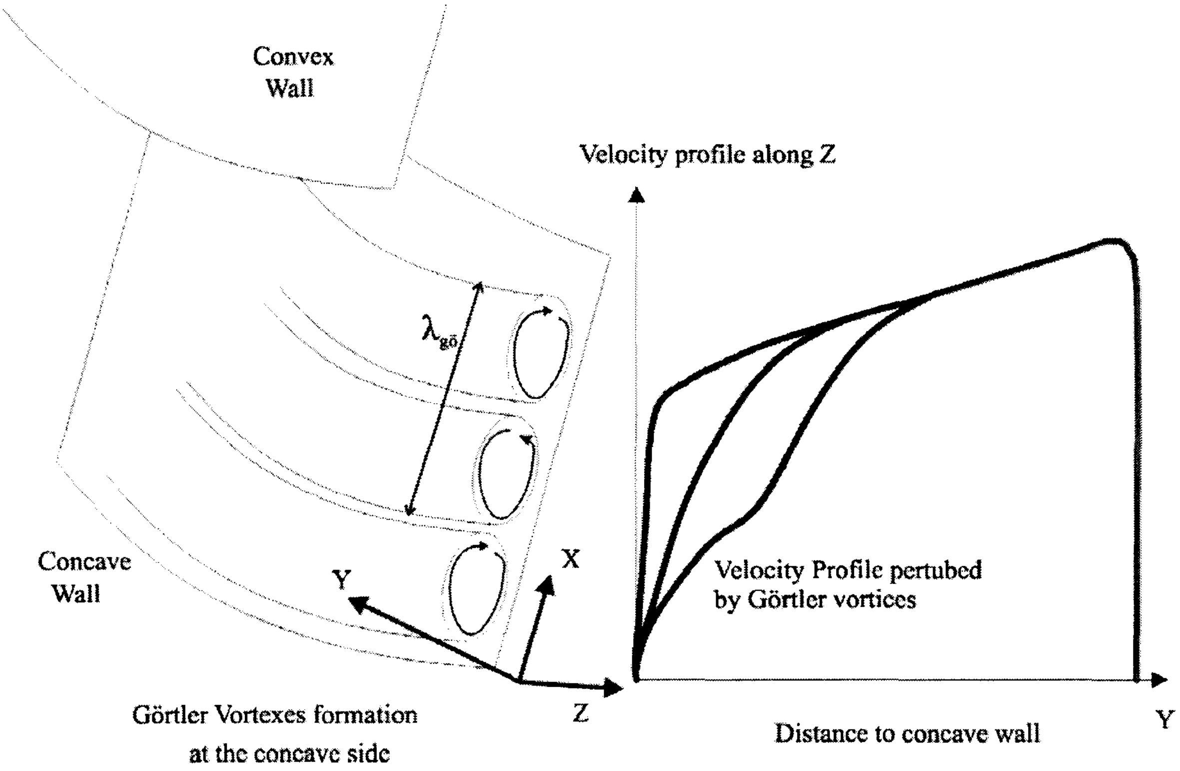

Figure 12 : Görtler vortices in turbulent boundary layer flow [Petitjeans, 1995].

Experimental secondary flow visualisations on concave heated plates were performed and have validated the theoretical approximation of the Navier Stokes equations [Jeschke, 1998].

The secondary velocity profile on the concave wall is assimilated to an oscillation of the velocity field. The wavelength $\lambda_{Gö}$ of this velocity oscillation depends mainly on the boundary layer thickness and on the Görtler number. For each instability wavelength, a critical Görtler number is defined, from which the instabilities appear. The wavelength can be compared to the width of the Görtler rolls. It decreases when the Görtler number increases [Görtler, 1940]. At higher Reynolds number, or higher curvatures, the size of the Görtler vortices theoretically decreases. An experimental investigation with high curvature ($R_c=10\ cm$ on the concave side with $D_h=4.3\ cm$) pointed out that the critical Görtler number can be very low: $Gö_{crit}{\sim}20$ [Petitjeans, 1995].

The Görtler instabilities were experimentally and numerically observed. Figure 13 shows the appearance of the Görtler rolls, adopting a mushroom configuration on the concave side of a low aspect ratio channel.

For rocket engine cooling channels, at high Görtler number, the minimal corresponding wavelength of the Görtler rolls seems to be higher than the dimensions of the cooling channels. For a boundary layer thickness of $\delta{\sim}1\ mm$, at $Gö{\sim}10^5$, the minimal width of the Görtler roll is about $0.3\ mm$ [Görtler, 1940]. It can thus be unexpected to observe Görtler instabilities on the concave walls of the cooling channels of rocket engines. Moreover, in the case of high aspect ratio (the two smallest sides of the channel are the convex and the concave one), the three dimensional velocity is modified. The presence of longitudinal walls (channel configuration) will strongly modify the main flow structure and the centrifugal instabilities. Indeed, the viscosity forces near longitudinal walls are preponderant and limit the centrifugal forces (main velocity reduction) near the lateral walls. This non equilibrium with the fluid far away from lateral walls (centrifugal forces are preponderant here) will develop special centrifugal instabilities: the Dean vortices.

Figure 13 : Görtler instabilities experimentally observed a-[Camci, 2002], b-[Ligrani, 2000] and numerically calculated c-[Girgis, 2002].

2.1.3. Dean Vortices

- *Description*

The fluid is driven to the concave wall, because of centrifugal forces. The concave wall automatically induces a mechanical reaction into the fluid structure providing a pressure gradient. This radial pressure gradient generates local forces on the fluid from the concave wall to the convex one, at any location of the fluid section. In the boundary layer thickness or more generally near the walls, the main fluid velocity is restricted by viscous forces. The centrifugal forces are decreasing, because of main velocity reduction, see Figure 15. Nevertheless, the pressure gradient executes its influence everywhere in a cross section of a channel, consequently pushing the lateral near wall fluid to the convex side. A secondary flow motion is thus appearing in curved channels which was fully analysed by Dean [Dean, 1927-1928], see Figure 14.

The theoretical approach of Dean, summarised by Berger, proposes an analytical resolution under particular assumptions [Berger, 1983]:

- Incompressible flows
- Constant pipe radius and constant curvature radius
- Pipe radius must be neglected to curvature radius (First order approximation of the momentum equations)
- Established main velocity component (constant along the channel)
- Typical laminar Poiseuille flow to define the streamwise velocity profile

In these studies, the Navier-Stokes equations were submitted to the preceding assumptions, and a non-dimensional number appears, characterising the secondary motion inside a channel section, noted De_1:

$$De_1 = \frac{1}{2}\mathrm{Re}^2\,\kappa$$

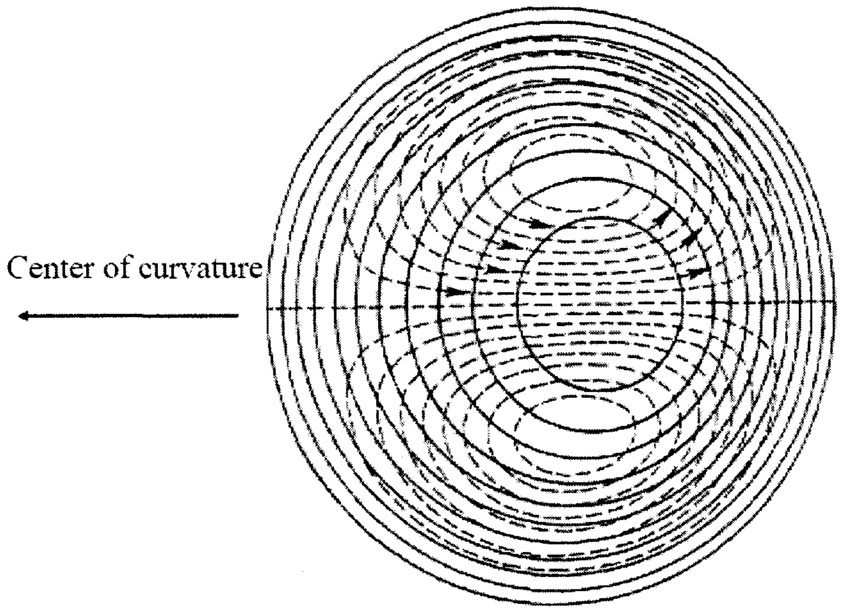

Figure 14 : Representation of Dean's secondary flows in a section of a circular pipe (Dashed lines) and main flow iso-velocity lines (full lines).

The fluid elements located in the centre of the pipe are pushed to the concave side by the centrifugal force. On the other hand, the elements located on lateral walls (upper or lower region of the represented channel in Figure 14) are principally submitted to pressure gradient, because of drastic decrease of main velocity (boundary layer behaviour) and of centrifugal acceleration. It results that the near lateral wall fluid elements flow to the convex wall as it is drawn in Figure 15. The secondary flows are enlightened in the Navier Stokes equations with a first order approximation [Dean, 1927], with relatively small curvature for laminar, adiabatic and incompressible flows. The term w_0 refers to the maximum axial velocity in the middle of a straight pipe.

$$\begin{aligned}
\frac{u_r}{w_0} &= \frac{1}{4}\mathrm{Re}\, D_h \sin\psi \frac{\left(1-r'^2\right)^2\left(4-r'^2\right)}{288R_C} = \frac{De_1}{\mathrm{Re}}\sin\psi \frac{\left(1-r'^2\right)^2\left(4-r'^2\right)}{288} \\
\frac{u_\psi}{w_0} &= \frac{1}{4}\mathrm{Re}\, D_h \cos\psi \frac{(1-r'^2)(4-23r'^2+7r'^4)}{288R_c} = \frac{De_1}{\mathrm{Re}}\cos\psi \frac{(1-r'^2)(4-23r'^2+7r'^4)}{288} \\
\frac{w}{w_0} &= \left(1-r'^2\right)\left[1-\frac{3r'D_h \sin\psi}{8R} + De_1 \frac{r'\sin\psi}{23040}\left(19-21r'^2+9r'^4-r'^6\right)\right]
\end{aligned} \qquad \textbf{(2.37)}$$

The cylindrical coordinates $\left(r = r'\frac{D_h}{2}, \psi\right)$ are described in Figure 15. The intensity of the secondary flow velocities $\left(u_r, u_\psi\right)$ is proportional to the Reynolds number, as it clearly appears in the equations. In a straight pipe, the laminar Poiseuille flow is defined by:

$$\begin{aligned}
\frac{w}{w_0} &= \left(1-r'^2\right) \\
u_r &= 0 \\
u_\psi &= 0
\end{aligned} \qquad \textbf{(2.38)}$$

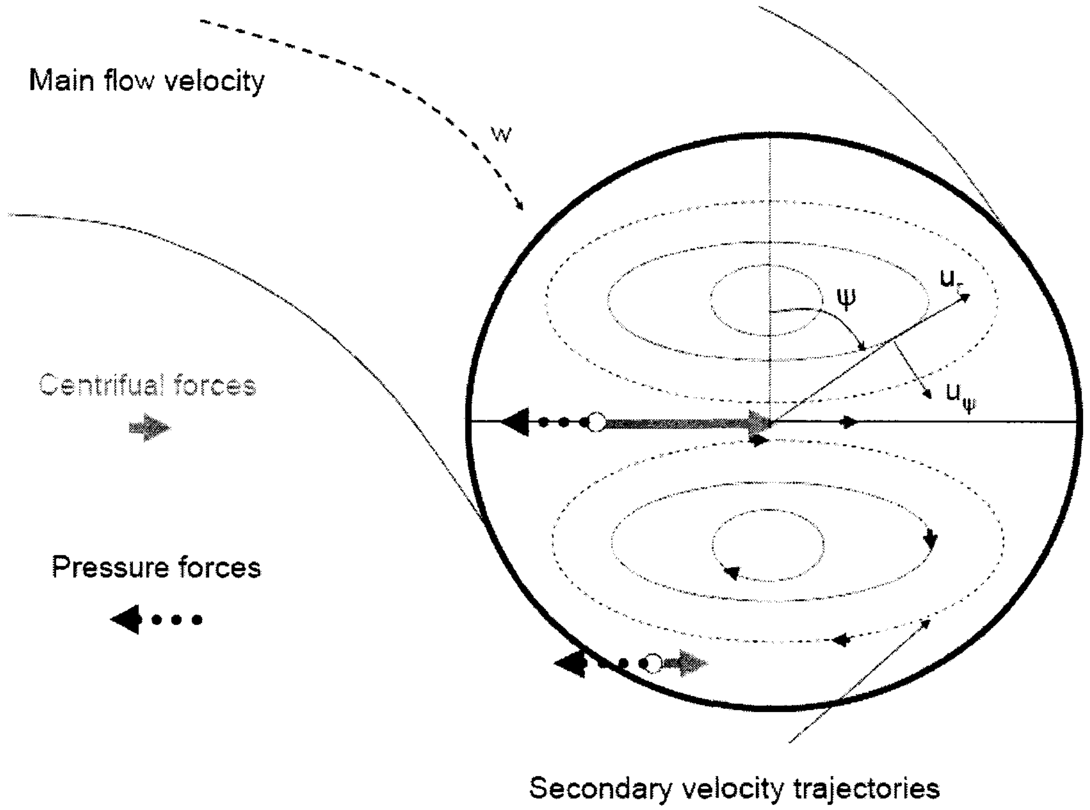

Figure 15 : Secondary flows trajectory and mechanisms of Dean vortices.

The combination of Navier Stokes equations, with a finer approximation (fourth order approximation) gives an expression of the secondary stream function. It can be directly correlated to the axial pressure loss, or to the corresponding mass flow rates ratio [Dean, Berger].

$$\frac{\dot{m}_{curved}}{\dot{m}_{Straight}} = 1 - 0.03058\left(\frac{De_1}{576}\right)^2 + 0.01195\left(\frac{De_1}{576}\right)^4 \qquad \textbf{(2.39)}$$

by constant pressure losses for the two configurations with $De_1 < 650$.

This mass flows ratio was experimentally tested and compared to the analytical solution (*0.5%* error) with $De_l=300$ [Dean, 1928]. The restricted conditions of this analytical model (Poiseuille flow, small curvature, approximation of the 4th order) lead to divergence with experiments when $De_l > 650$. Indeed, the error with experimental comparisons grows up to *30%* for $De_l \sim 2500$.

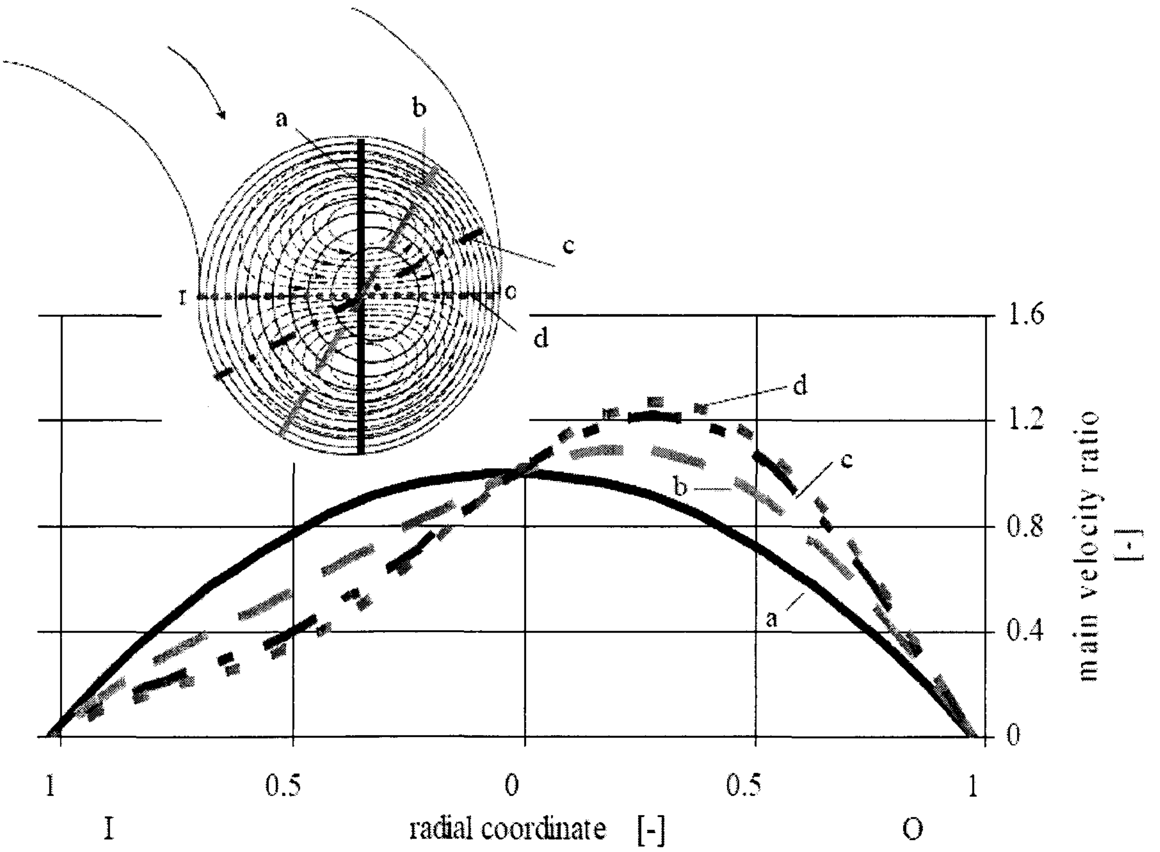

Figure 16 : Main flow profile in curved pipe for a Poiseuille laminar flow at *De ~ 300*, concave side on the right.

Theoretically, for a laminar flow within the scope of the initial assumptions of light curvature and small Reynolds number, the secondary stream lines pattern must be independent from the Dean number De_l or from the Reynolds number [Dean, 1927]. On the other hand, the velocity along the stream lines is directly proportional to the Reynolds number but the structure of the flow does not change. The velocity field equations investigated by R. Dean for a laminar Poiseuille flow are described in Figure 16. The main flow profile is represented over a section in a curved circular pipe, for different orientation (from a line perpendicular to the concave-convex axe to a parallel one).

It can be seen that the velocity profile along the full lines in Figure 16 does not have any transformation in comparison to the Poiseuille flow profile of a straight channel. The maximal deviation nevertheless appears along the perpendicular axe [IO] (line joining the concave side to the convex side): this is the symmetry axis of the Dean rolls.

The laminar Poiseuille flow profile is deviated to the concave side due to the presence of Dean's cells. In Figure 16, the coordinates are non-dimensionalized by dividing with reference values (radius of pipe and main flow velocity in the centre of a straight channel). An experiment used a hot wire probe to investigate the streamwise disturbance velocity and validated the displacement of the parabolic flow from the convex side to the concave one [Matsson, 1993].

In the last decades, another expression of the Dean number appeared to become the most used reference non-dimensional number to characterise the Dean vortices, in laminar as well as in turbulent flows, for many application fields (engineering, medicine, biology, ...):

$$De = \mathrm{Re}\sqrt{\kappa} = \sqrt{2De_1} \qquad \textbf{(2.40)}$$

For flows with higher Reynolds numbers, the stream lines are not static anymore and an outward movement of the location of the maximal velocity can be remarked for increasing Reynolds numbers [Berger, 1983]. Moreover, the secondary stream lines are deformed by the consideration of the boundary layer profile at pipe walls, as it can be seen in Figure 17. The laminar calculation can thus be improved by considering laminar boundary layer thickness instead of the classic Poiseuille profile [Adler, 1934]. The boundary layer concentrates the viscosity forces, where the centrifugal acceleration does not have an influence anymore. It can explain the concentration in the boundary layer of the fluid moving from the concave side to the convex one (where only the pressure gradient influences the fluid).

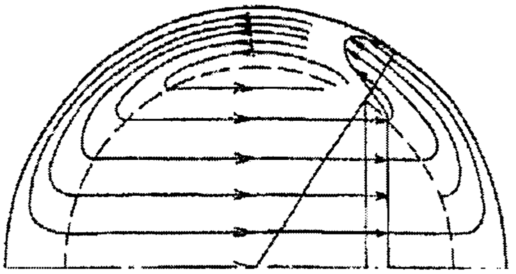

Figure 17 : Half upper section of a curved pipe (concave side on the right side), secondary flow streamlines (full lines) and boundary layer (broken line), [Berger, 1983].

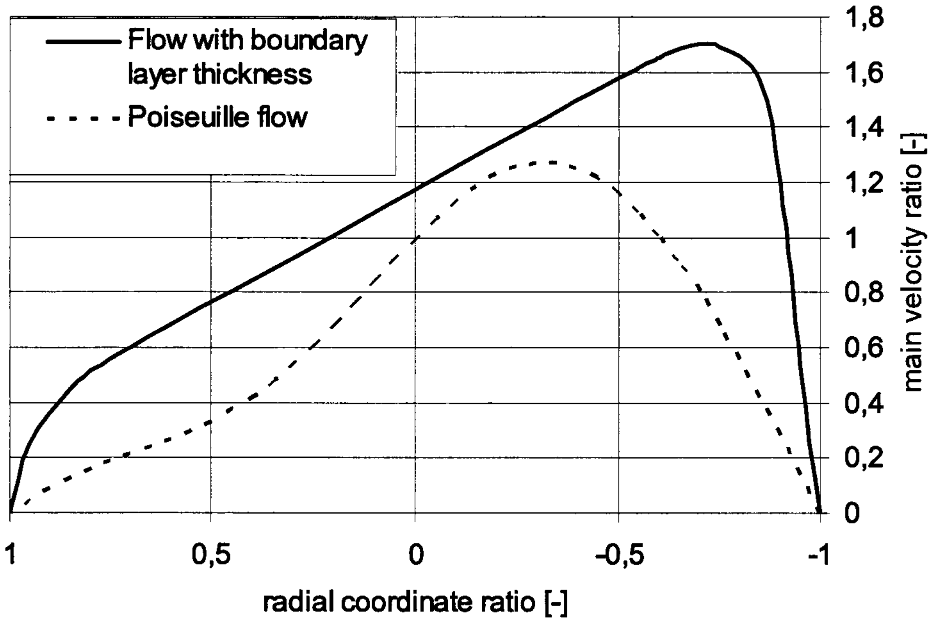

Figure 18 : Main velocity profile in curved tube (concave side on the right) for a Poiseuille flow (*Re = 300, De =30*), [Dean, 1927] and a flow with boundary layer thickness (*Re = 1800, De = 180*), [Adler, 1934].

In Adler's publication, the flow field was calculated by approximation of the Navier Stokes equation and with consideration of the laminar boundary layer thickness. The profile of the streamwise velocity in a light-curved tube is completely different from the one calculated with a standard laminar Poiseuille flow. Figure 18 illustrates the main velocity profile of a

Poiseuille flow *De ~ 30* [Dean, 1927] and of a laminar flow with higher Reynolds number, *Re = 1800*, *De = 180* [Adler, 1934], where the approximation of first order is not possible anymore.

Figure 19 illustrates the transition from a low Reynolds number (*Re < 350*) curved flow to a higher Reynolds number curved flow in pipes. Indeed, for Reynolds number higher than *350*, the consideration of the boundary layer thickness plays an important role in the flow field calculation.

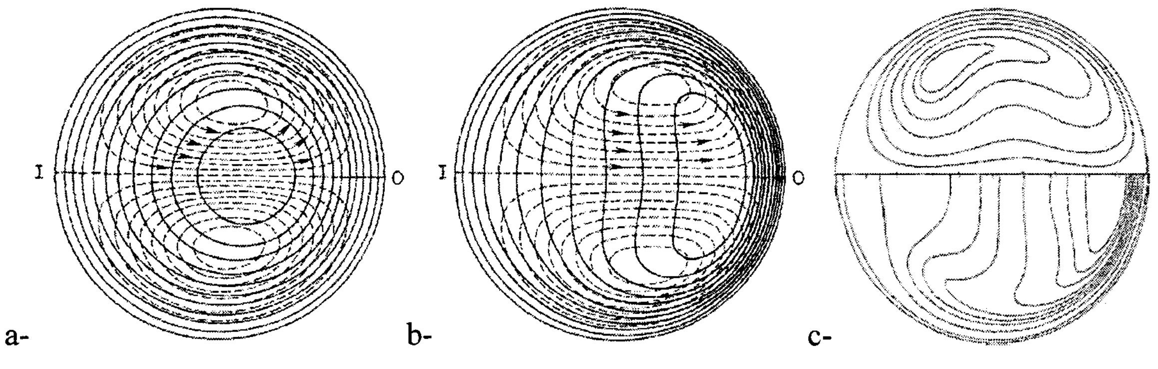

Figure 19 : Secondary stream lines (broken lines for a- and b-, upper graph for c-) and main velocity profile (full lines for a- and b-, down graph for c-) at different Dean numbers (a- De=34, b- De=215, c- De=1770), [Berger, 1983].

In fully turbulent curved flows, visualisations have shown that the Dean vortices induce additional non-isotropic turbulence. Indeed, PIV (Particle Image Velocimetry) and LDV (Laser Doppler Velocimetry) measurement methods were used to characterise the flow, its velocity field, its turbulence repartition, [Zhaoshung, 1993]. The velocity field measured by PIV determined the turbulence intensity repartition and the turbulent correlations. The streamwise correlations R_{uu}, R_{vv} and R_{ww} were experimentally measured on the concave and on the convex walls along the longitudinal axis (*z*).

$$R_{ww}(1-2) = \frac{\overline{w_1' w_2'}}{\sqrt{\overline{w_1'^2}\,\overline{w_2'^2}}} \qquad \textbf{(2.41)}$$

The subscript 1 is for the entrance of the channel and the subscript 2 represents a point along the channel. The streamwise correlations describe the spatial propagation of a turbulent structure. The calculation of the turbulent length scale from streamwise correlations can characterise the turbulent diffusion in all directions and gives an averaged length of a turbulent structure in one particular direction.

$$L_{ww}(r) = \int_0^\infty R_{ww}(r)dr \qquad \textbf{(2.42)}$$

From the PIV experimental results, it was observed that the turbulent length scale in the flow direction L_{ww} along the pipe is about twice the length scale L_{vv} of the cross stream (*y*), corroborating the anisotropy of the flow in pipes.

2.2. Heat Transfer in Cooling Channels

2.2.1. Straight Channels

For steady turbulent flows, the single-phase convection can be described with empirical correlations. Each configuration of convective heat transfer can be approached by typical correction factors, determined by empirics. The case of asymmetrical heat transfer in curved and high aspect ratio rectangular micro-channels is a very particular configuration, where existing empirical correlations strongly depend on geometry, heat flux and dynamic parameters. Several classic and more or less specific theoretical relations and empirical correlations are presented in this paragraph.

The subscripts *in* and *out* indicates the inlet and the outlet of channel, *b* and *w* indicate the bulk and the wall position inside the fluid

The Nusselt number characterises the ratio of convective heat flux to conductive heat flux.

$$Nu = \frac{hD_h}{\lambda} \tag{2.43}$$

h is the convective heat transfer coefficient defined with the local wall heat flux density in the cooling channel and a reference temperature difference between the flow and the wall temperature.

$$\dot{q} = h\Delta T_{ref} \tag{2.44}$$

Some reference temperature differences can be listed:

$$\Delta T_{ref}\Big|_{LOG} = \frac{(T_w - T_{in}) - (T_w - T_{out})}{\ln\left(\frac{T_w - T_{in}}{T_w - T_{out}}\right)} \tag{2.45}$$

$$\Delta T_{ref}\Big|_{BULK} = T_w - T_b \tag{2.46}$$

$$\Delta T_{ref}\Big|_{FILM} = \frac{T_w - T_b}{2} \tag{2.47}$$

$$\Delta T_{ref}\Big|_{INT} = T_w - \frac{1}{T_w - T_b}\int_{T_b}^{T_w} T(y)dT \tag{2.48}$$

$$\Delta T_{ref}\Big|_{IN} = T_w - T_{in} \tag{2.49}$$

The Prandtl number characterises the ratio of momentum diffusivity to the thermal diffusivity.

$$\Pr = \frac{\mu c_p}{\lambda} \tag{2.50}$$

- *Classic laminar correlation*

In a circular tube, by laminar, thermally and hydraulically developed flows, the theory calculates using $\Delta T_{ref} = \Delta T_{ref}\Big|_{LOG}$:

$$Nu = 3.657 \text{ for constant wall temperature,} \tag{2.51}$$

$$Nu = 4.364 \text{ for constant wall heat flux,} \tag{2.52}$$

With hydraulically developed flows but thermally developing, the heat transfer can be determined for constant wall temperature [Hausen, 1959]:

$$Nu = 3.657 + \frac{0.19\left(\mathrm{Re}\,\mathrm{Pr}\dfrac{D_h}{l_{tot}}\right)^{0.8}}{1+0.117\left(\mathrm{Re}\,\mathrm{Pr}\dfrac{D_h}{l_{tot}}\right)^{0.467}} \tag{2.53}$$

and for constant wall heat flux [Shah, 1975]:

$$\begin{aligned} Nu &= 1.953\times\left(\mathrm{Re}\,\mathrm{Pr}\frac{D_h}{l_{tot}}\right)^{1/3} \quad \text{if } \mathrm{Re}\,\mathrm{Pr}\frac{D_h}{l_{tot}} \geq 33.3 \\ Nu &= 4.364+0.0722\times\left(\mathrm{Re}\,\mathrm{Pr}\frac{D_h}{l_{tot}}\right) \quad \text{if } \mathrm{Re}\,\mathrm{Pr}\frac{D_h}{l_{tot}} < 33.3 \end{aligned} \tag{2.54}$$

- *Classic turbulent correlation*

The empirical Dittus-Boelter correlation is reliable for basic turbulent flows with $\Delta T_{ref} = \Delta T_{ref}\big|_{BULK}$:

$$Nu = 0.243\times\mathrm{Re}^{0.8}\,\mathrm{Pr}^{n} \tag{2.55}$$

The coefficient n was evaluated: $n=0.3$ for a cooling down of the fluid and $n=0.4$ for a heating of the fluid [Dittus-Boetler, 1930]. This empirical correlation can be applied to thermally and dynamically established flows, for a precise range of Prandtl and Reynolds numbers:

$$\begin{aligned} &0.7 \leq \mathrm{Pr} \leq 120 \\ &10^4 \leq \mathrm{Re} \leq 1.2\cdot10^5 \end{aligned} \tag{2.56}$$

- *Fluid properties dependence on temperature and entrance effect*

In the case of a straight channel, the heat transfer can imply the bulk-to-wall fluid properties′ differences (density, viscosity). This was already investigated by many authors. Thermal stratification does not exist at the entrance of channels. The heat flux at the entrance is very high, because the fluid temperature near the wall is lower than in an established thermally stratified channel. It needs a certain distance to establish the thermal boundary layer. That is why Taylor proposed an empirical correlation taking into account entrance influence and progressive thermal stratification [Taylor, 1967] with $\Delta T_{ref} = \Delta T_{ref}\big|_{BULK}$:

$$Nu = 0.023\times\mathrm{Re}^{0.8}\,\mathrm{Pr}^{0.4}\left(\frac{T_w}{T_b}\right)^{-\left(0.57-\frac{1.59}{x/D_h}\right)} \tag{2.57}$$

This empirical correlation supposes that the establishment of the thermal stratification needs *2.7 D_h*.

Hess proposed empirical results taking into account thermal stratification [Hess, 1965] and a direct viscosity wall to bulk profile, with $\Delta T_{ref} = \Delta T_{ref}\big|_{FILM}$:

$$Nu = 0.0208 \times \mathrm{Re}_0^{0.8}\ \mathrm{Pr}_0^{0.4} \left[1 + 0.01457\,\frac{\upsilon_w}{\upsilon_b}\right] \tag{2.58}$$

The subscript *0* indicates that the fluid properties are evaluated at the film temperature:

$$T_0 = \frac{T_b + T_w}{2} \tag{2.59}$$

- *Roughness and Prandtl number*

The most conventional correlation was proposed by Petukov and takes into account the friction factor influence to define the heat transfer in rough cooling channels [Petukov, 1973]:

$$\begin{aligned} Nu &= \frac{\xi/8\,\mathrm{Re}\,\mathrm{Pr}}{K + 12.7\sqrt{\xi/8}\left(\mathrm{Pr}^{2/3} - 1\right)} \\ K &= 1.07 + \frac{900}{\mathrm{Re}} - \frac{0.63}{1 + 10\,\mathrm{Pr}} \end{aligned} \tag{2.60}$$

A well known variation of the Petukov correlation was defined by Gnielinski and includes the thermal entrance effects [Gnielinski, 1976] with $\Delta T_{ref} = \Delta T_{ref}\big|_{LOG}$:

$$Nu = \frac{\xi/8\,(\mathrm{Re} - 1000)\,\mathrm{Pr}_b}{1 + 12.7\sqrt{\xi/8}\left(\mathrm{Pr}_b^{\ 2/3} - 1\right)}\left[1 + (d_h/L)^{2/3}\right]\left(\frac{\mathrm{Pr}_b}{\mathrm{Pr}_w}\right)^{0.14} \tag{2.61}$$

The two preceding correlations can be used in a large range of empirical cases (maximal deviation of *10%* with experiments), for the following restricted application domain:

$$0 < {}^{D_h}\!/_{L} < 1;\ \ 0.6 < \mathrm{Pr} < 2000;\ \ 10^4 < \mathrm{Re} < 10^6$$

Particularly in the domain of space sciences, a correction factor has been checked by Niino et al. to characterise the entrance effect (Boetler factor), [Niino, 1982]:

$$\psi_{ent} = \frac{Nu_{entrance}}{Nu_{classic}} = 2.88 \times \left(\frac{x}{D_h}\right)^{-0.325} \tag{2.62}$$

This factor is physically not allowed to be lower than *1*.

The roughness of the channel plays a major role to enhance the heat transfer. Indeed, high roughness will develop a turbulent boundary layer earlier which dissipates more thermal energy and enhances global heat transfer. The adiabatic rough- to smooth friction factors ratio is directly made use of for defining the role of roughness in heat transfer. In the publication [Niino, 1982], the Nunner's correction factor is explicitly detailed:

$$\psi_{rough} = \frac{Nu_{roughness}}{Nu_{smooth}} = \frac{1 + 1.5\,\mathrm{Pr}_b^{-1/6}\,\mathrm{Re}_b^{-1/8}\,(\mathrm{Pr}_b - 1)}{1 + 1.5\,\mathrm{Pr}_b^{-1/6}\,\mathrm{Re}_b^{-1/8}\,(\mathrm{Pr}_b\,\theta_{rough} - 1)}\,\theta_{rough} \tag{2.63}$$

where $\theta_{rough} = \frac{\xi_{rough}}{\xi_{smooth}}$ is the rough- to smooth adiabatic friction factor ratio.

For Prandtl number higher than *1* and important roughness $\left(k_{rel} = \frac{k_s}{D_h} = 0.049 \right)$, the preceding Nunner correlation was checked experimentally [Dipprey, 1962] and delivers very high deviation compared with expected experimental results (*40%*). He proposed a more adequate correlation for high Pr flows in high roughness tubes, in relation with the logarithmic law of the boundary layer thickness relation. The empirical correlation is not represented in this report because of relatively low Pr number and low roughness levels for the cooling channels of rocket engines application.

- *Sub- and Supercritical status*

In supercritical regions (pressure or temperature higher than the critical point), changes in phase are no longer possible. A small deviation in pressure or in temperature will induce a great change in fluid properties.

Hess investigated the supercritical status of the fluid and its role in the heat transfer process [Hess, 1965]. With or without change of phase (boiling film at the hot walls), the calculated heat transfer into supercritical or two-phase flows are of the same order of precision when compared with experiments: *+/- 20%.*

Nevertheless, for fluid at supercritical pressure near pseudo-critical temperature, heat capacity increases significantly and influences the global heat transfer. Taking as reference the Dittus Boetler relation with constant coolant mass flow and constant channel geometry, the thermodynamic parameters were differentiated near the critical point [McEligot, 2004]. Through the temperature critical points (for critical pressures range), heat capacity increase is more important than the other parameters' change.

$$\Delta h = \Delta\left(\frac{c_p^{\ 0.4} \lambda^{0.6}}{\mu^{0.4}} \right) \sim \Delta\left(c_p^{\ 0.4} \right) \qquad \textbf{(2.64)}$$

To characterise the supercritical heat transfer, a recent study summarised different experimental results of symmetrically heated circular tubes with supercritical hydrogen, with *Re* up to $5 \cdot 10^6$, *Pr* from *1* to *15* and heat flux density from *0.3* to *40* $MW.m^{-2}$ [Locke, 2005]. Many empirical correlations have been compared to the selected empirical results, taking into account the uncertainties of fluid parameters determination (up to *10%*). The Modified Benedict-Webb-Rubin equation was used to deliver fluid properties, see in 4.1.4.2. But the most reliable relation is the Shah and Quentmeyer one, in global accordance of *30%* over all compiled experiments (more than *2000* data points). This correlation integrates each fluid property $(\mu, \upsilon, \lambda, c_p, ...)$ from T_b to T_w, for example:

$$\mu = \frac{1}{T_w - T_b} \int_{T_b}^{T_w} \mu(T) dT \qquad \textbf{(2.65)}$$

The non dimensional numbers are all calculated with the preceding fluid properties, with $\Delta T_{ref} = \Delta T_{ref}\big|_{INT}$:

$$Nu = 0.0208 \times \mathrm{Re}^{0.8}\ \mathrm{Pr}^{0.4} \qquad \textbf{(2.66)}$$

Moreover, through the passage from supercritical liquid to supercritical gas above the pseudo-critical temperature, the heat capacity peak strongly modifies the heat transfer process. The Shah-Quentmeyer correlation predicts near pseudo-critical temperature experimental data better than other correlations. Anyway, the uncertainties of the fluid parameters near the supercritical point remain the most influential source of imprecision [Locke, 2005].

- *Streamwise acceleration*

Along a heated channel with a steady flow, the decrease of the density induces main stream acceleration, by mass flow conservation. The decrease of the Reynolds number is only caused by the dynamic viscosity increase along the channel. This streamwise acceleration (or streamwise pressure gradient) stabilises laminar flows and can produce a “relaminarisation” effect on turbulent flows: the heat transfer is thus as low as in laminar flow. A characteristic parameter of this effect was introduced, the acceleration parameter [McEligot, 2004] must be higher than 3.5×10^{-6} to observe the re-laminarisation phenomenon [Schlichting, 1963]:

$$k_v = \frac{\upsilon_b}{{w_b}^2}\frac{dw_b}{dx} \qquad \textbf{(2.67)}$$

According to different authors, the “laminar” heat flux appears in turbulent flows for higher acceleration parameters than 2 to 4×10^{-6}. This coefficient was calculated with the experimental conditions of the EH3C campaigns and of real cooling channels of rocket engines. The relaminarisation effect cannot appear in the cooling channel of rocket engines.

- *Asymmetric heating*

A calculation method was introduced to take into account the asymmetrical heating. Using standard empirical correlations for full-periphery heating, the Nusselt number is no more defined via hydraulic diameter, but via thermal diameter (Periphery length where the heat transfer cannot be negligible). The experiments of Sturgis showed that this method too much underestimates the real heat transfer in asymmetrically heated channels [Sturgis, 1999].

By investigating effects of inlet-induced flow separation on turbulent heat transfer in high aspect ratio channels, Sparrow precised that the influence of asymmetrical heating only appears in fully developed flow [Sparrow, 1982].

Experimental investigations, [Novotny, 1964, Sparrow, 1966], indicated that the aspect ratio does not have a real influence on asymmetrical heat transfer. The 2 longer sides of a high aspect ratio ($AR=5$ and 10) rectangular channel are uniformly heated.

The measurements of heat flux underestimate the classic Colburn used for circular pipe heat transfer by about 10%. In another experiment, the authors independently heated the two longer sides, for the channel with $AR=5$. In the case of only one heated wall, the Nusselt number is 20% lower than in the both heated walls configuration, for a turbulent flow (Re up to 1.5×10^5). Independently on the aspect ratio, the way of heating (symmetrical or asymmetrical) seems to have an influence on the heat transfer. The asymmetrical heating can have a significant role in the determination of the heat transfer characteristics in comparison to symmetrical heating. The fact that only one side is heated globally reduces the faculty of the fluid to absorb more heat. The cold side of the fluid is thus not required to enhance the heat transfer. Moreover, the case of curved channel accentuates the role of asymmetries in heat transfer. Therefore, the concave heated side case provides more convective heat transfer than the convex heated side case.

- *Aspect Ratio (AR) Influence*

Many authors have investigated the role of the aspect ratios *AR* (height by width) on heat transfer. The efficiency increase in heat transfer in high aspect ratio channels was checked and demonstrated many times [Carlile, 1992, Woschnak, 2003]. The various geometries change the friction factor as shown in paragraph (2.1.1). The reduction of the pressure losses for high aspect ratio cooling channels (HARCC) can firstly be used to increase mass flow and to improve heat transfer. Moreover, the use of HARCC allows increasing the number of cooling passages for identical cross sectional areas. The thin and long wall between two cooling channels uses the high thermo-conductivity of the wall material to better conduct the heat flux all over the channel perimeter. In terms of rocket combustor cooling, the use of HARCC increases the heat transfer surface due to long lateral walls and by the way reduces the hot gas side temperature. Quentmeyer tested a combustion chamber with several aspect ratios of cooling channels (*0.75*; *1.5* and *5*). For identical pressure drop through the different cooling systems, the temperature at the hot gas side decreases from *765 K* to *539 K* [Quentmeyer, 1992].

A similar experiment and an analytical calculation were managed by Wadel on a combustor with bifurcation of the cooling channels along chamber axis, [Wadel, 1996, 1997]. The number of channels was multiplied by *2*, allowing an increase of the aspect ratio in the throat section. The temperature wall was reduced from *780 K* to *600 K*. These experimental investigations were later corroborated by analytical analyses [Wadel, 1997] Forgetting about machining the technique of bifurcation of the channels at the throat section seems to be the most thermally efficient (about *7%* pressure drop increase for a reduction of the hot-gas side temperature up to *20%*). Nevertheless, the technical realisation brings about a couple of abrupt changes of geometries that could perturb the heat transfer and locally increase the wall temperature.

Woschnak et al. performed experiments with a single combustor divided into *4* sectors with *4* cooling channels of aspect ratio (AR=*1.7*, *3.5*, *9.2*, *30*), as shown in Figure 20, [Woschnak, 2003].

The mass flows of hydrogen through the *4* types of channels were quite identical allowing a good comparison between thermal efficiencies of channels. Constant widths of thermal fins for the 4 sectors had been required between all successive channels, for all configurations. The role of aspect ratio was correlated to the fin efficiency. HARCC geometry can develop a thermal stratification (reduction of the heat flux and increase of wall temperature) earlier than conventional aspect ratio channels, because of superposition of thermal boundary layers inside the channels from the two lateral walls. That creates a highly stratified fluid over a channel section. This thermal stratification avoids the cold bulk fluid to exchange energy with the hot walls of the bottom of the cooling channel. This can be assimilated as a thermal isolation layer. This has thus to be combined with the fin efficiency of the HARCC.

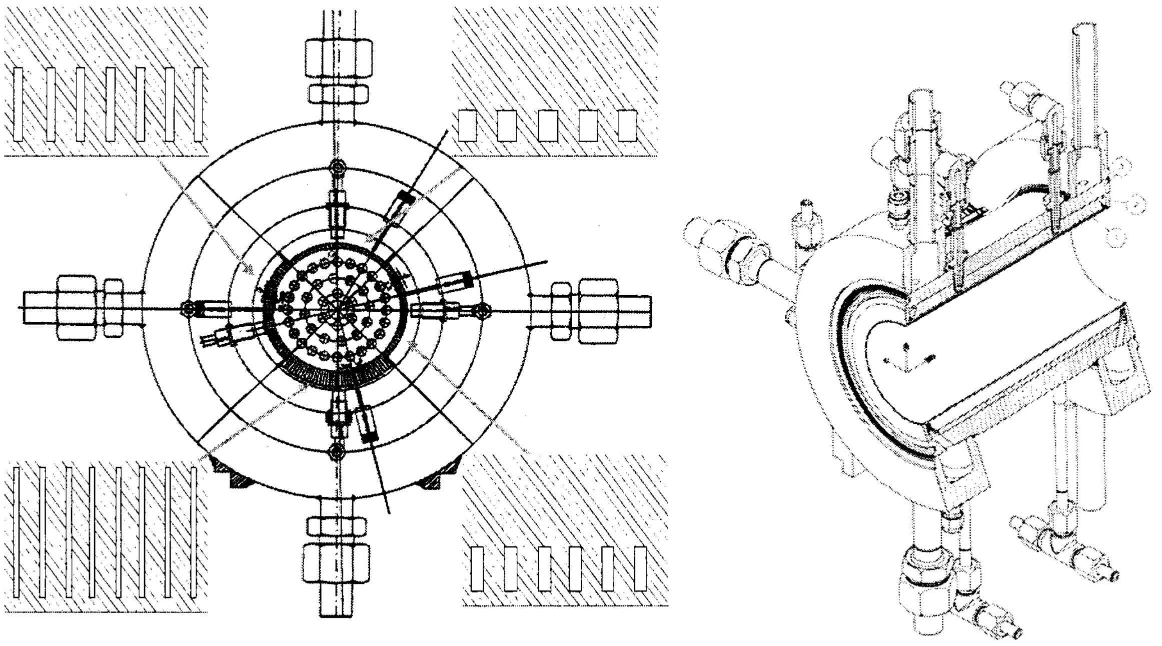

Figure 20 : Design of the *4* sector HARCC segment with different cooling channel geometries [Woschnak, 2003].

More recently, a campaign of experiments and numerical simulations was performed at the Purdue University [Wenneberg, 2005] in order to characterise the asymmetrical heat transfer in high aspect ratio cooling channels. The numerical investigations will be developed in the following chapter (2.3). Concerning the experiments, a combustor (peroxide-ethanol) delivers hot gas (*2380 K*) which directly flows around a single cooling channel, as shown in Figure 21.

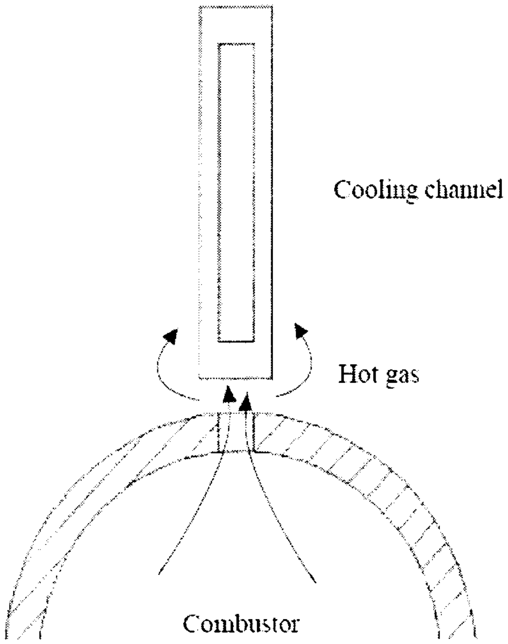

Figure 21 : Single cooling channel warmed up by jet from combustor [Wenneberg, 2005].

This single channel has an aspect ratio of 8 with a width of *2.54 mm* and a height of *20.32 mm*. The side walls are *1.27 mm*, where *32* thermocouples are implemented along the *0.762 m* channel (where the last *508 mm* are heated by the combustor hot jet). The hydrogen supercritical flow reaches a high Reynolds number (4.5×10^6) with an inlet temperature of *144 K* and an inlet pressure of *70 bar*.

The simulated local heat flux would be up to $20\ MW\ m^{-2}$. Experimental data have not yet been published, however, complementary computational fluid dynamic (CFD) simulation is already available [Wenneberg, 2006].

- *Capillary Heat Flux*

Choi established an empirical correlation [Choi, 1991] which characterises the heat transfer though capillaries (hydraulic diameter smaller than *0.08 mm*) for turbulent gas flows $Re < 20000$:

$$Nu = 3.82\times 10^{-6}\times \mathrm{Re}^{1.96}\,\mathrm{Pr}^{1/3} \tag{2.68}$$

With higher hydraulic diameters, Adams has brought a modification of the Gnielinski correlation [Adams, 1998], for high *Re* numbers (up to 2.5×10^4), available for $0.1\ mm < D_h < 1.1\ mm$ with $\Delta T_{ref} = \Delta T_{ref}\big|_{LOG}$:

$$Nu = Nu_{Gnielinski}\left\{1 + 7.6\times 10^{-5}\times \mathrm{Re}\left[1-\left(\frac{D_h}{1.164\cdot 10^{-3}}\right)\right]\right\} \tag{2.69}$$

2.2.2. Curved Channels

The dynamical forces caused by curvature have a strong influence on the heat transfer. Indeed, the perturbation of the flow structure (by increasing the global mixing ratio inside a fluid section) tends to enhance the global heat transfer. The heat transfer through the concave side will not be the same as the one through the convex one. In fact, asymmetrical dynamic behaviours of the fluid provide asymmetrical heat flux. To describe the modification of the heat flux in curvatures, many authors have proposed extensions of the well-known correlations to heat transfer in straight channels.

The way of heating plays a major role: full periphery heated channels (symmetrical heating) or a reduced number of heated sides of the channel (asymmetrical heating).

- *Symmetrical heating in curved high aspect ratio channels*

The friction factor defined for curved channels has been implemented in heat transfer standard correlations for straight channels. Indeed, in curved channels, the dissipated energy by higher friction (secondary vortices created by centrifugal forces) directly provides a higher mixing ratio. This enhanced mixing ratio is supposed to be directly dissipated into enhancement of heat transfer. Gnielinski has proposed to use his correlation of the Nusselt expression for straight channels, with application of a friction factor available for curved channels, to determine the curvature effects on heat transfer [Gnielinski, 1976]:

$$Nu_c = Nu_{Gnielinski}(\xi_c) \tag{2.70}$$

In a similar way, Mori analytically investigated the global modification of the heat transfer in curved channels, taking into account the theoretical thermal boundary layer development

[Mori, 1967]. For gases and for well established turbulent flows at relatively high Reynolds numbers (up to 5×10^4), he proposes the following analytical correlation:

$$Nu_c = \frac{\mathrm{Pr}}{26.2\left(\mathrm{Pr}^{2/3} - 0.074\right)} De^{1/5}\,\mathrm{Re}^{3/5}\left\{1 + \frac{0.098}{De^{4/5}\,\mathrm{Re}^{-3/5}}\right\}, \mathrm{Pr} \sim 1 \qquad \textbf{(2.71)}$$

By considering the Dittus-Boetler correlation for straight symmetrically heated tubes, the Prandtl number here has an influence on the heat enhancement due to curvature, see Figure 22.

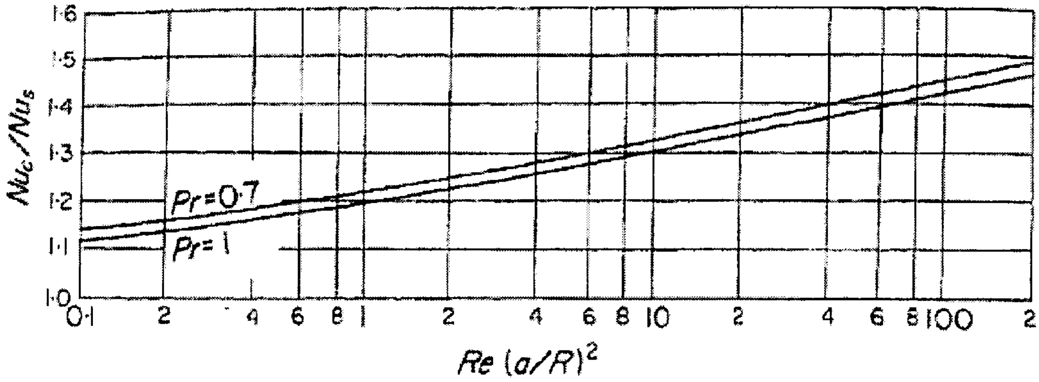

Figure 22 : Heat transfer enhancement in curved channel, for gas (Pr~1) turbulent flows (Re < 5×10^4), *a* is here the channel diameter and R the curvature radius [Mori, 1967].

This is not the case anymore, according to Mori, for fluid with higher Prandtl number. Further analytical investigations have concluded for high Prandtl number that:

$$Nu_c = \frac{\mathrm{Pr}^{0.4}}{41}\mathrm{Re}^{5/6}\,\kappa^{1/12}\left\{1 + \frac{0.061}{\left[\mathrm{Re}\cdot\kappa^{2.5}\right]^{1/6}}\right\} = \frac{\mathrm{Pr}^{0.4}}{41} De^{1/6}\,\mathrm{Re}^{2/3}\left\{1 + \frac{0.061}{De^{5/6}\,\mathrm{Re}^{-2/3}}\right\}, \mathrm{Pr} > 1 \qquad \textbf{(2.72)}$$

In this case, by considering the Dittus-Boetter correlation, the curved to straight heat flux enhancement $\frac{Nu_c}{Nu_s}$ becomes independent of the Prandtl number.

The centrifugal instabilities bring about asymmetrical distribution of the flow. In the case of Dean vortices, with full periphery heated channels, the heat transfer increases more on the concave side than on the convex one. Indeed, the "cold" fluid located in the centre of the pipe, is driven against the concave wall which increases the heat flux. By following the secondary Dean vortices, the fluid reaches the convex side but it is already heated by lateral walls. The heated fluid cannot improve the heat flux at the convex side. The heat transfer is more efficient on the concave side than on the convex side, due to the asymmetrical flow structure of the Dean vortices.

Taylor proposed a direct equivalence between the friction and the heat enhancements due to the curvature, [Taylor, 1968]. The curved to straight friction coefficient ratio defined by Ito was applied to the curved-to-straight Nusselt ratio by Taylor, [Ito, 1959]. This idea came earlier from Seban [Seban, 1963]. Taylor added the influence of the curvature, by taking into account the sense of the Dean vortices. Taylor implements a binary model where the sign + is used for the concave side case and the sign – for the convex one with $\Delta T_{ref} = \Delta T_{ref}\big|_{BULK}$.

$$\frac{Nu_{curved}}{Nu_{straight}} = \left[\mathrm{Re}_b\,\kappa^2\right]^{\pm 0.05} = \left[De^4\,\mathrm{Re}^{-3}\right]^{\pm 1/20} = De^{\pm 1/5}\,\mathrm{Re}^{\mp 3/20} \qquad \textbf{(2.73)}$$

Slightly modified versions of Taylor's empirical correlation were developed, taking into account the perseverance of the heat enhancement after the curvature. This was explained by a progressive damping of the vortices after the curvature which slowly reinstalls thermal stratification and preserves a higher mixing ratio than in the straight channel, even without any centrifugal acceleration. Niino and Kumakawa proposed sinusoidal attenuations of the initial Taylor correlation:

$$\begin{aligned}\psi_c &= \left[\mathrm{Re}_b\,\kappa^2\right]^{\pm 0.02} \times \left[1 + \frac{1}{3}\sin\left(\pi\sqrt{\frac{x_c}{L_c + 15D_h}}\right)\right] \\ &= De^{\pm 2/25}\,\mathrm{Re}^{\mp 3/50} \times \left[1 + \frac{1}{3}\sin\left(\pi\sqrt{\frac{x_c}{L_c + 15D_h}}\right)\right]\end{aligned} \quad \text{[Niino, 1982]} \qquad \textbf{(2.74)}$$

$$\begin{aligned}\psi_c &= \left[\mathrm{Re}_b\,\kappa^2\right]^{\pm 0.05\sin\left(\pi\sqrt{\frac{x_c}{L_c+37D_h}}\right)} \\ &= \left[De^{1/5}\,\mathrm{Re}^{-3/20}\right]^{\pm\sin\left(\pi\sqrt{\frac{x_c}{L_c+37D_h}}\right)}\end{aligned} \quad \text{[Kumakawa, 1986]} \qquad \textbf{(2.75)}$$

where L_C is the length of the curvature, x_c the axial coordinate which varies from the beginning of the curvature until *15* D_h (Niino proposition) or *37* D_h (Kumakawa proposition) after the curvature.

To obtain these empirical correlations, the wall of a rocket combustion chamber was cooled by different methods: radial water-cooled segments (calorimetric method) around the combustion chamber and axial hydrogen-cooling channels along the combustion chamber. It was supposed that heat flux does not vary from one cooling method to another. The first campaign used many water cooled sections to define the heat transfer from the combustion chamber through the cooled walls by water. For each cooled section, a heat flux was experimentally investigated with the calorimetric method (inlet and outlet temperature measurements with measured mass flow rate). Per section, a global heat transfer was defined. Afterwards, by collecting all heat flux from all segments, a heat transfer profile along the chamber axis was drawn and the maximal value of the heat transfer density was reached through the throat section walls (*30 MW* m^{-2}).

The second campaign uses a different cooling system: cooling channels following the chamber profile, with varied aspect ratios along the channel (from *5* to *8*). Temperature measurements were made inside the wall between channels, at many positions along the chamber. With the aid of an inverse method (see in 3.3) and to the data of heat flux from the first calorimetric campaign, the heat flux and the temperature distribution were numerically calculated. These experimental data allowed checking and improving empirical correlations of heat transfer, and what is more, accurately in the curved section of the nozzle throat. It was assumed that the two experimental cooling systems would render the same heat flux profile on the hot-gas side to correlate both campaigns.

Moreover, the initial Taylor correlation was used to define the curvature function ψ_c, and it normally only concerns full periphery heated channels (symmetrical heating).

Meyer performed experiments to investigate the effect of high aspect ratio on curvature heat transfer enhancement, in uniformly heated rectangular cooling passages [Meyer, 1995, 1997]. Two curved cooling channels present aspect ratios of *1* and *10*. Using Nitrogen as medium with symmetrical electrical heating (up to $1.7\ MW\ m^{-2}$), the curvature and the aspect ratio influences on heat transfer were investigated. High Reynolds and Dean numbers were reached (Re up to 10^6 an De up to 2×10^5). Theoretically, the two different aspect ratio configurations cannot be directly compared, because of different hydraulic diameters (*4.14 mm* for the $AR=1$ channel and *2.3 mm* for the channel with $AR=10$). Nevertheless, the influence of aspect ratio was not detected on heat transfer into curved channels. The curvature strongly modifies the heat transfer in all cases, up to *+40%* for the concave wall and down to *-20%* for the convex one. The empirical correlation of Taylor was taken as reference for a straight channel heat flux configuration [Taylor, 1967]. Figure 23 collects some experimental results for the channel with $AR=10$ of Meyer's experiment. The empirical correlation of Niino does not seem to work for the calculation of the convex heated side, because of results greater than one. Hence, this empirical correlation is only applied to concave side heat transfer calculation.

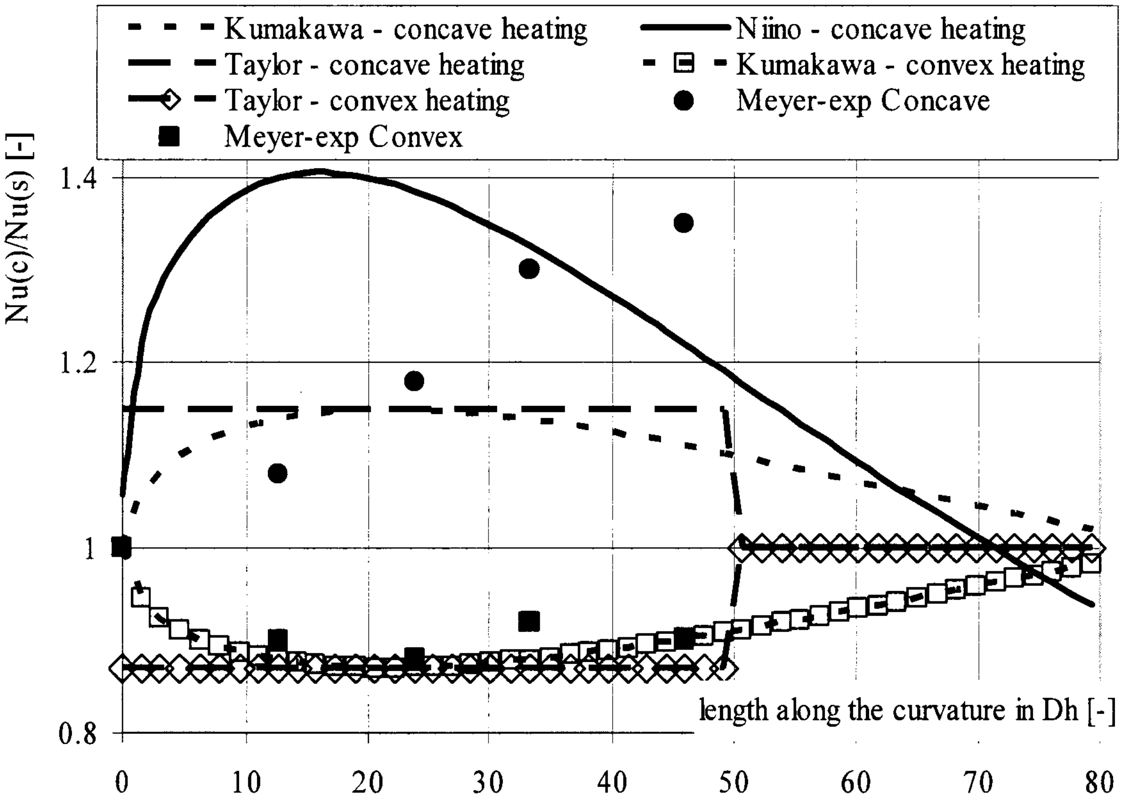

Figure 23 : Taylor, Ito and Kumakawa's empirical correlations and Meyer's experimental results.

In this experiment, the curvature ends after *49* D_h, where the Taylor empirical correlation indicates a curved to straight Nusselt number ratio of *1*.

Meyer's experiments seem to be better correlated by the Niino empirical correlation concerning the concave heat flux increase and by the Kumakawa empirical correlation concerning the convex heat flux decrease. Nevertheless, the maximum of the curved to straight Nusselt number ratio appears earlier with the empirical correlation of Niino: The ratio 1.4 is reached *15* D_h after the beginning of the curvature. The experiments show a maximum of *1.35* at *45* D_h after the beginning of the curvature.

- *Asymmetrical concave heating experiments in curved high aspect ratio channels*

For rocket engine configuration, the upper side of the cooling channel is located in the nickel jacket which is supposed to be adiabatic. This asymmetrical heating can bring another deviation in comparison to the last empirical correlations with symmetrical heating.

An asymmetrical heating has been performed by Sturgis on the concave wall of rectangular cooling channel (*5mm* on *2.5mm*, $AR=2$), [Sturgis, 1999]. Using FC-72 (liquid fluorinert) as coolant and copper for the electrical heat conductor (channel wall), a quite constant asymmetrical heat flux density of about $0.5\ MW\ m^{-2}$ was reached on the concave side. The following flow properties were experimentally reached: Reynolds number up to 1.3×10^5 and Dean number up to 3×10^4. A straight channel was asymmetrically heated for calibrating the classic empirical correlations in an asymmetrically heated straight channel.

The authors took the results of both channels to elaborate an empirical correlation which describes the heat flux enhancement due to curvature of concave heated channels. All the experimental results are corroborated by the following correlation with *+/- 10%* accuracy with $\Delta T_{ref} = \Delta T_{ref}\big|_{BULK}$:

$$\left(\frac{Nu_{Curved}}{Nu_{Straight}}\right)_{Sturgis} = \mathrm{Re}^{0.046}\,\kappa^{0.1} = De^{0.2}\,\mathrm{Re}^{-0.154} \qquad \textbf{(2.76)}$$

Here is one of the most enthralling experiments joining all representative conditions of rocket engine configuration. Asymmetrical heating and typical rocket channels curvature were experimentally tested [Neuner, 1996, 1998]. Air was used as coolant in large scaled models of high aspect ratio channels: a height of $0.256\ m$ and a width of $0.032\ m$ give $AR=8$ and $D_h=0.057m$. The channels were built in steel and were asymmetrically heated by electrical cartridges.

Only one-side of the channel was heated, reaching an asymmetrical heat flux density of $0.06\ MW\ m^{-2}$. Different configurations of the test bench provide special test conditions: Reynolds number from 10^5 up to 4×10^5 and Dean Number up to 7.3×10^4. Convex, straight and concave test sections can be mounted together, giving different asymmetrical heating conditions (concave or convex heating walls). Experimental results indicated a persistent increase of the Nusselt number inside and after the curvature. The Nusselt number for the heated curved walls should be an average of the globally measured heat flux through this section. It can be interesting to report the results of this experiment and the previously described empirical correlations in Figure 24.

The Kumakawa empirical correlation seems to be the most reliable correlation to describe concave heat flux enhancement by concave asymmetrical heating which was measured in this experiment. Niino's correlation predicts an earlier maximum of the curved to straight Nusselt number ratio (*8* D_h after the beginning of the curvature for Niino's correlation against *15* D_h for the experimental results). This observation was also registered in the experiments of Meyer.

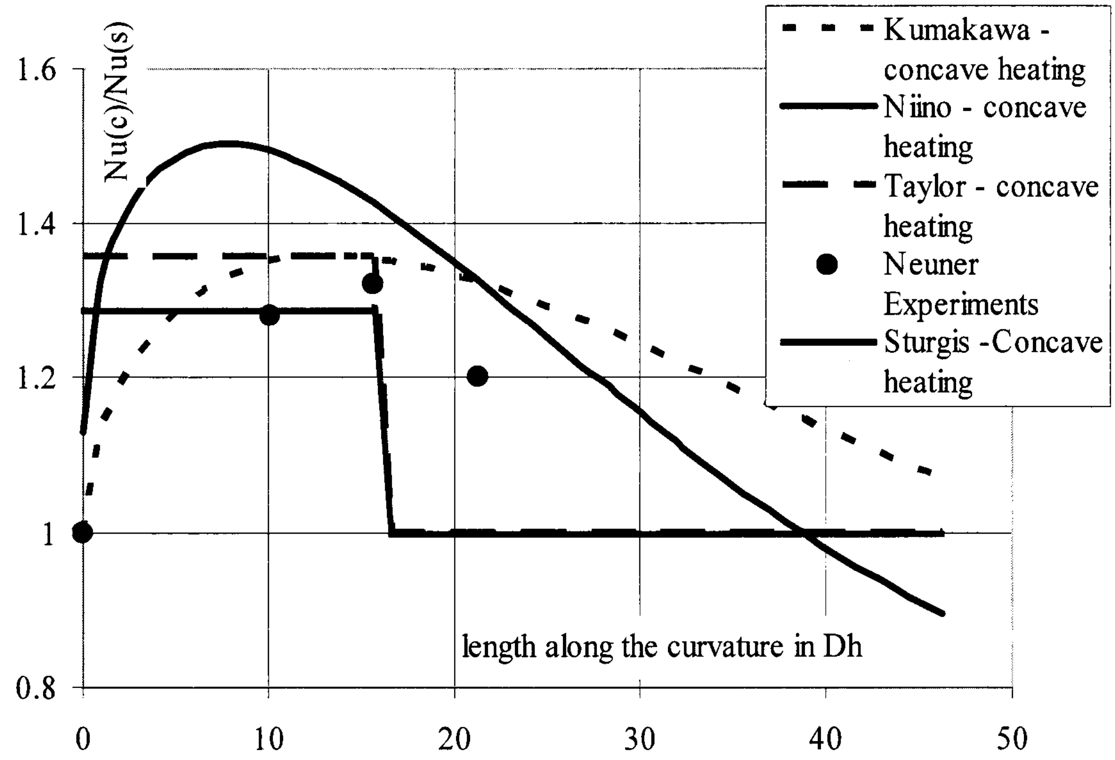

Figure 24 : Empirical correlations and Neuner's experimental results. The concave side is heated (asymmetrical heating) and the Nusselt number is calculated at the concave side.

Representative asymmetrical heat transfer characteristics in rocket cooling channels are difficult to be approached. In Neuner's experiment, the fluid is air at sub-critical condition, the global dimensions of the channels are over scaled (*~ 60 times*) and the asymmetrical concave heat flux remains very low (*0.06 MW* m^{-2}) in comparison to heat flux density through real combustion chamber walls (*up to 80 MW* m^{-2}).

2.3. Numerical simulations

Nowadays, 3D-numerical simulation could be considered as the method of most perspective to determine mechanical, thermal, and pressure loads on a structure. The main advantage of this computing method is the universal character and the relative precision of the results which increases with the recombination of several sources of information, like existing simulations, experiments and empirical correlations. A CFD simulation has to be extended all over the operating domain to test the robustness of the model: the influence of various parameters has to be characterised and evaluated, like boundary conditions, turbulence models, wall treatment, grid precision. The principle of the numerical simulations is described in Appendix 1.

2.3.1. Numerical simulations of momentum transfer in curved cooling channels

In the last 20 years, the heat and mass transfers in channels have been simulated by several codes and ways of calculation. Numerical simulations help to distinguish flow instabilities and turbulent behaviours which are very difficult to be measured experimentally or calculated theoretically.

The twisting and the bifurcation of Dean's vortices were observed in curved rectangular channels. The initial vortices pair configuration is broken down into multiple vortices. The *2* to *4* vortices pattern transformation was experimentally observed and numerically computed [Jayanti, 1992, Belfort, 2001, Zhang, 2001], see Figure 25. The twisting of the Dean vortices appears on the concave surface. Several assumptions can explain the dislocation of the initial Dean vortices pair.

- In corners of rectangular channel, the strong passage of vertical to horizontal shear stresses creates secondary motions (see in 2.1.1) which can interact with the Dean vortices.
- Due to these non-uniform shear stresses in corners, the fluid surface tension can be supposed to be high enough to break down the initial vortex. This assumption can only be studied thoroughly using sub-critical flows, with very high surface tension fluids.
- In pipes with high curvatures, the centrifugal forces and their consequent static pressure gradients are so high that the extreme shear stresses inside a pipe section will dislocate the initial secondary motion.
- Under high Görtler numbers, the appearance of Görtler vortices in the middle of the concave side can coexist with the Dean vortices. Figure 25 shows the influence of the aspect ratio of a channel on the interaction of Dean and Görtler vortices. For higher aspect ratios, the critical Görtler number must increase to observe Görtler mushrooms configurations at the concave side.

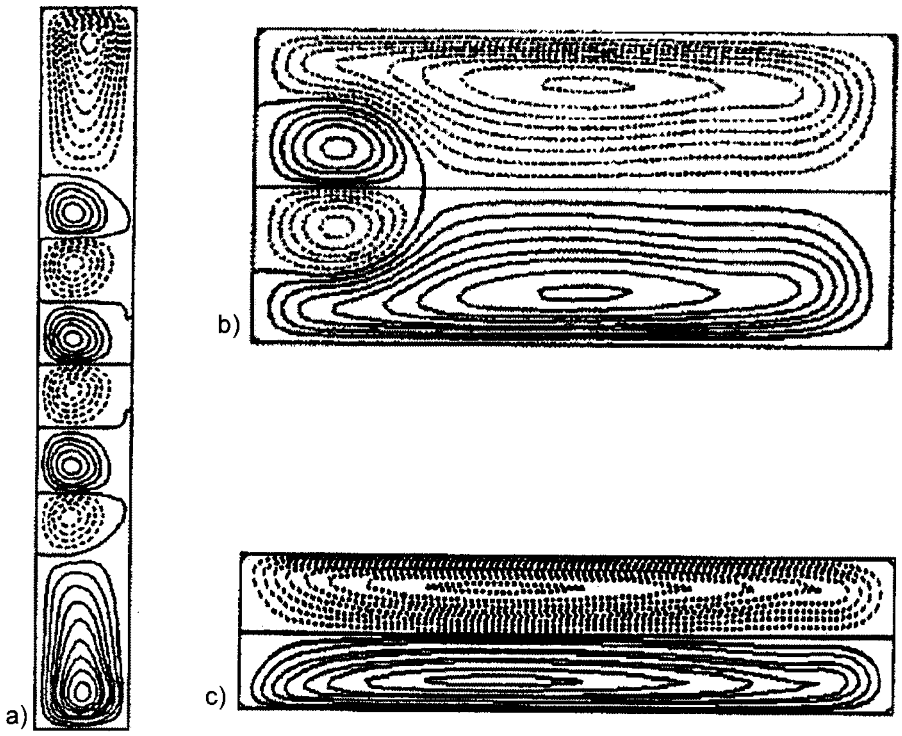

Figure 25 : Disappearance of Görtler vortices in the Dean vortices configuration, for Re=4000 and high curvature *K=0.3* (concave side on left), for different aspect ratio: a) *AR=0.125*, b) *AR= 2*, c) *AR= 4*. The concave sides are located on the left, [Zhang, 2001].

The Görtler and Dean centrifugal instabilities have not the same origin and should not be confused. The Görtler vortices only appear on the concave wall in high velocity gradient zones, particularly in boundary layers. The Dean vortices appear in the whole section of a curved pipe and are due to the influence of lateral walls.

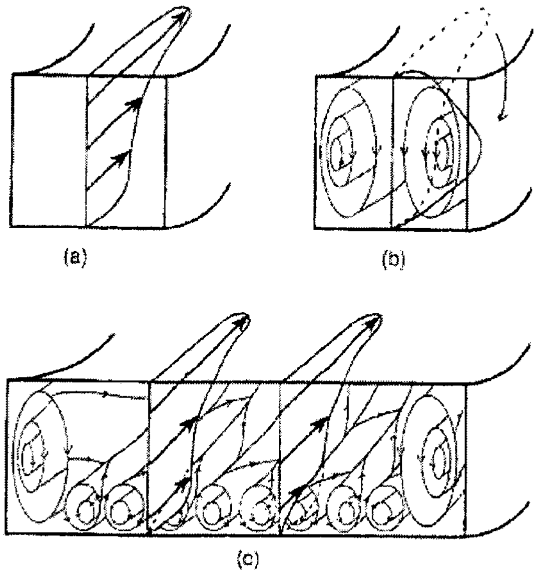

Figure 26 : Interaction of Dean and Görtler vortices [Petitjeans, 1995].

Petitjeans very well described the interaction between the two instabilities and the conditions required for exhibiting the Görtler vortices [Petitjeans, 1995]. Figure 26-a shows a main flow profile in a curved channel. In this configuration, the velocity flow profile is pushed to the convex side by mass conservation in a section (higher velocity on the convex side, where the radial pressure is lower). This velocity profile already checked by 2-dimensional numerical calculation (the Dean vortices are a 3-dimensional effect). Lateral walls are responsible for the appearance of Dean vortices. In the flow configuration with Dean cells, the secondary motion imposes a velocity profile displacement from the convex wall to the concave wall, seen in Figure 26-b. The mass conservation is characterised by the permanent secondary motion (Dean vortices) and not anymore by the radial pressure gradient.

Nevertheless, there is some flow configuration where both vortices can coexist: the Reynolds number and the Görtler number must both be high enough before Görtler vortices appear. The influence of lateral walls must be reduced in order to isolate the Dean vortices at the lateral walls and leave the Görtler vortices in the middle of the concave wall. In the case of very high aspect ratio channels it is probably impossible to observe Görtler vortices, because the Dean vortices are always decisive in terms of stability. Permanent secondary motions are more stable than shear stress variations inside the boundary layer thickness. In the case of lower aspect ratio channels (Figure 26-c), the Görtler rolls are located in the middle of the channel, because they are free of Dean vortices influence near the lateral walls [Petitjeans, 1995].

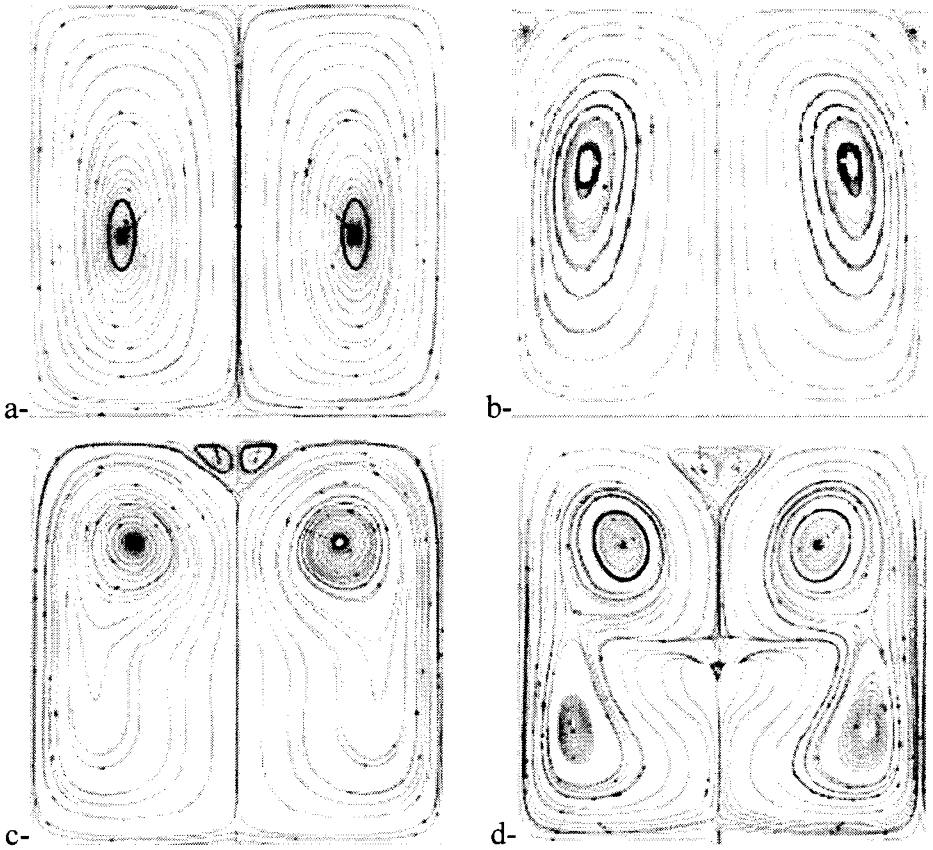

Figure 27 : Simulated Dean vortices breaking down [Tsai, 2006] at: a- *4.5°* after the beginning of the curvature b- *45°* c- *65.25°* d- *76.25°*.

At very low Reynolds numbers (*Re ~ 800*) with important curvatures ($\kappa \sim 0.3$), the Dean number can be relatively weak but twisting of the Dean vortices can be observed [Tsai, 2006]. In this numerical investigation (convective-diffusive schema of Petrov-Galerkin), the authors simulated a strong curved square duct with incompressible flow. They remarked that the initial Dean vortices were broken down into *2* and then *3* small vortices after *40°* in the curvature. The main velocity profile is thus modified and presents deceleration in the middle of the channel. Figure 27 shows the evolution of the secondary pathlines along the curvature. Until *45°*, the classic Dean vortices pair can be observed.

The upward movement in the edges (Dean vortices along lateral walls) of the concave side along lateral walls imply a small separation of the flow: Figure 28 very well illustrates this flow separation. It can be assimilated to the "edge vortices" due to the rectangular form of the channel.

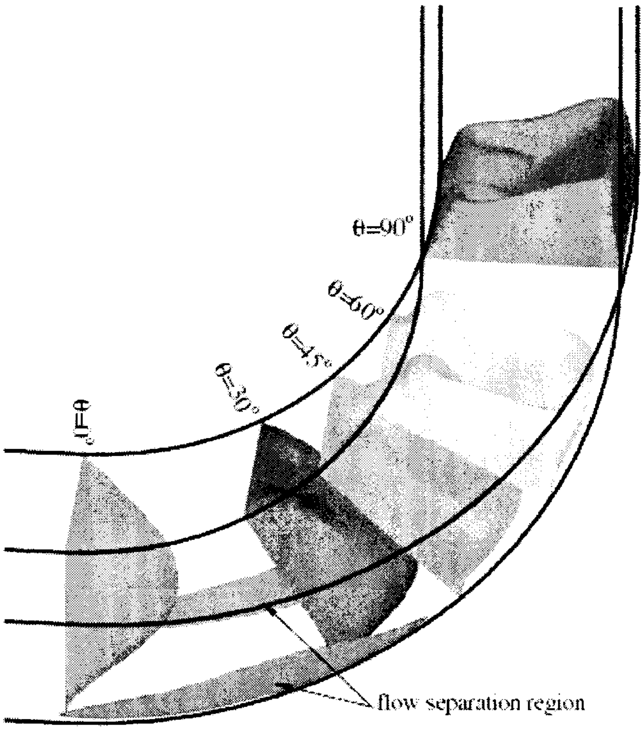

Figure 28 : Simulated velocity profile along an extremely curved channel [Tsai, 2006].

Another flow separation appears in the middle of the convex side which can be explained by the strong curvature (and strong radial pressure gradient). After *60°*, the global structure of the Dean vortices breaks up into *2* pairs of vortices and a possible Görtler vortex structure on the concave side.

The critical Reynolds numbers were numerically investigated. This is the reason why a *4*-cells structure of Dean vortices appears [Jayanti, 1992]. All these numerical simulations were calculated with laminar flow (Re up to *2000*) for *3* different curvatures ($\kappa = 0.1; 0.05; 0.02$) in a square section duct (*AR=1*). The critical Reynolds number grows up with the curvature radius. By $\kappa = 0.1$, $\mathrm{Re}_{crit} \sim 350$ and by $\kappa = 0.02$, $\mathrm{Re}_{crit} \sim 800$. Figure 29 illustrates the appearance of the 4-cells structure at the critical Reynolds number (here $\mathrm{Re}_{crit} = 580$ for $\kappa = 0.05$):

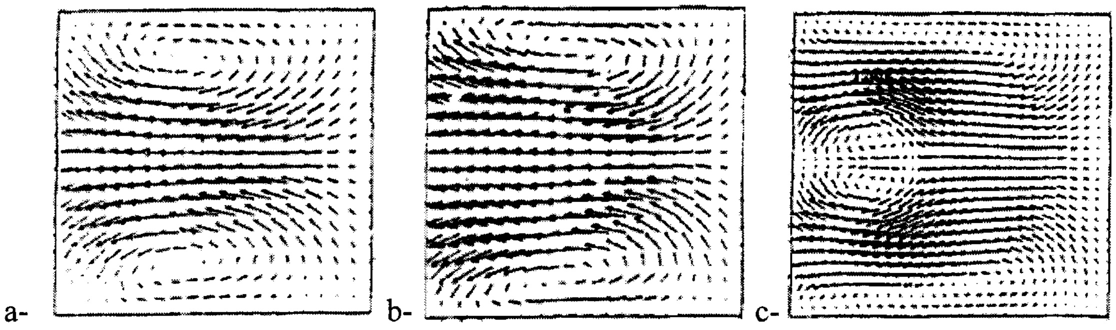

Figure 29 : Secondary flow pattern for $\kappa = 0.05$, *Re = 200* (a-), *400* (b-), *580* (c-), [Jayanti, 1992].

2.3.2. Numerical simulations of heat transfer in curved cooling channels

A numerical analysis was carried out by Yagley to investigate the influence of the aspect ratio of rectangular channel on asymmetrical heat flux (concave side) in low Reynolds number flow ($Re \sim 8\times10^3$) and in turbulent flow ($Re \sim 8\times10^4$), [Yagley, 1992].

The channels had a *90°* curvature with a factor $\kappa = \frac{D_h}{2R_c} \sim 0.02$ that is high. The numerical models use a simple turbulent model (isotropic single equation closure model) and semi compressible flow (compressible flow only in high viscous regions). Moreover, some terms were omitted to simplify the energy equation (kinetic energy, viscous dissipation...). The thermal boundary conditions define constant temperatures for the hot and the cold sides of the channel. A linear temperature gradient is used along the lateral walls to interpolate both low and high temperatures along the channel height. In spite of all these numerical simplifications, the laminar and the turbulent studies showed that the Dean vortices were broken up into several pairs of smaller vortices, as can be seen in Figure 30. These small bifurcated vortices are not so efficient in terms of heat transfer enhancement. The breaking down into multiple vortices is probably due to the extreme curvature and the aspect ratio which is studied in this test case. The influence of the aspect ratio was investigated in the laminar and turbulent case as well. The heat flux seems to be higher with higher aspect ratios and this corresponds to the theory (see 2.2.1). Moreover, the *4* channels that were studied (four different aspect ratios) have neither the same hydraulic diameters nor the same mass flows which obviously does not allow direct comparison of heat transfer in the different channels.

The choice of the right turbulence model and the right wall treatment represents one of the most important challenges for engineering numerical applications, to save time costs. Anisotropic models (like the Reynolds-stress models) are quite well adapted to approach recirculation, high shear stress gradient regions and curvatures [Gretler, 2000]. Concerning two equations models, a low-Reynolds model based on the k-ω turbulence resolution [Wilcox, 1986] showed good approximation of dynamical behaviours in curvature [Song, 2000] when the Reynolds stresses can be modified (transformation of isotropic model to non-linear model).

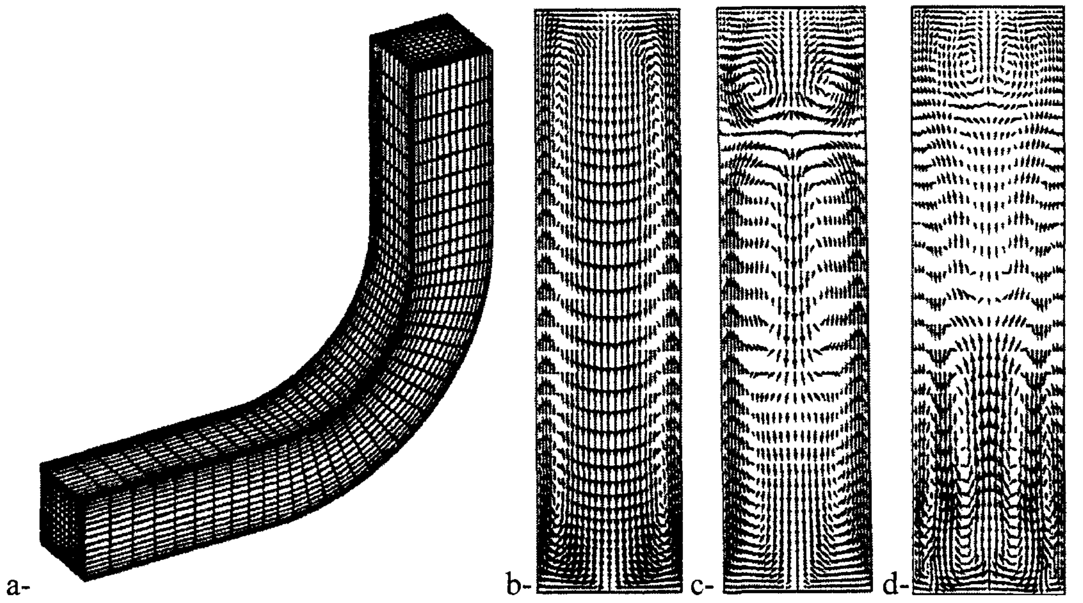

Figure 30 : Secondary motion from numerical simulation, at *Re* =$8 \cdot 10^4$ [Yagley, 1992]

a- Geometry with an aspect ratio of *1*

b-, c- and d- Simulation with an *4*-aspect ratio channel, section taken *1* D_h after the curvature (entire Dean vortices), *4* D_h and *7* D_h after the curvature (bifurcation of Dean vortices).

The turbulent characteristic lengths are measured in different directions (streamwise correlations R_{uu}, R_{vv} and R_{ww} in the axial and radial directions of a channel) and the difference exhibit a strong non-isotropic turbulence, see in 2.1.1, [Zhaoshung, 1993]. The RSM turbulence model, by treating turbulence as non-isotropic phenomena, would be the most adapted turbulence model to solve dynamic and heat transfer in internal turbulent flows, like asymmetrically heated cooling channels of rocket engines.

2.3.3. Numerical simulations for Rocket applications

A good classical example of a 3 dimensional numerical simulation of rocket engine cooling channels was performed with a k-ε turbulence model, with a logarithmic wall function or a two-layer model [Fröhlich, 1991].

Three sections are presented along the length of the cooling channel: at the entrance of the hydrogen collector (aspect ratio of *4.62*), at a curved section (aspect ratio of *8.46*) and just before the injection in the combustion chamber (aspect ratio of *4.75*). The fluid part of the channels is divided into different segments, by inserting output velocity and temperature profiles of the preceding segment, as inlet condition of the studied segment. The heat transfer characteristics were approximated from 1-dimensional calculation. Unfortunately, the heat transfer through fins can present high uncertainties in comparison to reality because only the fluid was modelled. By the way, wall heat transfer at boundary conditions, is considered to be difficult to be evaluated precisely. In the throat section, the Dean vortices can be well observed inside the cooling channel, and represent *1.3%* of the main flow velocity, that allows a perturbation of the thermal stratification and an enhanced global heat flux at this section, as can be seen in Figure 31.

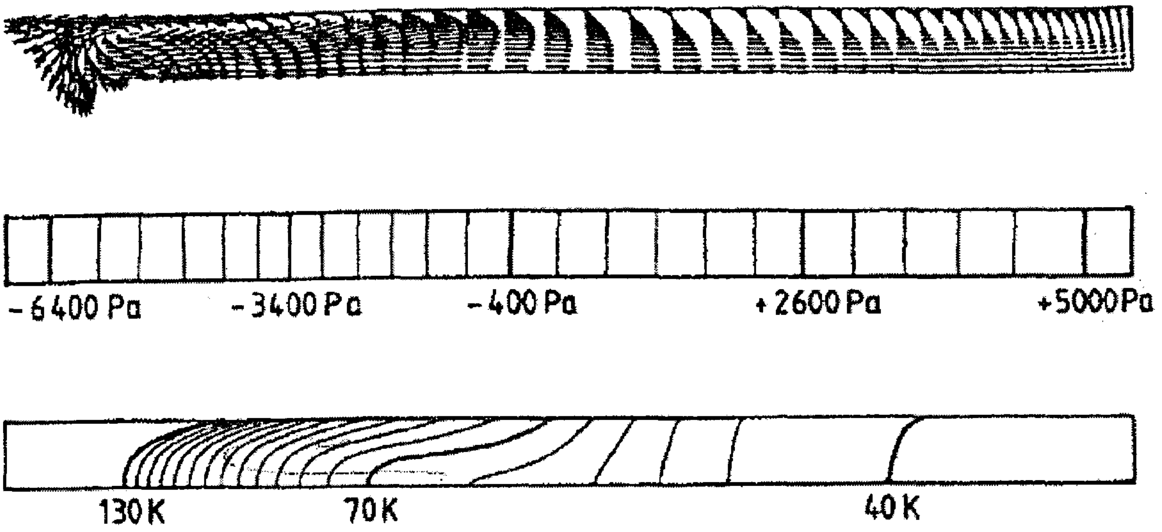

Figure 31 : Secondary vortices from numerical simulation at the converging part of a rocket engine, local static pressure and temperature distribution [Fröhlich, 1991].

It can be interesting to present numerical simulations done in straight channels to underline that the secondary motions appear and modify the velocity profile (see 2.1.1). In edges of a rectangular channel, the sudden orthogonal orientation of the shear stresses from a lateral wall to a juxtaposed one brings some local recirculations, up to *1-3%* of the main flow velocity, [Leuthesser, 1963]. Numerical simulations with LES resolution (Large Eddy Simulation) were provided to show the influence of corners and asymmetrical heating in straight channels on temperature and velocity profiles [Vazquez, Métais, 2002]. A heat mechanism was brought forward (ejection mechanism), in a straight channel with the following fluid properties: $Re=6000$, $Ma=0.5$ (Mach number). This calculation was at first isothermally compared with a DNS (Direct Numerical Simulation) test case to validate the LES simulation. The shear stress repartition from the LES over a fluid section seems to be well adequate with the DNS results, more particularly for the secondary motions in corners of rectangular channels. A second test case was proposed with one heated wall. The influence of asymmetrical heating on secondary vortices can be seen in Figure 32.

The secondary components of the velocity (secondary motions) are modified by the the asymmetrical heat transfer. More particularly, an amplification of the recirculation near hot walls can be noticed. These turbulence structures are called "ejection and sweep mechanisms" in this publication. Ejection pushes the hot fluid from the wall (typically at the hot wall side) whereas a sweep mechanism pulls the cold fluid location to the walls. The presence of initial vortices in edges of isothermal rectangular channels favours the heat transfer by perturbation of the thermal stratification. For lower values of heat transfer, a similar simulation $(T_b/T_w = 1.75)$ was calculated and did not differ much from the isothermal case. The modification of the secondary velocity profile (amplification of the edge vortices) seems to appear at a wall to bulk temperature ratio of *2.5*.

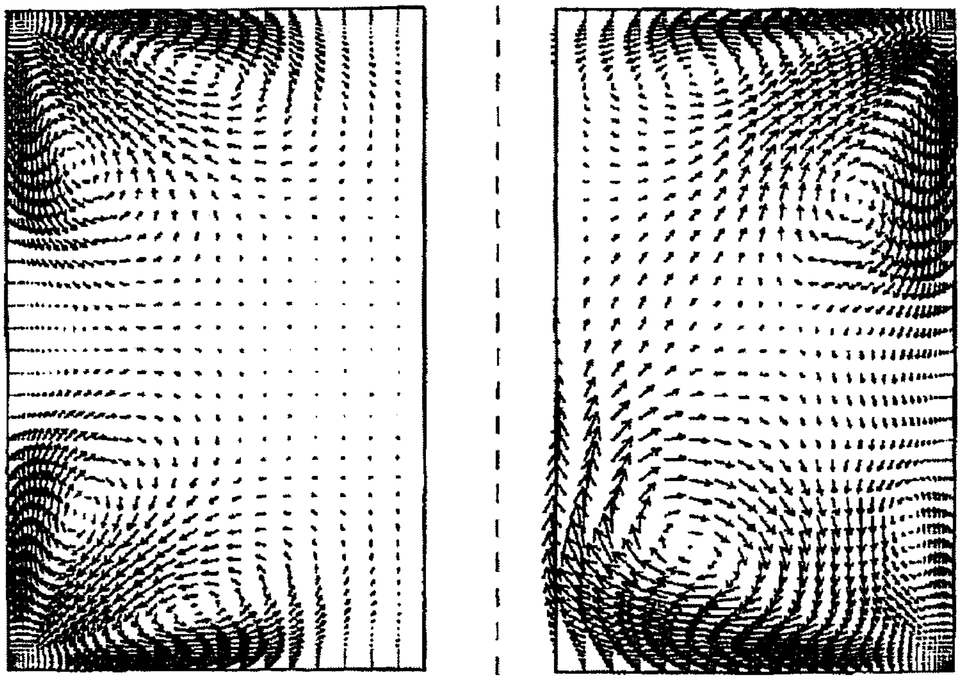

Figure 32 : LES numerical simulations of isothermal ($T_b/T_w = 1$, left) and asymmetrical heating ($T_b/T_w = 2.5$, right) of a turbulent flow in a square straight channel, [Métais, 2002].

2.4. Chapter conclusion

Some theoretical investigations, empirical correlations and numerical simulations have been collected in order to enlighten the heat and mass transfers in cooling channels. The particular configuration of curved cooling channels of rocket engines has been taken into account:

- Channel with small dimension ($D_h \sim 1mm$)

Some empirical correlations have been built in order to predict the pressure losses reduction through capillary tubes. For low Reynolds numbers (*Re=2000*), this decrease can reach *20%*. For higher and turbulent Reynolds numbers, the pressure losses difference between capillary tubes and normal tubes disappears.

- Rectangular cross-section, High Aspect Ratio Cooling Channel, HARCC, up to *15*

The rectangular cross-section geometry creates some "edges" vortices which reduces the pressure losses by *8%* for *AR>7*. Theory and numerical simulations (LES) predicted the formation of these vortices.

The use of HARCC allows an increase of the heat transfer up to *25%* for a limited pressure losses gain (about *7%*).

- Curved channel, $R_c \sim 100$ *mm*

In term of pressure losses, different correlations calculate an increase of the friction factor by curved channel from *20%* up to *50%*.

The curvature of cooling channels induces the formation of Dean and Görtler vortices (only at the concave side) which perturb heat transfer. In HARCC, only the Dean vortices appear.

Empirical correlations and experiments show an influence of the curvature on the heat transfer, up to *+50%* at the concave side and down to *-20%* at the convex side.

- High heat flux density (up to $80\ MW\ m^{-2}$)

The very high heat flux density can be a source of additional deviations between empirical models and reality. Mainly due to reduced experimental data reliability, the empirical correlations have not been extended to high heat flux configurations.

- Asymmetrical heat flux through concave or convex side (smaller side)

The asymmetry of the heat transfer reduces the heat transfer by about *10-20%* in comparison to full-perimeter heated channel.

The heat and momentum transfers in cooling channels of rocket engines have been listed, in order to delimit the role of each particularity of this configuration. The scatter between different empirical correlations, experimental results and numerical simulations incite to provide reliable experimental results which have to recreate all the particularities of the curved cooling channels of rocket engines.

3. Experimental Method

In order to enlighten the curvature effects on the heat transfer in cooling channels of rocket engines, the empirical correlations and the numerical simulations must be validated by experimental tests. These experiments have to provide conditions similar to those in real rocket cooling channels:

- ergols as coolant under high pressure and cryogenic temperatures
- small dimensions of cooling channels
- rectangular and HARCC channels
- asymmetrical high heat flux density

This chapter describes design, qualification and the EH3C experimental conditions.

3.1. Test Specimens

3.1.1. Thermal nozzle

3.1.1.1. Design

A DLR patented invention [Suslov, Torres, 2004] proposes the application of the principle of an aerodynamic nozzle to the thermal domain, in order to create a high heat flux density close to the real heat transfer conditions. Through an aerodynamical nozzle section (for example a Laval nozzle), the fluid accelerates and can reach sonic velocity in the throat section. The special profile of a nozzle transforms pressure energy to kinetic energy. This principle has been extrapolated to thermal problems, imposing some analogies between velocity and temperature fields, kinetic and thermal energies, heat flux and mass flow densities. A rod of high thermal conductivity material has been designed with a convergent cross section. One side is heated and the other one is cooled down, imposing a thermal gradient through the thermal nozzle. Assuming that no heat losses can be observed, the heat flux will be constant at any section of the “thermal nozzle” from the convergent to the nozzle throat. The heat flux density will vary proportionally to the inverse of the cross section, the maximal heat flux density will be reached at the throat section (see Figure 34).

A special convergent profile has been numerically and experimentally investigated. The aerodynamic profile of Vitoshinski [Dejc, 1974], see Figure 33, was applied to manufacture a test specimen of high conductivity material (copper alloy Elbrodur G), where l is the length of the throat section, x the abscissa coordinate and r, r_1, r_0 are the different heights of particular points of the profile, see Figure 33.

The melting temperature of the copper alloy was taken as thermal limit for the hot side of the thermal nozzle (about *750 K*). On the opposite surface, a cooling system (cooling channels) was designed. Electrical power was supplied at the hot side to control the temperature (*1 kW*). The aim of this device is to obtain the maximal and uniform heat flux density through the throat section. The profile of Vitoshinski can be optimised, by varying geometrical parameters, here $X=3$. Originally, this shape parameter is used to optimise aerodynamical profile. A transposed application was realised in the thermal field.

$$r = \frac{r_1}{\sqrt{1-\left[1-\left(r_1/r_0\right)^2\right]\frac{\left(1-\frac{X\cdot x^2}{\left(l\sqrt{X}\right)^2}\right)^2}{\left(1-\frac{x^2}{\left(l\sqrt{X}\right)^2}\right)^3}}} \tag{3.1}$$

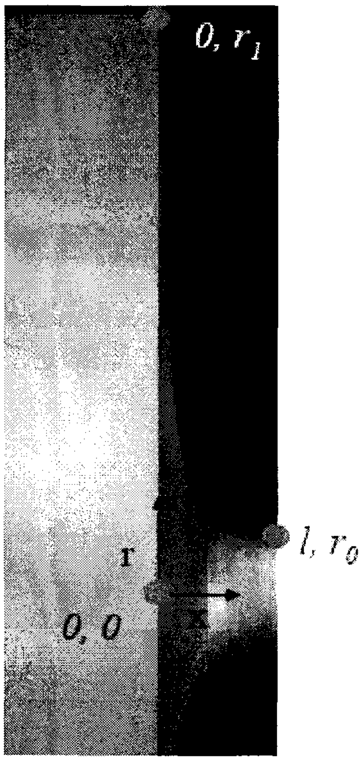

Figure 33 : Definition of the Vitoshinski aerodynamic profile on a solid "thermal nozzle".

With numerical simulations, the value for the shape-parameter *X* was determined. This parameter influences the geometry of the "nozzle profile", finding a compromise between maximal input heat flux and parallelism of iso-temperature lines in the throat section. An abrupt profile (low value of *X*) would perfectly provide parallel temperature lines through the throat (uniform repartition of the heat flux, 10% variation about the averaged value) with a relatively low averaged value (*14 MW* m^{-2}), see Figure 34a. On the contrary, an extremely shaped profile (high value of X) will accept a higher heat flux density through the throat (*20.4 MW* m^{-2}), but not uniform (*22%* variation about the averaged value), see Figure 34b. In the nozzle section, the iso-temperature lines are distorted. These numerical simulations were performed with the finite element method, taking into account the heat flux in the material. All these simulations use a constant temperature at the two opposite surfaces, *750 K* for the heated surface and *77 K* for the cooled surface which correspond to the melting temperature of the material and the liquid nitrogen temperature. A computer program has been written to explore different values of the shape-parameter *X*. For each calculation with a specific profile, the averaged value of the heat flux density is evaluated as well as the heat flux density deviation over the throat section.

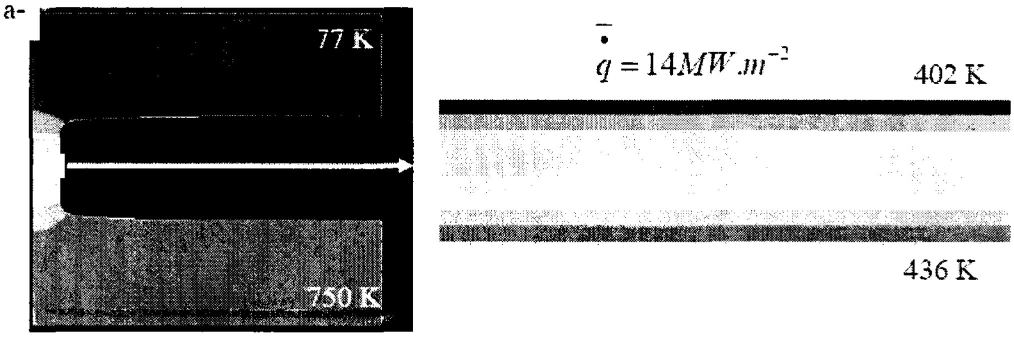

X = 0.05 Temperature profile

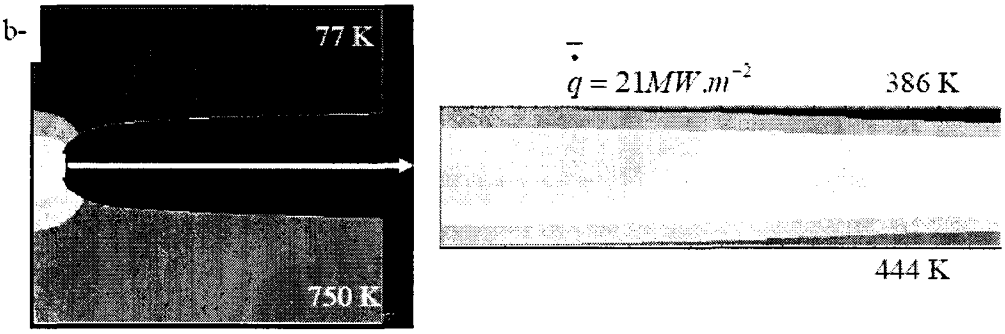

X = 100 Temperature profile

Figure 34 : Thermal nozzle profile influence on uniformity and value of heat flux density, a- extreme sharper profile b- blunt profile.

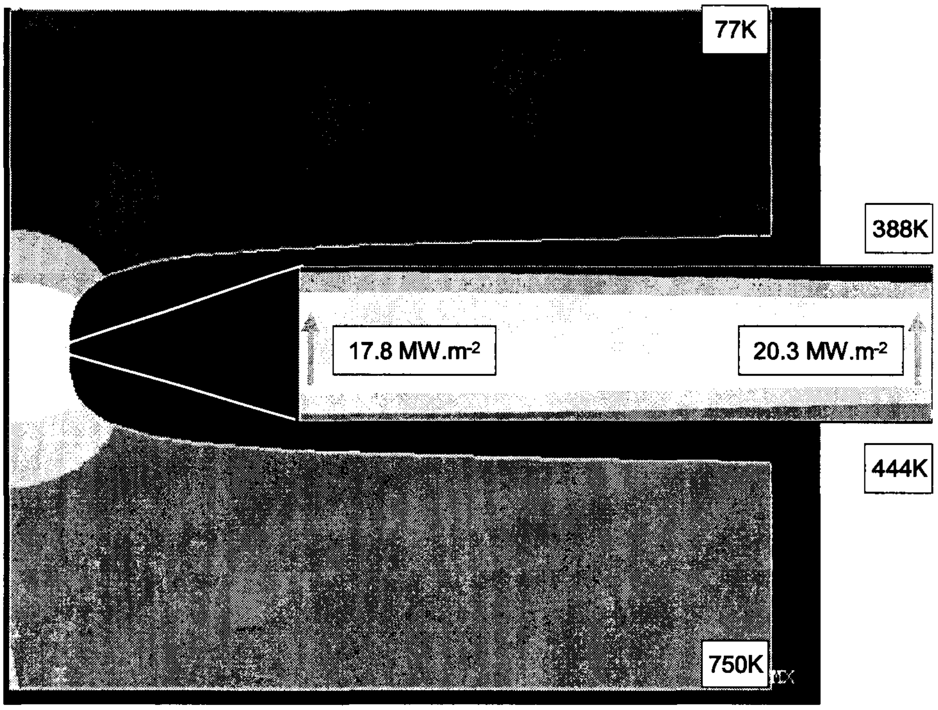

Figure 35 : Temperature profile in the thermal nozzle, X=3.

From the numerical simulations, a design profile was defined with a shape-parameter $X=3$. These numerical results firstly indicate that the principle of "thermal nozzle" can be exploited on an acceptable range of heat flux variation in the throat section for a quite high heat flux. These results must be now compared to experimental results and the machining of the profile must be mechanically tested. The selected shape is thus a compromise between the two extreme thermal behaviours, providing a high ($19 MW\ m^{-2}$ averaged) and quite uniform heat flux density at the throat section (*12%* variation), see Figure 35.

3.1.1.2. Manufacturing and Experiments

The "thermal nozzle" was manufactured at DLR (see Figure 36) and tested with an electrical heat controller and water cooling system. Three thermocouples were implemented in the throat section, parallel to the iso-temperature lines.

A test bench was designed to carry out experiments with this thermal nozzle test specimen, providing vacuum all around the test specimen, in order to prevent heat losses through natural convection and to avoid oxidation of the material. The hot side of the thermal nozzle was loaded with several temperatures (up to *670 K*) and the cooled side was supplied with liquid water (about *15°C*).

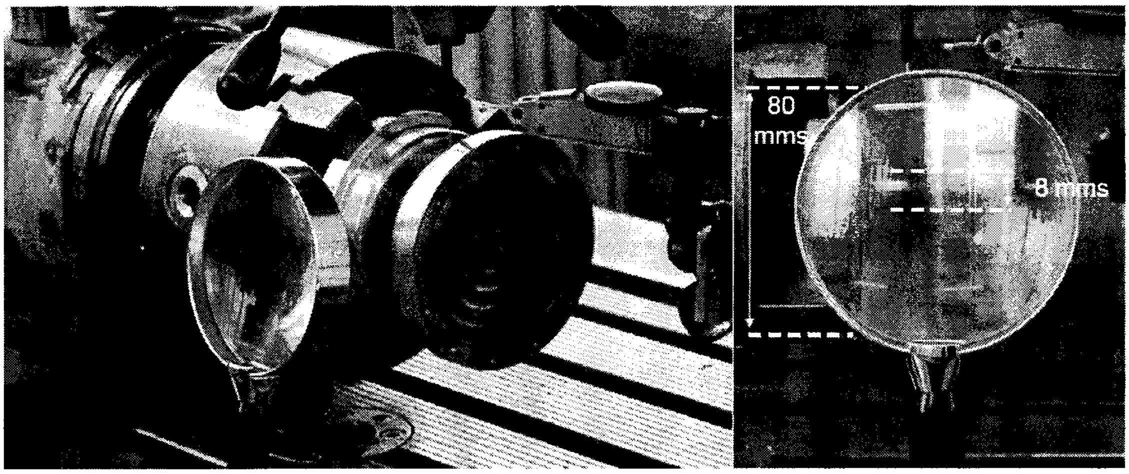

Figure 36 : Machining of a thermal nozzle (80 mm diameter, 8 mm diameter at the throat).

Three different campaigns delivered similar experimental results, insuring repeatability of the tests and good reliability of measured temperatures (no perturbation of the thermal field due to sensors implementation). The measured temperature in the throat section (*3* thermocouples) is perfectly comparable with numerical simulations (*2 K* maximal difference) and the global heat transfer corresponds well to the numerically calculated and the calorimetrically measured one. These experimental and numerical investigations validate the theoretical principle of the thermal nozzle. These results are satisfactory enough to develop a new test specimen, electrically heated with a thermal nozzle, to investigate the heat transfer enhancement in curved cooling channels of rocket engines.

3.1.2. EH3C (Electrically Heated Curved Cooling Channel)

3.1.2.1. Design, manufacturing and assembly

In reference of the DLR-patent (Suslov, Torres), a thermal nozzle brings asymmetrical heat flux density into a throat section. This principle was adapted from a *3*-dimensional design to a *2*-dimensional one, allowing the machining of a cooling channel at the throat section. A single cooling channel can be mounted on the thermal nozzle at the throat section, in order to provide controlled high and homogeneous heat flux density. The single channel concept allows better sensor implementation in comparison with real engine configurations. The 2D thermal nozzle profile of the EH3C test specimens refers to the Vitoshinski profile with the optimised geometrical parameter $X=3$. Then, the geometry of the hot surface was optimised in order to deliver the highest heat flux density through the throat section taking into account feasibility. Figure 37 describes the principle of the 2D thermal nozzle, in which a single cooling channel is machined.

A straight channel test specimen and a curved one with asymmetrical concave heating were machined to study the concave curvature effects on asymmetrical heat transfer.

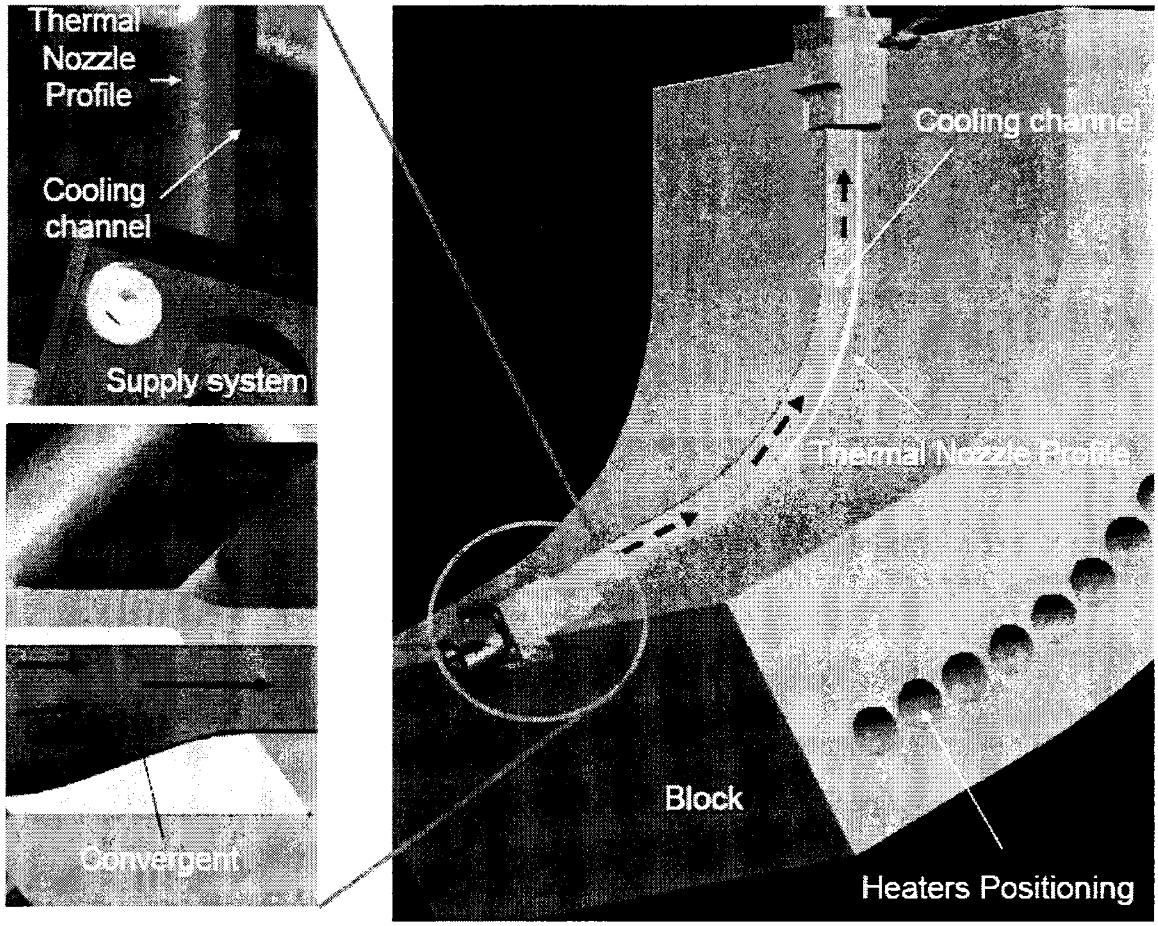

Figure 37 : Principle of Electrically Heated Curved Cooling Channel test specimen EH3C.

The lower part (manufactured in copper alloy) of the test specimen is heated by cylindrical electrical heaters (cartridges). Afterwards, the "thermal nozzle" concentrates the heat flux through the thinnest section where a cooling channel is milled. Geometrical parameters of the cooling channels can be machined identical to rocket cooling channels, representative fluids can be used as coolant (hydrogen, methane...), relative high asymmetrical heat flux density can be achieved and quite homogeneous heat flux density can be provided at the throat section. Moreover, a very precise control of the heat flux can be assured by an accurate electrical regulation system.

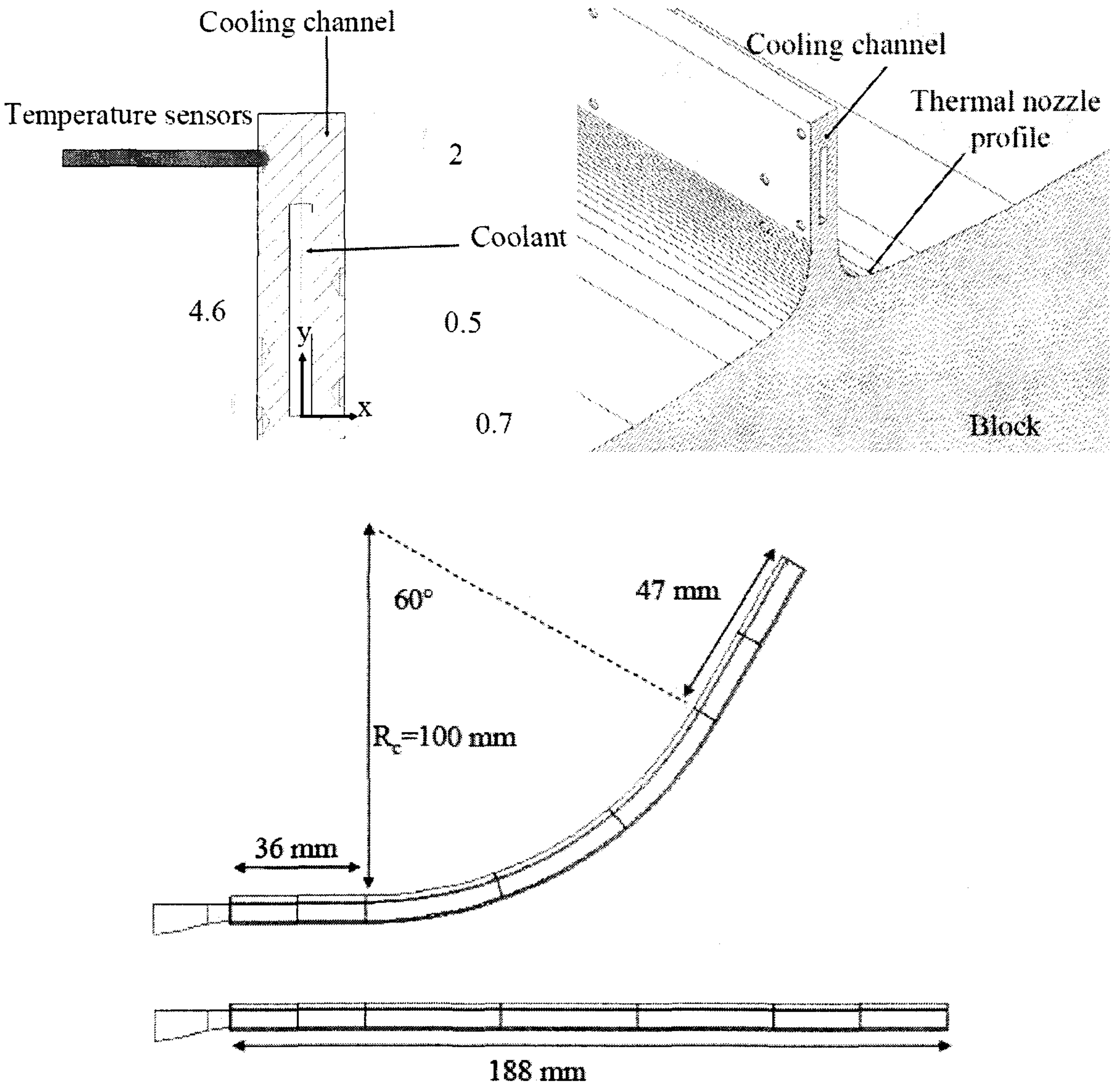

Figure 38 : Dimensions of the EH3C cooling channels.

To define the experimental conditions and the design of the EH3C test specimen, some experimental investigations [Woschnak, 2003] and the real machining process of the Vulcain *2* rocket engine [Fröhlich, 1991] were taken into account. A rectangular channel was milled along the throat section of the thermal nozzle, with a representative aspect ratio close to a typical Vulcain 2 aspect ratio (refer to the Appendix 2 for detailed process of construction.)

The dimensions of both straight and curved EH3C channels refer to the cooling channels of the combustion chamber HARCC [Woschnak, 2001], with the aspect ratio of *9.2* (see Figure 38):

- Height of a channel: $h_c = 4.6\,mm$
- Channel width: $w_{ch} = 0.5\,mm$
- Channel cross section: $S = h_c \cdot w_{ch} = 2.3\,mm^2$
- Wall width (fin width): $w_w = 0.7\,mm$
- Length of the cooling channel: $l_{tot} = 188\,mm$

The curvature radius and the length of the curvature of the concave channel for the EH3C test specimen took the real curvature geometry of the rocket nozzle profile at the throat section as reference. Some geometrical dimensions of the Vulcain 2 engine were taken into account in order to approximate the real experimental conditions to the EH3C conditions [Fröhlich, 1991]. To counterbalance the Re number deficit of EH3C experimental conditions (see later) in comparison with the real engine fluid parameters, the curvature dimensions of the EH3C curved test specimen have been accentuated in comparison with the real curvature parameters:

$R_c = 100\,mm$ and a turning angle of $\theta = 60°$.

Concerning the asymmetrical heat flux density provided by the "thermal" nozzle, additional numerical simulations were performed to verify the role of the thermal nozzle in the 2-dimensional configuration. The implementation of a cooling channel in the throat section could modify the temperature and heat flux profile at the throat section. Two simulations were performed: one with a heat transfer condition at the lower part of the channel (like in a real rocket) and the second one with the thermal nozzle block maintained at constant temperature at the hot side (EH3C configuration), see Figure 39. The real rocket configuration uses a constant heat transfer coefficient h_{hot} with a constant hot gas temperature (*3500 K*). In the EH3C configuration, the thermal nozzle block is modelled with the adequate convergent profile of Vitoshinski. A constant temperature is applied at the lower part of the thermal nozzle, corresponding to the heating temperature of the electrical cartridges. The same heat transfer coefficient *h* was applied on the channel walls as boundary conditions. The value of $h=50000\ W\,m^{-2}\,K^{-1}$ is maintained constant over the channel walls in both configurations and comes from the HARCC investigations of Woschnak, [Woschnak, 2003]. A constant coolant temperature was applied to the channel (*77 K*) in order to calculate the heat transfer. The test specimen geometry was divided into two parts for symmetry reasons. These simulations were only performed in order to characterise the influence of the thermal nozzle in comparison with real cooling channels of rocket engines.

The temperature and the heat flux density profiles along the width of the channel were thus compared along the separation line, corresponding to the hot gas side for the real rocket configuration and to the nozzle throat for the EH3C configuration (see the separation line definition in Figure 39). Figure 40 presents the temperature profiles (dashed lines, left axis) and the heat flux density profiles (full lines, right axis) for the real rocket configuration (black lines) and the EH3C configuration (red lines). These profiles represent one half of a real one, because of symmetry conditions used in the numerical simulation. The abscissa $x=0$ is located in the middle of the channel and the abscissa $x = 0.95\,mm$ is in the middle of the fin (channel wall extremity). There is $\Delta y = 0.8\,mm$ between the separation line (nozzle throat or hot gas side) to the channel.

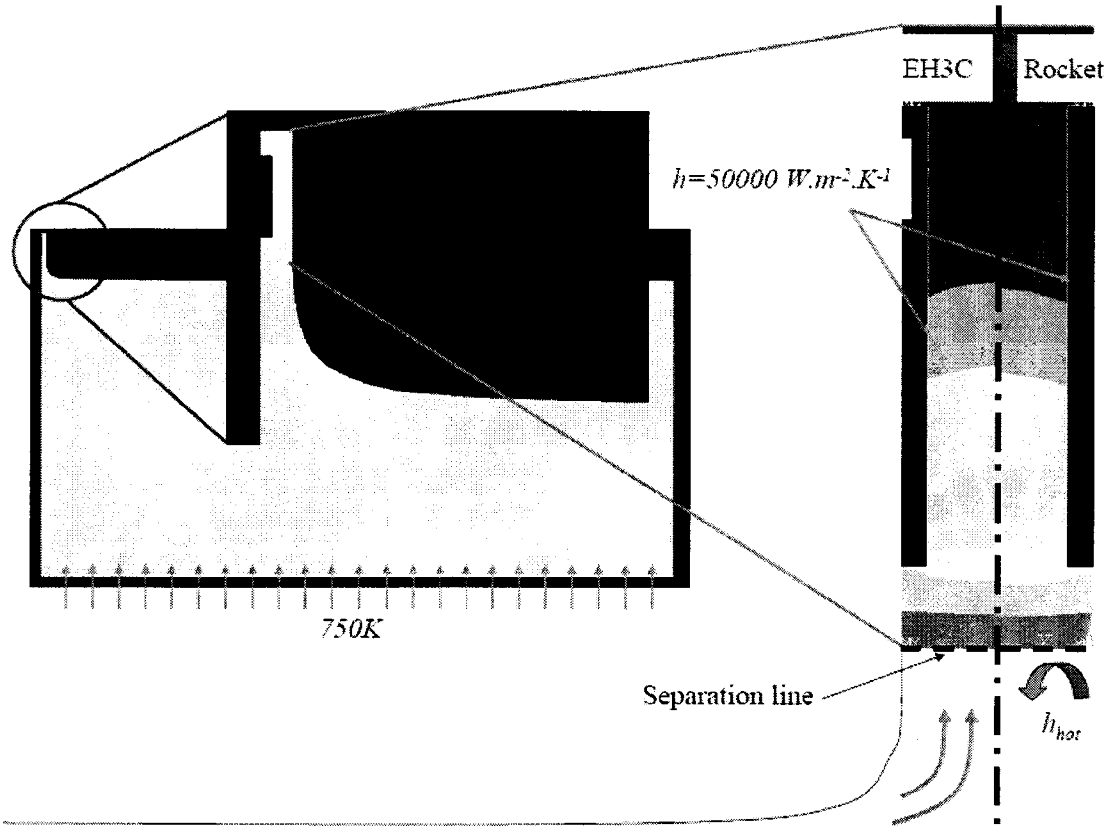

Figure 39 : Numerical simulations comparing the heat flux and the temperature profiles at the "hot gas side" of the cooling channel in real configuration and EH3C configuration.

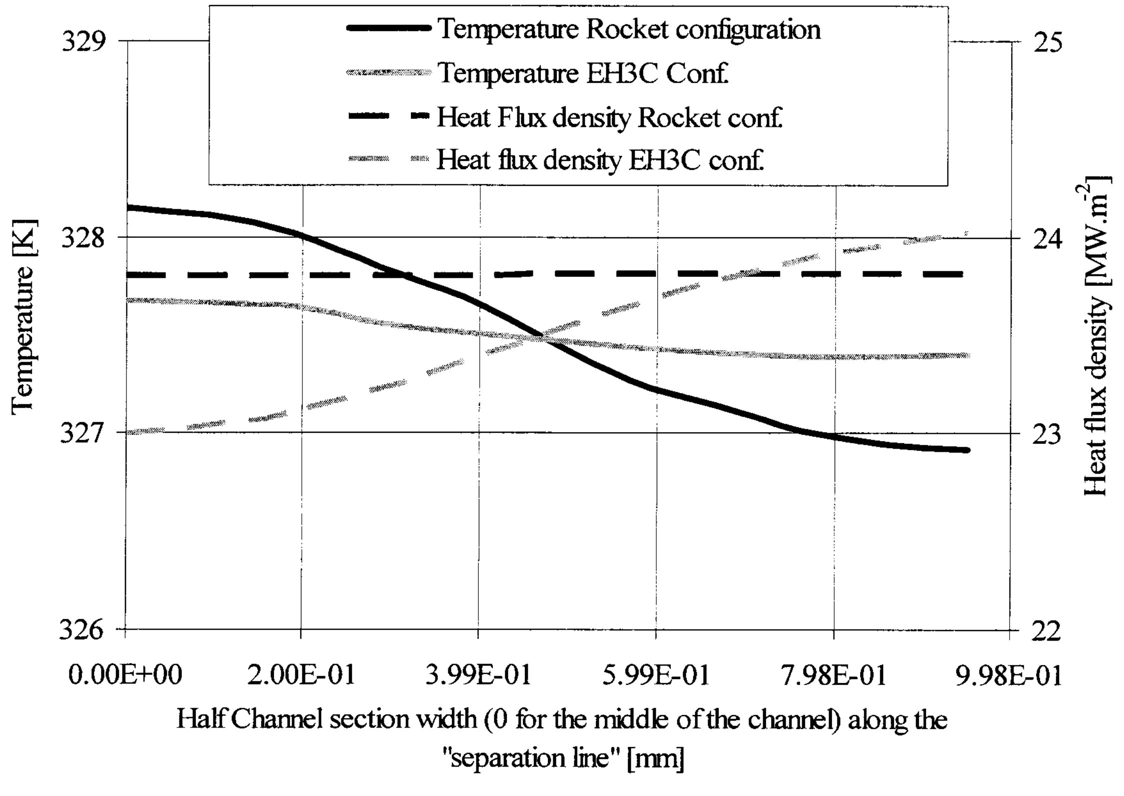

Figure 40 : Temperature and heat flux density profiles at the lower width of the channel for real rocket configuration and EH3C configuration.

The implementation of the thermal nozzle does not have a strong influence on the temperature and heat flux profile taken at the hot side of the channel. Less than *0.7 K* separates the two temperature profiles, although the two configurations differ by about *4%* for the heat transfer profiles.

Moreover, the height of the thermal nozzle base was determined to minimize the influence of the circular geometry of the electrical cartridges on the longitudinal heat flux transfer. Indeed, if the electrical heaters are located too close to the channel, the heat flux profile along the channel would be influenced by the circular geometry of the heaters. Moreover, the temperature at the extremity of the cartridges can be too extreme for the material (more than *900 K*), see Figure 41.

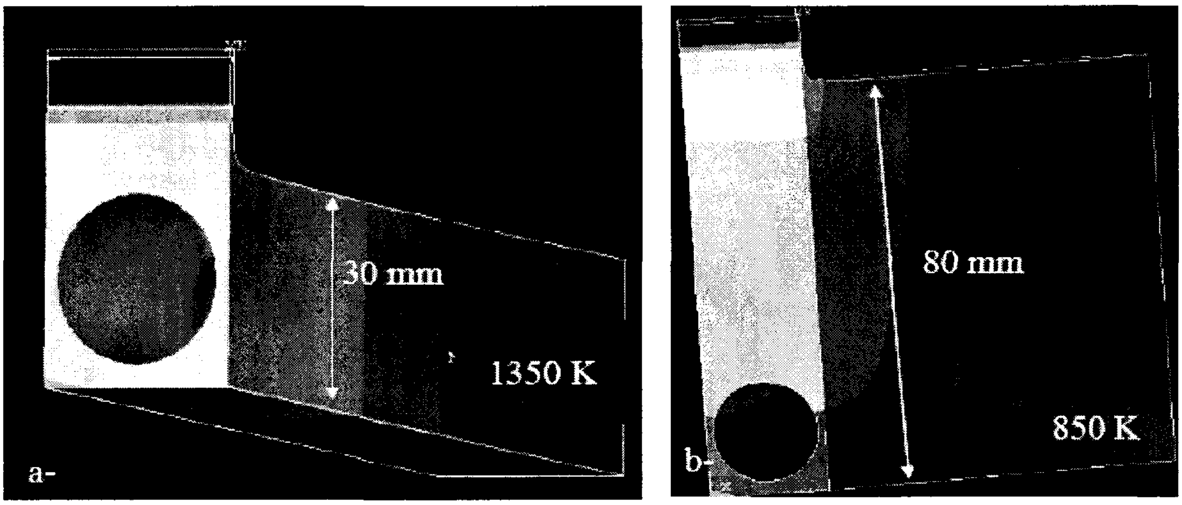

Figure 41 : Height optimisation of the thermal nozzle, a- 30 mm, b-80 mm

A sufficient distance must separate the heaters from the channel. This height was optimised with *3*-dimentional numerical simulation of the nozzle and of the cooling channel. A minimal height of *80 mm* is needed to deliver a smooth heat density profile along the interface between the block and the channel.

The test specimen construction can be divided into several steps (refer to Appendix 2 for more details):

- End milling of thermal nozzle profile
- Milling of cooling channel
- Electro-plating to enclose the channel
- Nickel layering
- Drilling of sensors and cartridges holes

For the EH3C experiments, a special test bench was designed and built, in order to deliver adequate regulated flow of high pressure fluids under cryogenic temperatures, see Appendix 6.

3.1.2.2. *Roughness of the EH3C cooling channel*

The roughness of the channel plays an important role in the development of the hydrodynamic and thermal boundary layers, and strongly modifies heat transfer by local energy dissipation. For these reasons, the roughness was measured on the lateral walls of the channel by realising a milled half channel with the same manufacturing conditions of those of the real EH3C test specimens. The averaged roughness of the lateral walls is really small: $k_{lat} < 0.1\mu m$. The bottom of the channel is directly formed by the milling cutter teethes and presents higher averaged roughness. Different tracks have been milled at different milling rotating velocities, different tool curvilinear velocities and with different tool teeth profiles. All the measured results are contained in a restricted values domain, $k_{bot} \approx 0.25\mu m$ (see Figure 42). The upper width of the channel cannot be measured because of inaccessibility. Nevertheless, the upper part of the channel is located at the convex side and does not have a strong influence on the concave side heat transfer. A value of $k_{up} \approx 2\mu m$ was assumed because of the electro-plating process. The contact between the galvanised copper and the wax is not really smooth. These values of roughness give an evaluation of the relative roughness for the EH3C configuration:

$$\begin{aligned} (k_{rel})_{lat} &= \frac{k_{lat}}{D_h} = 1.1 \times 10^{-4} \\ (k_{rel})_{bot} &= \frac{k_{bot}}{D_h} = 2.7 \times 10^{-4} \end{aligned} \qquad \textbf{(3.2)}$$

This gives an approximation of the friction factor with the Moody diagram [Gersten, 1992] that locates the flow in the transition phase between typical rough and typical smooth flow, $\xi \sim 0.017$ for $Re=10^5$ corresponding to the EH3C test configuration.

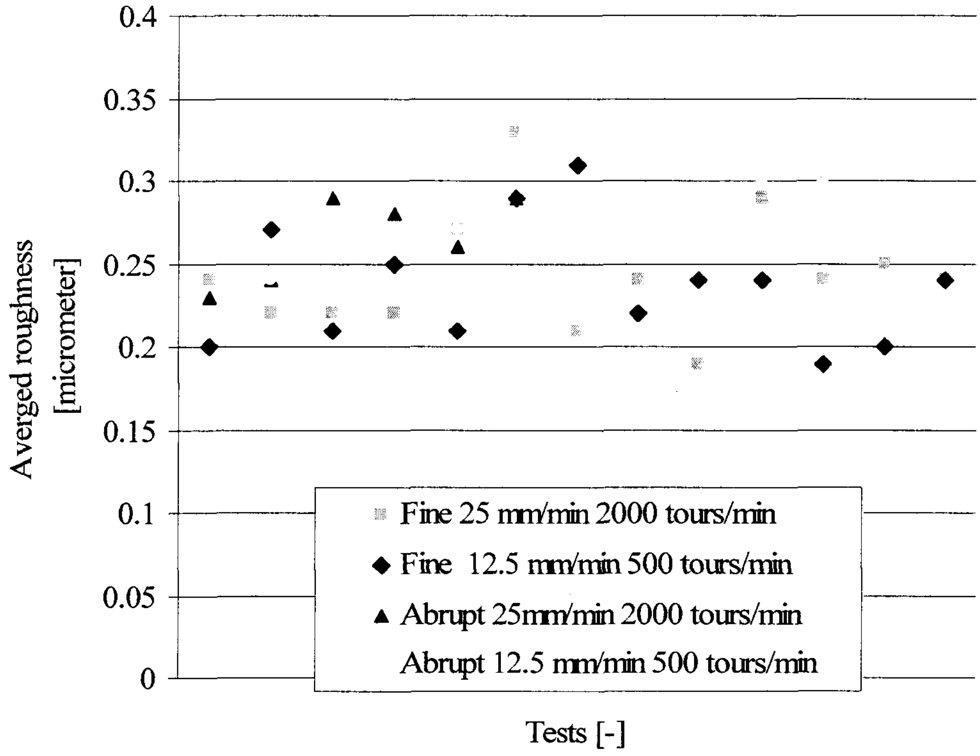

Figure 42 : Averaged roughness measurement of the lowest part of the channel (concave and heated side).

3.1.2.3. *Electrical and Heat Transfer Layout*

With all the heat flux calculations presented in Appendix 3, it is possible to evaluate the electrical need for the regulation system of the test bench. The selected electrical cartridges can deliver *1.2 kW* in order to heat the fluid (*875 W*) and to compensate the heat losses (up to *80 W* per heater).

3.1.2.4. *Flow requirements of the EH3C experiments*

Mechanical and thermal limits of the EH3C test specimens impose a reduced level of pressure (*40 bar*) for coolant in the EH3C configuration to ensure adequate service life of the test specimens and to respect the security requirements of the test bench use. Moreover, the test bench (see Appendix 6) can cool down the fluid in a liquid nitrogen bath that defines an entrance temperature in the EH3C of *80 K*. Two different coolants were investigated in the EH3C test campaign, hydrogen at *80 K* and methane at *290 K*. For the hydrogen case, the block was heated up to *400°C*. For the methane case, the block reached *200°C*.

Under the flow requirements presented in Appendix 4, it is possible to evaluate the expected dimensionless numbers at the entrance of the channels

- Hydrogen down to *80 K* and up to 4*0 bar* at the entrance of the channel.

$$\mathrm{Re}(H_2) = \frac{\rho_1 u_1 D_h}{\mu_1} = 5\times10^5 \tag{3.3}$$

$$\mathrm{Pr}(H_2) = \frac{\mu_1 Cp_1}{\lambda_1} = 0.74 \tag{3.4}$$

The De for the EH3C curved channel is equal to:

$$De(H_2) = \mathrm{Re}\sqrt{\kappa} = 3.3\times10^4 \tag{3.5}$$

- Methane at *290 K* and *40 bar.*

The other test configuration uses methane as coolant but under ambient temperature at the entrance of the channel. The characteristic numbers were estimated at the entrance of the channel for methane at *290 K* at *40 bar*, for a mass flow rate of $7\ g\ s^{-1}$ (see in 4.2).

$$\mathrm{Re}(CH_4) = \frac{\rho_1 u_1 D_h}{\mu_1} = 2.4\times10^5 \tag{3.6}$$

$$\mathrm{Pr}(CH_4) = \frac{\mu_1 Cp_1}{\lambda_1} = 0.799 \tag{3.7}$$

With the EH3C methane configuration, the *De* is equal to:

$$De(CH_4) = \mathrm{Re}\sqrt{\kappa} = 1.6\times10^4 \tag{3.8}$$

3.1.2.5. *Structural Layout and experimental qualification (prototyping)*

Experimental investigations were made to check the feasibility of the EH3C experiments, in terms of manufacturing and of mechanical resistance to extreme thermal loads, see Appendix 5. This qualification phase concerns the fabrication and the test of two different prototypes, with the same geometry of the EH3C designed test specimen but without block to save material. The qualification phase contains:

- Check of the end milling process of the thermal nozzle (verification of the dimensions).
- Check of the milling process of the cooling channel (verification of the channel dimensions after machining).
- Check of the integrity of the nickel layering at high temperature and oxidant environment.
- Check of the tightness and mechanical integrity of the channel and the supply systems under high pressure (10 bar helium and 50 bar water test).
- Check of the thermal resistance of the channel under high thermal stresses.

Some numerical simulations were performed to determine the stress distribution inside the specimen structure (ANSYS), due to pressure difference (outside-inside the channel) and due to thermal stresses (refer to Appendix 5).

The theoretical life cycle corresponding to the level of this deformation (0.8 % total deformation) indicates a service life of more than *100* cycles. The EH3C campaigns would not require more than *10* tests per test specimen, the investigated number of thermal cycles was stopped at *20*. The experiments confirmed that the structure of the two prototypes withstands the thermal loads, more than *20* cycles, without failure which is enough to qualify the resistance of EH3C test specimens (refer to Appendix 5). This numerical and experimental qualification phase is considered as satisfactory to begin the construction of the EH3C test specimens.

3.2. Measurement Methods

3.2.1. Sensors implementation and Notations

The cooling channel is equipped with *98* thermocouples with a diameter of *0.5 mm*. To fix the position of the thermocouples, small holes of *0.1 mm* depth were drilled in the outer wall of the channel. The thermocouples positions are divided into *14* sections along the channel length and *7* heights in the channel wall. Figure 43 shows the positions of the sensors in the *14* axial and the *7* radial positions. The origin of the coordinates is taken at the entrance of the channel and at the bottom of the channel. The coordinates of the measurement points of the different thermocouples are listed in Appendix 7.

The y-distances separating the measurement points are not equal, but the height positions were chosen to approximately have the same temperature difference between two successive thermocouples: $T_{1,j} - T_{2,j} \approx T_{2,j} - T_{3,j} \approx T_{3,j} - T_{4,j} \approx ...$

Along the channel length, $15\ D_h$ or $10\ D_h$ separates two successive axial positions. The previous numerical simulations with the finite element method (see in 3.1.2) were used to evaluate the heights of the different sensors, approximately giving the same temperature differences between sensors.

The different heights of the sensors were evaluated with numerical simulations (see 4.1.3).

At the two channel extremities, two pressure sensors were implemented. Moreover, a precise pressure difference sensor directly measures the pressure drop in the channel and checks the indication of the two previous values. The pressure sensors have a measurement accuracy of *+/-5%* and the pressure drop sensor has a measurement accuracy of *+/-1%*.

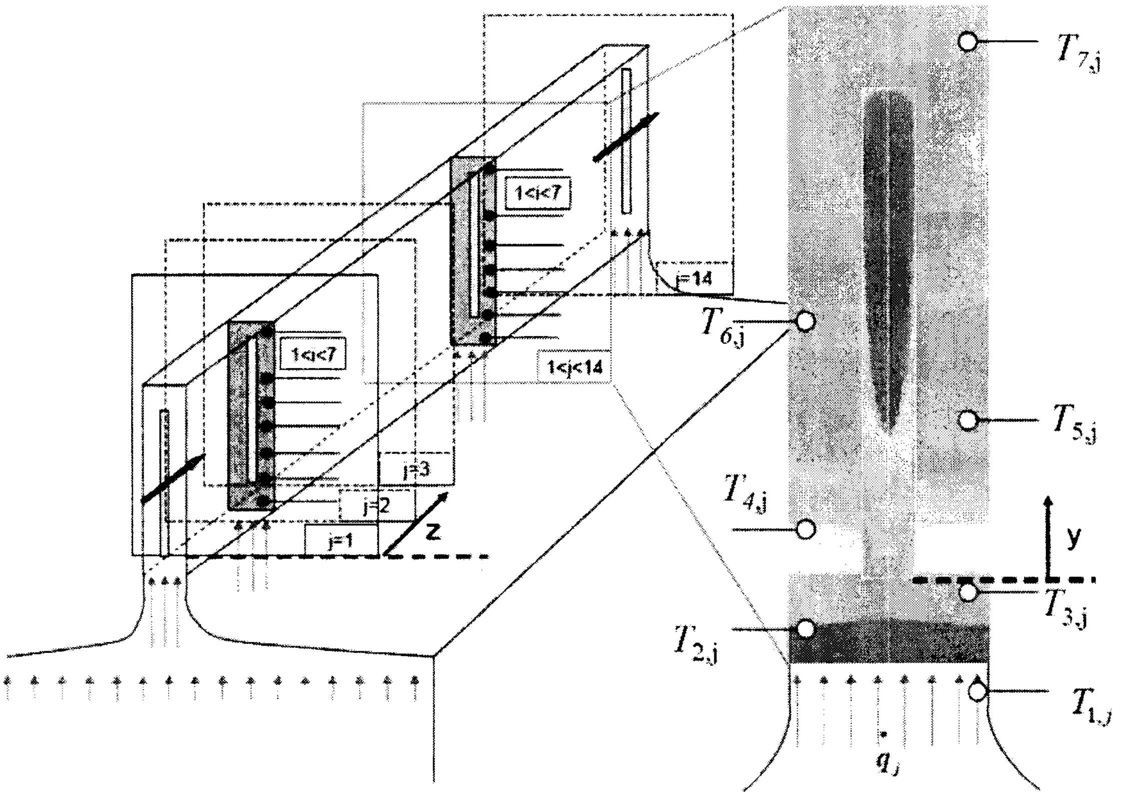

Figure 43 : Implementation of the 98 thermocouples in the EH3C test specimen walls.

3.2.2. EH3C Calorimetrical Method

A classical method of estimating the enthalpy gain of the fluid between inlet and outlet of the cooling channel was used. A Coriolis mass flow rate sensor gives a precise value of the mass flow rate (*+/- 2%*) and *2* thermocouples were added to the supply systems at the inlet and the outlet of the EH3C test specimens (*+/-5K*). The thermocouples thus measuring the total temperature at the inlet and outlet of the channels in the middle of the channel. The global heat flux can be calculated by following the 1 dimensional equation of heat enhancement:

$$\dot{Q} = \dot{m} c_p \left(T_{out} - T_{in}\right) \quad \textbf{(3.9)}$$

The heat capacity of hydrogen was investigated at the inlet and the outlet of the channels and along the channel length, (see Appendix 9). The heat capacity of hydrogen varies along the channel length: *10%* between the inlet and the outlet of the channel. The heat capacity was averaged between the inlet and the outlet of the channel to calculate the experimental enthalpy gain. With this fluid property approximation and the measurement errors, a global measurement accuracy can be estimated for the determination of the heat gain along the channel for the hydrogen test case:

$$\frac{\Delta \dot{Q}}{\dot{Q}} = \pm\sqrt{\left(\frac{\Delta \dot{m}}{\dot{m}}\right)^2 + \left(\frac{\Delta c_p}{c_p}\right)^2 + \left(\frac{\Delta(T_{out}-T_{in})}{(T_{out}-T_{in})}\right)^2} = \sqrt{0.0004+0.0025+0.0014} = 6.6\% \tag{3.10}$$

3.2.3. Influence of sensors implementation on the thermal field

The positions of the holes drilled in the channel walls were chosen with the aid of a three dimensional numerical simulation, in order to detect a possible perturbation of the temperature repartition inside the structure, due to the presence of sensors. A hole with *0.6 mm* diameter and *0.2 mm* depth does not have much influence on the temperature distribution inside the channel walls. Figure 44 shows the numerical simulations of the channel containing thermocouple bores. The difference is below 1 K as compared to channel without holes.

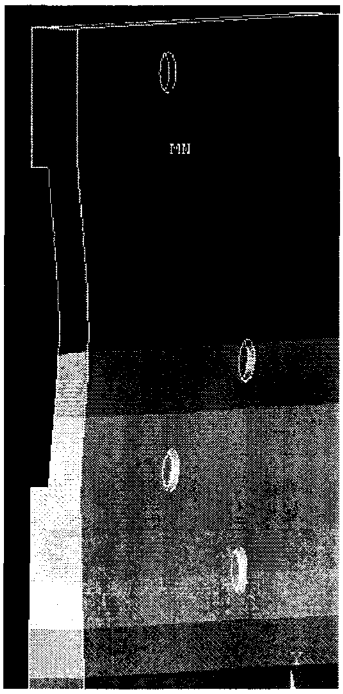

Figure 44 : Influence of thermocouple bores on the thermal profile (non-scaled deformation).

It has already been proven that the free convection between the environment and the channel walls can be neglected (see 3.1.2.3). Another source of heat transfer modification in the cooling channel can be the heat conduction through the thermocouples lengths. This axial heat flux $\dot{q}_{tc}$ along the thermocouple length has to be estimated. The temperature along the thermocouples varies between the measured one (T_{meas}) and the ambient temperature of the containment, noted T_{cont}. The thermocouple is approximated as an infinite rod with a cross section S_{th}, a perimeter P_{th} and a thermal conductivity λ_{th}, with heat losses to the containment through free convection ($h_{cont}=10\ W\ m^{-2}\ K^{-1}$). The temperature along the thermocouple axial position l_{th} and the heat losses through the thermocouple are obtained by analytical calculation [Saccadura, 1980].

$$\frac{T(l_{th})-T_{cont}}{T_{meas}-T_{cont}} = e^{-ml_{th}}$$
$$m = \sqrt{\frac{h_{cont}P_{th}}{\lambda_{th}S_{th}}} \qquad \textbf{(3.11)}$$

$$\dot{Q}_{th} = -\lambda_{th}S_{th}\left(\overrightarrow{grad(T)}\cdot\overrightarrow{u(l_{th})}\right)\Big|_{l_{th}=0}$$
$$\dot{Q}_{th} = \sqrt{\lambda_{th}S_{th}h_{cont}P_{th}}\left(T_{meas}-T_{cont}\right) \qquad \textbf{(3.12)}$$

The extreme case has been considered, where the measured temperature is about *150 K* and the ambient temperature is about *400 K* which would bring heat to the channel walls through the contact surface between the sensors and the channel wall. Taking the nickel conductivity as reference, it is possible to evaluate the maximal heat flux along the thermocouple length which will be absorbed by the cooling channel. Considering all the *98* thermocouples at the same time:

$$\dot{Q}_{th}\Big|_{ALL} = -0.13\cdot 98 \sim -13W \qquad \textbf{(3.13)}$$

The heat conduction through thermocouples can be neglected in comparison to the global absorbed heat by the fluid (*7.5 kW* global heat, see 5.2.4). It represents about *0.1%*. The adiabatic condition at the channel walls can be applied because of negligible free convection and negligible heat conduction through the thermocouples.

3.2.4. Uncertainty of temperature measurement

The measurement uncertainties can have many different sources. From the contact point between sensor and test specimen until the measurement acquisition system, some errors have been listed and evaluated. The global measurement uncertainty can be expressed as a sum of different errors. Each error can be defined as a systematic error and a stochastic one, following the Gauss theory. For a precise source i of error, $\overline{\Delta T_i}$ is the systematic error and $\Delta T_i'$ is the stochastic one. The total measurement uncertainty is thus defined by $\Delta T = \sum_i(\Delta T_i) = \sum_i\left(\overline{\Delta T_i}\right) + \sum_i(\Delta T_i')$

- Calibration of the thermocouple, systematic error

In rocketry sciences, the sensors have to cover a very large temperature range from cryogenic temperatures (liquid hydrogen) up to combustion gas temperature (up to *3500 K*). Useful ranges of sensors have to be extended to the entire temperature range, whereas thermocouples are not so precise in extreme temperature ranges. A global experimental investigation on accuracy of type K thermocouples at low temperature range was studied within the scope of a DLR patent [Suslov, 2006]. The error component due to thermocouple class imprecision (here thermocouple K) was estimated by the following , for low temperature (*<0°C*). This empirical relation was elaborated from different thermocouples (different materials, different manufacturing processes, precision classes…) at different temperature ranges (more than *200* points from liquid helium temperature, *4 K*, until ambient temperature).

T_{real} is the real temperature and T_{meas} is the measured temperature.

$$T_{real} = \sqrt{a - bT^2_{meas}} \qquad \textbf{(3.14)}$$

a and *b* are two constants which can be determined by two referenced points (here at *0*°C in iced water and at *77.3 K* in liquid nitrogen).

The EH3C typ K thermocouples were evaluated by determining the proper coefficients *a* and *b* of these thermocouples, and the correction is shown in Figure 45. Two measurement points were used for this calibration: in iced water and in liquid nitrogen.

$$\begin{aligned} 273.15 &= \sqrt{a - b273.07^2} \\ 76.57 &= \sqrt{a - b71.09^2} \end{aligned} \qquad \textbf{(3.15)}$$

that gives $a = 864.8\ K^2$ and $b = -0.989\ [-]$

This correction factor was directly added to the measured temperatures (see in 5.2) and is considered as a source of systematic measurement error.

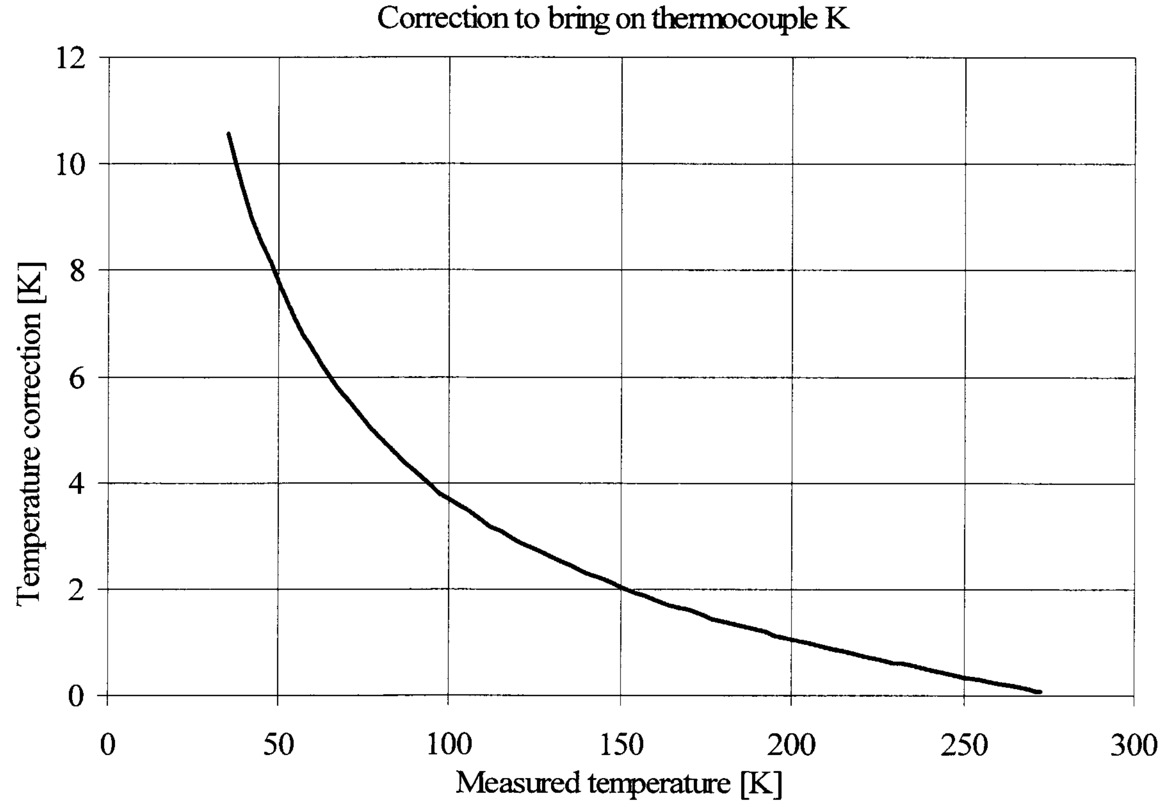

Figure 45 : Temperature correction of thermocouple K in low temperature range.

- Thermocouple positioning ΔT_1

The positioning of the thermocouples can be estimated by taking into account the geometrical imprecision due to the mechanical boring operation and due to the probable thermal contact location of the thermocouples in their emplacements. This error was evaluated by taking the maximal error from the geometrical definition of the thermocouples implementation. This gives a global measurement error for this source of error ΔT_1. The thermocouples have a diameter of *0.5 mm*. The holes in the channel for the sensors implementation have a diameter of *0.6 mm* for a depth of *0.1 mm*, as described in

Figure 46. The thermal contact where the thermocouple measures the temperature is more or less contained in a domain around the symmetry axe of the thermocouple: +/- *0.2 mm* around the symmetry line was estimated for all thermocouples. With the notations e_{max} and e_{min} in Figure 46, it comes: $e_{\max} - e_{\min} = 0.4\,mm$

The imprecision on the real location of the thermal contact leads to measurement errors, depending on the heat flux density working perpendicularly to the thermocouple axis. Indeed, the positioning inaccuracy can be correlated here to the expected temperature:

$$\Delta T_1 = \overline{\Delta T_1} + \Delta T_1{}' = \pm \overline{\dot{q}} \frac{e_{\max} - e_{\min}}{2\lambda} \tag{3.16}$$

$$\Delta T_1 = \pm 5.715 \times 10^{-7} \overline{\dot{q}} \tag{3.17}$$

The copper alloy conductivity can be taken as constant (*350 W m^{-1} K^{-1}*) and $\overline{\dot{q}}$ is the heat flux perpendicular to the thermocouple axe which can be assimilated in the EH3C case as the global heat flux (no other components of the heat flux).

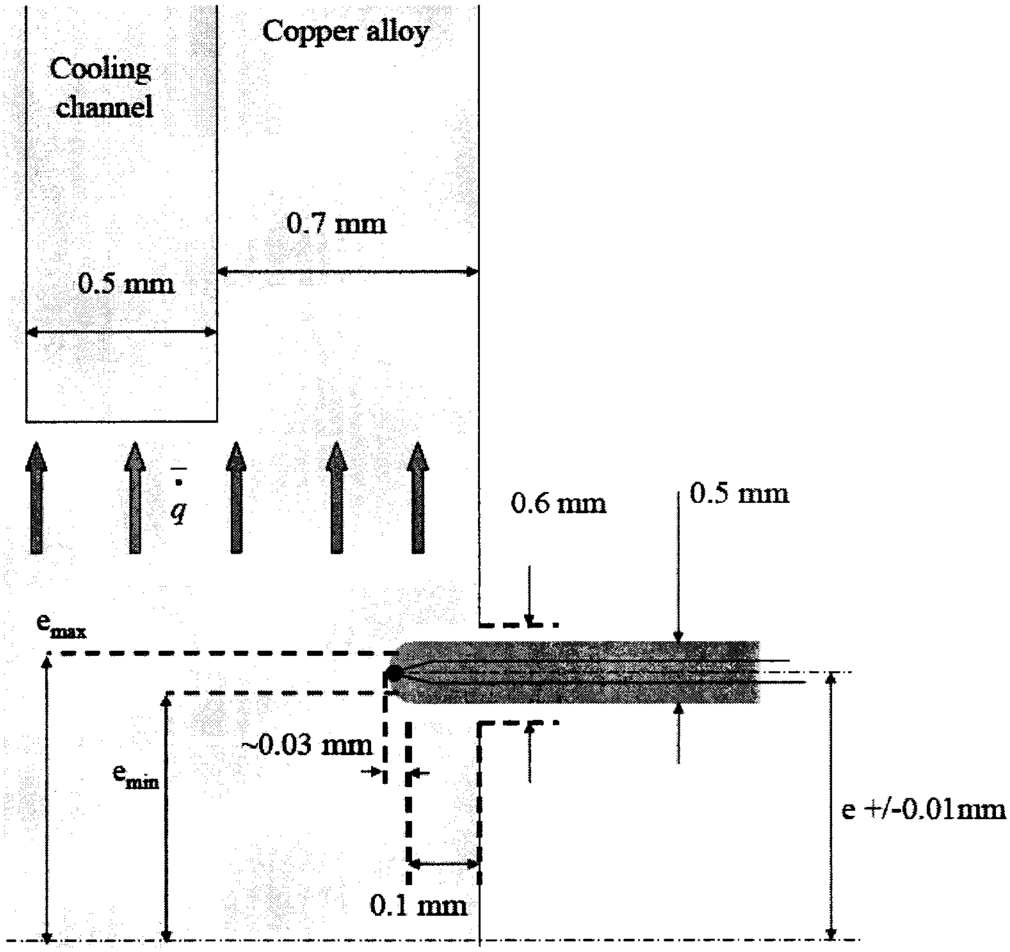

Figure 46 : Description of the thermocouple implementation.

A bad thermal contact can induce thermal resistance through different material layers (air, oxidant layer, dust...) between sensor extremity and test specimen. That perturbs the measured value and depends on experimental conditions. Nevertheless, the spring system (designed to press the thermocouples in their location) avoids a large measurement error due to bad thermal contacts (see Figure 107 for detailed construction)

From the numerical simulations of the experimental conditions (see paragraph 4.2), the temperature profiles of the fin were correlated to the heat flux density profiles along the fin for the methane and the hydrogen experimental tests (see in Figure 47). The data were collected in the middle of the straight channel. Temperature always decreases along the fin but the heat flux density has a maximum corresponding to the edge of the channel. Indeed, the temperature profile along the fin has an inflection point located at the bottom of the cooling channel. These temperature-heat flux density relations were interpolated by polynomial functions and implemented in the model to determine the measurement errors due to the positioning.

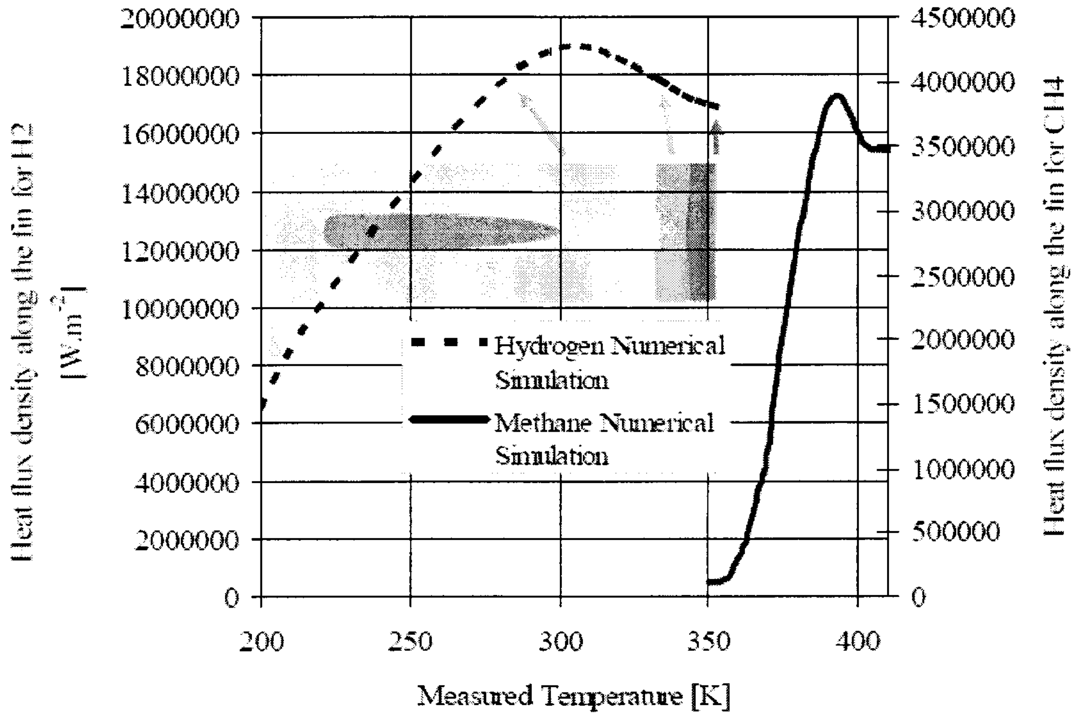

Figure 47 : Heat flux density profile related to temperature profile from the methane and the hydrogen numerical simulations of the experimental conditions.

- Influence of the reference temperature (cold junction) on the thermocouples accuracy: component ΔT_2

The thermocouples measure a temperature difference and not an absolute temperature. Indeed, the Seebek effect is used for two different metals both joined at two points: the hot point (the measured temperature) and the "cold point" (reference temperature). This reference temperature (so-called cold junction) can be different for each thermocouple because of the sensor connection location on the electronic card. Normally, one extern and precise temperature sensor is used to determine the reference temperature for all thermocouples. That is why this extern sensor has to be located as close as possible to the electronic junction of all thermocouples. Many sensors are used here (resistance sensor Pt100) and are implemented in each electronic card: *4* precise resistance temperature sensors define the reference temperature for the *4* electronic cards (each 25 thermocouples). The relatively good precision of these temperature sensors Pt100 (less than *0.02 °C* deviation) allows limiting the systematic deviation due to imprecise measurement of the reference temperature. Nevertheless, only one precise sensor is used to determine the reference temperature of one electronic card (*25* thermocouples). The thermocouples junction of the same card can be located up to *30* centimetres away from the Pt100 and that could bring about *1K* difference depending on thermocouple position.

$\Delta T_2 = \pm 1\ K$

- Acquisition error ΔT_3

The data transmission from voltage through temperature can be inaccurate, depending on electronic card resolution, extern perturbation (radiation, electronic noises...). Figure 48 illustrates the electronic resolution and precision of the cards for the thermocouples K. Indeed, the resolution domain of the acquisition card (*+/- 100 mV*) corresponds to an electronic resolution accuracy of:

$$\Delta V_R = \frac{200.10^{-3}}{2^{16}} = 3.0518\mu V \qquad \textbf{(3.18)}$$

This theoretical resolution was reduced by the manufacturers in their specifications $\Delta V_P = 30.518\mu V$ which corresponds to a global card precision. The resolution and the precision were calculated in temperature with application of standard polynomial function for thermocouples K between measured temperature and provided signal.

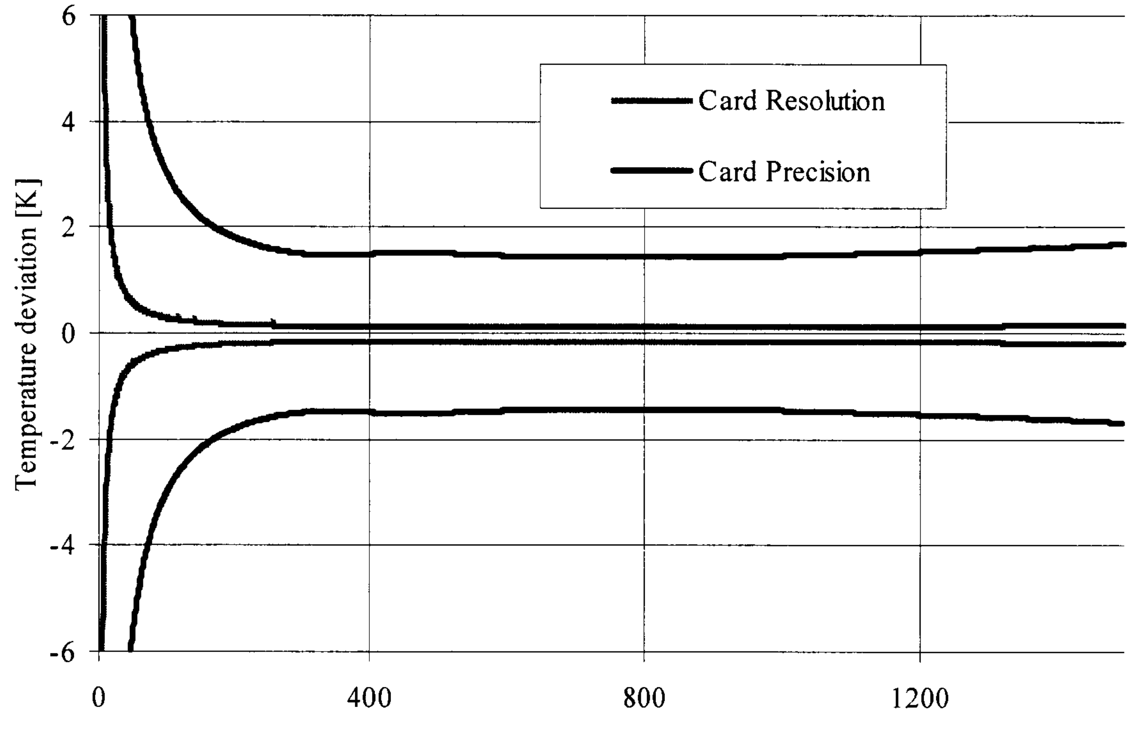

Figure 48 : Temperature imprecision due to measurement system.

The card precision curve was interpolated over the temperature range, with the following function:

$$\Delta T_3 = \begin{cases} \pm 1.5K \text{ if } T_{meas} > 273 \\ \pm\left(8\cdot 10^{-9} T_{meas}^4 - 6\cdot 10^{-6} T_{meas}^3 + 0.0017 T_{meas}^2 - 0.222 T_{meas} + 13.202\right) \text{else} \end{cases} \qquad \textbf{(3.19)}$$

This measurement error was defined by a polynomial interpolation of the card precision curve, for the temperature range [*40 ; 270 K*].

- Temporal stochastic error ΔT_4

The measurement system allows saving data under high frequency samples. Each sensor provides a voltage which is recorded with a sampling rate of *1000* Hz. A very precise stochastic study can be done. A single sensor was investigated to calculate the typical stochastic error in the frame of the EH3C experiments. At first, the steady conditions must be reached to have a reliable and constantly averaged value among time. Afterwards, an averaging is realised for all samples: from the first measured data to the *10500*th, all the preceding samples are needed to calculate the average. For the kth sample, the average $\overline{T_k}$ is calculated:

$$\overline{T_k} = \frac{1}{k}\sum_{i=1}^{k} T_i \qquad \textbf{(3.20)}$$

Taking the last averaged as reference for the stochastic investigation, $\overline{T_{10500}} = T_{real}$, the stochastic deviation can be calculated in function of the samples. Figure 49 describes the stochastic error depending on the samples. The shape of this function can be used to validate the stochastic precision of a system.

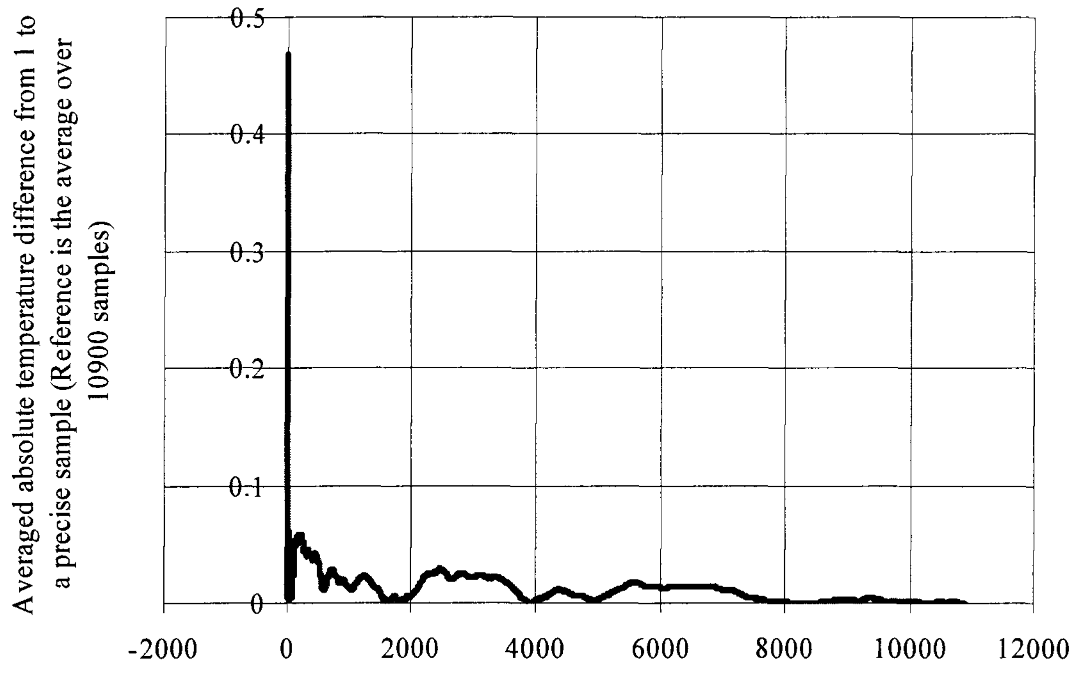

Figure 49 : Averaged temperature difference from *1* to *10900* samples.

After *20* samples, the stochastic error is under *0.08 K* and remains under this value. This means that the temporary oscillation of the measured data can be averaged over *20 ms* and the global result would not change more than *0.08K*. The stochastic deviation can be neglected.

- Global error measurement

All the preceding error sources can be synthesised. The measured temperature is noted $T_{i,j}$ in reference to Figure 43. The corresponding measurement error is defined as follows:

$$\Delta T_{i,j} = \sum_k \left(\Delta T_{i,j}\right)_k \tag{3.21}$$

$$\Delta T_{i,j} = 5.715 \cdot 10^{-7} \overline{\dot{q}_{i,j}} + 1 + \begin{cases} 1.5K \text{ if } T_{meas} > 273 \\ \left(8 \cdot 10^{-9} T_{i,js}^4 - 6 \cdot 10^{-6} T_{i,js}^3 + 0.0017 T_{i,j}^2 - 0.222 T_{i,js} + 13.202\right) \text{else} \end{cases} \tag{3.22}$$

Concerning the experiments with cryogenic hydrogen, Figure 50 illustrates the different error components and the global temperature measurement error which is contained between *+/-7* and *+/-13 K*.

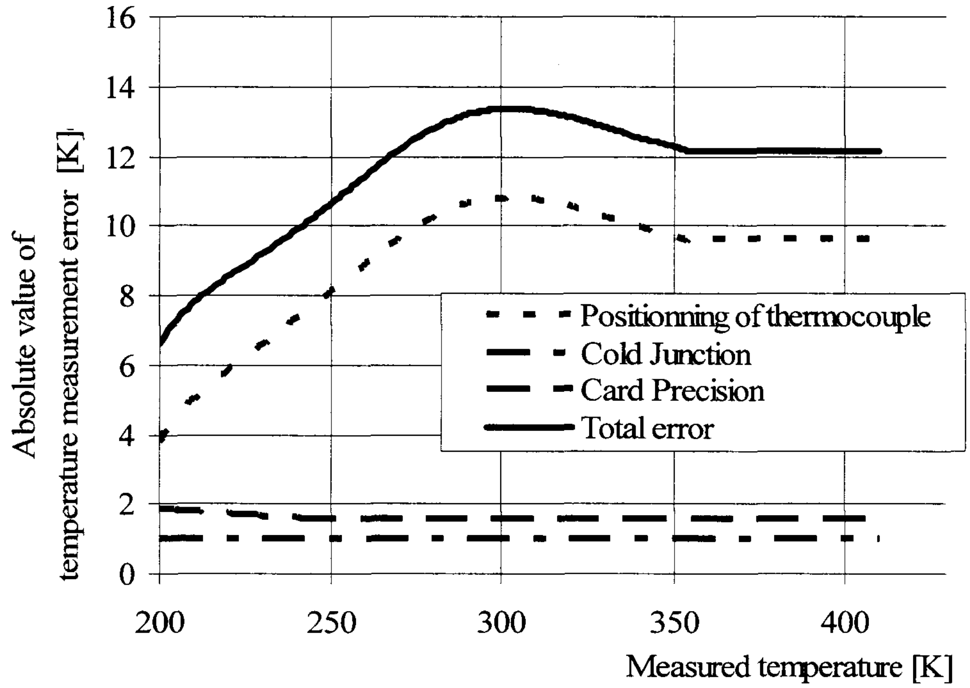

Figure 50 : Temperature measurement error under EH3C test condition with cryogenic hydrogen.

The experimental test case with methane is characterized by lower heat flux density and higher temperatures and the calculation of measurement errors was worked out (see Figure 51).

All the measurement errors for both test cases have been implemented in the experimental data analysis (see 5.2).

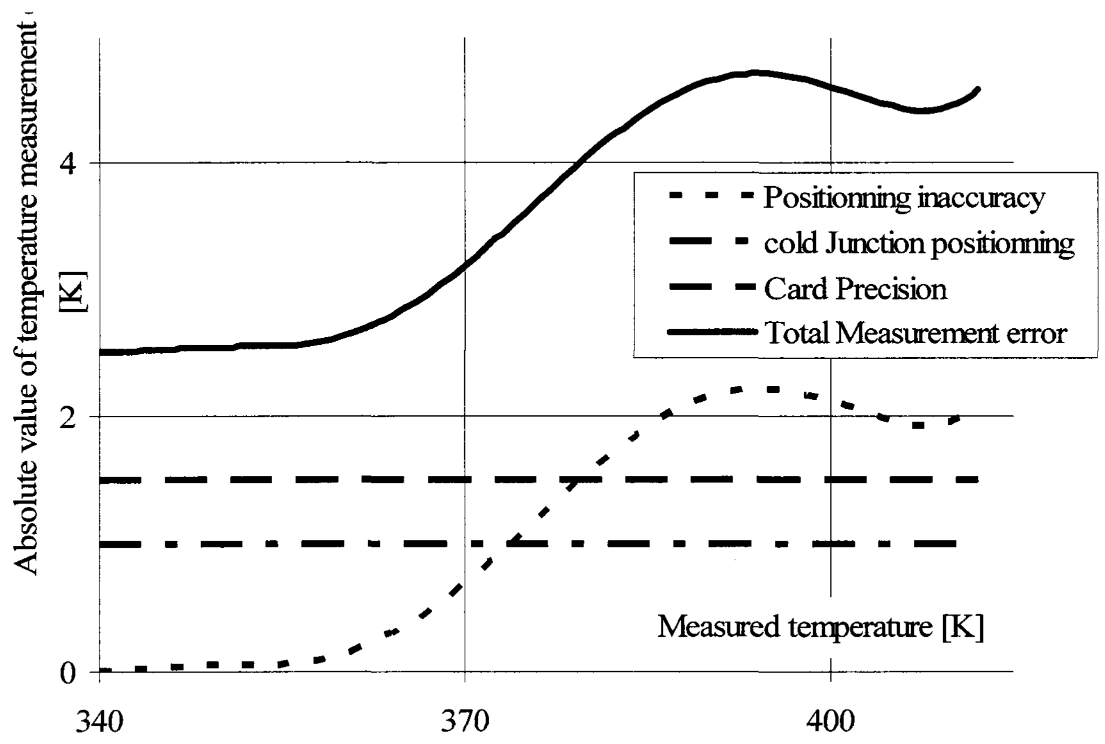

Figure 51 : Temperature measurement error under EH3C test condition with methane at ambient temperature at the entrance of the channel.

3.3. EH3C Inverse Method

3.3.1. Method Presentation

The "inverse method" is an automatic routine to find the best heat flux distribution along the channel walls to correspond to the measurements. A "forward model" defines a temperature field from known heat transfer data. The EH3C experiments are not able to measure directly the heat transfer coefficient, because of difficult implementation of sensor and small dimensions of the channel. An inverse method is required where a mathematical definition is available in several publications [Snieder, 1998, Raynaud, 2000]. The inverse methods are used in a large application field (engineering, meteorology, seismology, informatics, mathematics). In most of the cases, this transformation is not linear. The convergence of the method, the unicity and the existence of the solution and the stability of the inverse problem are not so easy to obtain in practice. Indeed, measurement noises can be amplified and treated by the inverse method which increases the instability of the process. The amount of experimental data is finite and directly determines the precision of the solution. That explains the careful need for a treatment of the inverse problems.

For each EH3C test configuration, an experimental test delivers the measured temperatures $T_{i,j}^{EXP}$ at *14* different axial channel sections (*j*) and *7* radial points per section (*i*), inside the cooling channel wall. To obtain information on heat transfer through channel walls, an inverse model has to be applied to obtain the heat transfer coefficients *h(s)* from the experimental temperature data where *s* is the coordinate along the cooling channel surface. A particular definition of the heat transfer coefficient was used in the inverse method in order to only refer to the experimental conditions with $\Delta T_{ref} = \Delta T_{ref}\big|_{IN}$:

$$h_j(s) = \frac{\left.\dot{q}\right|_{wall}}{\left(T_{wall} - T_{inlet}\right)} \tag{3.23}$$

The measured inlet temperature at the channel is used as reference temperature for the inverse method and for the numerical simulations too. This definition of the heat transfer coefficient with the particular choice of the reference temperature can be explained by the fact that the experimental bulk, film, wall or outlet temperatures cannot be directly determined by experiments. The inlet temperature is quite homogeneous all over the inlet cross section and can be reliable to determine the heat transfer coefficients.

A set of successive numerical finite elements simulation of the channel structure (without fluid modelling) is required to match thermal heat flux at the channel walls to the experimentally obtained temperatures.

$$\left(T_{i,j}^{EXP}\right) \xrightarrow{\text{Inverse Method, f}} \left(h_j(s), T_j^{NUM}\right) \tag{3.24}$$

In the EH3C case, the inverse method uses the experimental data to deliver a 2D heat transfer coefficient profile at the internal channel wall and a 2D numerical temperature profile all over the structure. The inverse method was applied in 2 dimensions to all cross-sections j.

This inverse method is based on an iterative process which is able to evaluate and adjust the output parameters (like heat flux coefficients) in order to match the input data (like measured temperatures). At each loop, the numerical output parameters (numerical temperatures) are compared to the input ones (experimental temperatures) and the heat transfer coefficient profile is thus adjusted for the next loop. This inverse method couples the heat transfer coefficients, the measured temperatures and the "numerical" temperature with a function f in order to organize the next iterative calculation. The definition of this function is crucial to stabilize the inverse method, to avoid divergence, to optimize the convergence and to assure precise results.

The initial output parameters for the first loop can be random values or predetermined values. This starting point can be very important, because some inverse methods are so unstable that the initial points influence the converging final solution, as long as the inverse method does not guarantee the existence and the uniqueness of the solution.

For the loop (k) of the inverse method, a comparison is made between $\left(T_{i,j}^{EXP}\right)^{(k)}$ (experimentally measured data at the point i,j) and $\left(T_{i,j}^{NUM}\right)^{(k)}$ (computed temperature at the point i,j from the inverse method at the loop (k)). Afterwards, the heat flux coefficients are modified through a function which uses the previous comparison, in order to obtain the new set of heat flux coefficients $h_j^{(k+1)}(s)$.

$$f\left(h_j^{(k)}(s), \left(T_{i,j}^{NUM}\right)^{(k)}, T_{i,j}^{EXP}\right) \tag{3.25}$$

The software ANSYS was used to model a channel section with the block, where thermal boundary conditions are applied.

On the internal channel walls, the heat transfer coefficients $h_j^{(0)}(s)$ are used for the first loop of the iterative process. The lowest part of the block is maintained at constant temperature. This applied temperature comes from the experimental set and is the regulated temperature of the electrical cartridges. All other surfaces of the block take into account the heat losses which have already been calculated through free convection with the nitrogen contained in the containment and through the radiative process (see in 3.1.2).

3.3.2. Parameterisation

Different parametrisation models for the spatial variation of heat transfer coefficient *h(s)*, have been tested (Figure 52).

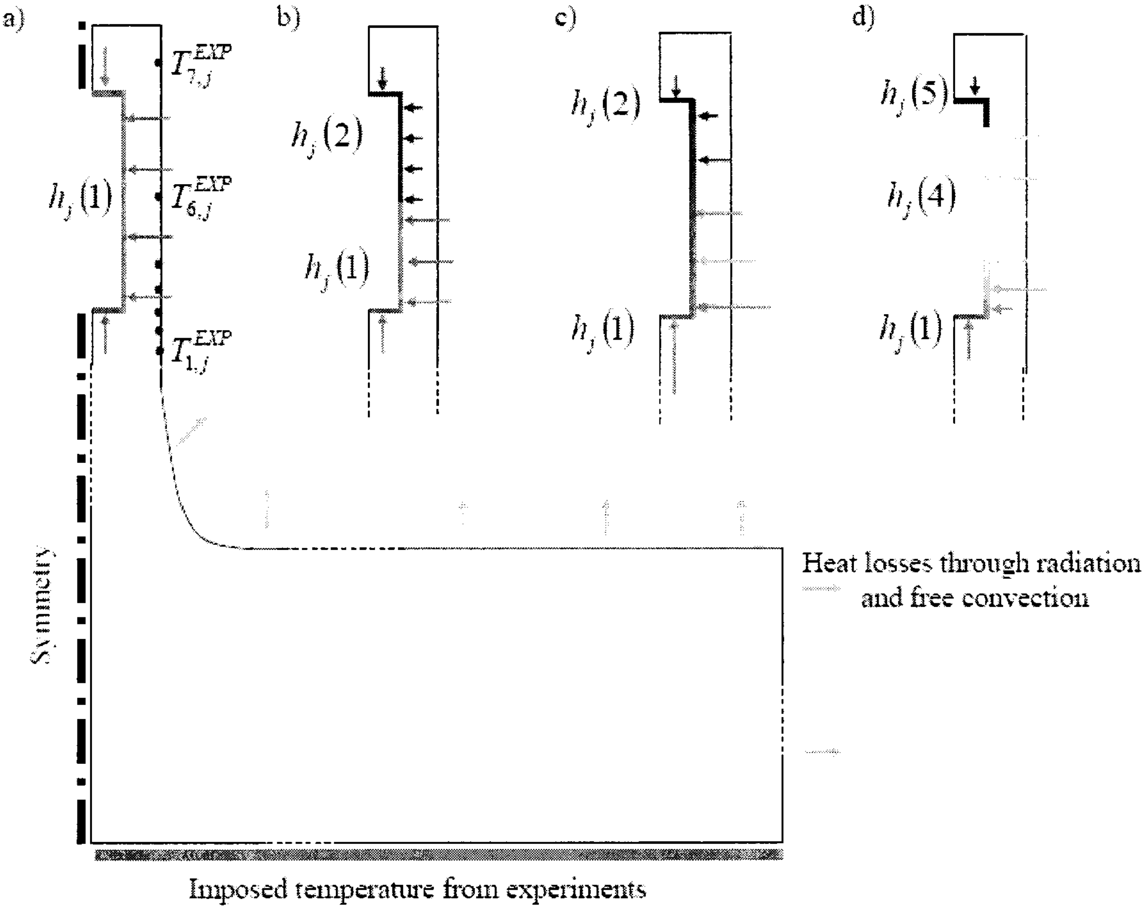

Figure 52 : Parameterisation of the heat transfer coefficient along the internal channel periphery.

The first basic model proposes a unique heat transfer coefficient all over the channel perimeter (*a*). The models (*b*) and (*c*) have 2 degrees of freedom, adopting an abrupt step of the heat transfer coefficient into two zones (upper part of the channel height and lower part) or a linear profile of the heat transfer coefficient along the height of the channel (case *c*). In the case (*c*), *2* heat flux coefficients were defined, one for the hot side of the channel (corresponding to the concave side of the curved channel) and another one for the cold one. A linear interpolation between the two coefficients defines the heat transfer coefficient along the channel height. Finally, a more complex distribution of the heat transfer coefficients was tested (case *d*), with the use of a *5* degrees of freedom model.

The different cases were tested and the methods with a heat transfer coefficient parameterisation with more than three degrees of freedoms are unstable. The case *d* cannot converge, despite the interesting number of degrees of freedom. Considering stability and uniqueness of solutions, the models *c* and *a* were selected. Moreover, the linearised profile (*c*) corresponds better to the real heat transfer coefficient profile than the models (*a*) or (*b*), in reference to the numerical simulations (see Chapter 4).

3.3.3. Minimization of least square

Different methods were tested. The best stable method with only *1* or *2* degrees of freedom is a conjugate gradient method (CGM), using the least square method. An error deviation value S is thus defined and has to be minimised:

$$S_j = \sum_{i=1}^{7} \left[\left(T_{i,j}^{NUM} \right) - \left(T_{i,j}^{EXP} \right) \right]^2 \qquad \textbf{(3.26)}$$

In order to check if the square summation method presents local and global minima of S_j, both degrees of freedom (case *c*) were independently investigated [*0 - 50000* $W\,m^{-2}\,K^{-1}$] for a given experimental set of temperatures. For each pair $h_j(1), h_j(2)$, a finite elements calculation of a 2D section of the EH3C test specimen was used to calculate the error deviation value S (Figure 53).

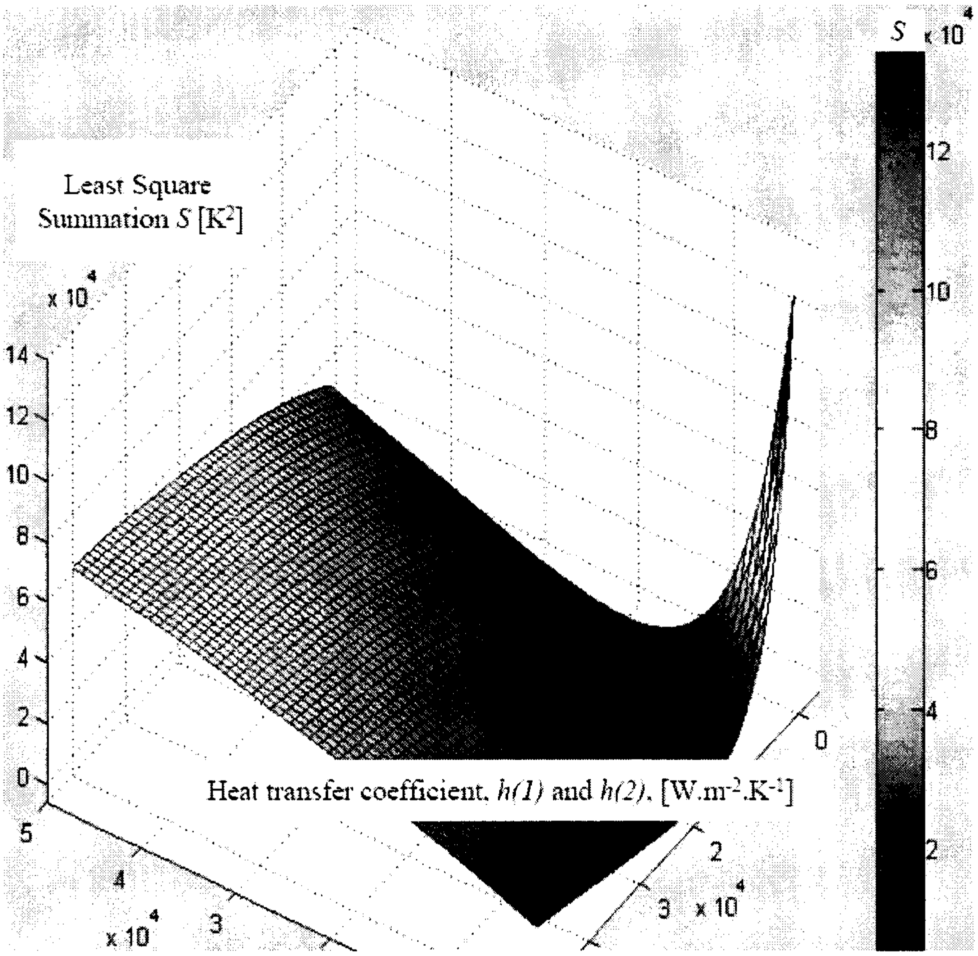

Figure 53 : Square summation profile for the inverse method using the linear profile of heat flux coefficient models (c).

The shape of the square summation depends on the initial experimental set. The square summation was calculated for different experimental sets and the global behaviour of the shape does not vary a lot: a unique global minimum of the optimisation function (here S) is always obtained.

The CGM is available in the software Ansys to optimise a parameter raw (here the *2* degrees of freedom) in order to minimize a numerical parameter (here the square summation *S*). This method directly uses an investigation of the least square to determine the heat transfer coefficients corresponding to the optimised solution.

The CGM calculates several local gradients in different directions at the iteration (*k*)

$$\left(\frac{\partial^2 S}{\partial h(1)\partial h(2)}\right) \tag{3.27}$$

The sharper direction is selected and all error deviation values *S* are calculated on this axis. The minimum on the axis is thus used as "new" starting point and the operation begins once more until the global minimum is found. In the case (*c*), it is ensured to find the unique convergence point because of unity of the problem. Nevertheless, the convergence parameters and the gradient parameters have to be optimised to save calculation time (*10* minutes for one experimental set for well adapted parameters). In Figure 54, the square summation is represented as iso-lines in the (h_1, h_2) plane. The minimum here is located at the point (*8575, 11050*) and was found with only *3* iterations.

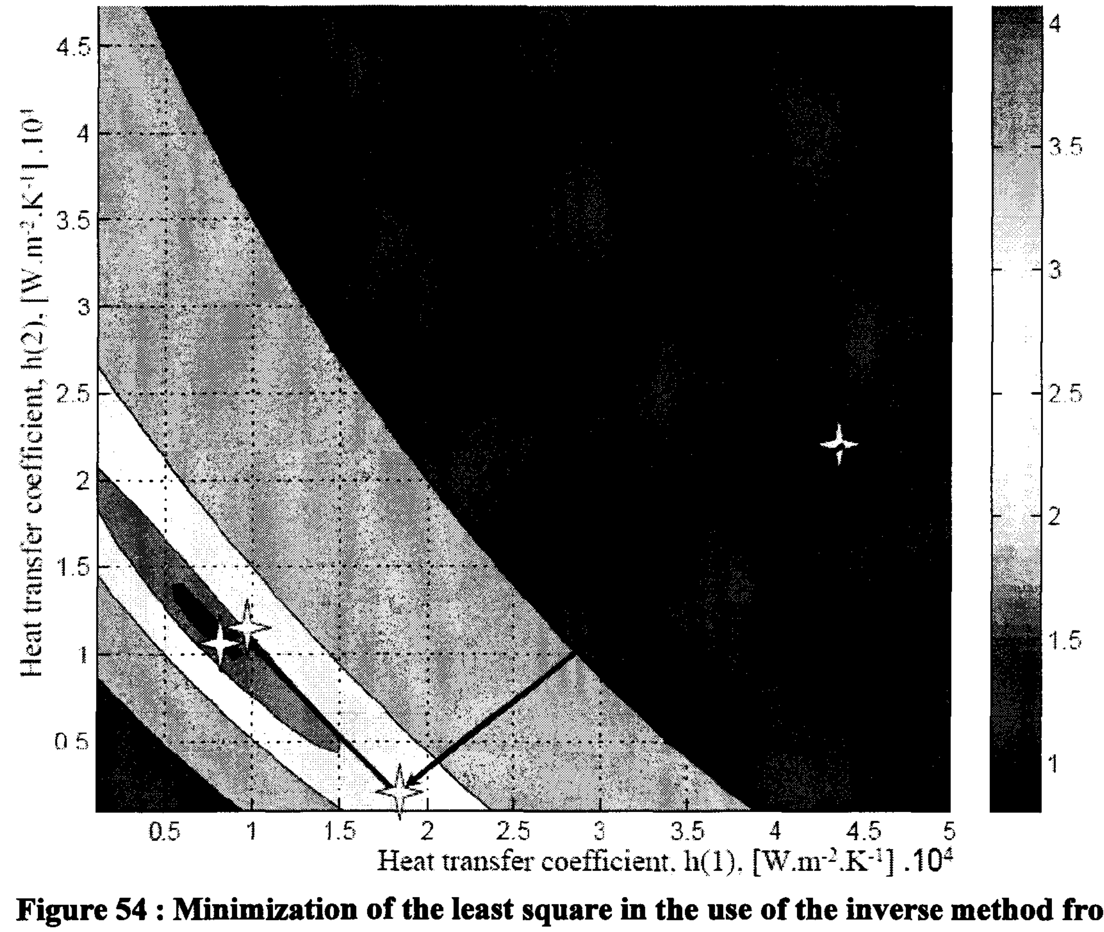

Figure 54 : Minimization of the least square in the use of the inverse method from EH3C experimental data.

The numerical simulation with finite elements has to be tested in order to check its robustness. The mesh was investigated by changing the quality and the refinement of the grid. Figure 55 shows the mesh influence on the results and it can be seen that the inverse method becomes independent of the mesh from *12000* elements. A mesh of *18000* elements was chosen to exploit the experimental results with the CGM inverse method.

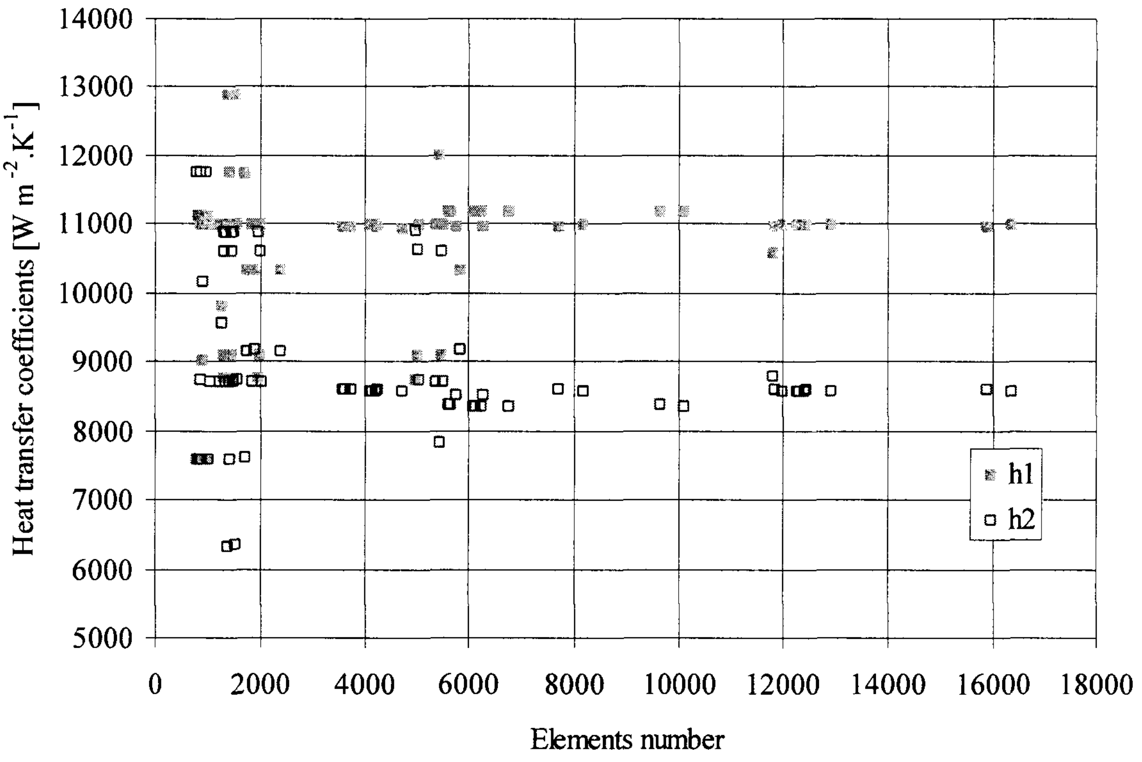

Figure 55 : Mesh influence on the inverse method results.

The material properties were investigated, too, in order to check the convergence of the inverse solution depending on thermal parameters of the copper alloy. This parameter influence can be neglected with the use of the inverse method. Indeed, the use of constant properties (conductivity, heat capacity) or variable properties, function of temperature, [Oschwald et al., 2004] does not significantly change the converged values of the heat flux coefficients (less than *0.2%*). Even the model with variable material properties was used and programmed in the inverse method code.

The sensibility of an inverse method, which characterises the amplification or attenuation of data perturbation through the inverse method has to be investigated. In this case, the temperature measurement errors can have more or less influence on the results of the inverse method. Two investigations were made, corresponding to the channel wall discretisations *a*) and *c*) of Figure 52. The first case refers to a unique heat transfer coefficient imposed all over the channel periphery, whereas the second investigation differentiates the upper value of the heat transfer coefficient to the lower one. The inverse method was applied with the "least square" method over the *7* thermocouples measurement and the automatic conjugate gradient method, in a particular channel section ($j=8$ for the straight channel) for the experiment with the cryogenic hydrogen. The measured values will be presented later (see in 5.2.4). All experimental values were fixed and the inverse method was applied twice for each configuration (one single heat transfer coefficient or two coefficients linearly interpolated). After obtaining the convergence of the inverse method, the temperature obtained by the thermocouple $T_{3,8}$ was changed by an artificial measurement error of $T_{3,8}+\delta T$. The inverse method was applied once more with the following experimental set: ($T_{1,8}$; $T_{2,8}$; $T_{3,8}$ + δT; $T_{4,8}$; $T_{5,8}$; $T_{6,8}$; $T_{7,8}$). The obtained values of the heat transfer coefficients were compared to the first calculation for the two configurations. The temperature deviation δT was changed from *-20K* up to *+20K*. The case of one single heat transfer coefficient at the channel wall does not indicate a significant variation of the coefficient, whereas the temperature measurement error can reach *+/- 20K* for the thermocouple $T_{3,8}$. Indeed, the heat transfer coefficient changes up to *4%* by a temperature measurement error of *20 K*. For the two heat transfer configuration, the sensibility of the inverse method is much higher. A temperature change of *+10 K* for the temperature $T_{3,8}$ implies a modification of *+22%* for the cold side heat transfer coefficient and *-40%* for the hot side coefficient. This behaviour can be explained by the asymmetrical way of heating: a higher value of temperature in the channel structure at the position $T_{3,8}$ implies a higher heat transfer coefficient at the cold side and a lower one at the hot side. This very high sensibility corresponds to a very precise case: the measurement error of one thermocouple can be attenuated by the fact that there are *6* other measurement points which can statistically limit the deviation of the others data. Unfortunately it is time consuming enterprise to investigate all thermocouples together with the interdependence and the interaction of the measured temperatures together. Nevertheless, the investigation of the measurement error on the thermocouple $T_{3,8}$ is the most influencing case and corresponds to the worst case.

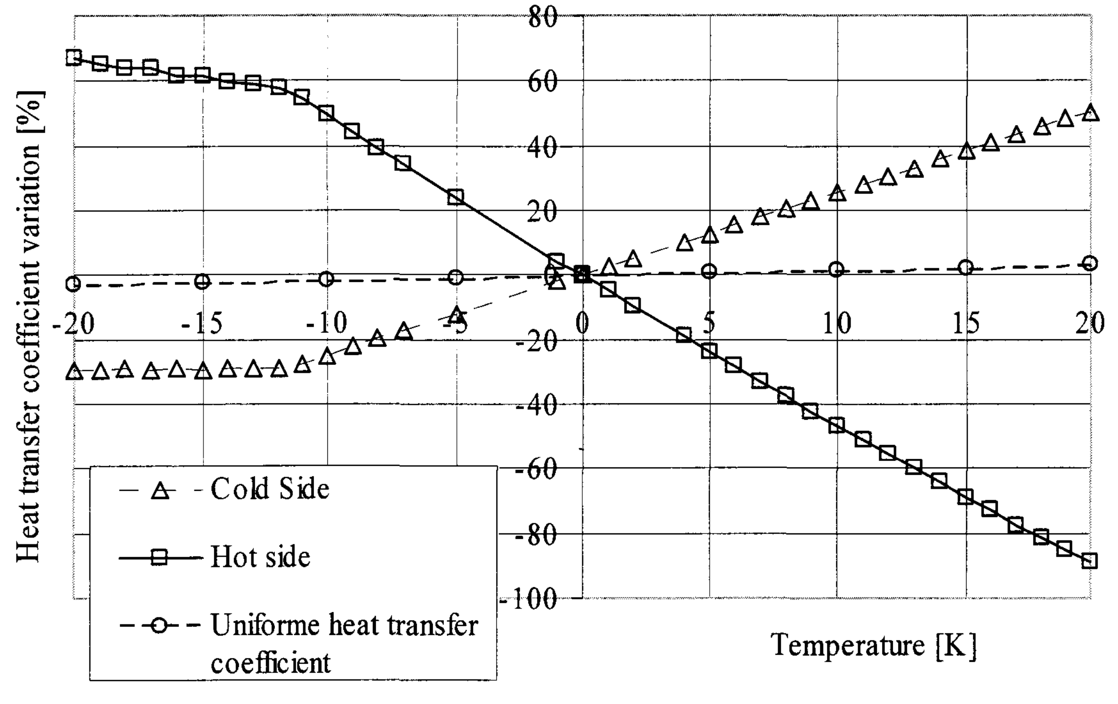

Figure 56 : Inverse method sensibility, temperature measurement error influence on heat transfer coefficient determination.

For the case (*a*), an error analyse of the heat transfer coefficient can be realised using the inverse method for one cross section *j*.

$$\Delta h_j = \sqrt{\sum_i \left(\frac{\partial h_j}{\partial T_i}\Delta T_{i,j}\right)^2} \qquad \textbf{(3.28)}$$

The maximal temperature measurement error of the hydrogen experiment was applied to the *7* temperatures data and corresponds to $\Delta T_{i,j} = 13K$, see Figure 50. The deviation of the uniform heat transfer coefficient was taken at the measurement point $T_{3,8}$ (*4%* for *20 K* deviation), and applied to all measurement points *i*, see Figure 56.

The global measurement error concerning the heat transfer coefficient can thus be evaluated:

$$\frac{\Delta h_j}{h_j} = \sqrt{7}\,\frac{0.04}{20}\,13 = 6.8\% \qquad \textbf{(3.29)}$$

This measurement error with one heat transfer coefficient at the cooling channel wall is acceptable. Within the scope of this experimental work, in order to investigate the role of the curvature on the heat transfer, it can be helpful to dissociate the concave side to the convex one in terms of heat transfer. The parameterisation cases (*c*) and (*a*) are used to analyse the EH3C experimental data.

3.4. Chapter conclusion

The EH3C experimental tests are based on a single curved cooling channel which is electrically heated by cartridges. The advantage of electrical set up is the faculty to implement sensors in comparison to the combustion chamber, where the implementation is difficult and the data unprecise.

A specific profile of the EH3C electrical heating process allows a very high asymmetrical heat flux in comparison to all other similar experiments. This specific profile was optimised, designed and manufactured to qualify the EH3C experimental process to obtain high heat flux density.

Two test specimens were designed, one straight single channel and one curved single cooling channel with adequate heating systems. The channel geometries are similar to real engine configuration: *0.5 mm* width over *4.6 mm* height with a wall width of *0.7 mm*.

The electrical heating systems were optimised in accordance to the flow and power requirements. Numerical simulations with the finite elements method helped a lot in this phase of qualification and optimisation of the test specimen, particularly by comparing with real engine cooling channels.

At first, the sensors implementation is described: *98* thermocouples in the channel wall, *2* thermocouples, *2* pressure sensors at the inlet and outlet of the fluid and one pressure drop sensor. The calibration operations and the measurement inaccuracies are enumerated. The position of the thermocouples in the wall appears to be the higher source of incertitude. Indeed, by very high heat flux density, a small imprecision of the sensor position generates a relevant measurement error.

To better approach the heat transfer process in the cooling channels, an inverse method was tested with different parametrisation models. To enlighten the curvature effect on the heat transfer, two values of the heat transfer coefficients were dissociated (two degrees of freedom parameterisation model), one at the concave side and the other at the convex side of the cooling channel, ensuring a compromise between the precision of the delivered experimental results and their richness.

The large number of sensors (*98*), the real micro-dimensions of the cooling channels, the use of real coolant and the expected heat flux density can qualify the EH3C experimental realisation as a technically innovative challenge.

4. Numerical simulations

The EH3C experiments were numerically simulated with a Computational Fluid Dynamic (CFD) programme: CFX.

In this chapter, the numerical investigations for the EH3C experiments were made with two different boundary conditions at the lowest part of the channel, a uniform heat flux density (Von Neumann wall boundary condition) and a temperature profile condition (Dirichlet wall boundary condition). Different meshes were investigated. The robustness of the code and different turbulence models were tested, as well as different solid and fluid property models.

4.1. Uniform heat flux density as boundary condition

4.1.1. Geometry of the numerical model and boundary conditions

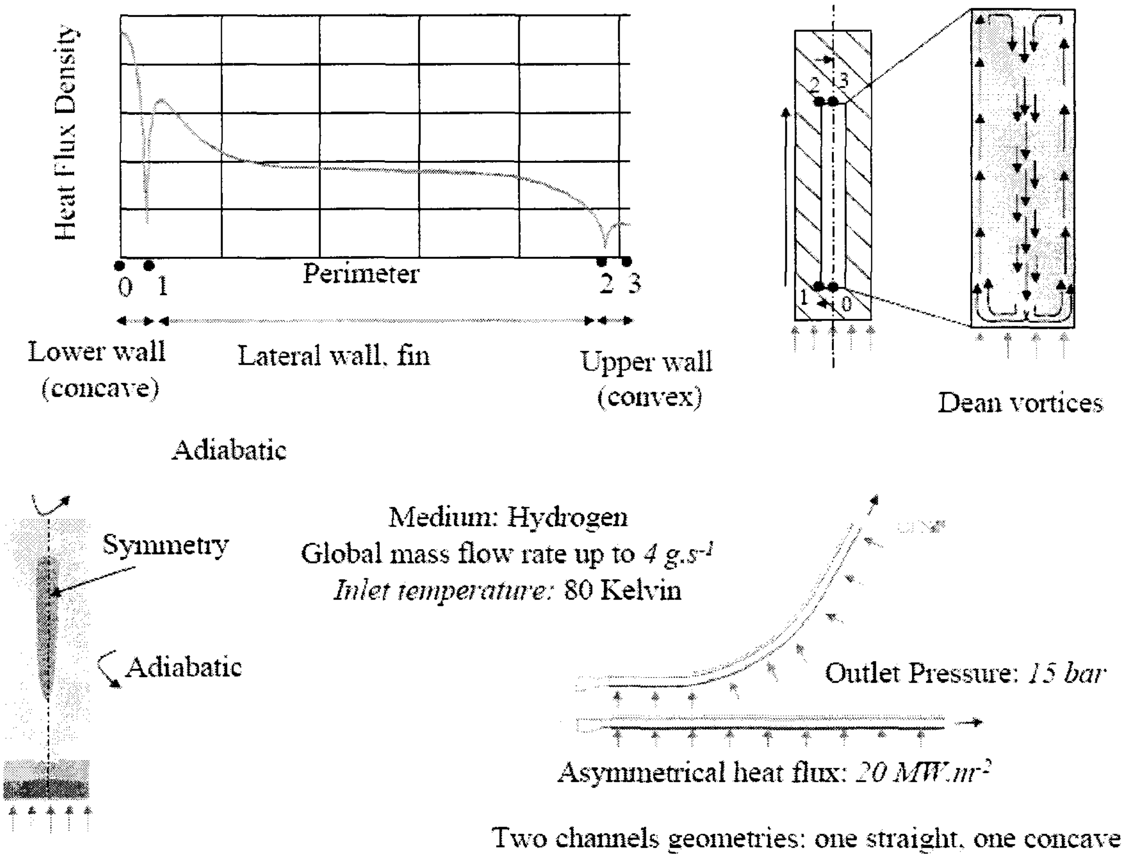

Figure 57 : Boundary conditions of the numerical model and typical heat transfer profile.

The geometry of the numerical model refers to the geometry already presented in the paragraph 3.1.2.1. The numerical model only considers half of the channel for obvious symmetry reasons. The inlet of the channel was modelled too: it concerns the convergent section allowing a smooth growing of the thermal and dynamic boundary layers.

The boundary conditions (B.C.) used for the computation correspond to the experimental conditions of the EH3C campaign, as shown in Figure 57:

- Mass flow rate $4\ g\ s^{-1}$ at the inlet ($2\ g\ s^{-1}$ for the modelled half of channel)
- Pressure outlet: *15 bar*
- Symmetry on the median lines
- Heat flux density: $20\ MW\ m^{-2}$ on the lower wall
- Adiabatic wall on the other external walls
- Fluids: hydrogen and methane
- Solid: copper alloy (Elbrodur G)
- The measured averaged roughness of the different walls was taken into account in the numerical turbulence models.

A typical way of presenting results from the numerical simulation is presented in Figure 57. The profiles of the heat flux density and of the heat transfer coefficients can be drawn along the channel periphery to allow a comparison of the heat flux profile between straight and curved channels.

4.1.2. Meshing investigation

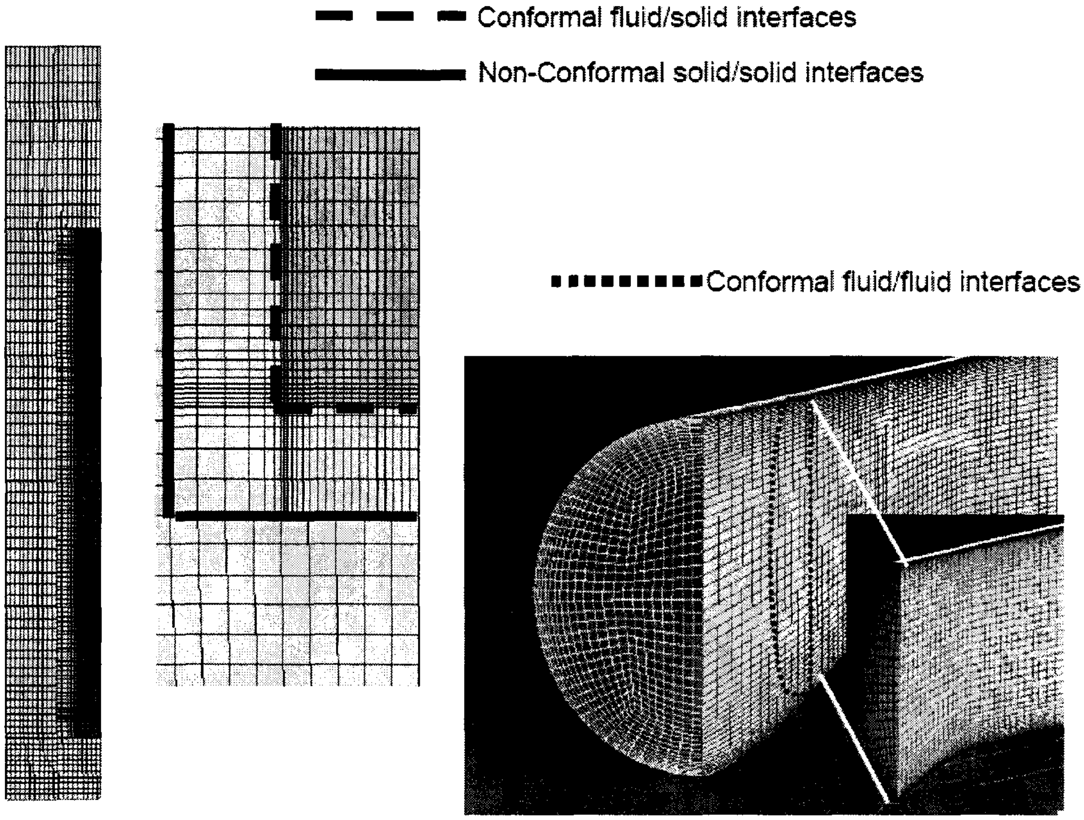

Figure 58 : Cross sectional Grid of solid (yellow) and fluid (blue) regions.

Several grids with different numbers of nodes were designed in order to check the grid influence on convergence. All the calculations for this comparison were carried out using a standard k-ε model with wall function, with first cell height adapted to the flow ($12 < y^{+} < 70$).

The entire grid is structured, both in the solid and fluid regions. To ensure better flow and thermal results in sensitive fluid domains, conformal mesh interfaces were adopted for the fluid/solid and the fluid/fluid interfaces (refer to Figure 58). All the solid/solid interfaces are non-conformal. The solid/solid non-conformal interface reduces the number of nodes in the solid outer region while keeping the global accuracy of the simulations, particularly in the flow domain (see Figure 58).

Two kinds of grids were designed, either for using a wall function (first fluid cell in the fully turbulent region of the boundary layer), or for using a low-Reynolds model (more than *10* cells inside the viscous sublayer). The first grid (mesh 1), with globally *1* million nodes, is a *60x15* grid with *530* nodes streamwise in the fluid zone. In the inner solid zone, a matching number of nodes was set and the outer solid region uses a coarser grid.

The second grid (mesh 2) is identical to the first one with an alternate distribution of the nodes streamwise, with stretched cells in the straight parts (before and after the curvature), and a finer distribution inside the curvature, going from *300* to *400* nodes. This was done to check the influence of the cell aspect ratio (streamwise length on height ratio of cell) on the results. A first comparison can be drawn between these discretisation models and it does not have a strong influence on the results (less than 2% change between the mesh 1 and mesh 2).

Mesh	1	2	3	4	5	low Re
Cross section [nodes]	*60×15*	*60×15*	*80×20*	*80×20*	*120×20*	*140×40*
Streamwise [Nodes]	*530*	*530*	*530*	*1170*	*530*	*530*
Nodes [Millions]	*1*	*1*	*1.7*	*3.6*	*2.5*	*4.5*
CPU time [hours]	*5*	*5*	*7*	*17*	*12*	*65*
Maximum cell aspect ratio (straight)	*62*	*130*	*190*	*170*	*140*	*1800*
Maximum cell aspect ratio (curved)	*64*	*50*	*60*	*23*	*60*	*770*
near-wall treatment	log law	log law	log law	log law	log law	low Re model
y^+ range for $Re \sim 10^5$	*[12;70]*	*[12;70]*	*[12;70]*	*[12;70]*	*[12;70]*	*[0.15;2.5]*
1st cell height, [mm]	*0.006*	*0.006*	*0.004 to 0.006*	*0.004 to 0.006*	*0.004 to 0.006*	*0.0003 to 0.0004*

Table 2 : Information on grids.

The next step was to increase the number of nodes in the cross section, a *80x20x530* grid was designed, with a total of *1.7* million nodes (mesh 3). A similar meshing was made with the same cross section distribution, but with much more streamwise nodes, to check the streamwise influence especially in the curved region. The mesh 4 presents *1170* nodes in the streamwise direction (1000 in the curvature) with a total of *3.6* million nodes.

The last grid (mesh 5) is a *120x20x530* grid, with a total of *2.5* million nodes and was designed to observe the influence of the cross section meshing on results. All the information concerning the different meshing is collected in Table 2.

The comparison of the different meshes 3 and 4 on numerical results indicates that the streamwise node repartition can be limited at *530.* To investigate the cross section meshing, the comparison of heat transfer in plane *j=9* for the grids 1, 3 and 5 is illustrated in Figure 59. The different heat flux profiles seem to converge while nodes increase in the cross section. Indeed, the results of the grid 5 (the finest grid) are between the results of grid 1 (the most disparate) and grid 3. As a conclusion, mesh 5 looks appropriate for this numerical model.

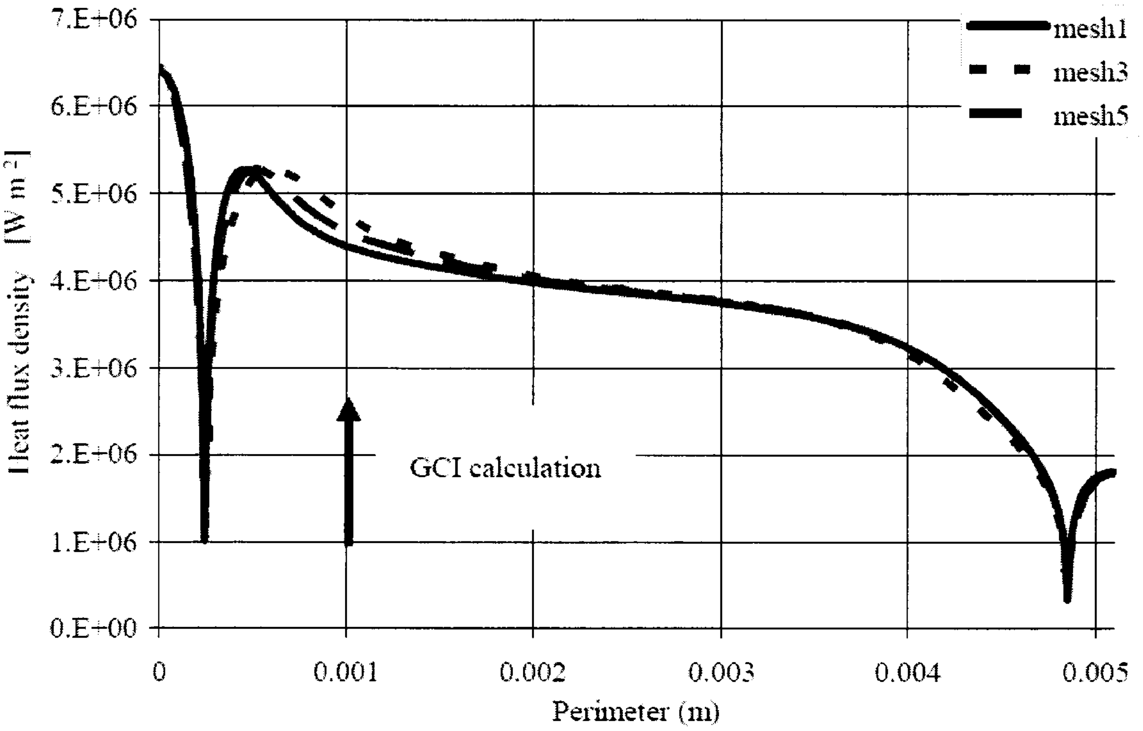

Figure 59 : Heat flux density distribution along the perimeter in plane *j=9* with different grids.

A method for reporting of grid refinement was applied in order to characterise the precision of the different meshes. The use of a Grid Convergence Index (GCI) can quantify the incertainties due to grid convergence. This error estimation was derived from the second order approximation of Richardson extrapolation ([Roache, 1994]). The parameter was calculated with the heat flux density $\dot{q}_{(i)}$ at the channel wall (*0.001 m* along the perimeter, see Figure 59) with the mesh *(i)*.

The estimated fractional error $E_{(i-j)}$ delivers a related error of the coarsed mesh *(j)* in comparison to the finest mesh *(i)*. r is the fine to coarse cells numbers ratio.

$$E_{(i-j)} = \left(\frac{\left| \dot{q}_{(j)} - \dot{q}_{(i)} \right|}{\dot{q}_{(j)}} \right) \left(r^2 - 1 \right)^{-1} \tag{4.1}$$

The estimated fractional error coefficients were estimated for the different grids and can be summarised in Table 3:

Mesh	1	3	5
Nodes [Millions]	*1*	*1.7*	*2.5*
Estimated fractional error (GCI)	$E_{(1-3)}$	$E_{(3-5)}$	$E_{(1-5)}$
	3.9%	*4.7%*	*0.4%*

Table 3 : Estimation of "Fractional error" with the GCI method.

All related fractional error coefficients indicate that the mesh refinement does not bring about essential improvement (less than 5%). The best grid (5) is thus used to analyse all numerical results.

4.1.3. Numerical parameters influence

The roughness was set up at the fluid/solid interface to match the roughness of the experimental channel which is characterised by the milling of the channel and the property of galvanic layer. The values are $0.3\ \mu m$ for the lower wall, $0.1\ \mu m$ for the side wall and estimated at 3 µm for the upper wall. These data were measured (see 3.1.2).

Another simulation with smooth walls was computed as a reference simulation. The results are shown in Figure 60. As expected, the results are identical for both simulations, with difference less than *0.1%*. So in our case, roughness does not have any influence on the results with $Re \sim 10^5$.

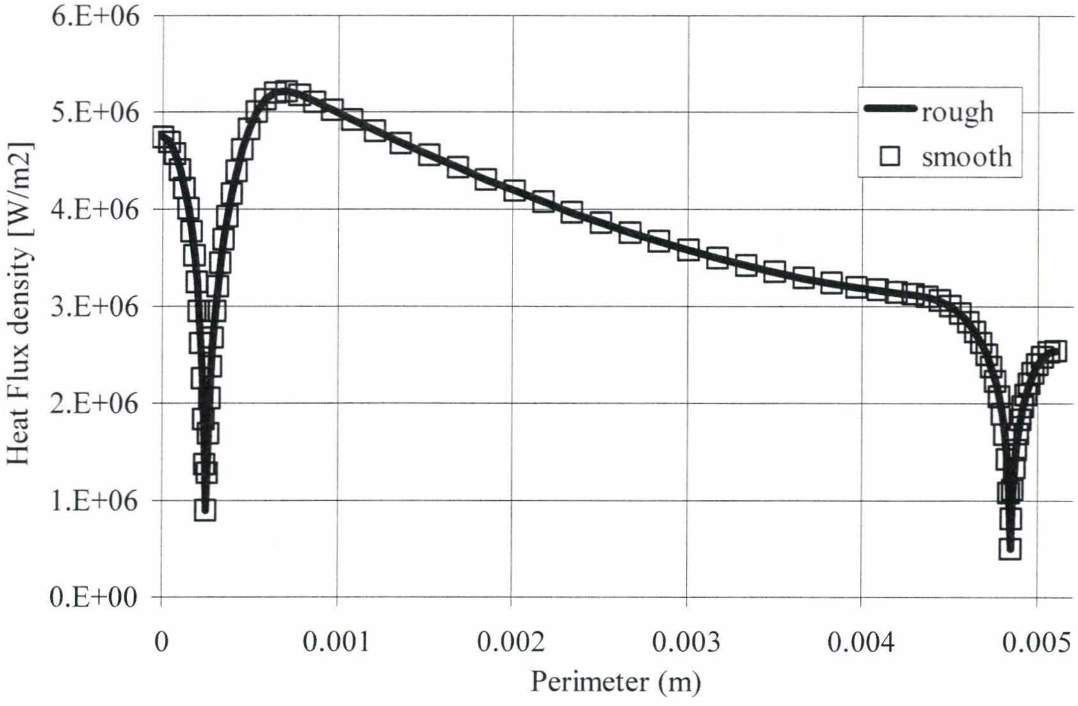

Figure 60 : Comparison smooth/rough walls numerical simulations in plane *j=12.*

Several parameters, mostly for turbulence modelling, are available to determine the inlet fluid boundary conditions (B.C). It is possible to change the turbulent intensity and the eddy length scale. Two simulations with different values for these parameters were realised to compare them with a reference simulation made with default values. These initial conditions are presented in Table 4. As a result, a difference below *0.1 %* was noted between the different simulations. Thus this inlet parameter does not have any influence in this EH3C numerical test case.

	Turbulent Intensity	Eddy Length Scale
Reference	*1%*	*Auto.*
Sim. 1	*10%*	*Auto.*
Sim. 2	*1%*	*0.5 mm*

Table 4 : Inlet turbulence conditions tested for the numerical simulations.

Two discretisation schemes can be used. These schemes are first and second order upwind. An additional scheme called “high resolution” is available, and consists in a blending of first and second order upwind, 1st order for regions with high gradients, and 2nd order for regions with low gradients, allowing both accuracy and robustness. This high resolution discretisation scheme was used and represents a gain of calculation time of about *10%* in comparison to a first order schema. The numerical results were compared with the two discretisation schemes and no difference was noted.

4.1.4. Material and Flow Properties

The modelling of fluid and solid is one of the most critical problems as to providing reliable numerical simulations. The thermal and dynamical types of behaviour strongly depend on the basic fluid properties, like density and viscosity. The solid model must be based on an appropriate conductivity model to properly calculate the energy equation. Different models of material properties were tested numerically in order to evaluate the impact of the change of fluid and solid models on the heat and mass transfer process in the EH3C configuration.

4.1.4.1. Solid Properties

Two different models of copper alloy properties were used. The first model is a model of copper using constant properties. Its characteristics are as following:

- Density : $8933\ kg\ m^{-3}$
- Thermal Conductivity : $401\ W\ m^{-1}\ K^{-1}$

The second model is based on experimental measurements of the copper alloy [Oschwald, 2004] and uses polynomial expression for thermal conductivity (Table 5), to match with Elbrodur properties which is the material used for the experiment.

$$\lambda = c_0 + c_1 T + c_2 T^2 + c_3 T^3 + c_4 T^4 + c_5 T^5 + c_6 T^6 \qquad \textbf{(4.2)}$$

The interpolation comes from experimental results which can be observed in Figure 61.

i	0	1	2	
[-]	$W\,m^{-1}\,K^{1}$	$W\,m^{-1}\,K^{2}$	$W\,m^{-1}\,K^{3}$	
c_i	202.6011	1.3787	-1.1504×10^{-2}	
i	3	4	5	6
[-]	$W\,m^{-1}\,K^{4}$	$W\,m^{-1}\,K^{5}$	$W\,m^{-1}\,K^{6}$	$W\,m^{-1}\,K^{7}$
c_i	6.7138×10^{-5}	-2.0282×10^{-7}	2.9330×10^{-10}	-1.6264×10^{-13}

Table 5 : Coefficients used to model the thermal conductivity of the Elbrodur G.

The calculations for both models were made with a standard k-ε model and logarithmic wall function. The results are shown in Figure 62. The difference is up to *10%*, the solid model should also be implemented in the numerical model. In all the following simulations, the solid material (copper alloy Elbrodur G) was modelled with the aid of the thermal conductivity model presented in the Table 5.

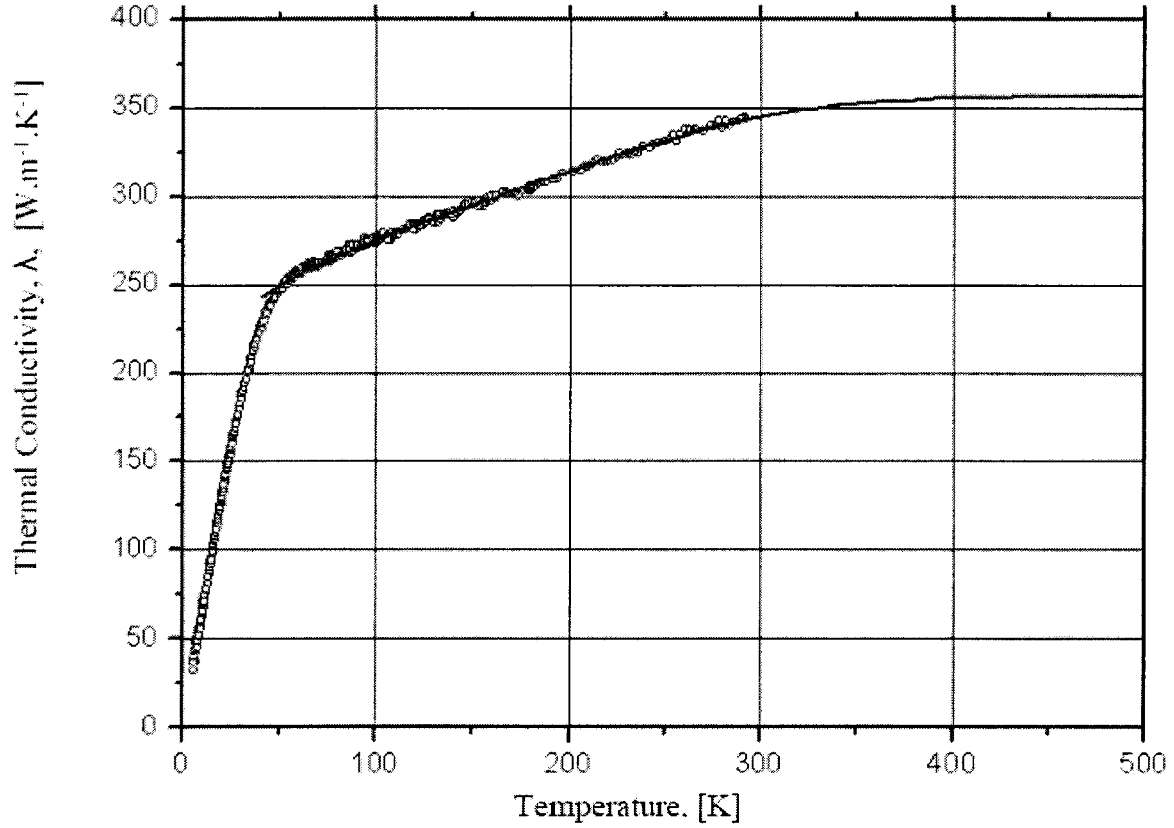

Figure 61 : Elbrodur G thermal conductivity dependence on temperature [Oschwald, 2004].

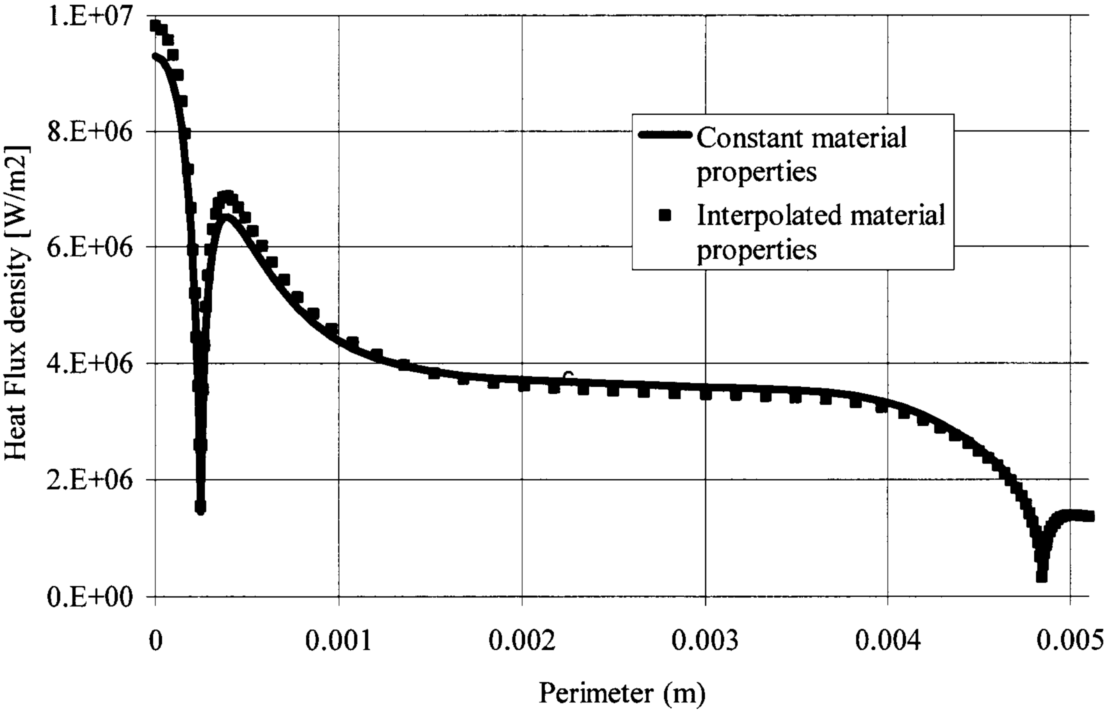

Figure 62 : Heat Flux distribution along the perimeter in plane *j=5* for different solid models.

4.1.4.2. Physical and thermodynamic fluid properties

Different real gas models were tested and compared, both considering compressible fluid (here hydrogen). Two kinds of fluid models are available in the CFD software. The first one is an ideal gas model of hydrogen with constant properties. The second model is a real gas model and uses the Redlich-Kwong state equation, [Redlich-Kwong, 1949]. The Redlich-Kwong model can be considered as valid for extended pressure (up to *500 bar*) and temperature (from *100 K* up to *400 K*) domains. This corresponds well to the fluid domain of the EH3C configuration. The temperature and pressure distributions along the channel in the bulk domain are described in Figure 63.

For the numerical simulation, a table of fluid properties was generated. This was done with the aid of the software CFX-TASCflow. The standard Redlich-Kwong equation of state was used in the simulations (refer to Table 6), [Redlich-Kwong, 1949].

$$P = \frac{R_0 T}{V_m - b} - \frac{a}{\sqrt{T} V_m (V_m + b)} \tag{4.3}$$

where $V_m = \dfrac{M}{\rho}$ is the molar volume [m^3 mol^{-1}]

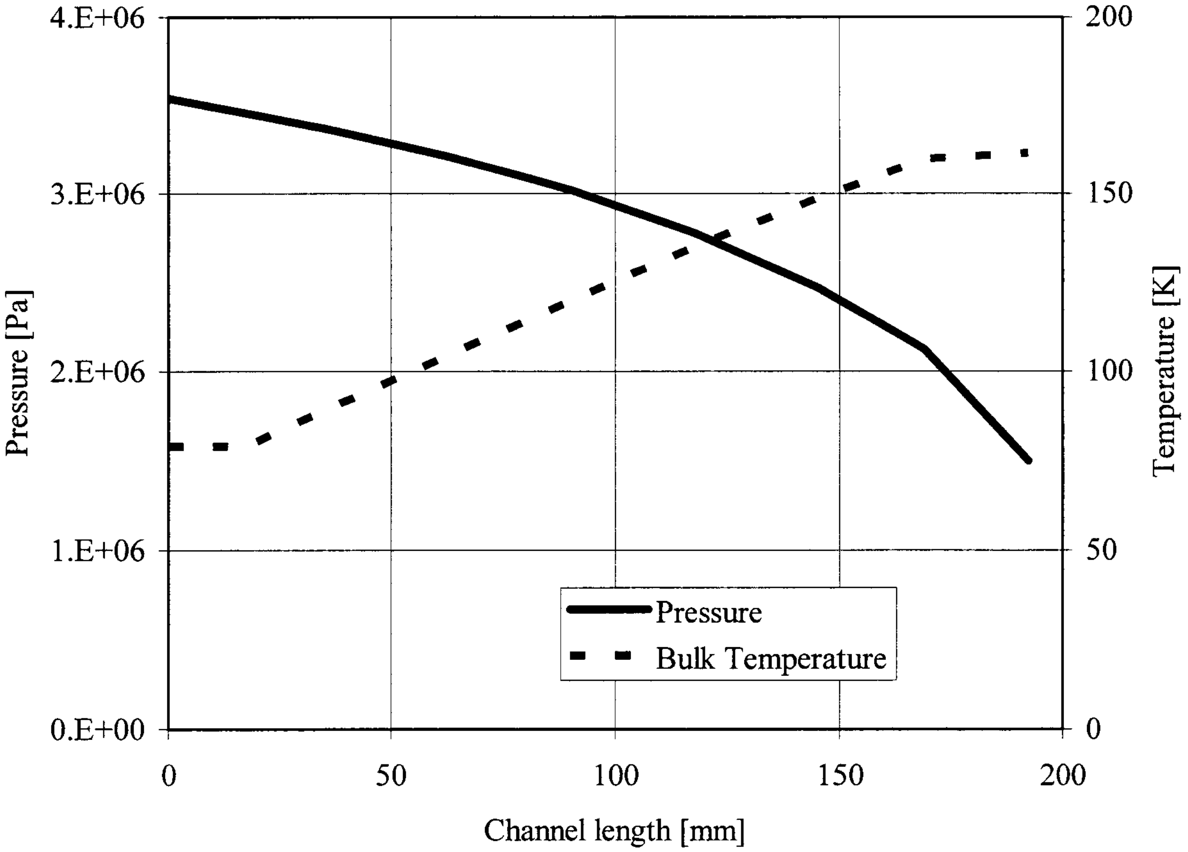

Figure 63 : Temperature and pressure profile along the channel length in the bulk section.

R_0	P_c	T_c	a	b
$[J\ mol^{-1}\ K^{-1}]$	[Pa]	[K]	$[kg\ K^{0.5}\ m^5\ s^{-2}\ mol^{-2}]$	$[m^3\ mol^{-1}]$
8.314472	Critical pressure	Critical temperature	$\frac{0.42748 \cdot R_0^2 \cdot T_c^2}{P_c}$	$\frac{0.008664 \cdot R_0 \cdot T_c}{P_c}$

Table 6 : Parameters for the Redlich-Kwong model [Redlich-Kwong, 1949].

The calculations with the ideal gas model and the real gas model are made with a standard k-ε turbulence model and a logarithmic wall function. The results are presented in Figure 64. The difference between these models is locally up to *10%*. The final numerical results were obtained with the Redlich-Kwong fluid model.

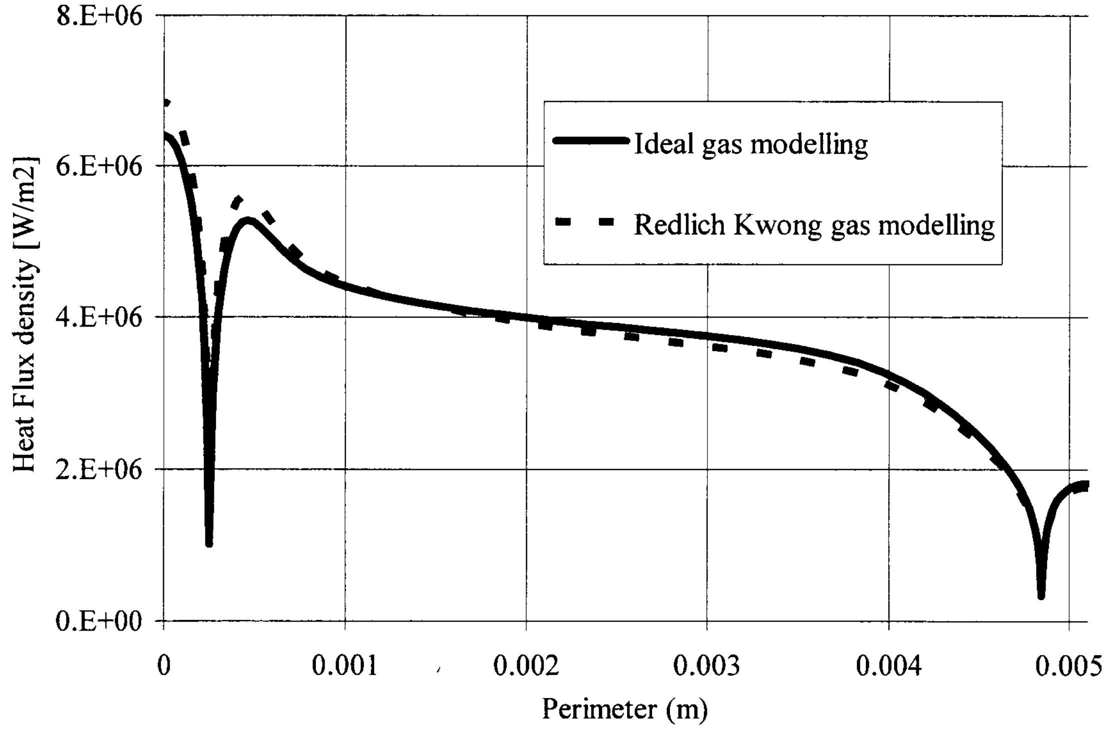

Figure 64 : Heat Flux distribution along the perimeter in plane j=9 with real and ideal gas models.

Other fluid property models exist and were investigated in the EH3C fluid properties range (supercritical hydrogen for [*15-40 bar*] and [*80-400K*]). They have been developed for 20 years, and the well known models are succinctly quoted here :

- Mc Carty, 1981
- Mc Carty, Weber, 1972
- Peng, Robinson, 1976
- Bennedict Webb Rubbin, Younglove, 1982, NIST data base.

None of the models presents any variation in comparison to the Redlich-Kwong model. Indeed, the models diverge by defining density, viscosity when approaching the critical point (*33 K* and *13 bar* for the hydrogen). The EH3C test case is too far away from the critical point to differentiate the various real gas models. The real gas model of Redlich-Kwong was used to model the fluid properties for the numerical simulations of the EH3C experiments with a temperature profile as boundary conditions at the lowest part of the channel (see 4.2).

4.1.5. Turbulence models

Several turbulence models were investigated: k-ε, SST, RSM BSL (Reynolds Stress Model Baseline), k-ω, SST LRM, RSM Baseline LRM, see Appendix 1 for the models description. Three of them were selected to be analysed more in detail, because of the relevance of the numerical results delivered : the k-ε, SST and the RSM Baseline LRM.

The k-ε and SST models are 2-equation models and the BSL model is a non-isotropic 7-equations model solving the Reynolds stress tensor (see Appendix 1 for more details). The calculations were carried out with the finest mesh 5 for the logarithmic wall treatment laws and the LRM mesh for the 2-Layers wall treatment. An ideal gas fluid model and the solid model with constant properties were used. The heat flux profile at the curved channel wall of the cross-section *j=5* obtained with these models are shown in Figure 65.

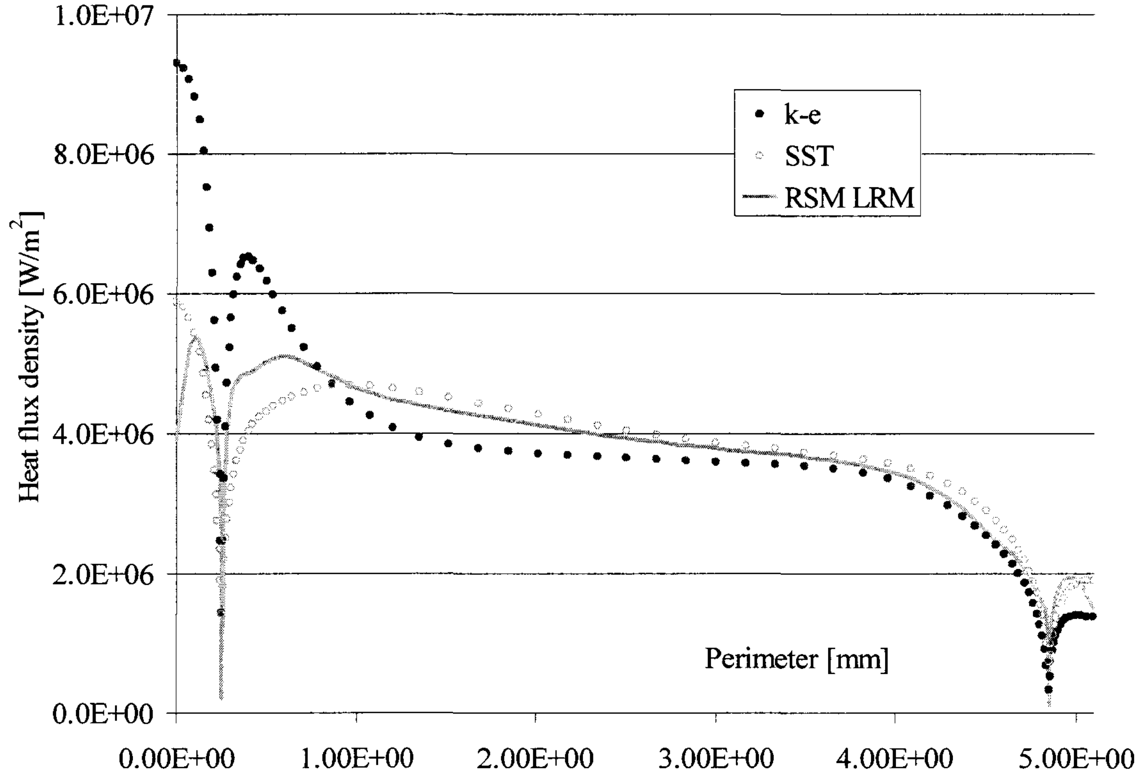

Figure 65 : Heat Flux distribution along the periphery of the curved channel section *j=5*, for different turbulence models resolution.

The turbulence models seem to converge into the same heat flux behaviour, except from the k-ε model which accentuates the asymmetry of the heat flux. The RSM model simulation exhibit some particular behaviour of the heat transfer at the corners of the channels. With this RSM model, close to the corner, the heat transfer is limited in the middle of the lowest part of the channel and enhanced in the edges. This is due to additional secondary motions, the "edges" secondary flows which are illustrated in Figure 66.

The "edges" vortices are only enlightened with the RSM model. These secondary motions appear in the corners of the straight and the curved channels, see Figure 66. These "edges" vortices can be compared to those observed in LES simulations [Münch, 2005, Salinaz, 2002], see in 2.3.3 and are in fact very similar in shape and intensity, although a RANS model is used in our case. This shows that RSM turbulence models are very capable of taking into account the anisotropy of the turbulence. Theory already predicted the appearance of these recirculations in rectangular channels, see in 2.1.1, [Leutheseer, 1963].

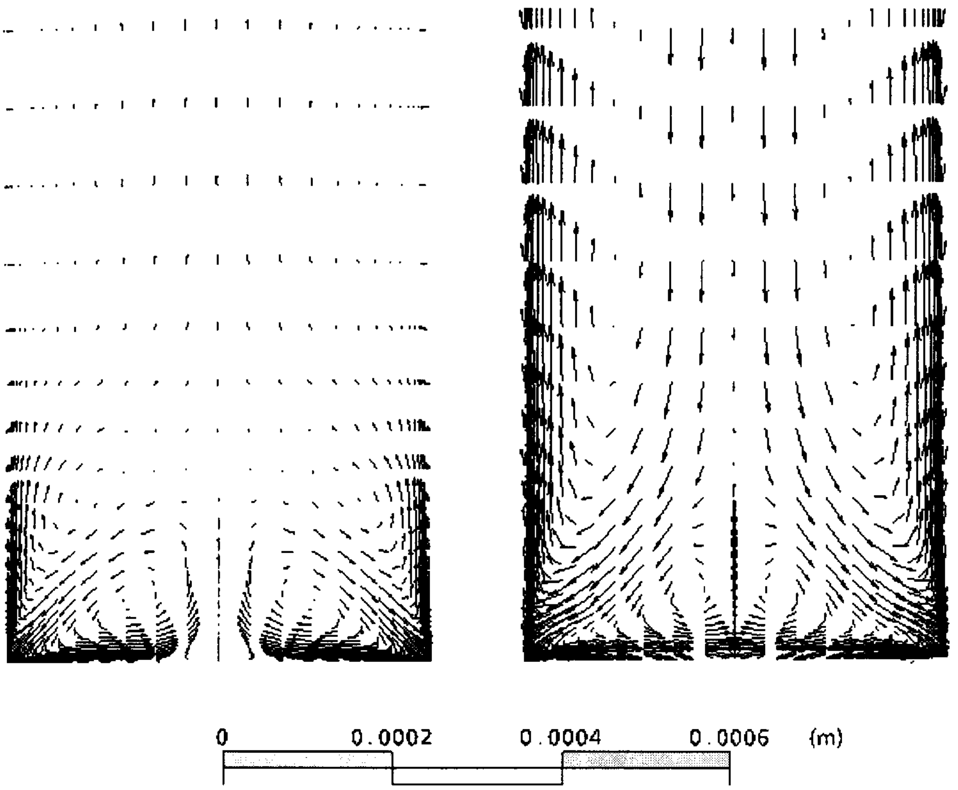

Figure 66 : Secondary velocity profiles in plane *j=5* for the straight channel (left) and the curved channel (right) with RSM turbulence model.

In these numerical simulations, for the straight channel configuration, the "edges" vortices remain constant in intensity (up to *4%* of the axial main flow velocity at the entrance of the channel) and shape all over the channel length. Concerning the curved channel, these edges vortices are mixed up with the Dean vortices. The upper part of the "edges" vortices are absorbed by the centrifugal secondary motions (see in the curved configuration of Figure 66 right).

Figure 67 illustrates the secondary motions of the Dean vortices and the edges vortices, as well as the temperature profile inside the same channel section for the SST and RSM models. In the middle of the channel, the two kinds of vortices still coexist but after a certain distance along the channel, the Dean vortices become preponderant and totally absorb the "edges" vortices. The heat flux profiles at this location become similar between the SST and the RSM models.

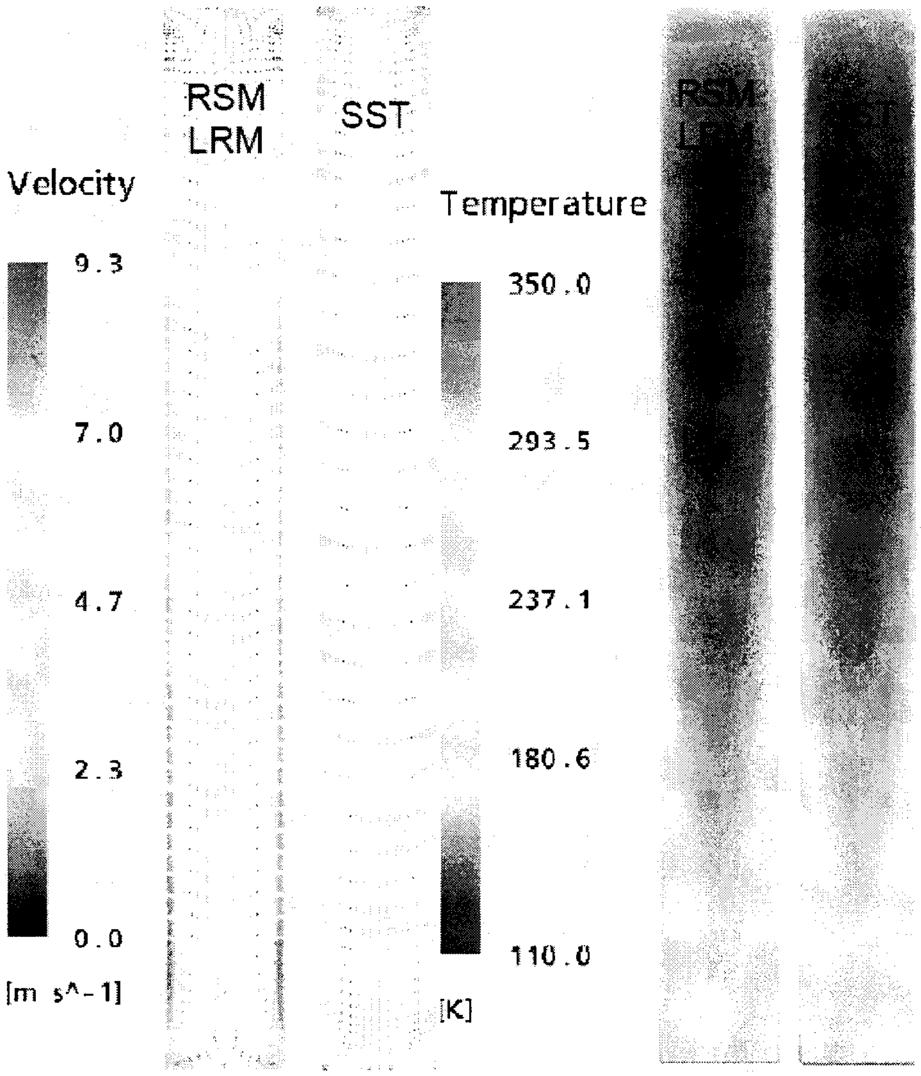

Figure 67 : Secondary velocity (left diagram) and temperature (right diagram) distribution in plane *j*=*5* for RSM LRM (both left sections) and SST models (right sections).

4.2. Numerical Simulations of the EH3C experimental test cases

4.2.1. Simulations of the test specimen with the blocks

The EH3C test specimens (channel and blocks) were numerically simulated. The straight and curved blocks were drawn, meshed and defined as copper alloy. The "thermal nozzle" profile between the blocks and the channels follows the real geometry of the test specimens. The geometries of the channels are exactly the same as described in the preceding numerical simulations (4.1) but the curved and straight blocks are added under the channels, as it can be seen in Figure 68. A SST model with wall function was taken to model the turbulence and the wall treatment. All the numerical parameters (roughness, time steps, convergence criteria, discretisation models…) are similar to the preceding simulations (see in 4.1). Some boundary conditions (adiabatic channel walls, symmetries, fluid interfaces) are identical as well. The constant heat flux density at the lowest part of the channels is not taken into account anymore because of the presence of the blocks. The surface under the blocks is maintained at the heating temperature given by the electrical regulators, (refer to the experimental conditions in 5.2.1 or in Table 7 page 109). The inlet temperature of the fluid, the outlet pressure and the mass flow rate refer to the experimental conditions as well. The lateral walls of the blocks are considered as adiabatic. The methane and the hydrogen were simulated with an ideal gas model. The thermal conductivity of the material was modelled with the interpolated function described in the paragraph 4.1.4.1. The temperature fields obtained with the hydrogen flow are presented in Figure 68.

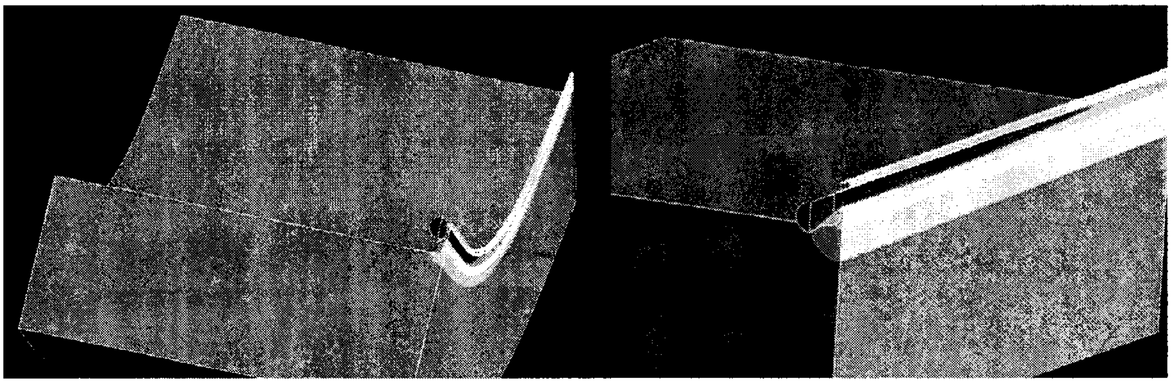

Figure 68 : CFD temperature fields of the curved and straight test specimens (channels and blocks) with hydrogen flow.

The temperature and the heat flux profile are investigated in the interface between the block and the channel at a precise cross-section of the channel ($j=5$). With the aid of the thermal nozzle profile, the heat flux density is maximal in this interface. The temperature remains constant (less than 1K difference) along the channel-block interface in the cross-section $j=5$, although the heat flux density reaches *5%* deviation. The boundary condition of constant heat flux density at the block-channel interface is not so adequate to the EH3C experiments in comparison to constant temperature.

The numerical simulations with the blocks were firstly compared with the experimental results (see in the paragraph 5.2.4.1). The very good reliability of the temperature field given by the thermocouples line T_{2j} validates the use of the temperature profile of the block – channel interface for the numerical simulations without block. With this good reliability of the numerical results at the channel-block interface, it is not necessary to model the heat losses through convection and radiation between the block and the environment. The experimental temperature of the electrical cartridges used as boundary condition at the lowest face of the block is fully convenient.

In order to improve the experiments modelling with the aid of the CFD programme, the blocks consum a lot lot of nodes, which are needed for the fluid part. Indeed, the fluid must be modelled with a finer mesh (grid 5). A boundary condition at the lowest part of the channel, corresponding to the block-channel interface must be defined to replace the block's role. Along the channel length, the temperature at this interface increases because of the fluid heating. This temperature profile was interpolated from the simulations with the block and thus exported in channel simulation without block, using the fine grid 5.

4.2.2. Simulations without blocks

The numerical simulations without block use a very fine mesh (Mesh 5 for the logarithmic wall treatment and the "Low Re Mesh" for the Low-Reynolds Model wall treatment, see in 4.1.2). The Table 7 page 109 summarises all boundary conditions and turbulence models applied to these numerical simulations.

	Fluid model	Config.	Heat B.C.	Mesh	T inlet	Turb.	P outlet	Wall treat	Mass flow
			[K]		[K]		[bar]		[g.s^{-1}]
H_2-S1	H2-IG	Straight + Block	643K at block	Mesh 1	*77*	SST	*26*	Log	*3.305*
H_2-S2	H2-RK	Straight	Temp. profile	Mesh LRM	*77*	RSM - BSL	*26*	LRM	*3.305*
H_2-S3	H2-RK	Straight	Temp. profile	Mesh 5	*77*	k-epsilon	*26*	Log	*3.305*
H_2-C1	H2-RK	Curve + Block	649K at block	Mesh 1	*82.5*	SST	*19.5*	Log	*3.319*
The same simulations for the curved channel with hydrogen flows were realised with and without block (SST Log with block; RSM-LRM, k-epsilon, SST-LRM without block) and with the experimental conditions of the curved channel data set.									
CH_4-S1	CH4-IG	Straight + Block	*465* at block	Mesh 1	*296*	SST	*23*	Log	*6.999*
CH_4-C1	CH4-IG	Curve + Block	*465* at block	Mesh 1	*285*	SST	*17.9*	Log	*7.102*

RK: Redlich Kwong model; IG: Ideal Gas Model; T: temperature; P: Pressure;

Table 7 : Description of the numerical simulations of the EH3C experimental test cases.

4.2.3. Thermal simulations without fluid

The block in the curved configuration has a larger heated surface than in the straight configuration. This enlargement provides an additional heat source due to the surface restriction between the base and the curved channel. To enlighten this phenomenon, the two block configurations were modelled with an identical heat transfer coefficient all over the fluid-solid interfaces in the cooling channel. By the way, the fluid side is perfectly identical for the straight and the curved channels.

A convective heat transfer coefficient of $50000\ W\ m^{-2}\ K^{-1}$ was applied on the channel surfaces of the straight and the curved channels. The experimental temperatures of the electrical heaters were applied on the lowest block side.

The curved and the straight channels have exactly the same cross section (width, height, length and block-channel interface). The only difference between the two simulations is the block geometry which has a *1.6* larger base in the curved case. The temperature and the heat flux density profiles at the channel-block interface are drawn along the channel length in Figure 69 and Figure 70.

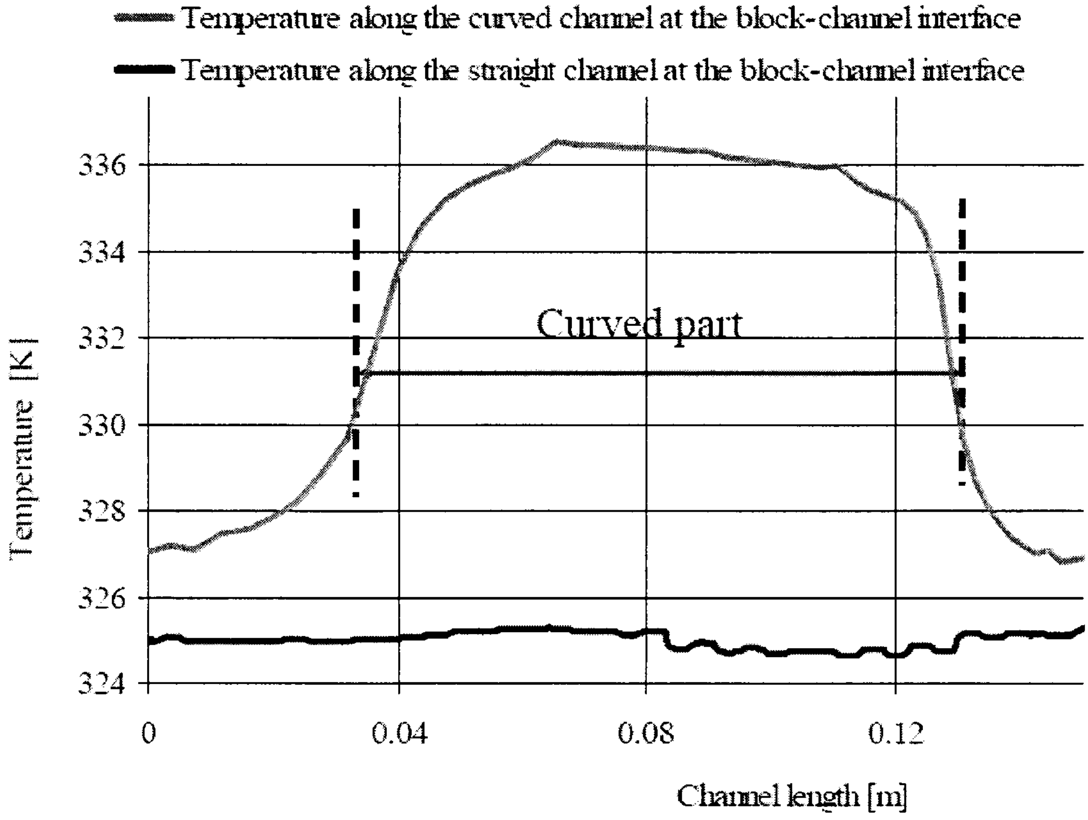

Figure 69 : Numerical temperature profiles along channels length at the block-channel interfaces with constant convective heat coefficient.

The simulation without fluid shows that the curved geometry of the block has a strong influence on the thermal field of the channel. Indeed, the curved block provides a higher heat flux in the channel section. The heat flux at the channel – block intersection in the curvature is about *6.4%* higher for the curved channel test case and the temperature is *11 K* higher in the curved part. This is due to the geometry of the curved block.

These simulations without fluid are extremely important. They prove that the block geometry difference between the straight and the curved configuration has a strong impact on the boundary conditions at the hot side of the channel in terms of heat flux or temperature field.

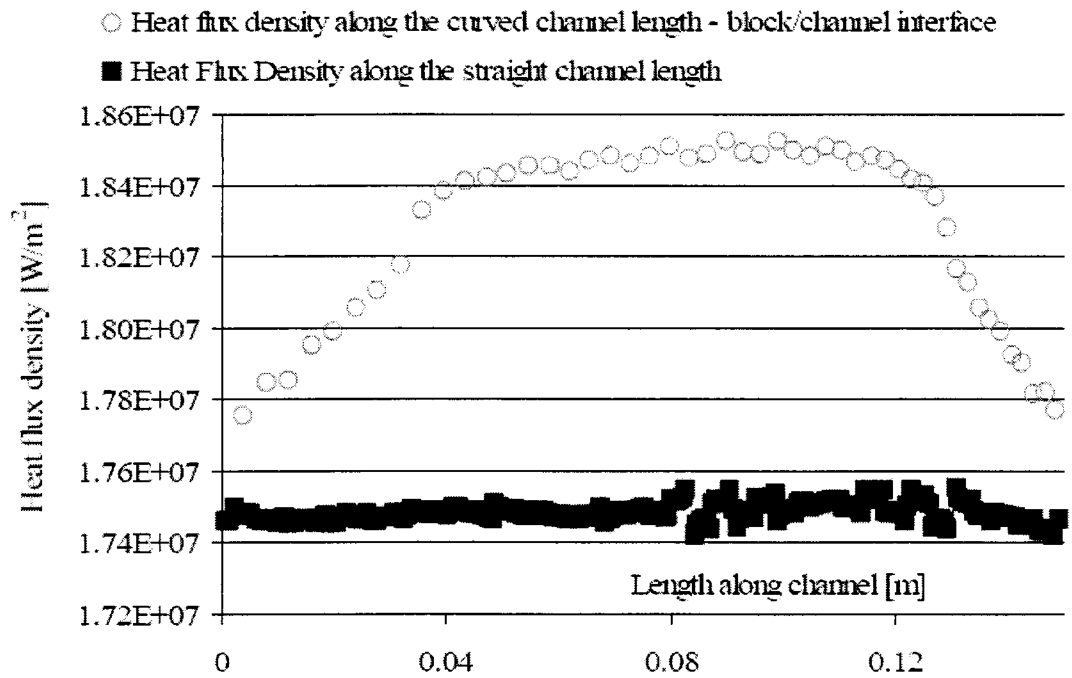

Figure 70 : Numerical heat flux density profiles along channels length at the block-channel interfaces with constant convective heat flux coefficients.

4.2.4. Numerical results

In order to be able to compare the experiments with the numerical simulations, an adapted heat transfer coefficient was defined. The classic heat transfer coefficient is usually defined with the local heat flux at a point of the fluid–solid interface, and the near to wall temperature difference (temperature of the wall in the solid and temperature near the wall in the fluid). Experimentally, it was impossible to directly measure the temperatures near the wall inside the fluid. It was thus decided to take the inlet temperature as reference temperature (see 3.3.1):

$$\dot{q} = h_{EH3C}\left(T_{wall} - T_{inlet}\right) \tag{4.4}$$

The estimation of the outlet stagnation temperature can be the most difficult problem because of the thermal stratification. At the outlet of the channel, a large panel of temperatures is available between the hot wall and the bulk region in the middle of the channel. In order to define a realistic outlet stagnation temperature that can be compared to the experimental results, a mixed temperature was defined to take into account the thermal stratification of the outlet cross-section of the channels. In each numerical element, an averaged heat flux was calculated, with the corresponding surface of the element, the fluid properties and the flow characteristics which are available in the numerical results.

$$T_{average} = \overline{T} = \frac{\int_{section} c_p \dot{m} T dS}{\int_{section} c_p \dot{m} dS} \tag{4.5}$$

The globally absorbed heat along the channels was thus evaluated with this mixed temperature at the outlet of the channels.

$$\dot{Q}_{calo\_CFD} = \dot{m} c_p \left(\overline{T} - T_{in}\right) \qquad \textbf{(4.6)}$$

The inlet stagnation temperature is constant over the inlet cross-section of the channel. An averaged heat capacity is taken between the inlet and the outlet of the channel from the real gas models (4.1.4.2). Anyway, the heat capacity of the fluids does not vary much along the channel, taking into account the real fluid properties. The hydrogen heat capacity varies less than *5%* along the channel length: $12290\ J\ kg^{-1}\ K^{-1}$ at the entrance of the channel against $13050\ J\ kg^{-1}\ K^{-1}$ at the outlet, see Appendix 9. An averaged value was used.

The Table 8 resumes all outlet mixing temperatures.

		CFD SST Log							
Medium	Channel	T inlet	T outlet (Bulk, Wall)		T Mixing Outlet				
		[K]	[K]	[K]	[K]				
H2	Straight	*77*	*160.8*	*363.3*	*187.1*				
H2	Curve	*82.5*	*169.97*	*373.3*	*195.1*				
CH4	Straight	*296*	*344.35*	*412.5*	*351.7*				
CH4	Curve	*285*	*332.8*	*411.2*	*340.8*				
		CFD RSM LRM				CFD k epsilon			
		T inlet	T outlet (Bulk, Wall)		T Mixing outlet	T inlet	T outlet (Bulk, Wall)		T Mixing Outlet
		[K]	[K]	[K]	[W]	[K]	[K]	[K]	[W]
H2	Straight	*77*	*161.55*	*362.69*	*191.8*	*77*	*159.09*	*362.52*	*193.7*
H2	Curve	*82.5*	*173.1*	*372.8*	*201*	*82.5*	*175.6*	*371.93*	*204.7*

Table 8 : Temperatures at the inlet and the outlet of the channels from numerical simulations.

4.2.4.1. Numerical simulations of hydrogen tests

- Heat transfer coefficients

Figure 71 presents the heat transfer coefficient along the straight channel perimeter at different longitudinal abscissae. Three perimeters were used to compare the different turbulence models: the plane 2 is located at *z=21 mm* after the inlet of the channel (corresponding to the straight inlet of the curved channel), the plane 8 is located at *z=111 mm* (directly in the curvature) and the plane 12 at *z=161mm* (straight outlet after the curvature).

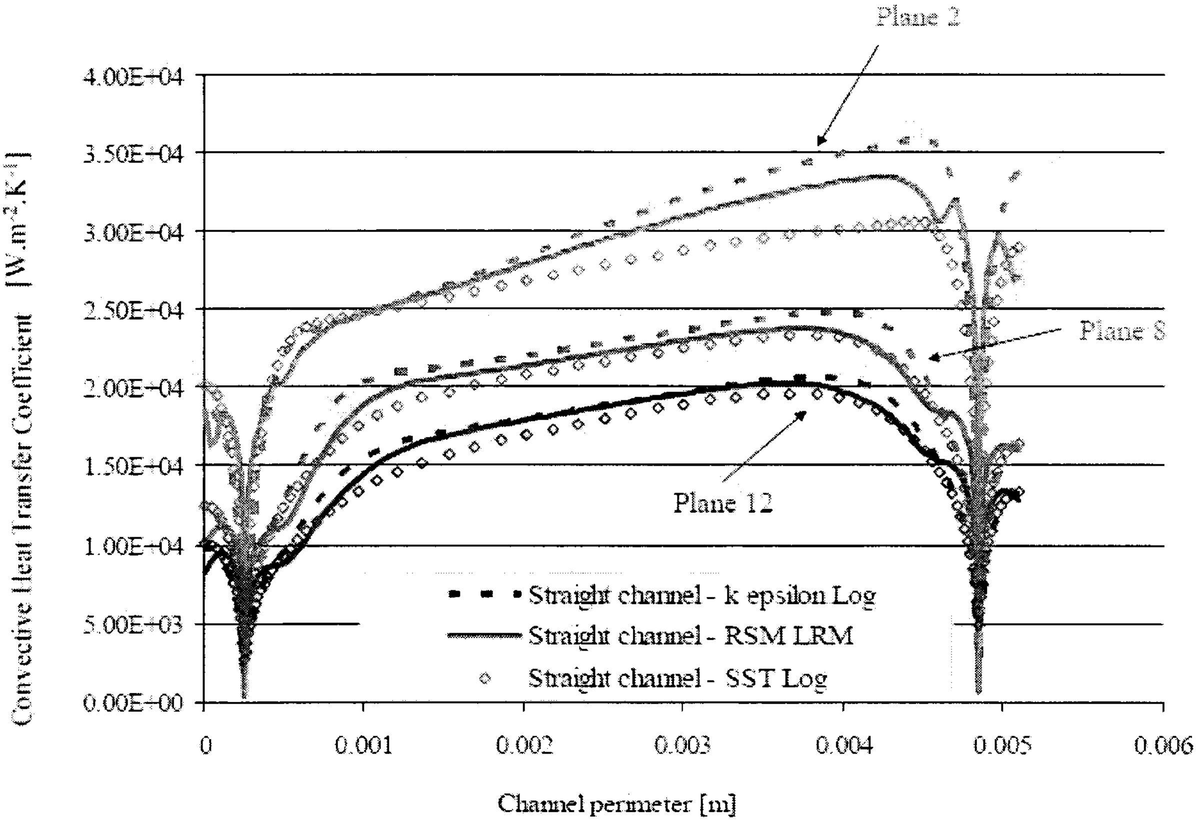

Figure 71 : Convective heat transfer coefficients along straight channel perimeter at different cross-sections and for different turbulence models for the hydrogen flow.

For a defined channel cross-section, a difference can be observed between the upper part of the channel (the cold side of the channel) and the down side of the channel (the hot side of the channel): the asymmetrical heating induces a higher wall temperature at the down side of the channel and a higher heat transfer. The thermal stratification is more important at the "hot" side of the channel. The difference of the heat transfer coefficient profile along the perimeter can be explained by the thermal stratification which can be neglected in the upper part of the simulated channels. This tendency disappears along the channel, because of progressive creation of thermal stratification in the cold side of the channel. All the turbulence models follow the same behaviour as to what concerns the description of the heat transfer coefficients. Nevertheless, the RSM-LRM shows recirculation in edges and exhibit a local deformation of the heat transfer coefficient in the corners of the channels, as it has been already explained in 4.1.5. The same numerical data exploitations were worked out for the curved channel (see in Figure 72.)

All the turbulence models do not identically treat the heat transfer in the curvature (Plane 8). The slope of the heat transfer coefficient along the channel height is similar for the k-ε and the SST turbulence models. The calculation of the "edges" vortices by the RSM LRM has an influence at the concave side: the RSM expects a heat flux coefficient of *10000* although the SST calculates *17000* and the k-ε *30000*. Moreover, the "edges" vortices influence the heat transfer profile along the channel height, where the slope of the coefficients with the RSM LRM has a behaviour opposite to the two others models. This can be explained by the interaction of the "edges" vortices and the Dean vortices, as it has been previously shown (refer to the paragraph 4.1.5).

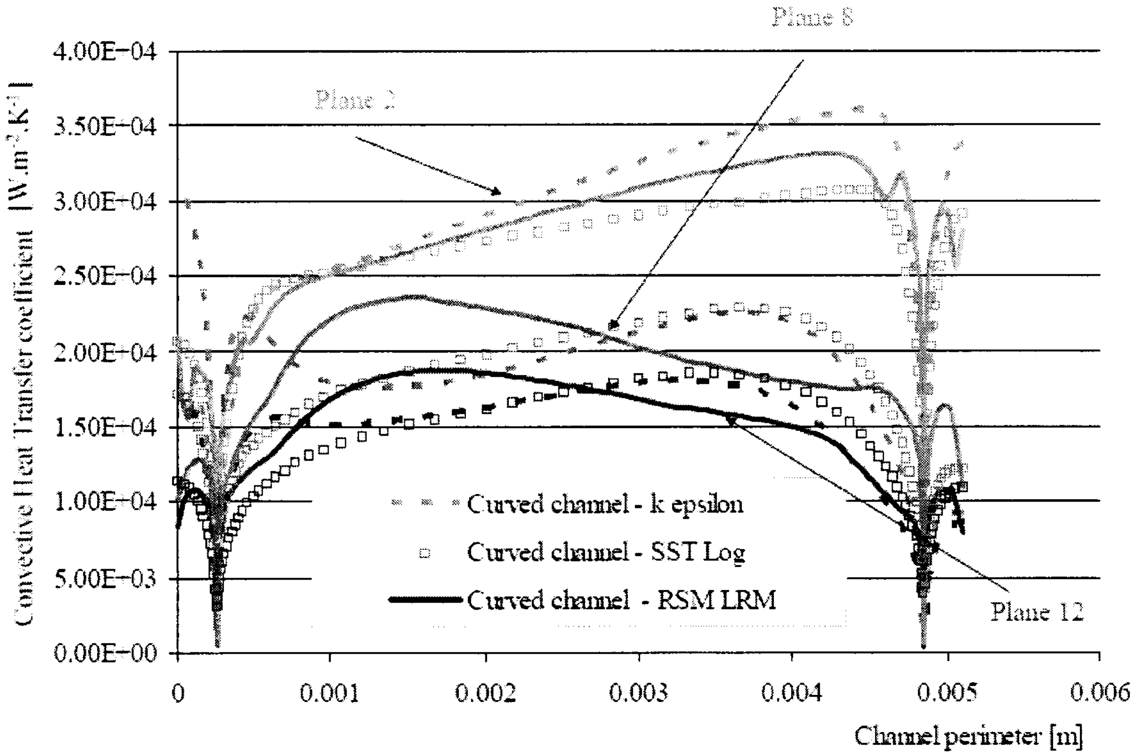

Figure 72 : Convective heat transfer coefficients along curved channel perimeter at different abscissa and for different turbulence models for the hydrogen flow.

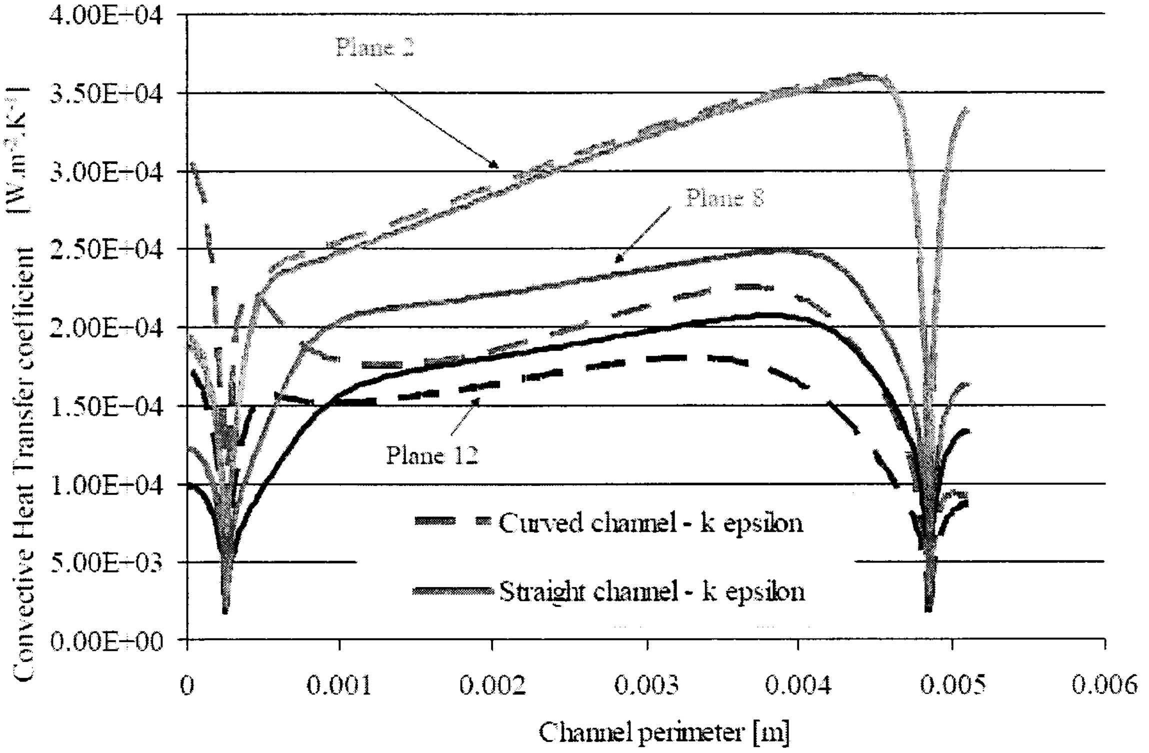

Figure 73 : Heat transfer coefficients along channel perimeter at different cross-sections of the curved and straight channels for the k-ε turbulence models and for the hydrogen flow.

In a same graphic, the results of the straight and the curved simulations can be presented, firstly for the k-ε model (Figure 73) and thus for the RSM LRM model (Figure 74).

The heat transfer coefficient along the periphery of the channel at the cross-section $j=2$ presents similar results for both channels. This plane is located upstream of the curvature and it is logical to have the same behaviour. In the curvature ($j=8$) and downstream of the curvature (plane 12), the profile of the heat transfer coefficient strongly varies along the perimeter. Indeed, the thermal stratification is perturbed by the Dean vortices and the global heat transfer coefficient increases at the concave side (the "hot" side).

In the curvature, the local heat transfer increases at the concave side and decreases at the convex side. Locally, at the concave side, the heat transfer coefficient increases more than 2 times in the curvature than in the straight channel with the use of the k-ε model.

Concerning the RSM-LRM model, the increase of the heat transfer coefficient at the concave side is not so high, because of the presence of the "edges" vortices which maintain the Dean vortices away from the concave wall (see Figure 74). Nevertheless, the Dean vortices have a direct influence on the heat transfer at the lateral walls, more than in the two others turbulence models.

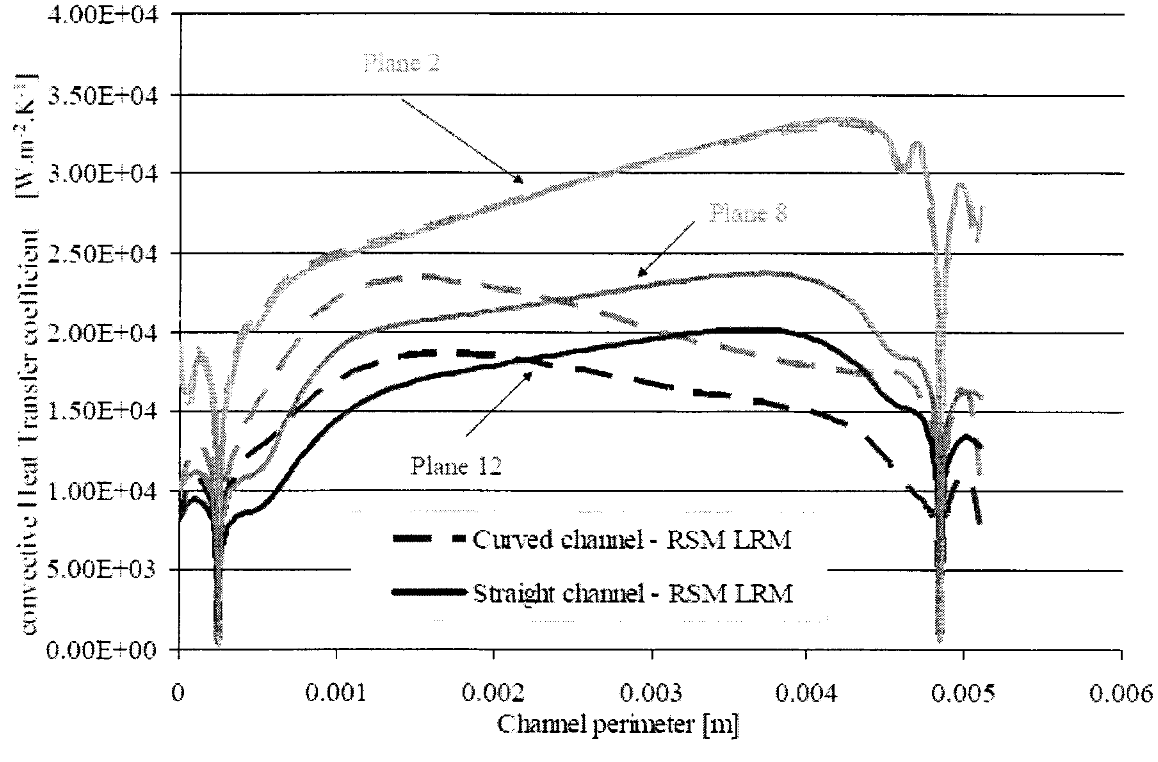

Figure 74 : Heat transfer coefficients along channel perimeter at different cross-sections of the curved and straight channels for the RSM-LRM turbulence models and for the hydrogen flow.

The local heat flux coefficient at the concave side (down side) and at the convex side (upper part of the channel) are averaged over the width of the channels at different cross-sections along the channels, for the straight and the curved channels. The curved to straight ratio of these averaged coefficients was calculated for all different turbulence models. This can be assimilated to a Nusselt number ratio, because of quite identical values of thermal conductivity and characteristic lengths for the straight and the curved channels. The profiles of these curved to straight heat transfer coefficient ratios are presented in Figure 75.

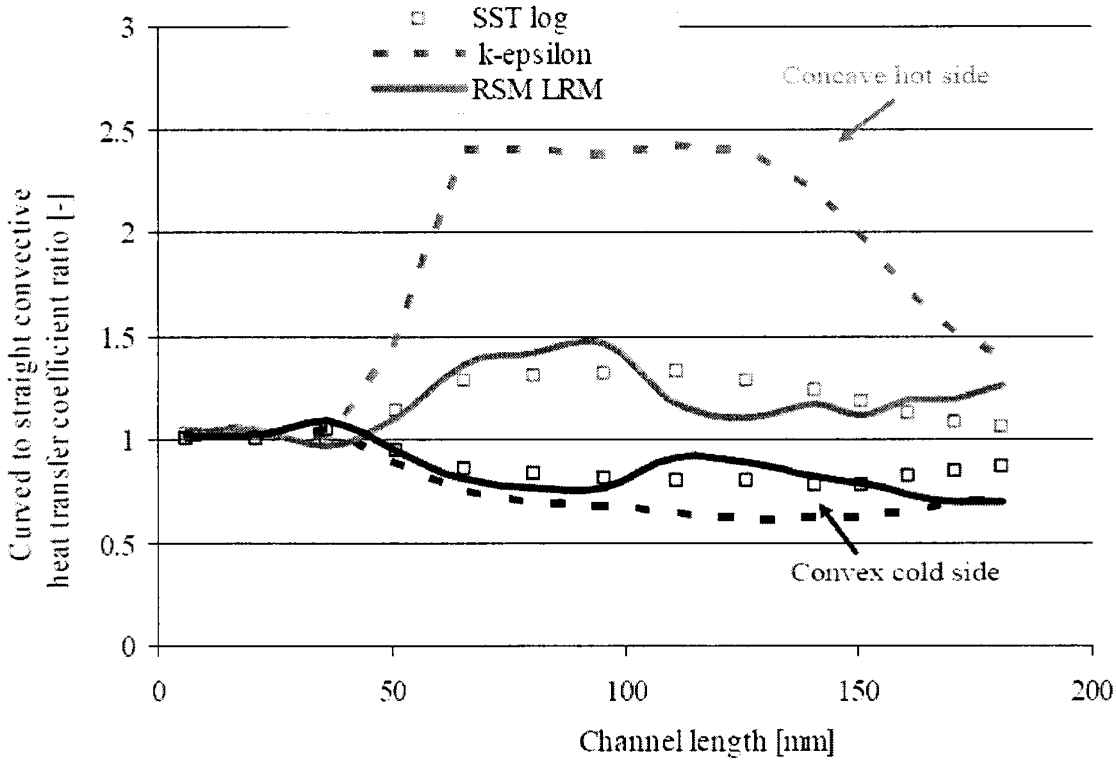

Figure 75 : Curved to straight heat transfer coefficient ratio along channel length from the numerical simulations with hydrogen.

As it has been previously remarked, the k-epsilon turbulence model with a logarithmic wall resolution presents a large increase of the Nusselt number at the concave side for the curved simulation. The local heat transfer increases by *2.4* times due to the Dean vortices with the k-epsilon model. The two other models are comparable and present a local increase of the heat transfer coefficient in the curvature up to *40%*. These results are only a local average of the heat transfer coefficient values on the concave and convex sides which represent less than 10% of the global heat exchange surface of the cooling channels (width of *0.5 mm* against *4.6 mm* height). The behaviour of the curved to straight coefficient heat transfer ratio for the RSM-LRM can be explained by the interaction of the Dean vortices and the "edges" vortices. At the beginning of the curvature, the Dean vortices seem to be preponderant in comparison to the "edges" vortices. In the middle of the curvature, the opposite phenomenon can be remarked which limits the heat transfer at the concave side.

- Temperatures

In each "experimental" point, where thermocouples are implemented, the temperature can be read from each numerical simulation. This gives a profile of temperature along the channel for *14* axial planes and for *6* different heights. The lowest and the hottest thermocouple data cannot be modelled, because its implementation is located in the block and only the channels are numerically modelled. Indeed, the temperatures that appear in Figure 76 and in Figure 77 are the simulated thermocouples data $T_{2,j} \rightarrow T_{7,j}$.

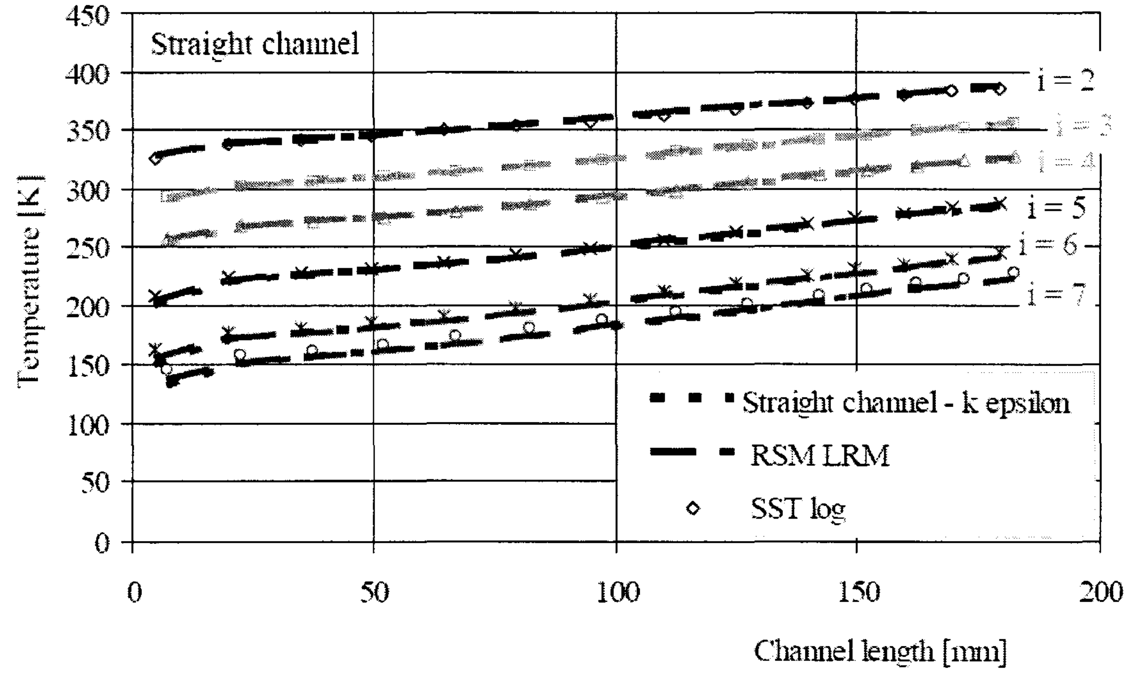

Figure 76 : Numerical simulation of the thermocouples data: temperature profile along the straight channel for all turbulence models.

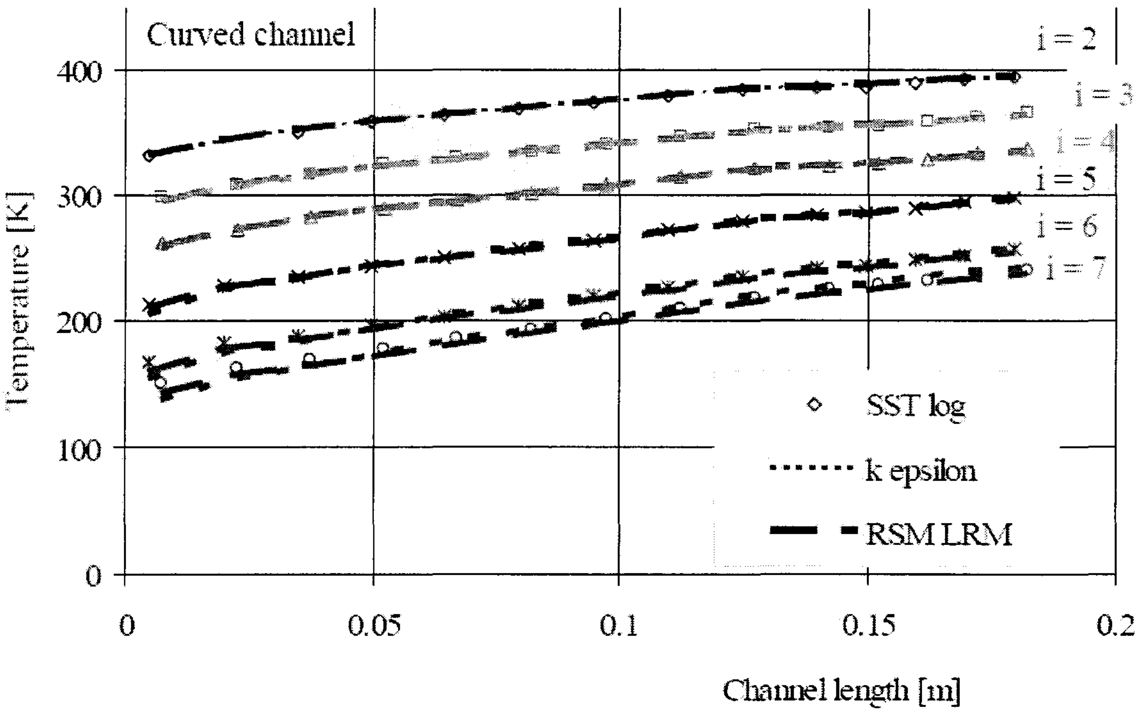

Figure 77 : Numerical simulation of the thermocouples data: temperature profile along the curved channel for all turbulence models.

The simulated temperatures at the thermocouples points show that neither the turbulence models nor the wall treatments have any influence on the results: all models render the same temperature profile in the channel walls. It means that the turbulence models can be differentiated at the fluid-solid interface but not in the temperature profile of the fin. Indeed, the thermal fin absorbs every heat flux sensibility from the fluid walls. The use of the inverse method can displace a temperature comparison to a heat flux coefficients comparison (see in 5.2).

4.2.4.2. Numerical simulations of methane tests

The curved and the straight channels were simulated with their blocks, using the SST model and the Mesh 1. The constant experimental temperature at the lowest block surface was used as heat source. The convective heat transfer coefficients along the channel periphery can be seen in Figure 78.

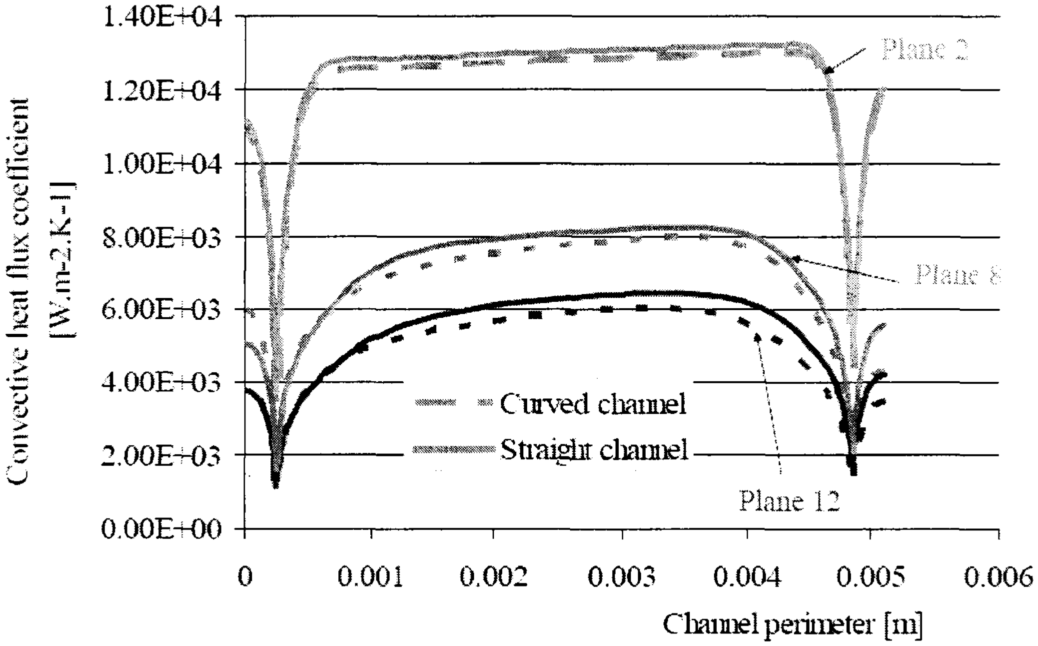

Figure 78 : Curved and straight heat transfer coefficient along channel perimeter at different abscissae and for the SST-log turbulence models, for the methane flow.

Inside a channel section (for example the plane *j=2*), the convective heat transfer coefficients are quite constant all over the perimeter of the channel. The heat transfer coefficient remains constant in the down side of the channel (hot side) and in the upper part of the channel (cold side).

The influence of the curvature at the concave side was numerically calculated. About *20%* heat coefficient increase was remarked.

4.3. Chapter conclusion

Numerical CFD investigations were performed in order to simulate the EH3C experiments. The EH3C numerical model was firstly tested in terms of robustness, of convergence and of sensibility as to different numerical parameters.

Concerning the logarithmic wall treatment, different meshes were investigated and the grid 5 with *2.5* millions nodes was selected to model the EH3C experiments. The numerical results converge quite rapidly (about *12* hours) with an eight computers cluster.

The Low-Reynolds number wall treatment requires a finer mesh (*4.5* Millions nodes) and a longer convergence time is thus needed (about *70* hours).

With a standard turbulence model (k-ε), different numerical parameters were studied in order to test their influence on the heat transfer in the curvature of the cooling channel. The roughness, the inlet turbulence conditions and the discretisation schema do not have any influence on the heat transfer.

Nevertheless, the model of the fluid and solid properties (heat capacity, density, thermal conductivity, etc.) play a major role in the determination of the heat transfer, up to *15%* deviation. Some real material and fluid properties were thus included in the numerical code. The choice of the turbulence model has the greatest influence on the heat transfer in the curvature. With the k-ε model a local heat transfer enhancement of up to *230%* is expected at the concave side. The RSM with a two layer wall treatment shows a limited influence of the Dean vortices on the concave heat transfer. It calculates the appearance of additional secondary vortices in edges of channels which push the Dean vortices away from the concave side.

At the channel walls, the turbulence models have a strong influence on the heat transfer. In the structure of the thermal fin, where the thermocouples are implemented, the temperature field is exactly the same for all turbulence models. Experimentally, it is thus impossible to directly select a turbulence model with the measured temperatures. An inverse method is needed to change the experimental data set from temperatures to heat transfer coefficients.

The curved and straight blocks were simulated with identical cooling channels, to differentiate the block's role and the fluid part. The curved block is responsible for about *6%* more heat flux and an increase of *11 K* at the channel-block interface, due to the larger block base in the curved test specimen.

Different boundary conditions were tested and more particularly the heating condition of the channel which is one of the key values of these numerical and experimental investigations. In one numerical case, a constant heat flux was applied to the lowest wall of the channel. A simulation of the channels with their block enlightened the fact that the right boundary condition at this wall is a temperature profile along the channel length. The simulations of channels with blocks in accordance with the EH3C experimental results determined the boundary condition temperature profile used to for the numerical simulation of the cooling channels.

5. Tests Results

Two campaigns were performed at the EH3C test bench under different experimental conditions to study the heat transfer in cooling channels. The first campaign focuses on pressure losses through non-heated channels. The second campaign uses the electrical heaters to provide an asymmetrical heat flux. The main particularity of this experiment is the high heat transfer density reached by means of electrical heating. Hydrogen and methane were tested in the straight and the curved channels in order to investigate the influence of curvature on the asymmetrical heating and on pressure drops.

To begin with, a steady flow is established in the cooling channels without heat flux. The pressure losses were measured at different mass flow rates for methane, hydrogen and water flows in the straight and curved channels.

In a second campaign, the blocks are heated and the temperature field of the channel wall is measured. For one test, the preparation needs about one week (mounting of the channel specimen, implementation of all sensors, leakage tests, check up of the test bench, sensors, electrical devices and of the measurement systems...). About another day is needed to perform a test, in cryogenic conditions (hydrogen configuration) and with heated blocks.

The experimental procedure of a test is described in Appendix 8.

5.1. Non-heated flow investigations

An experimental campaign was managed in order to characterise the pressure losses in the high aspect ratio channels for several configurations: hydrogen, methane and water as fluids, for both straight and curved channels. The inlet pressure remains constant for all tests: *40 bar* for the hydrogen and methane flows and *2 bar* for the water flow investigation. The blocks were not heated and all the test specimens are at the ambient temperature. The mass flow rate was changed and the corresponding pressure losses were measured by differential pressure sensors, located at the inlet and outlet of the EH3C test specimen. Empirical correlations from the paragraph 2.1.1 deliver friction factors which can be compared to the experimental data.

5.1.1. Water Investigation

Some particular tests have been provided in the laminar domain to validate the empirical correlation in this Reynolds number range. These investigations use the straight channel with incompressible fluid (water at *2 bar* and ambient temperature). The friction factor was thus calculated from the test results (pressure losses, mass flow rate, hydraulic diameter, length of the channel, density of water) and the results are illustrated in Figure 79.

$$\xi = \frac{(\Delta p)D_h}{\frac{1}{2}\rho w^2 l_{tot}} = \frac{2(\Delta p)\rho S^2 D_h}{\dot{m}^2 l_{tot}} \tag{5.1}$$

With the aid of corresponding measurement accuracies of experimental data (mass flow rate, pressure losses), the measurement error according to the friction coefficient can be evaluated : *+/- 3%.*

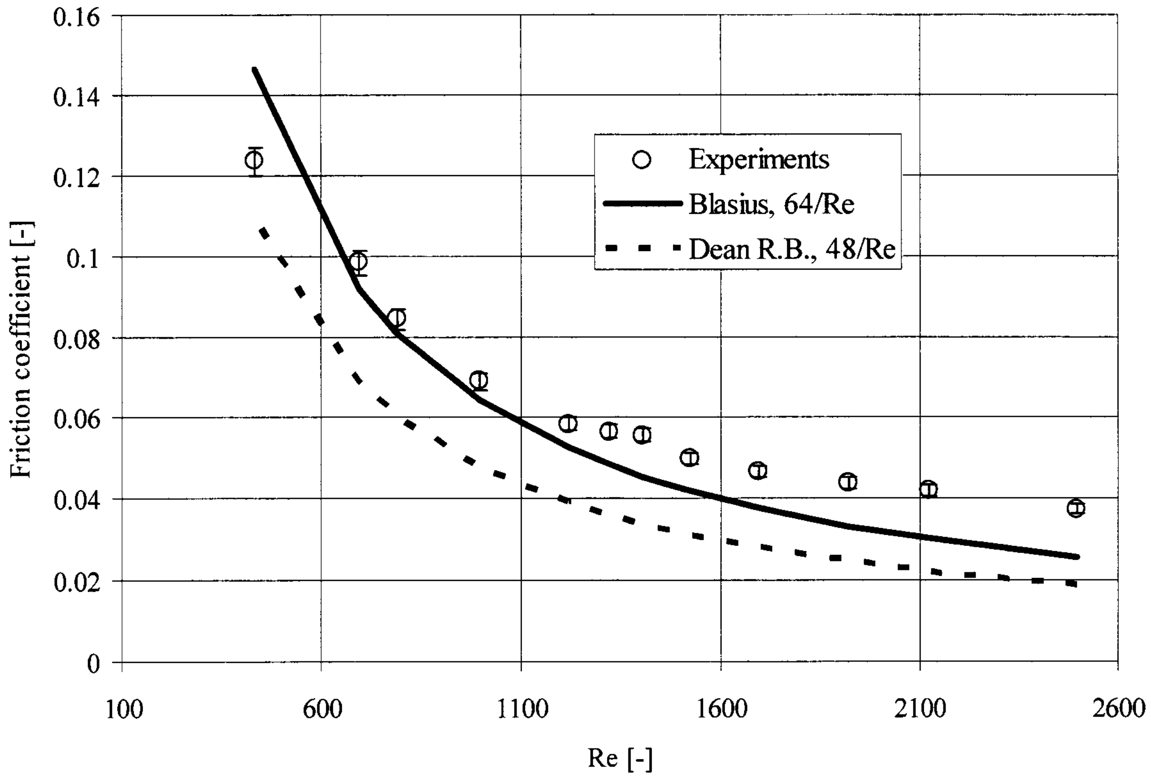

Figure 79 : Friction coefficient along the straight channel for laminar flow of incompressible fluid (water).

Theory (Blasius) and an empirical correlation (Dean R. B.) were compared to the experimental set of laminar flow (up to a Reynolds number of 2400), see in 2.1.1. The experimental results partially confirm the theory (Blasius relation). A higher experimental friction coefficient appears for higher Reynolds numbers. This can be explained by the transition between laminar and turbulent flow, where a higher friction coefficient appears. Because of unconventional channels (micro dimension, rectangular, high aspect ratio), the classic transition value of *2400* can be shifted to lower Reynolds number range, as it appears in these experimental results. Nevertheless, the experimental data do corroborate the theory: $\xi = 64 \times \mathrm{Re}^{-1}$ and not the empirical correlation of R. B. Dean who developed the model for laminar flows in rectangular channels with high aspect ratio.

5.1.2. Hydrogen Investigation

The non-heated tests were performed in both channels with hydrogen below 40 bar at the inlet of the channels. Different mass flow rates were tested, in the subsonic domain. As a theoretical reference, the Fanno flow model was used with the friction coefficients from different empirical correlations. Thus, the inlet and outlet static pressure ratio is compared to the experiments which are presented in Figure 80.

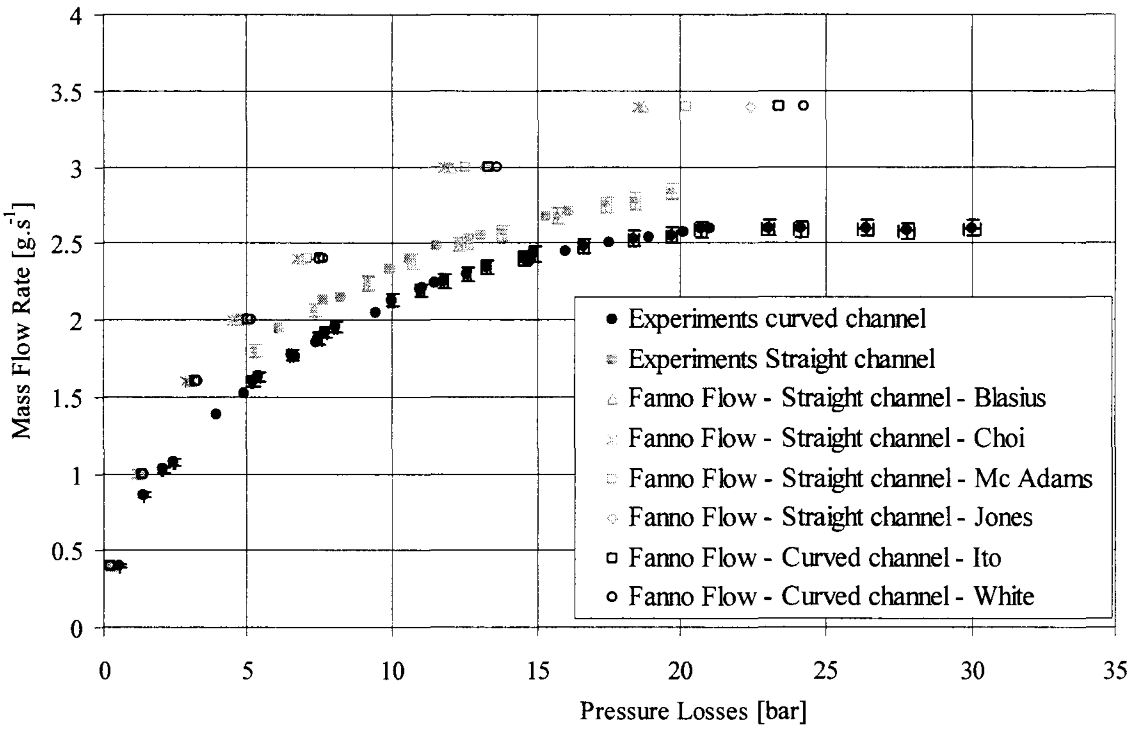

Figure 80 : Experimental and Fanno flow model pressure losses with hydrogen flow in the non-heated straight and the curved channels.

The Table 9 resumes the empirical correlations used in these investigations (see in 2.1.1):

[Blasius, 1911]	[Choi, 1991]	[Mc Adams, 1932]	[Jones, 1976]
$\xi = 0.3164 \times \mathrm{Re}^{-0.25}$	$\xi = 0.14 \times \mathrm{Re}^{-0.182}$	$\xi = 0.0056 + \dfrac{0.5}{\mathrm{Re}^{0.32}}$	$\xi = 0.3164 \times \mathrm{Re}^{*-0.25}$
[Ito, 1959]	[White, 1929]		
$\dfrac{\xi_c}{\xi_s} = \left[\mathrm{Re} \cdot \kappa^2\right]^{1/20}$	$\dfrac{\xi_c}{\xi_s} = 1 + 0.075 \times \left[\mathrm{Re} \cdot \kappa^2\right]^{0.25}$		

Table 9 : Empirical correlations of straight and curved friction coefficients.

The curved channel pressure loss is higher for a given mass flow rate than the straight pressure loss, shown by the Fanno flow model and the experiments. The empirical correlations corroborate this pressure loss increase in the curved case, due to the secondary motions (Dean vortices). Nevertheless, all empirical correlations underestimate the pressure losses along the channel. This certainly comes from the manifolds at the inlet and the outlet of the channels (convergent and divergent parts before and after the channels). For technical reasons (difficult access to the micro channel), the pressure sensors are unfortunately located outside of the manifolds and take into account the pressure loss through the convergent and the divergent parts. An estimation of these additional pressure losses can be investigated, in reference to abrupt pressure losses ([Idelchik, 2005, VDI, 1997]). The operating point with $\dot{m} = 2.5 \mathrm{g\,s}^{-1}$ was selected to investigate the additional pressure losses due to the inlet and outlet manifolds. The density of hydrogen is supposed to be constant at the inlet manifold $\rho_{in} = 3.27\,\mathrm{kg\,m^{-3}}$ and at the outlet manifold $\rho_{out} = 2.22\,\mathrm{kg\,m^{-3}}$ with the aid of NIST data base, [NIST, 2005]. Considering the worst case (abrupt change of pipe diameter), the maximal abrupt friction coefficient was estimated ([Idelchik, 2005, VDI, 1997]):

$$\Delta p_{ABRUPT}\big|_{in} = 0.4\frac{\rho_{in} w_{in}^{\ 2}}{2} = 0.7\times10^5\ \mathrm{Pa} \tag{5.2}$$

$$\Delta p_{ABRUPT}\big|_{out} = 0.44\frac{\rho_{out} w_{out}^{\ 2}}{2} = 1.2\times10^5\ \mathrm{Pa} \tag{5.3}$$

These additional pressure losses reach 2 bar in the worst case. This is not enough to explain the difference between the measured and the calculated pressure losses. Nevertheless, the curved to straight pressure losses ratio can be extracted from theory and from experiments to evaluate the curvature influence on pressure drops.

5.1.3. Methane Investigation

The same experiments were performed with methane at ambient temperature. The mass flow rate was changed and the corresponding pressure losses were registered, (see Figure 81).

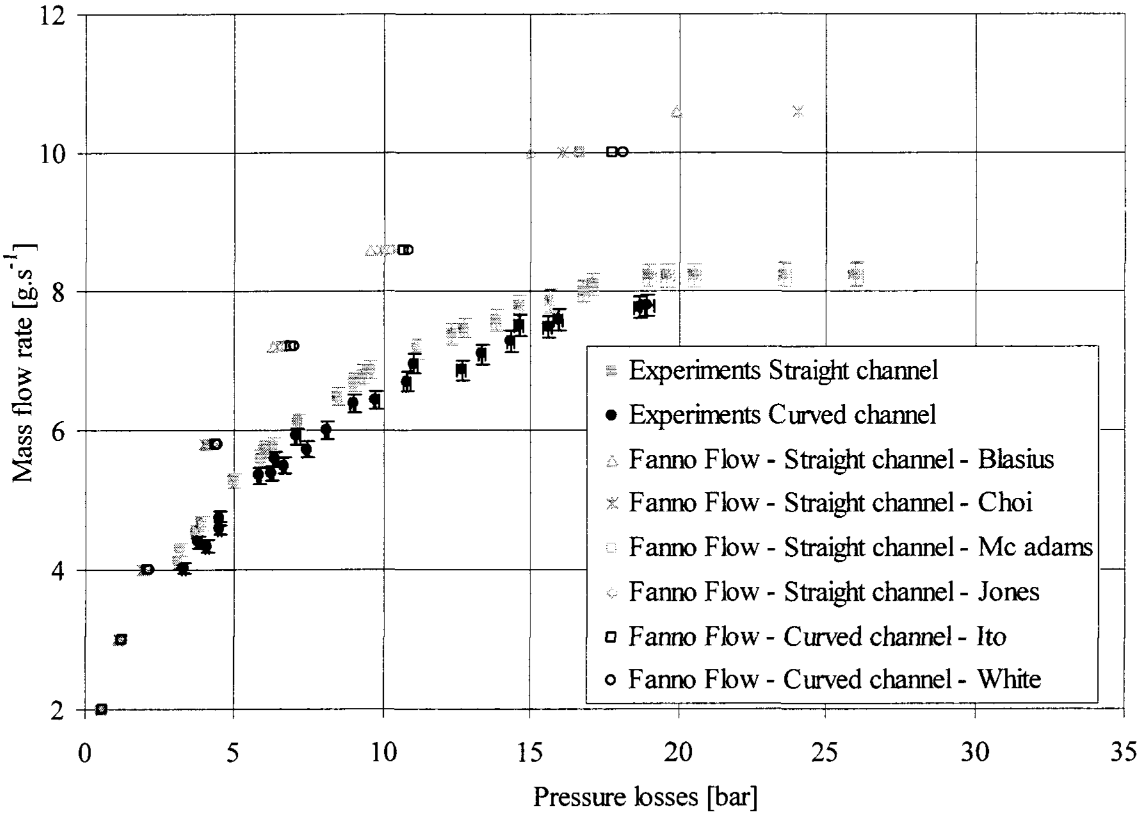

Figure 81 : Experimental and Fanno flow model Pressure losses with methane flow in the non-heated straight and in the curved channels.

The same conclusions as for the hydrogen investigations can be presented. The pressure losses in the curved channel are higher than in the straight channel for the experiments and the Fanno flow models. The manifold pressure losses are not taken into account in the empirical correlations which can explain the underestimation of the pressure losses with the empirical correlations.

The estimation of these additional pressure losses was made (refer to 5.1.2), with a mass flow rate $\dot{m} = 8\,\mathrm{g\,s^{-1}}$, an inlet constant density $\rho_{in} = 28.7\,\mathrm{kg\,m^{-3}}$ and an outlet constant density $\rho_{out} = 16.0\,\mathrm{kg\,m^{-3}}$:

$$\Delta p_{ABRUPT}\big|_{in} = 0.4\frac{\rho_{in} w_{in}^{2}}{2} = 0.8\times10^{5}\ \mathrm{Pa}$$

$$\Delta p_{ABRUPT}\big|_{out} = 0.44\frac{\rho_{out} w_{out}^{2}}{2} = 1.65\times10^{5}\ \mathrm{Pa}$$

To directly compare the influence of the curvature, the curved to straight pressure losses ratio was investigated. The calculation of this ratio only enlightens the curvature influence, because the manifold pressure losses are the same for the straight and the curved flows.

5.1.4. Curved to straight pressure losses ratio for non heated cases

The acceleration of the fluid along the channel does not have a strong influence on the total temperature of the fluid (about *5 K* less measured at the outlet of the channel). The viscosity being constant (quasi isothermal flow), the Reynolds number is constant along the channel with constant mass flow rate. For a fixed experimental mass flow, the pressure losses in the straight and the curved channels were compared, and this curved to straight ratio is illustrated with the corresponding Reynolds number. The same curved to straight ratio was deduced from the Fanno flow models. Concerning the empirical results, some empirical correlations to determine the friction factor in curved channel (presented in the part 2.1.1) need a "straight" correlation as reference. This is the case of the empirical correlation of White, and the classic correlation of Blasius was taken as reference to define the friction factor of White in curved channels.

In this case, all combinations are possible to define a curved to straight pressure losses ratio. The highest and the lowest combinations were chosen: The association of the White's empirical model (curved channel) with Jones' empirical correlation (straight channel) delivers the lowest results (less than *5%* influence of the curvature in terms of pressure loss). On the other hand, the combination of the empirical correlation of White (curved channel pressure loss) and Blasius (straight) gives pressure loss increase up to *30%*. All experimental points are located between *20%* increase for relatively low Reynolds numbers and up to *50%* near the sonic blockage (i.e. the highest Reynolds number that can be achieved). The experimental manifolds' effects are contained in the two pressure loss measurements (straight and curved) which implies that the curved to straight ratio merely indicates the influence of the curvature on the pressure loss. All empirical correlations underestimate the influence of the curvature on pressure losses (see Figure 82 for the hydrogen investigation and Figure 83 for the methane one).

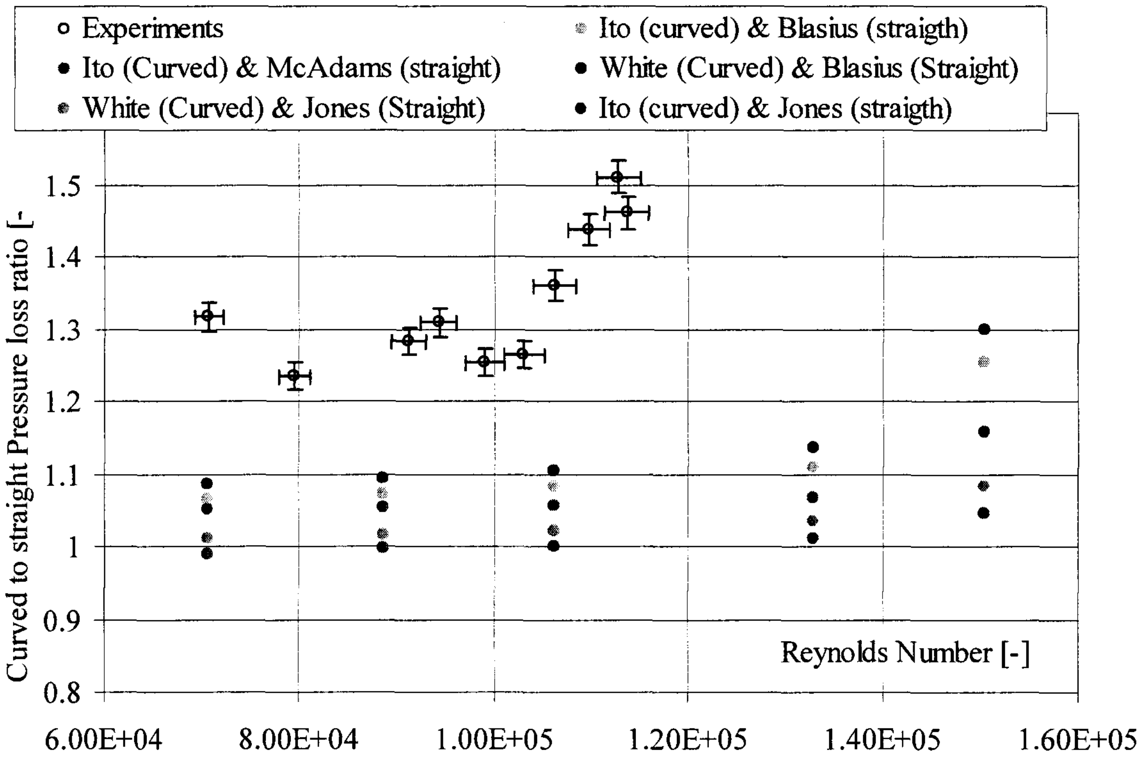

Figure 82 : Curved to Straight Pressure losses ratio for hydrogen flow for non-heated channels.

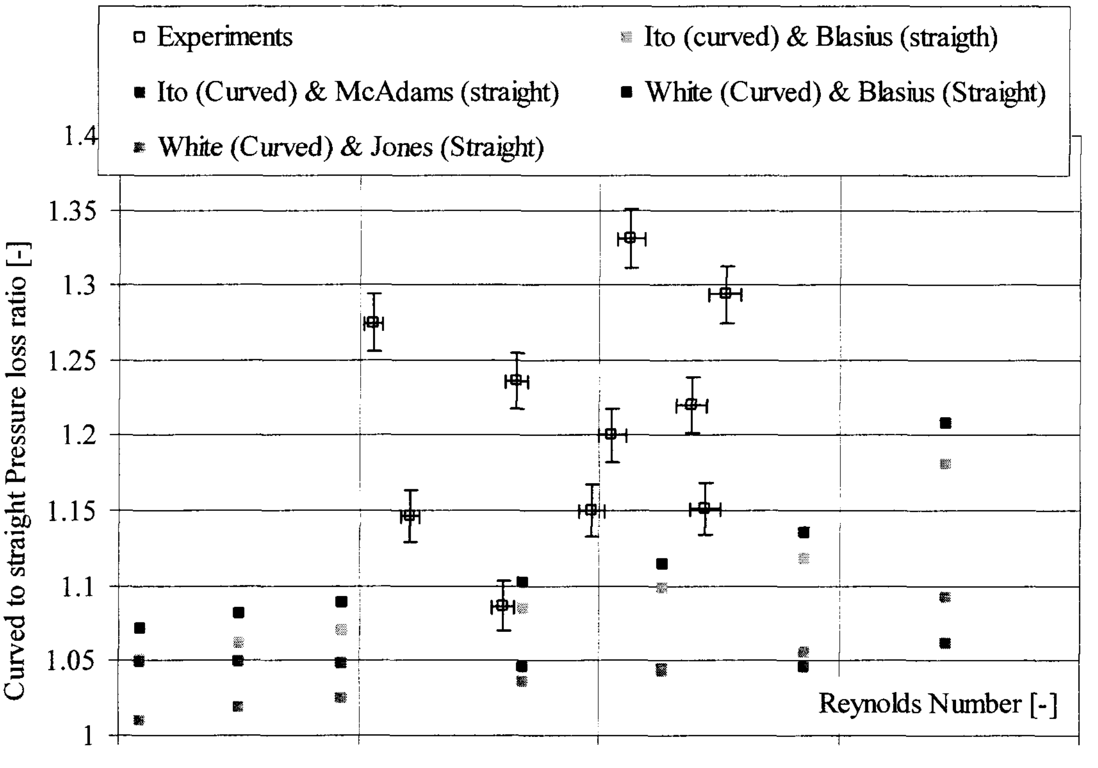

Figure 83 : Curved to Straight Pressure losses ratio for methane flow for non-heated channels.

Both methane investigations (experimental and from empirical correlations) indicate that the curvature has a restricted influence on the pressure losses in comparison to the hydrogen case. Nevertheless, the experimental data (*15%* up to *30%* increase) are all above the empirical correlations' predictions (*6%* up to *20%* increase).

5.2. Campaign with "heating"

5.2.1. Experimental conditions

The experimental conditions with heating are described in Table 10. This concerns the inlet and outlet pressures and temperatures, as well as the mass flow rates for both channel configurations and both coolants.

An evaluation of the characteristic numbers can be made at the inlet of the channels (Table 10), taking into account the fluid properties at the inlet of the channels (see Appendix 9).

Medium	Channel	Heating temp. of the block	T inlet	T outlet	P inlet	P outlet	Pressure difference	Mass flow rate
		[K]	[K]	[K]	[bar]	[bar]	[bar]	[g.s^{-1}]
H_2	Straight	*643*	*78*	*231*	*37.4*	*26*	*12.4*	*3.305*
H_2	Curve	*649*	*78*	*238*	*38*	*19.5*	*17.5*	*3.319*
CH_4	Straight	*465*	*296*	*373*	*37*	*23*	*14*	*6.999*
CH_4	Curve	*465*	*285*	*366*	*36.4*	*17.9*	*18.6*	*7.102*

Table 10 : Description of the campaign with "heating".

	$\mathrm{Re} = \dfrac{\dot{m} D_h}{S_c \mu_1}$	$\mathrm{Pr} = \dfrac{\mu Cp}{\lambda}$	$De = \mathrm{Re}\sqrt{\kappa}$
H_2	3.32×10^5	0.746	2.23×10^4
CH_4	2.33×10^5	0.791	1.56×10^4

Table 11 : Characteristic experimental numbers of the "heating" campaign.

5.2.2. Pressure losses investigation

The experimental pressure losses of the different tests of the "heating" campaign (see Table 10) have been compared to the numerical simulations, where the pressure losses data are summarised in Table 12. The numerical simulations took into account the inlet manifold, considered as adiabatic with the environment.

The comparison with experiments is presented in Figure 84. All numerical simulations underestimate the real pressure losses through the asymmetrical heated channels, in all configurations (straight or curved, hydrogen or methane).

The pressure losses difference between experiments and numerical simulations can have the following explanation: the heat exchange of the fluid is higher than expected in the inlet manifold. That brings additional pressure losses in comparison to the numerical results and additional thermal stratification in the fluid, as well as a global temperature shifting, as it will be seen in the paragraph 5.2.4.

		CFD SST Log					
Medium	Channel	P inlet	P outlet	DP			
		[bar]	[bar]	[bar]			
H2	Straight	*36.5*	*25.6*	*10.9*			
H2	Curve	*34.1*	*20.3*	*13.8*			
CH4	Straight	*36.6*	*23*	*13.6*			
CH4	Curve	*34.5*	*17.9*	*16.6*			
		CFD RSM LRM			CFD k epsilon		
		P inlet	P outlet	DP	P inlet	P outlet	DP
		[bar]	[bar]	[bar]	[bar]	[bar]	[bar]
H2	Straight	*36.9*	*25.6*	*11.3*	*36.7*	*25.6*	*11.1*
H2	Curve	*34.5*	*20.3*	*14.2*	*34.5*	*20.3*	*14.2*

Table 12 : Pressure losses from numerical simulations for the heated methane and hydrogen flows for different turbulence models.

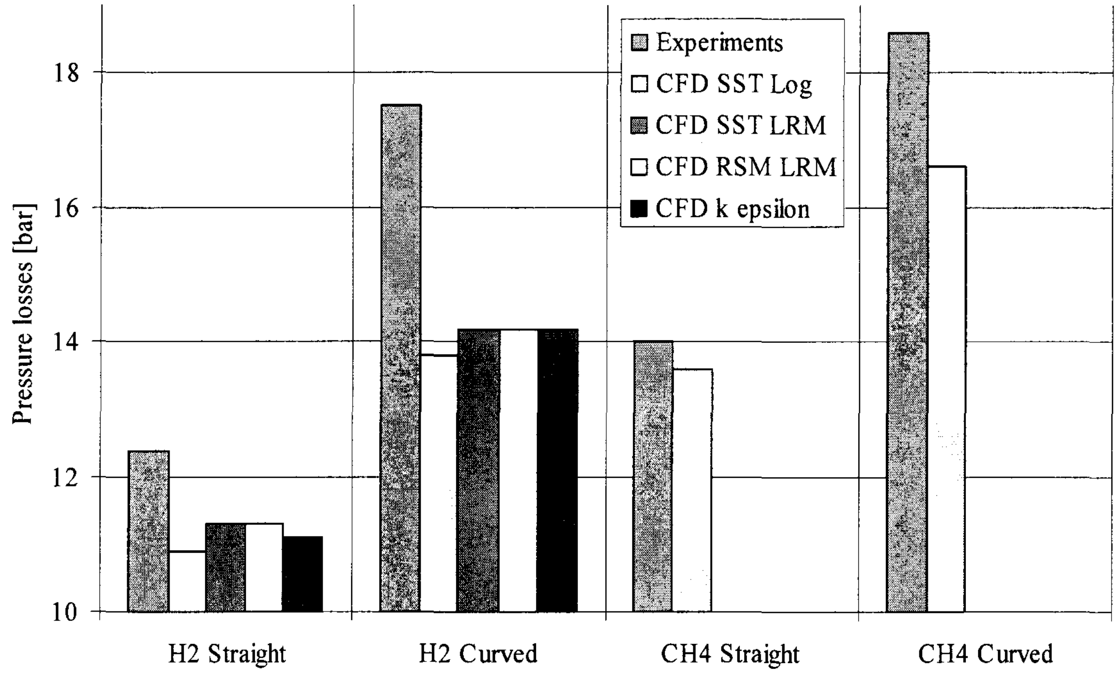

Figure 84 : Pressure losses of experiments and numerical simulations of the heated channels with methane and hydrogen flows.

To enlighten the curvature effect, we can calculate the curved to straight pressure losses, $\frac{\Delta p_c}{\Delta p_s}$ in the case of heated channels. The heating through the inlet and outlet manifolds brings about additional pressure losses, noted Δp_{mani} which are supposed to be equal in both configurations. The measured pressure losses are equal to:

$$\Delta p_{meas} = \Delta p + \Delta p_{mani} \tag{5.4}$$

The measured curved to straight ratio is thus defined by:

$$\frac{\Delta p_c}{\Delta p_s} = \frac{\Delta p_{c,meas} - \Delta p_{mani}}{\Delta p_{s,meas} - \Delta p_{mani}} = \frac{\Delta p_{c,meas}}{\Delta p_{s,meas}} \underbrace{\left(\frac{1 - \frac{\Delta p_{mani}}{\Delta p_{c,meas}}}{1 - \frac{\Delta p_{mani}}{\Delta p_{s,meas}}} \right)}_{\Delta_{mani}} \tag{5.5}$$

The coefficient Δ_{mani} was evaluated with the results of the numerical simulations, where the inlet and outlet manifolds are considered as adiabatic. In the experimental tests, the manifolds are not fully adiabatic, as it will be shown in the paragraph 5.2.2.

$$\Delta_{mani} = \frac{1 - \frac{1}{12}}{1 - \frac{1}{17}} = \frac{0.9167}{0.9412} = 0.974 \tag{5.6}$$

Δ_{mani} being close to 1, the measured curved to straight ratio can be assimilated to the curvature effect. The curved to straight ratios of pressure losses are illustrated in Figure 85.

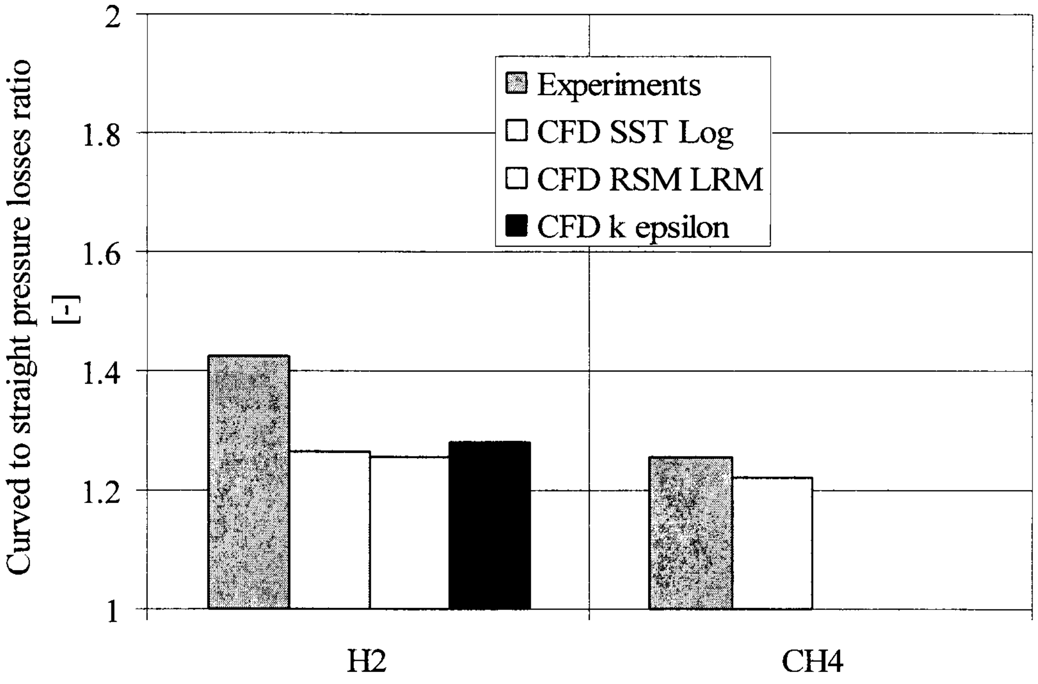

Figure 85 : Curved to straight pressure losses from experiments and numerical simulations of heated channels.

This configuration of heated channels confirms the results of the preceding study of the non heated tests. Indeed, the curved to straight ratio of pressure losses is still higher for the hydrogen configuration than for the methane flow. But both heated cases confirm the same influence of the curvature with or without heating. The experimental curved to straight pressure losses ratio reaches *40%* for the experimentally heated and cryogenic hydrogen flow (up to *50%* for the non-heated tests). For the methane case, the experimental ratio reaches *30%* for the non-heated as well as the heated case. The numerical simulations of the heated methane and hydrogen flows corroborate the empirical correlations: *28%* increase due to the curvature in the heated hydrogen case (numerical simulation) against up to *30%* for the hydrogen test at ambient temperature from the Fanno flow model. For the methane investigation, the numerical simulation of the heated flow renders an increase of *23%* for the heated case and up to *20%* for the non heated case. The asymmetrical heating does not have any influence on the role of the curvature in term of pressure losses. Of course, the heating of the fluid brings additional pressure losses in a channel (about *40%* more by $17\ MW.m^{-2}$) but the curvature effects on the pressure losses are quite the same, with or without extern heat input (heated case or not) .

5.2.3. Calorimetrical heat transfer investigation

5.2.3.1. Experimental results

For each test configuration, a calorimetric analysis is made: the temperature increase of the fluid along the cooling channel is directly measured, as well as the mass flow. With an accurate estimation of the heat capacity at the inlet of the fluid, a first evaluation of the heat absorbed by the fluid along the channel can be calculated.

$$\dot{Q}_{calo} = \dot{m}\, c_p \left(T_{outlet} - T_{inlet}\right) \tag{5.7}$$

The calorimetric method was applied to the straight and curved configurations and for both coolants. The results can be observed in Figure 86 and Figure 87.

For both fluid configurations, a global heat increase can be observed for the curved configuration. *4.4%* more heat flux was calculated from measurements for the curved hydrogen case and *7%* correspond to the methane case. This heat increase can be explained by different reasons.

Firstly, the presence of Dean vortices introduces a modification of the thermal stratification, with an increase of the heat transfer at the concave side and a probable decrease at the convex side. Globally, more than *60%* of the heat transfer is located at the concave side. This heat flux distribution induces a higher global heat transfer in comparison to the straight channel case.

On the other hand, the block geometry constitutes a larger base for the curved channel which can dissipate more thermal energy. The block is maintained at constant temperature for the straight and the curved channels. The heated surface is *1.6* larger for the curved block and through a longitudinal surface reduction, the heat flux density can be different in the curvature at the channel location. Numerical simulations were managed in order to identify the role of the curved block geometry on the channel heat transfer increase (see the part 4.2). From numerical simulation (see in 4.2.3), the expected role of the curved block is about an increase of *6%*.

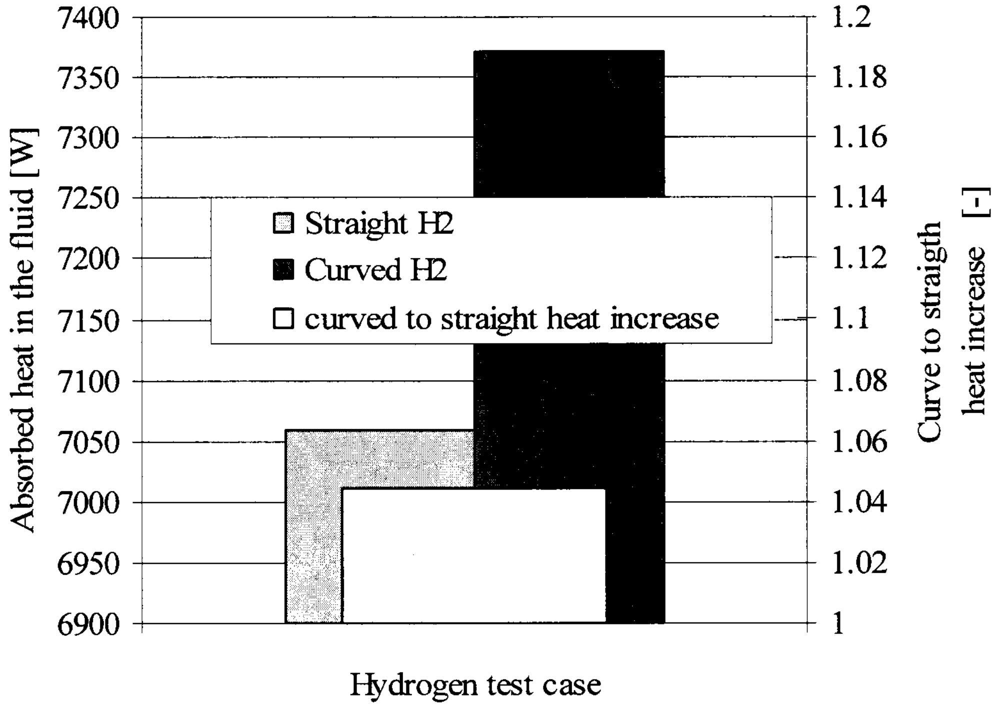

Figure 86 : Absorbed heat for the hydrogen flow by calorimetric method.

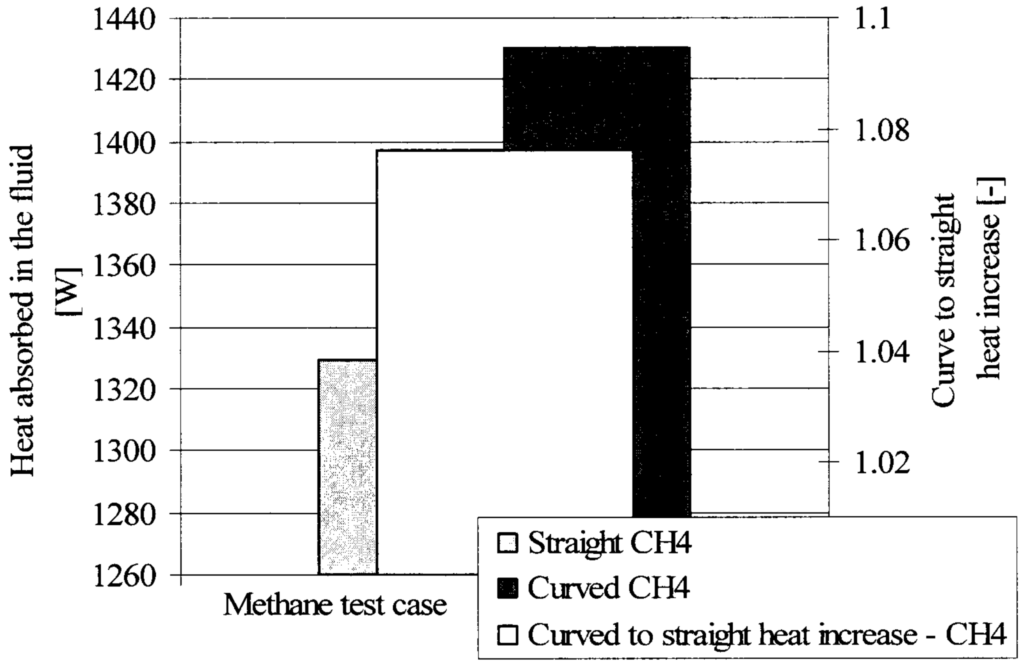

Figure 87 : Absorbed heat for the method flow by calorimetric method.

5.2.3.2. *Comparison with numerical simulations*

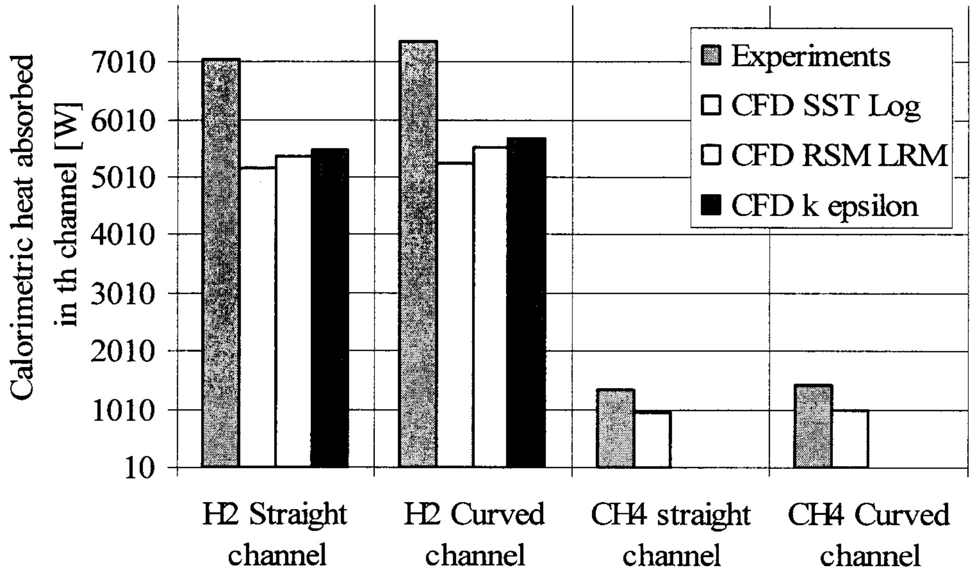

Figure 88 : Measured and simulated absorbed heat flux from calorimetrical method.

The numerical simulations and the special calculation of the absorbed heat have already been presented in paragraph 4.2.4.1.

The numerical simulations underestimate the global heat flux absorbed by the fluid by about *30%*.

The pre-heating of the manifold is the main reason that could explain this difference between experimental results and numerical simulations. The fluid temperature is higher in the experiments than in the CFD, as it will be shown in paragraph 5.2.4.2.

Moreover, the experimental outlet temperatures are all higher than the averaged temperatures calculated from the numerical simulations. In reality, the outlet convergent mixes the fluid more than expected and the thermocouples in the fluid measures a higher mixing temperature.

To enlighten the curvature influence and to neglect the influence of the manifolds, it is necessary to evaluate the coefficient $\Delta_{\Phi mani}$ as it has already been done for the pressure loss investigations (see in the paragraph 5.2.2):

$$\frac{\Phi_c}{\Phi_s} = \frac{\Phi_{c,meas} - \Phi_{mani}}{\Phi_{s,meas} - \Phi_{mani}} = \frac{\Phi_{c,meas}}{\Phi_{s,meas}} \underbrace{\left(\frac{1-\frac{\Phi_{mani}}{\Phi_{c,meas}}}{1-\frac{\Phi_{mani}}{\Phi_{s,meas}}} \right)}_{\Delta_{\Phi mani}} \tag{5.8}$$

where Φ is the heat flux absorbed by the channels. It comes:

$$\Delta_{\Phi mani} = \frac{1-\frac{1900}{7365}}{1-\frac{1900}{7060}} = \frac{0.742}{0.731} = 1.015 \tag{5.9}$$

The coefficient $\Delta_{\Phi mani}$ is close to 1, it is thus possible to dissociate the measured curved to straight heat flux ratio to the manifold heat fluxes.

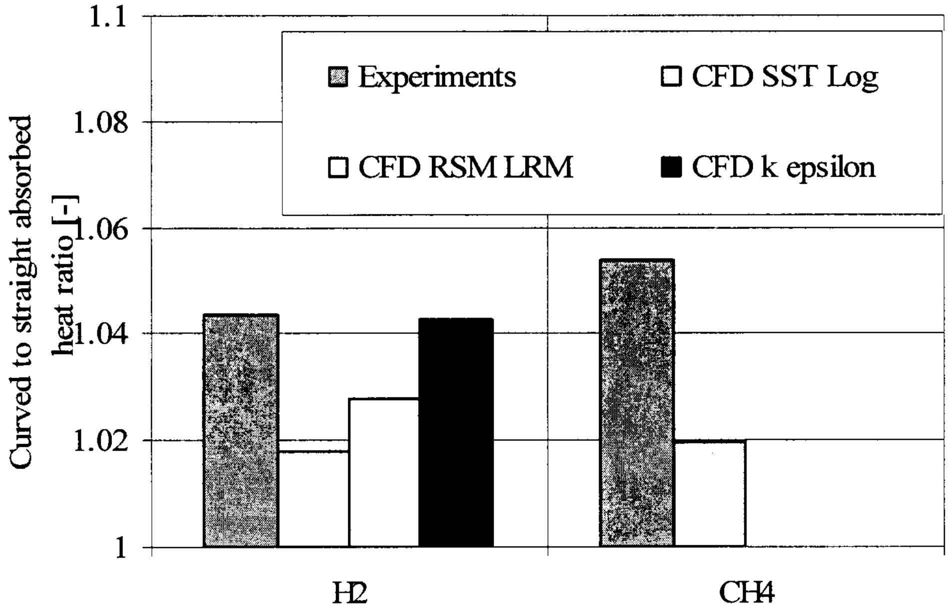

Figure 89 : Curved to straight absorbed heat flux ratio.

The experimental heat flux increase in the curved channel is about *4.5%* for the hydrogen test and *5.5%* for the methane test. This heat increase is mainly due to the geometry of the curved block (*6%* increase expected). The Dean vortices do not have an influence on the global heat transfer absorbed by the fluid in this experimental configuration.

Nevertheless, the k-epsilon model seems to be the most accurate model to describe the heat transfer ratio, in terms of global absorbed heat ratio. Locally, this tendency must be checked because it has already been shown that the local heat flux increase at the concave side seems to be really overestimated with the k-epsilon model, in comparison to all other models and the empirical correlations. This local investigation is feasible via data analysis of the measured temperatures and the use of the inverse method.

5.2.4. Thermal investigations into the hydrogen test case

5.2.4.1. Temperature measurements

The test case of hydrogen investigation is presented in this paragraph with all thermocouple data along the channel wall. For these experimental results, all components of the measurement errors were calculated for each thermocouple (see in the paragraph 3.2.4) and have been implemented in the graphic of the experimental temperature data (see Figure 93).

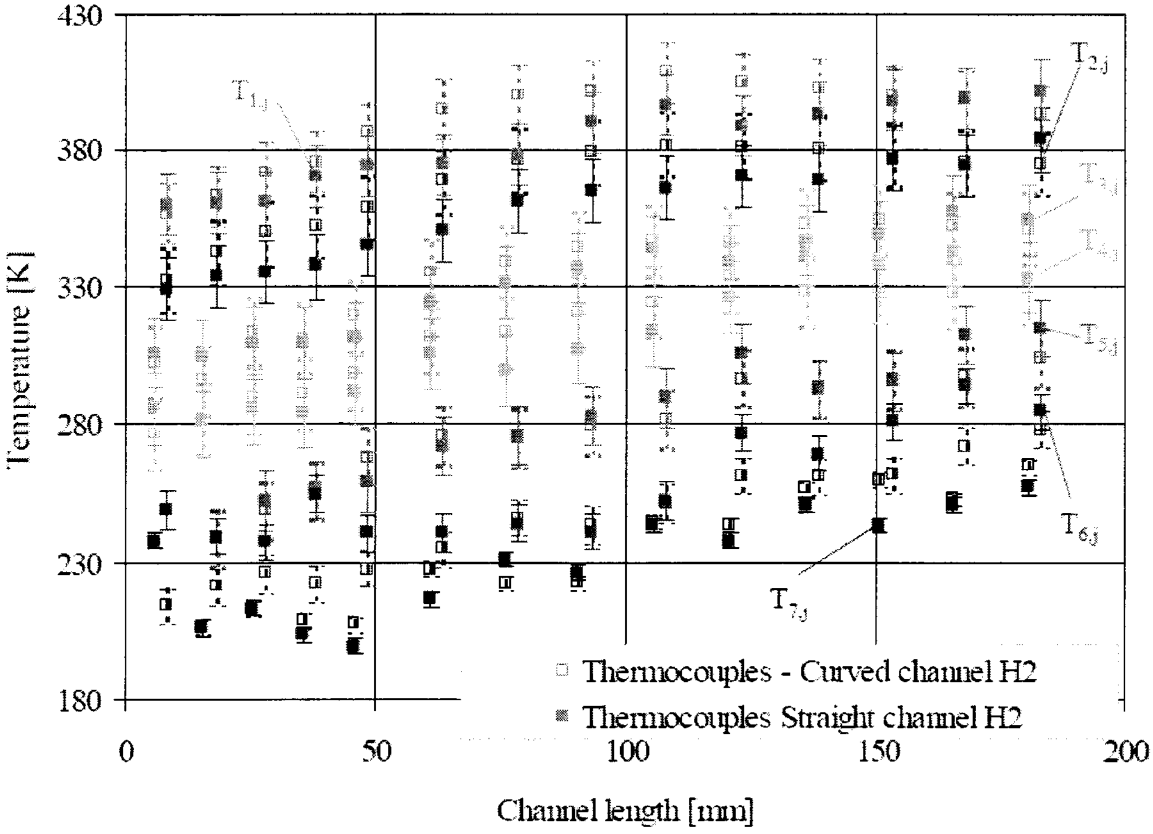

Figure 90 : Experimental temperatures data along the straight and the curved channels for hydrogen tests with uncertainty calculation.

The thermal stratification along the channel height and along the channel length is respected. More than *150 K* difference is experimentally measured between the highest temperature ($T_{1,5}=375K$ for example) and the thermocouple with the highest emplacement ($T_{7,5}=200K$).

Another possibility to present the experimental results is to collect the measured temperatures for a precise cross section of the cooling channel along the channel height (axe y). Figure 91 presents the measured data of the straight and the curved channels at the longitudinal cross section $j=3$ (before the curvature), $j=7$ (in the curvature) and $j=12$ (after the curvature).

The cooling channel is positioned at the height $y=0$. A small influence of the curvature can be remarked for the cross section $j=7$ in the curvature, where the measured data of the curved channel are higher than for the straight configuration. The interpretation will be given in the following paragraph 5.2.4.2.

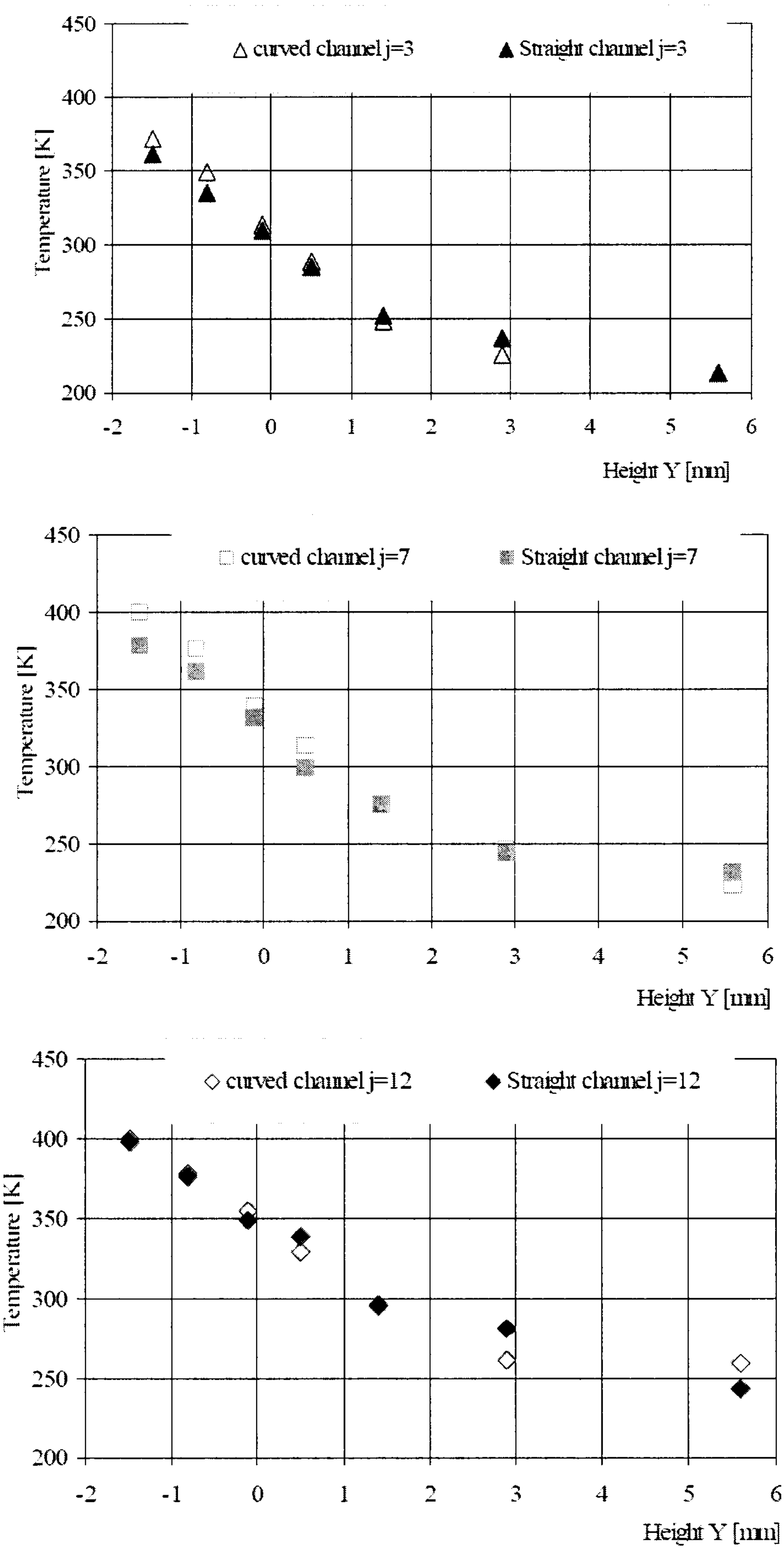

Figure 91 : Measured temperatures at the cross sections *j=3;7;12* for hydrogen tests.

A repeatability campaign was managed in order to validate the experimental data. Two experimental analyses were made at two different days, with the same soft- and hard-ware. The repeatability tests are presented in Figure 92.

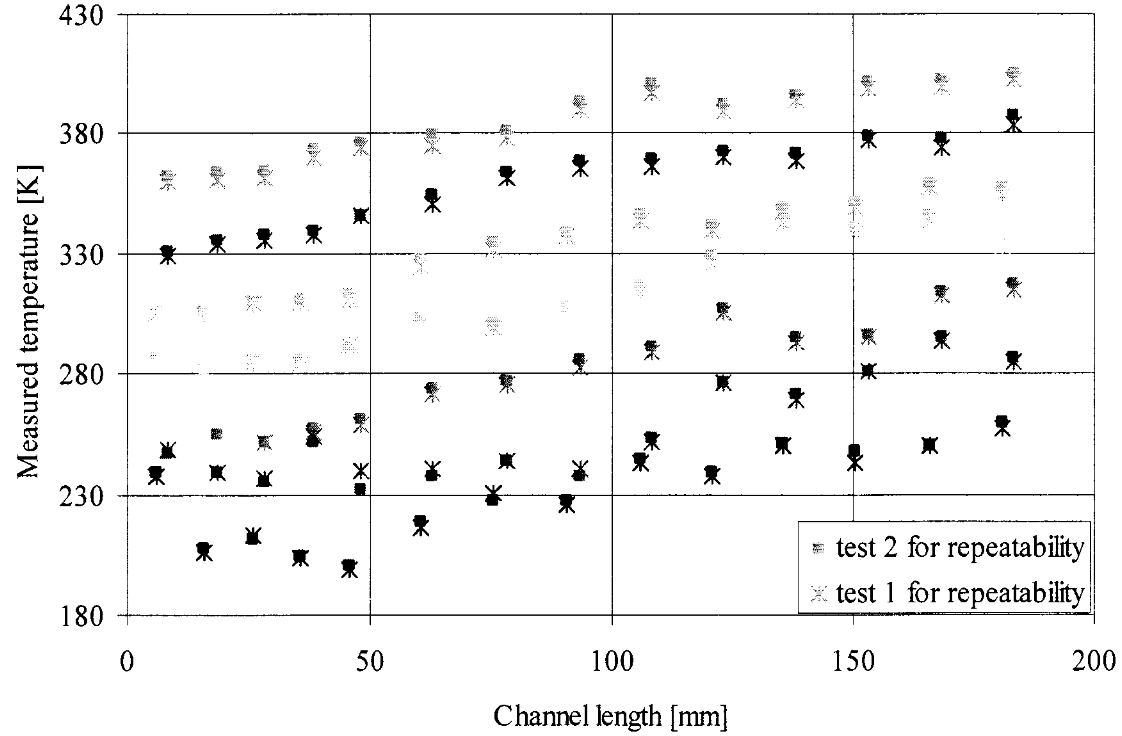

Figure 92 : Repeatability tests with cryogenic hydrogen flowing through an EH3C test specimen.

97 thermocouples provide the same temperature for both tests with +/-1K accuracy. Only 1 thermocouple deviates *7K* between the two tests. A bad implementation of the thermocouple $T_{6,5}$ was the origin of this temperature deviation. It was corrected for the data analysis.

5.2.4.2. Comparison of temperatures with numerical simulations

Only one turbulence model is used in the comparison with the experiments, because all models converge on the same temperature values where the sensors are located, as it can be seen in paragraph 4.2. The first line of thermocouples $T_{1,j}$ were not numerically simulated because their positions are outside of the meshed domain.

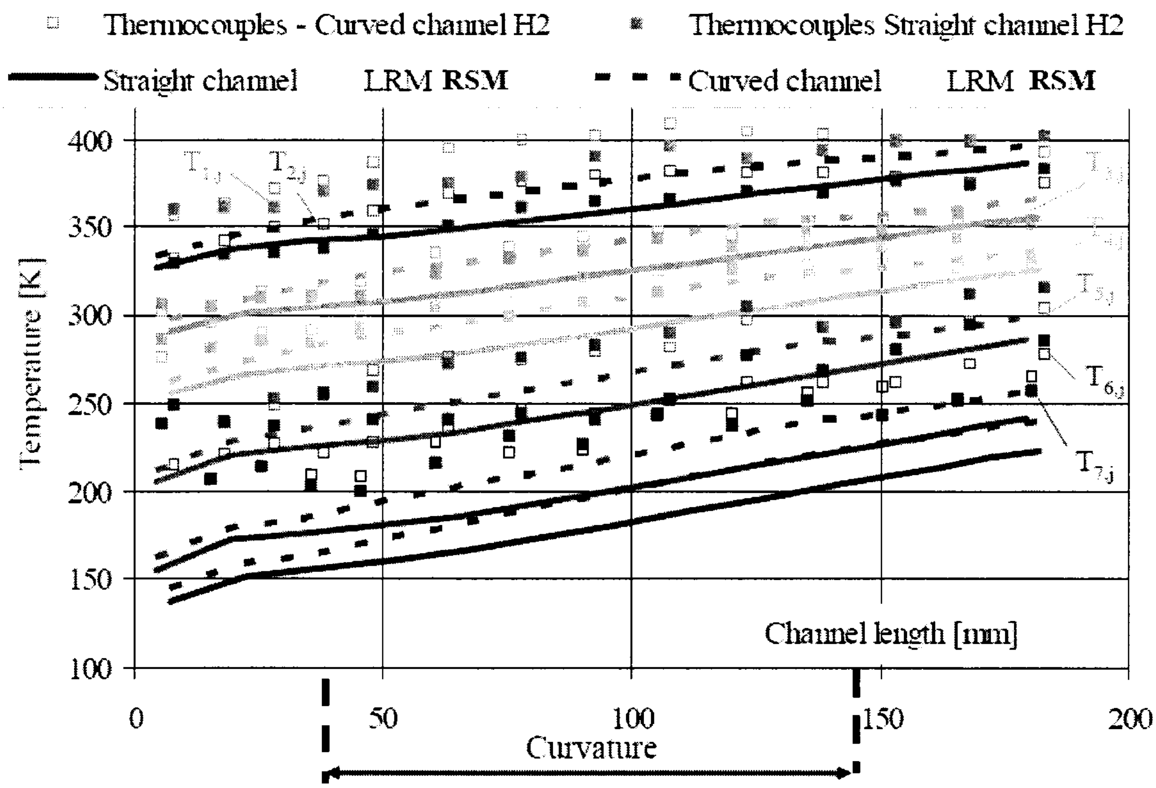

Figure 93 : Experimental and numerical temperature data along the straight and the curved channels for hydrogen tests.

The very good correspondence between the simulated temperatures of the line T_{2j} and the experimental data assumes that the boundary conditions of the hot side are realistic. This means that the heat losses through radiative and convective processes through the block can be neglected. Moreover, the temperature increases numerically and experimentally in the curvature in comparison with the straight configuration, due to the three dimensional effect of the curved block which brings additional heat.

For the upper temperature sets (T_{3j} to T_{7j}), we can observe a deviation which increases along the channel height. A maximal deviation is observed for the coldest thermocouple line, in comparison to the numerical simulations. The numerical simulations assume lower temperature at the top of the channel: $T_{7,5\_CFD}=160K$ and $T_{7,5\_Experiments}=200K$). This indicates that the hot side of the channel is really well simulated but not the cold side. This phenomenon exists for both straight and curved channel: it is also possible to investigate the curvature effect with the aid of the inverse method.

5.2.4.3. Inverse method, two heat transfer coefficients

For all data sets (*7* measured temperatures for each channel cross-section) the inverse method was applied with the case *c*, (see in paragraph 3.3.2). *28* heat transfer coefficient values are obtained per channel. Two heat transfer coefficients were delivered per cross-section, one for the upper part of the channel and the second one for the hot side of the channel. The heat transfer coefficients are presented over the channel length at each cross-section, see Figure 94. Moreover, the inverse method calculation took into account the three dimensional effect of the curved block in the curvature part.

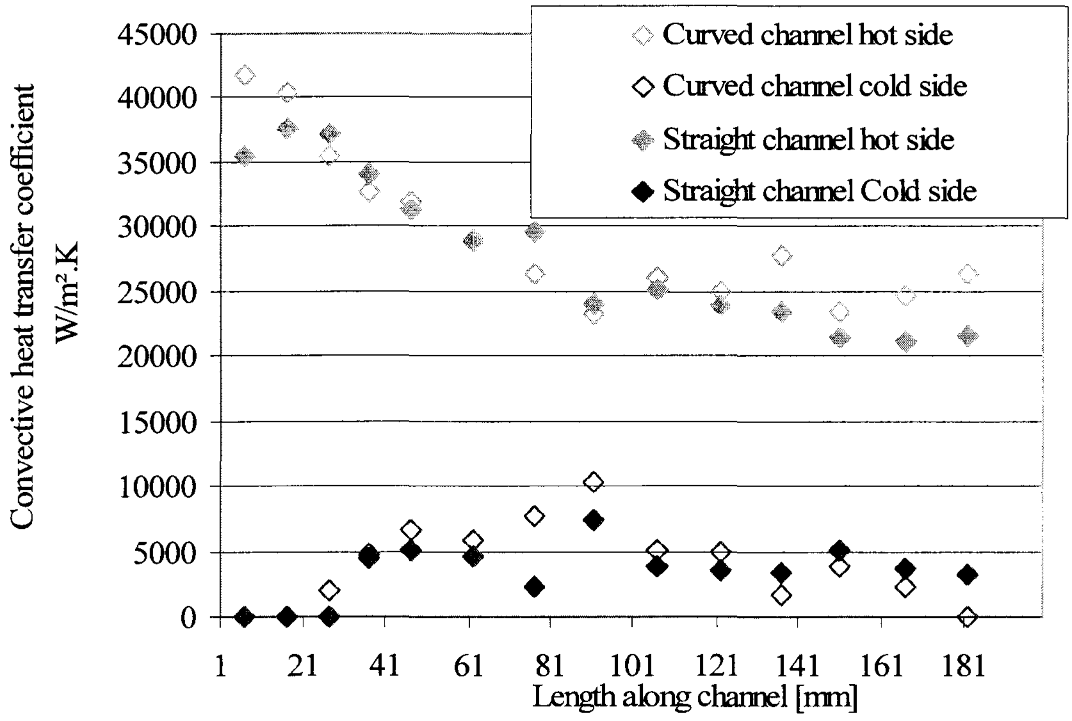

Figure 94 : Heat transfer coefficients determined by the inverse method for the hydrogen campaign at upper and lower sides.

The curved to straight convective heat transfer coefficient ratio can be calculated from the numerical simulations and from the inverse method results. This allows a comparison of the curvature effect between the numerical simulations and the experiments. On the cold side, the experimental values of the heat transfer coefficient are so small, ~ *5000* $W \cdot m^{-2} \cdot K^{-1}$, for both channels, that the cur ved to straight ratio is imprecise. That is not the case with the heat flux coefficients at concave side (the hot sides) which can be analysed.

5.2.4.4. Curved to Straight heat transfer coefficient ratio at the hot side

The curved to straight heat transfer coefficients ratio at the concave side was calculated with the numerical simulations and the experimental results (Figure 95). A weighted averaged of the numerical heat transfer coefficients was made for the "hot" side of the channel, taking into account the dimensions of the numerical cells.

In this experimental set with hydrogen, the effect of the Dean vortices can be neglected at the concave side. An increase of the heat transfer coefficient at the hot side of the channel (more than *1.2*) can only be remarked at the end of the curvature. Nevertheless, all experimental curved to straight ratios are contained between *0.9* and *1.15* which does not constitute a strong influence of the curvature on the heat transfer at the concave side.

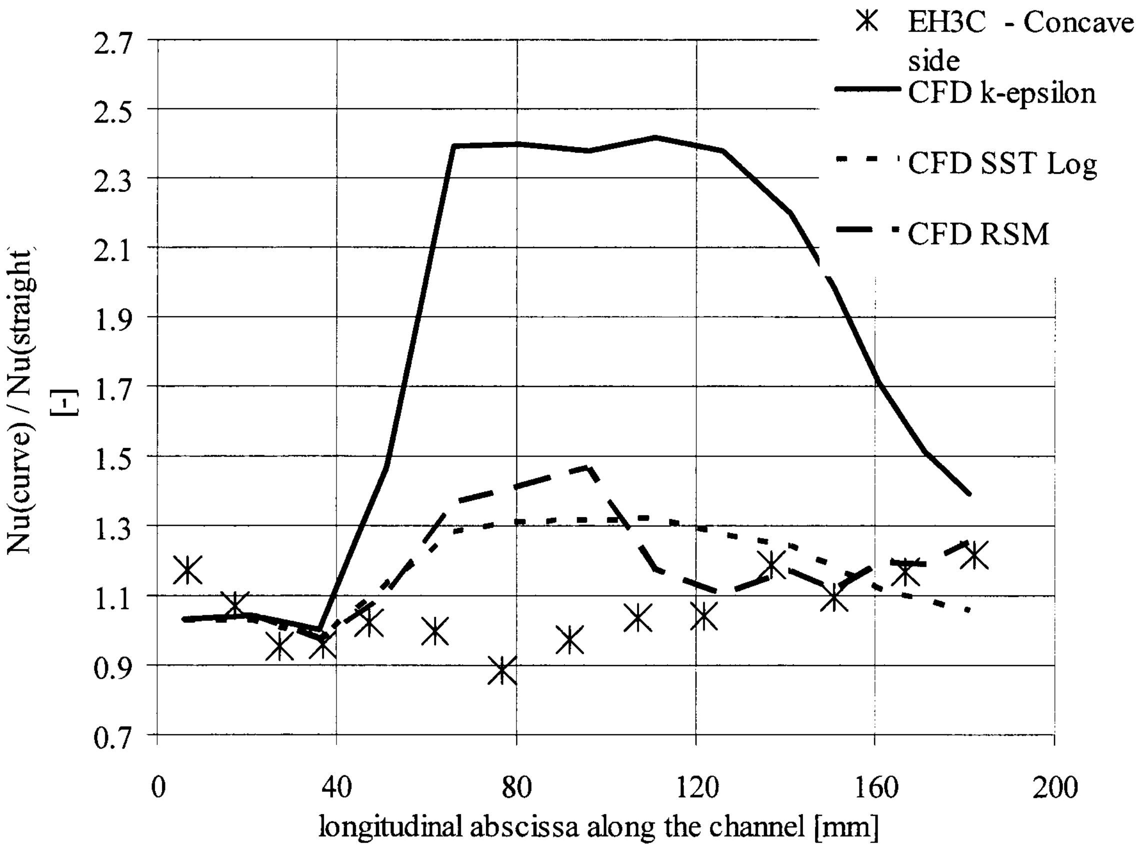

Figure 95 : Curved to straight heat transfer coefficient ratio from hydrogen flow (experiments, numerical simulations).

All numerical simulations and particularly the k-epsilon model overestimate the heat transfer increase at the concave side. The RSM model takes into account the edge vortices and their influence appears at *z=100 mm* and provides a decrease of the curvature influence which corresponds to the experimental results. The RSM model seems to be the most adequate turbulence model for this experiment, by the fact that the edge vortices are modelled.

In reference to the paragraph 3.3.3, the measurement errors with the case *c* of the inverse method are very high (more than *50%*). Hence it can be useful to use the inverse method with the simplest model of parametrisation corresponding to a small measurement error (*6.8%* on the experimental determination of the averaged heat transfer coefficient).

5.2.4.5. Inverse method, one heat transfer coefficient

For all data sets the inverse method was applied with the case *a*, (see in paragraph 3.3.2). *14* heat transfer coefficient values are obtained per channel. The heat transfer coefficient profiles are presented over the channel length, see Figure 94. From the inverse method, it is possible to extract the heat flux at the block-channel interface. The numerical heat flux values match quite well the experimental ones along the channel length, see Figure 96.

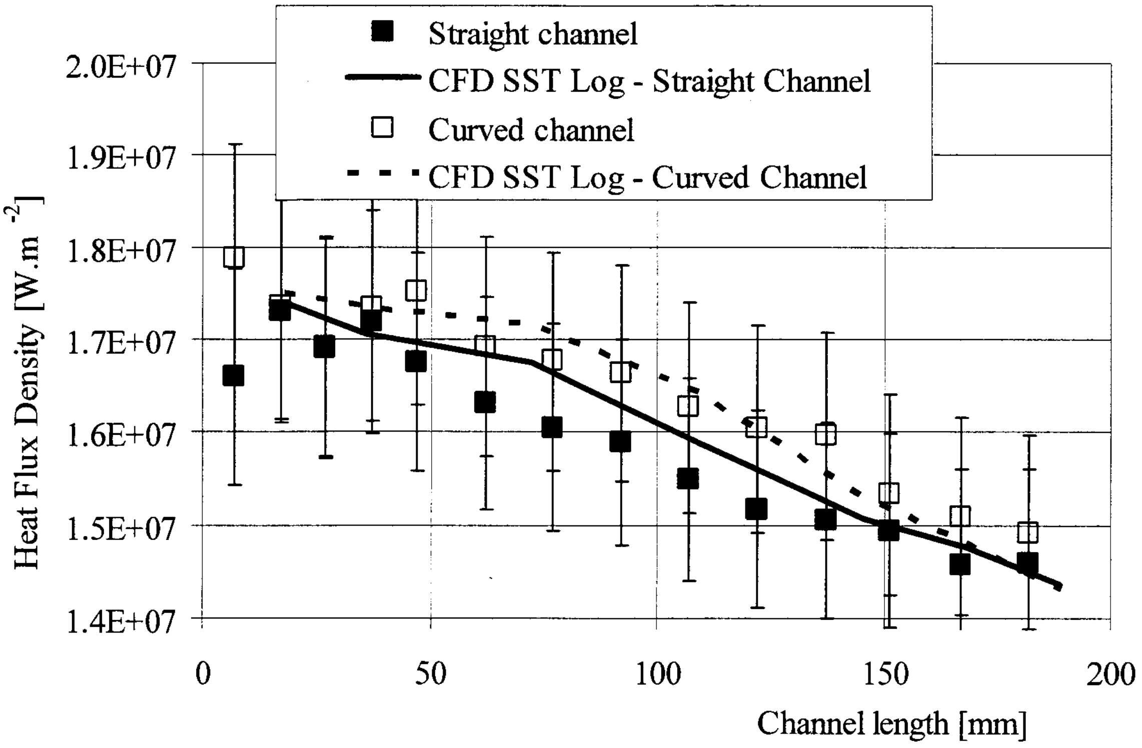

Figure 96 : Curved and straight heat flux profiles from hydrogen flow (experiments, numerical simulations).

With the results of the inverse method, the curved to straight ratio of heat transfer coefficient can be calculated and presented over the channel length, see Figure 97, and compared to the empirical correlations presented in 2.2.2. see in Table 13. The heat transfer coefficients ratio can be assimilated to Nusslet numbers ratio, because of similar heat conductivity of material and identical hydraulic diameters for the curved and straight test cases.

[Taylor, 1968]	[Niino, 1982]
$\frac{Nu_c}{Nu_s} = De^{\pm 1/5}\,\mathrm{Re}^{\mp 3/20}$	$\frac{Nu_c}{Nu_s} = De^{\pm 2/25}\,\mathrm{Re}^{\mp 3/50} \times \left[1+\frac{1}{3}.\sin\left(\pi\sqrt{\frac{x_c}{L_c+15D_h}}\right)\right]$
[Sturgis, 1999]	[Kumakawa, 1986]
$\frac{Nu_c}{Nu_s} = De^{0.2}\,\mathrm{Re}^{-0.154}$	$\frac{Nu_c}{Nu_s} = \left[De^{1/5}\,\mathrm{Re}^{-3/20}\right]^{\pm\sin\left(\pi\sqrt{\frac{x_c}{L_c+37D_h}}\right)}$

Table 13 : Empirical correlations of the curved to straight Nusselt numbers ratio.

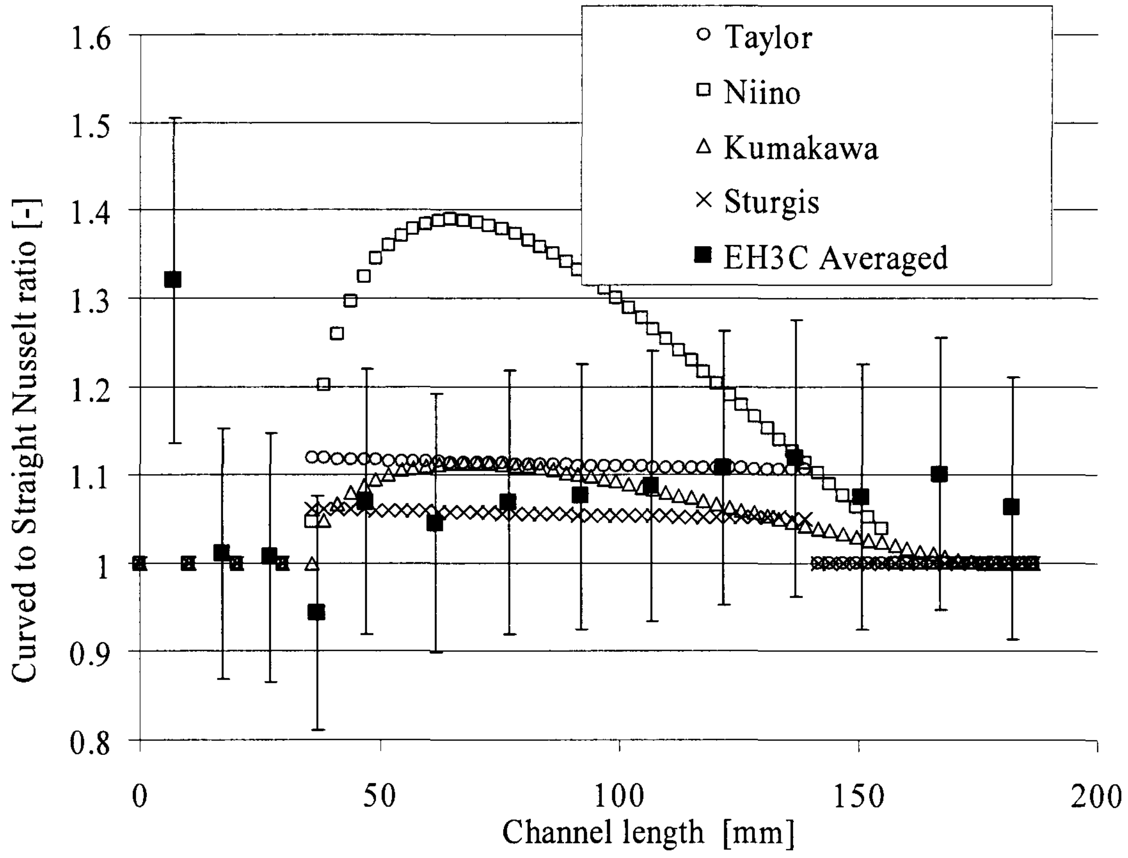

Figure 97 : Curved to straight averaged heat transfer coefficients ratio from hydrogen flow (experiments, numerical simulations).

The heat transfer coefficients increase in the curvature (36 < x < 147mm) up to *12%* according to the experimental results from the inverse method with one degree of resolution. The corresponding measurement error is calulated with the ratio of measurement errors: *14%* of maximal measurement errors are estimated for the heat Nusselt numbers ratio. A comparison with the numerical results and the empirical correlations can be made. In terms of amplitude, the empirical correlation of Niino appears to be inadequate to model the curvature influence in the EH3C test conditions. After the curvature, the perseverance of the Dean vortices seems to be under-estimated by the empirical correlation of Kumakawa: *30* hydraulic diameters after the curvature, the heat transfer coefficient is still *8 – 10%* higher in the curved channel compared with the straight one.

5.2.5. Thermal investigations on the methane test case

5.2.5.1. Temperature measurements

The error calculation was added for all temperature measurements, as can be seen in Figure 98.

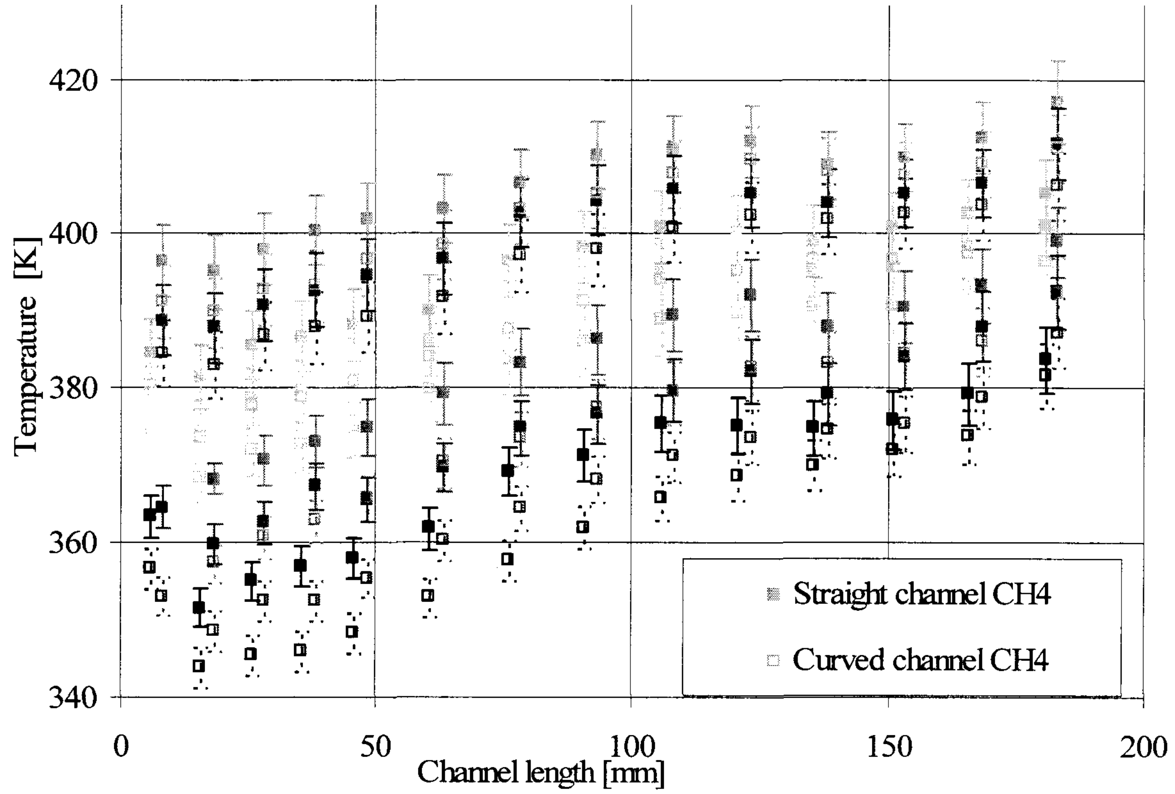

Figure 98 : Experimental temperature data along the EH3C channels for methane flow with measurement error calculation.

Like with the hydrogen investigations, it is interesting to present the result for different cross sections, here j=3, j=7 and j=12, see Figure 99.

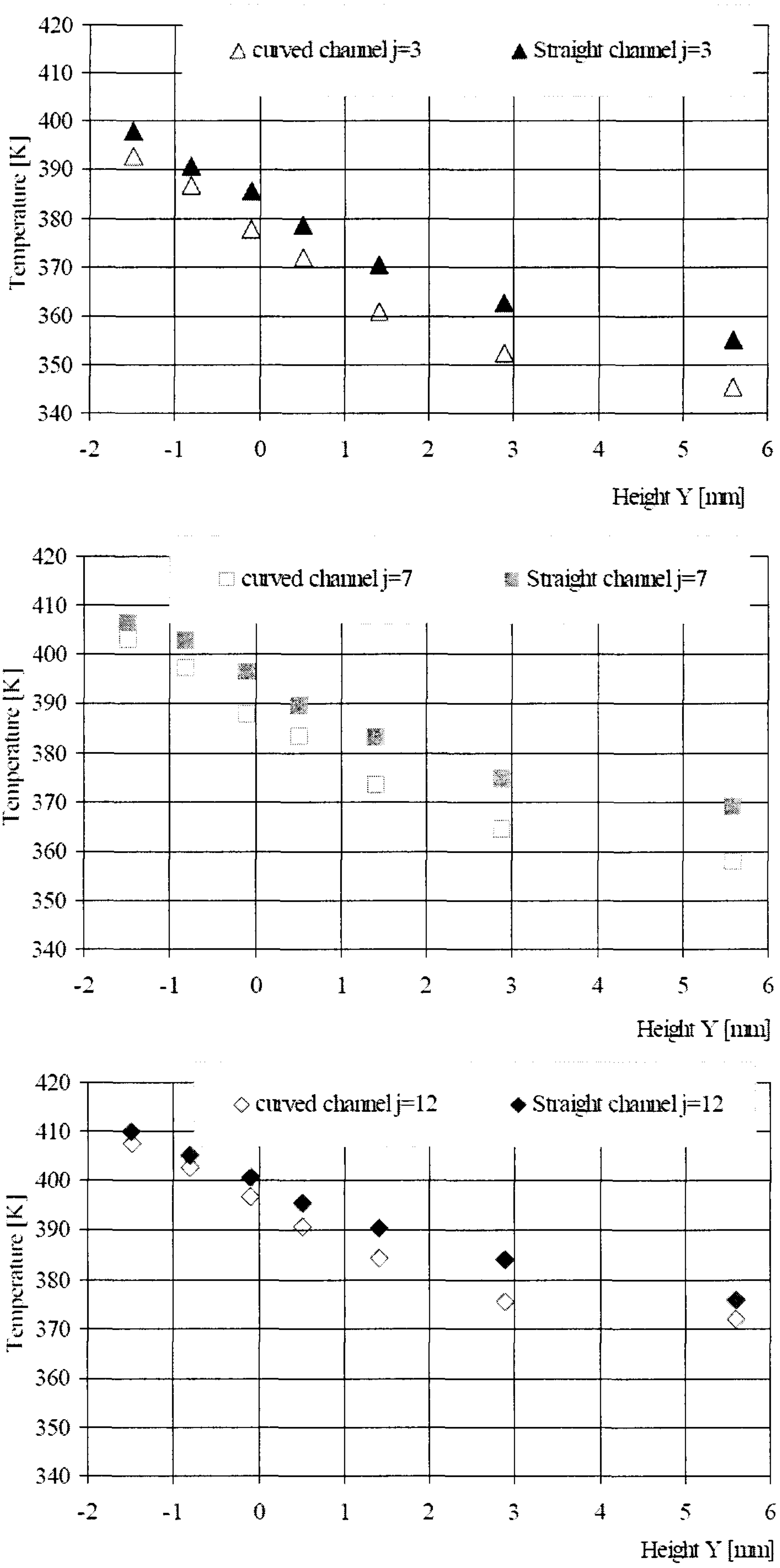

Figure 99 : Measured temperatures at the cross sections *j=3,7,12* for methane tests.

5.2.5.2. *Comparison with results from numerical simulations*

The measured temperatures and the numerical simulation are illustrated in the same graphic (see Figure 100).

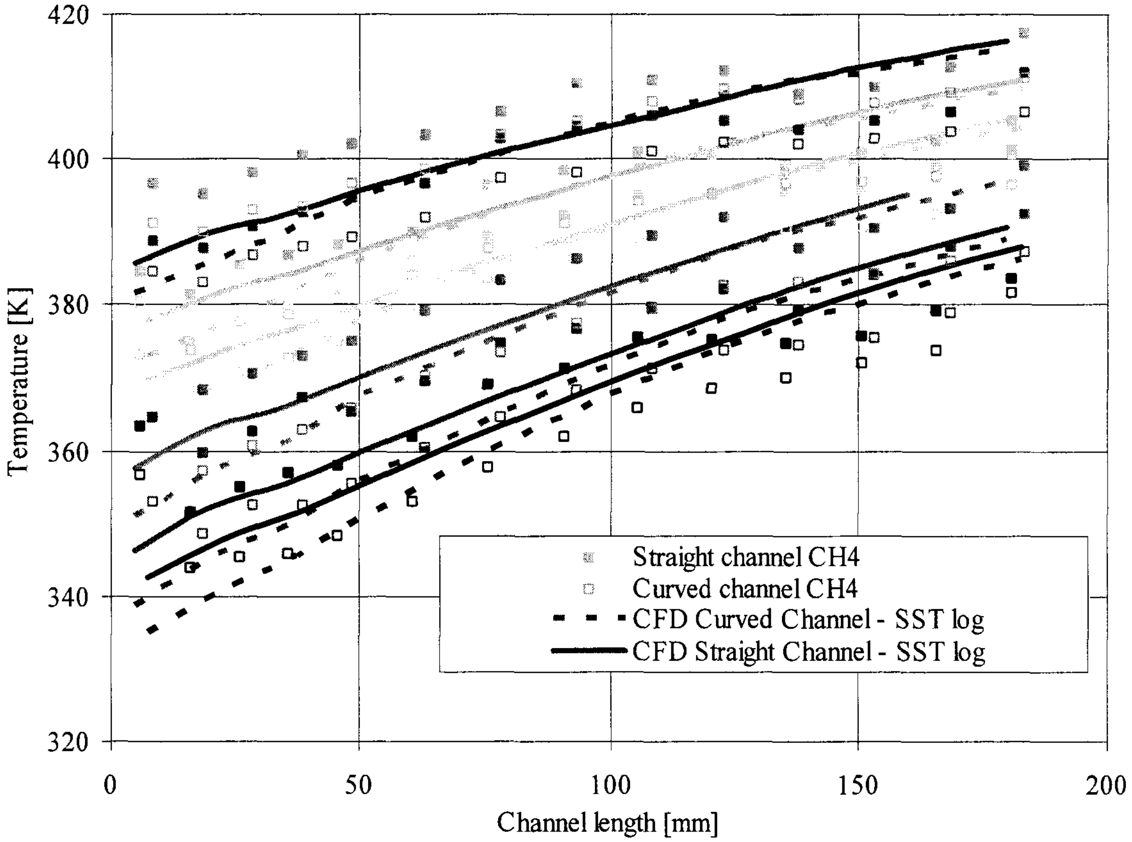

Figure 100 : Numerical and experimental temperature data along the EH3C channels for methane flow.

The numerical results and the experimental temperatures correspond better than in the hydrogen test case. The use of the inverse method allows to analyse the role of the curvature on heat transfer.

5.2.5.3. *Inverse method, two heat transfer coefficients*

The inverse method was applied to all channel cross-sections where thermocouples are implemented. The convective heat transfer coefficients calculated with the inverse method at the hot and cold sides are presented in Figure 101 .

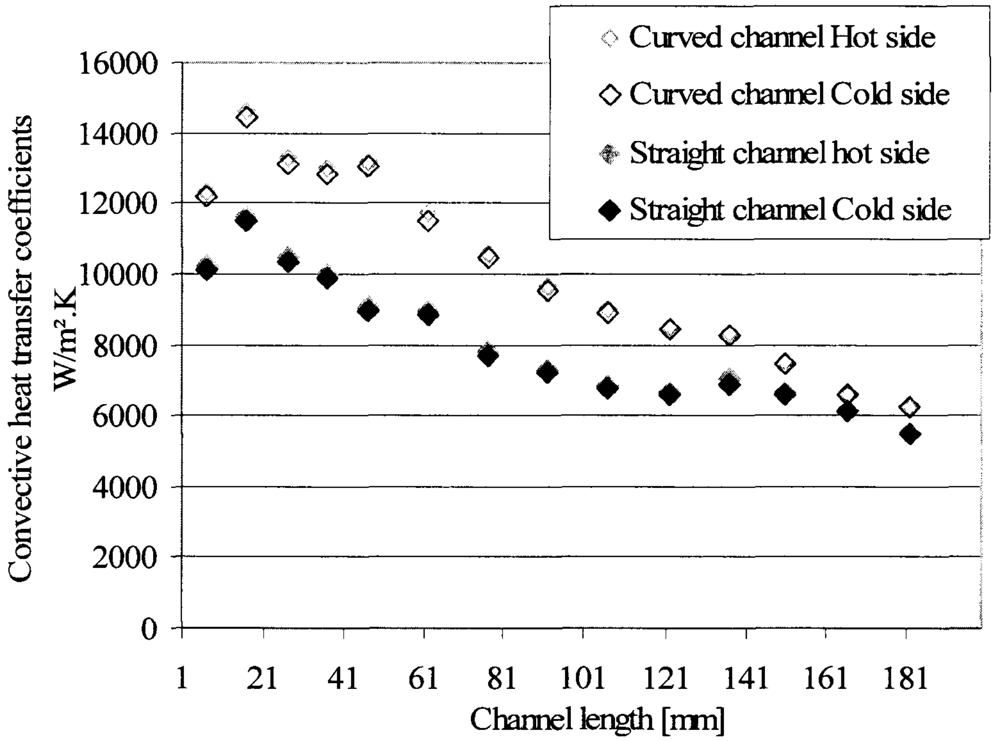

Figure 101 : Heat transfer coefficients determined by the inverse method for the methane campaign at upper and lower sides.

The heat transfer coefficients are the same at the "cold" and "hot" sides, for both channel investigations. The curvature role can be enlightened by comparing the "hot" heat transfer coefficients from the straight and curved channels.

5.2.5.4. Curved to Straight heat transfer coefficient ratio at the hot side

At the concave side, the curved to straight heat transfer coefficient ratio was calculated along the channel length and directly compared with the numerical simulations. Figure 102 illustrates the calculated ratios from EH3C experiments and from numerical simulation for the methane investigation.

Unlike the hydrogen case, the influence of the Dean vortices seems to be more pronounced, in a range of *1.1* up to *1.2* and quite well modelled by numerical simulations, see Figure 102.

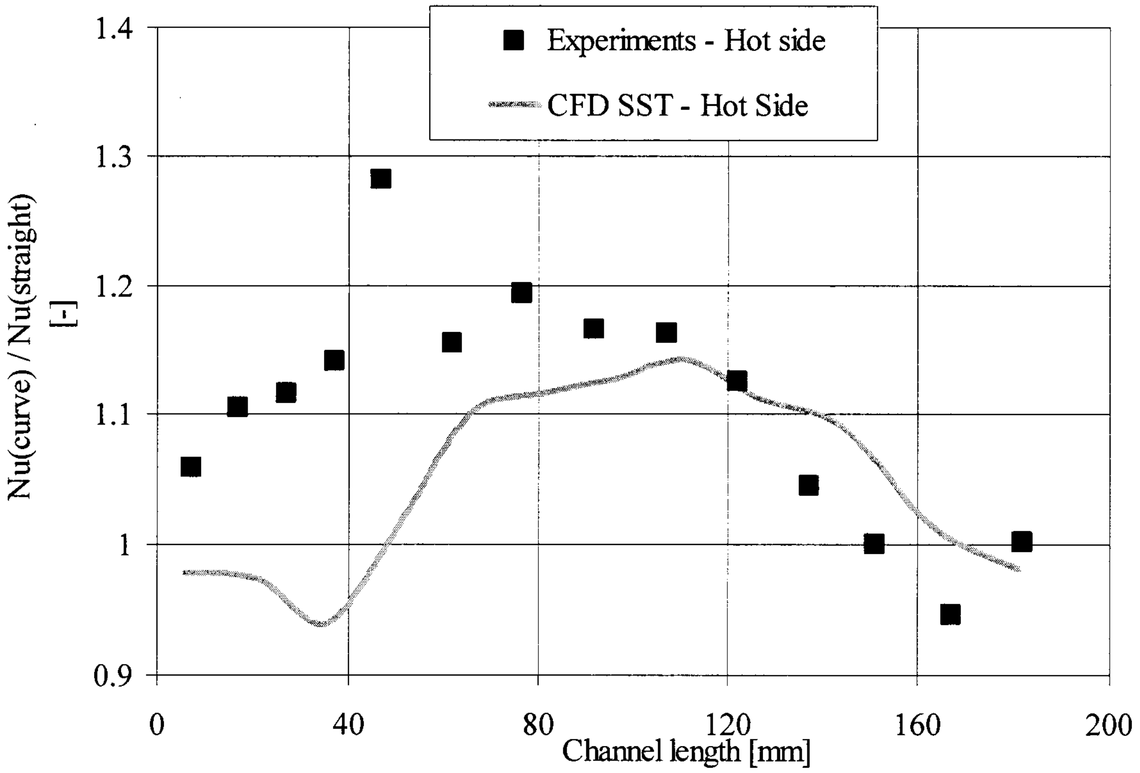

Figure 102 : Curved to straight heat transfer coefficient ratio from methane flow at the hot side (experiments and numerical simulations).

5.2.5.5. *Inverse method, one heat transfer coefficients*

The inverse method was applied by considering one averaged heat transfer coefficient per cross section, refer to Figure 103.

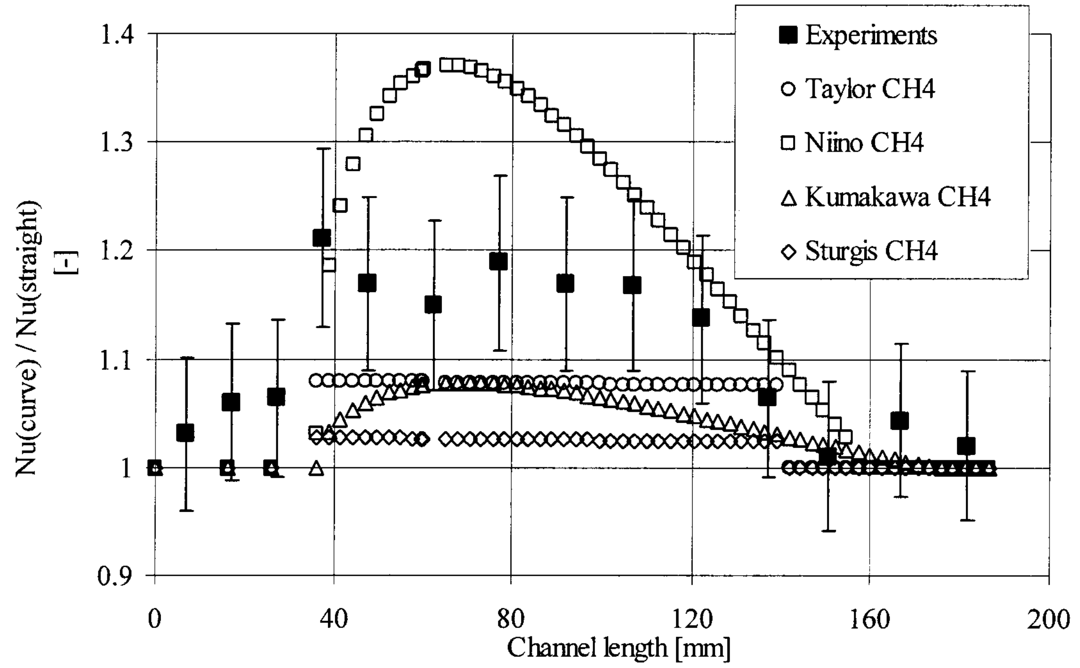

Figure 103 : Curved to straight heat transfer coefficient ratio from methane flow (experiments, numerical simulations, empirical correlations).

The experimental investigation on averaged heat transfer coefficient (*6%* measurement error) indicates that the empirical correlations do not perfectly match the results. In terms of intensity of heat flux coefficient increase, the experimental results reach *20%* increase. The empirical correlation of Niino seems to overestimate the curvature influence whereas all other correlations underestimate it. In terms of shape of heat transfer coefficient ratio along the channel, the empirical correlation of Niino is quite adequate.

5.3. Chapter conclusion

Methane and hydrogen were investigated experimentally in curved cooling channels. The temperature measurements were used to deliver heat transfer coefficients at the channel walls through an inverse method process. The way of using the inverse method influences measurement accuracy. With one averaged heat transfer coefficient model over the channel perimeter, the corresponding measurement error is below *7%* which is below the errors of similar experiments (refer to 2.2.2). By applying a heat transfer coefficient at the concave side and another one at the convex side of the channel, the results are local and more interesting, but the corresponding measurement error is very high (more than *50%*). Both analyses were carried out.

With the averaged heat transfer coefficient analysis, the hydrogen experiments deliver an increase of the heat transfer coefficient in the curvature of *10%*. For the methane investigation, this increase reaches *20%*. For both fluid investigations, the influence of the Dean vortices on the heat transfer still exists after the curvature (*30* hydraulical diameters after the curvature). This perseverance of the Dean vortices and their effect on the heat transfer were modelled by the Niino and Kumakawa empirical correlations. The experimental amplitude of the curvature effect on the heat transfer coefficient was not matched by any existing empirical correlation.

Concerning the local investigation at the concave side, the hydrogen experiments do not indicate any influence on the heat transfer (less than *10%*). The numerical simulations are not adequate to simulate the curvature influence. Only the RSM model seems to match much better the experimental results than the other turbulence models. For methane investigation, the experimental concave heat transfer coefficient and the numerical simulation correspond very well: both indicate an increase of the heat transfer coefficient of *20%*.

6. Summary and Outlook

6.1. Summary

The literature review has shown that the specific and extreme thermal and dynamical environment of a curved asymmetrical heated micro-channel result in unreliable performance of the classic empirical correlations. The very specific case of cooling channels of rocket engines is often estimated with poorly adapted empirical correlations or numerical simulations. Moreover, high thermal loads and asymmetry are two preponderant elements of the real case of regenerative cooling systems. The EH3C campaign presents a lot of advances: the high instrumentation of the EH3C channels (*98* thermocouples, *3* pressure sensors) allows a complete experimental interpretation of the curvature influence on heat transfer. The flow characteristics and channel geometry were representative of real operating conditions and high asymmetry in the heat flux density of up to $17\ MW\ m^{-2}$ was achieved experimentally. Moreover, both the manufacture of the test sepecimen and the experimental conditions were highly controlled, including precise control of the fluid dynamical and thermal steady state conditions. The EH3C campaign allowed several numerical models and empirical correlations to be either rejected or validated. The collected knowledge does not only concern the experimental tests of the EH3C project, but the numerical simulations helped to understand the physics of the inaccessible phenomena which occur inside channels.

6.1.1. Curvature influence on global heat increase and pressure losses

For both media, the numerical simulations underestimate the role of the curvature in terms of pressure loss. Approximately *10% - 20%* higher than the level predicted by CFD and theory was measured experimentally, for the non-heated channels case as well as the heated channels configuration, see Table 14. Experimentally, the presence of heat flux does not play a major role in the curvature influence on the pressure losses.

$\left(\frac{\Delta p_{curve}}{\Delta p_{straight}}\right)$	Fluid	CFD/Theory	Experiments
« Non-heated » campaign	H_2	*~10%*	*30-50%*
	CH_4	*~10%*	*20-30%*
« Heated » campaign	H_2	*~25%*	*40%*
	CH_4	*~25%*	*25%*

Table 14 : Curvature influence on pressure drop.

Experimentally, the curvature always increases the pressure drop by ~ 40% for hydrogen and by ~ 25% for methane, regardless of whether or not the fluid is heated. The underestimation of the curvature role by theory or numerical simulation has to be taken into account in determining the energetic optimisation of the cooling system of rocket engines.

Concerning the global heat increase, the experimental and the numerical investigations provide the same results in accordance with energy conservation. Approximately *5%* heat increase was measured and numerically calculated for the hydrogen test case, and *7%* for the methane case.

$$\left(\frac{\dot{Q}_{curve}}{\dot{Q}_{straight}}\right)_{CFD} \approx \left(\frac{\dot{Q}_{curve}}{\dot{Q}_{straight}}\right)_{EXP} = \begin{cases} 5\% \text{ for the hydrogen case} \\ 7\% \text{ for the methane case} \end{cases} \quad \textbf{(6.1)}$$

Approximately *5%-6%* of the heat increase is due to the geometry difference between the straight and the curved channel, maionly due to the block geometry difference. The Dean vortices do not influence the global heat increase of the fluid in the hydrogen case, however a difference of approximately *2%* was observed in the methane case.

It is interesting to note that the curvature implies higher pressure losses than expected for neglected heat transfer gain due to the curvature. This fact is important for the optimisation of real curved cooling channels of rocket engines.

6.1.2. Curvature influence on heat transfer for hydrogen at the concave side

For the hydrogen test case, the curved to straight heat coefficients ratio at the concave side is higher in numerical simulations than the experimental results.

$$\left(\left.\frac{Nu_{curve}}{Nu_{straight}}\right|_{Concave,H2}\right)_{CFD} \approx 1.3 > \left(\left.\frac{Nu_{curve}}{Nu_{straight}}\right|_{Concave,H2}\right)_{EXP} \approx [0.9-1.15] \quad \textbf{(6.2)}$$

For this hydrogen test measurement, the Dean vortices do not have a local influence at the hot side. The curvature does not locally influence the heat transfer at the concave side.

The presence of edge vortices can annihilate the influence of the Dean vortices. Indeed, numerical simulations with the RSM turbulence model exhibited these edge vortices. In the configuration of HARCC, the hot side of the channel is entirely occupied by the edge vortices. The Dean secondary motions are denied access to the concave side and the local heat transfer cannot be enhanced by the centrifugal forces. The RSM turbulence model seems to better characterise the local influence of the curvature on the concave heat transfer when comparing the numerical results with the experiments. Nevertheless, all numerical models overestimate the change in heat flux due to the curvature at the concave side.

6.1.3. Curvature influence on heat transfer for methane at the concave side

For the methane test case, the ratio of heat transfer coefficients on the concave side of the curved channel to a straight channel is similar for the experimental results and for the numerically calculated ones.

$$\left(\left.\frac{Nu_{curve}}{Nu_{straight}}\right|_{Concave,CH4}\right)_{EXP} \approx [1.1-1.2] \sim \left(\left.\frac{Nu_{curve}}{Nu_{straight}}\right|_{Concave,CH4}\right)_{NUM,SST} \quad \textbf{(6.3)}$$

The SST turbulence model seems to be quite reliable in capturing the effect of curvature on local heat transfer at the concave side of cooling channels for methane at ambient temperature.

6.1.4. Curvature influence on averaged heat transfer coefficient

Using the inverse method with one averaged heat transfer coefficient over the channel periphery, the methane and hydrogen test results are presented in Figure 104. The empirical correlation of Niino was modified in order to better match the EH3C experimental results. The influence of the Dean vortices on heat transfer was extended *40* hydraulic diameters downstream of the curvature. The coefficient *b* was taken equal to *0.05* for the hydrogen test case and *0.15* for the methane test case.

$$\frac{Nu_c}{Nu_s} = De^{\pm 2/25}\,\mathrm{Re}^{\mp 3/50} \times \left[1 + b\sin\left(\pi\sqrt{\frac{x_c}{L_c + 40D_h}}\right)\right] \qquad \textbf{(6.4)}$$

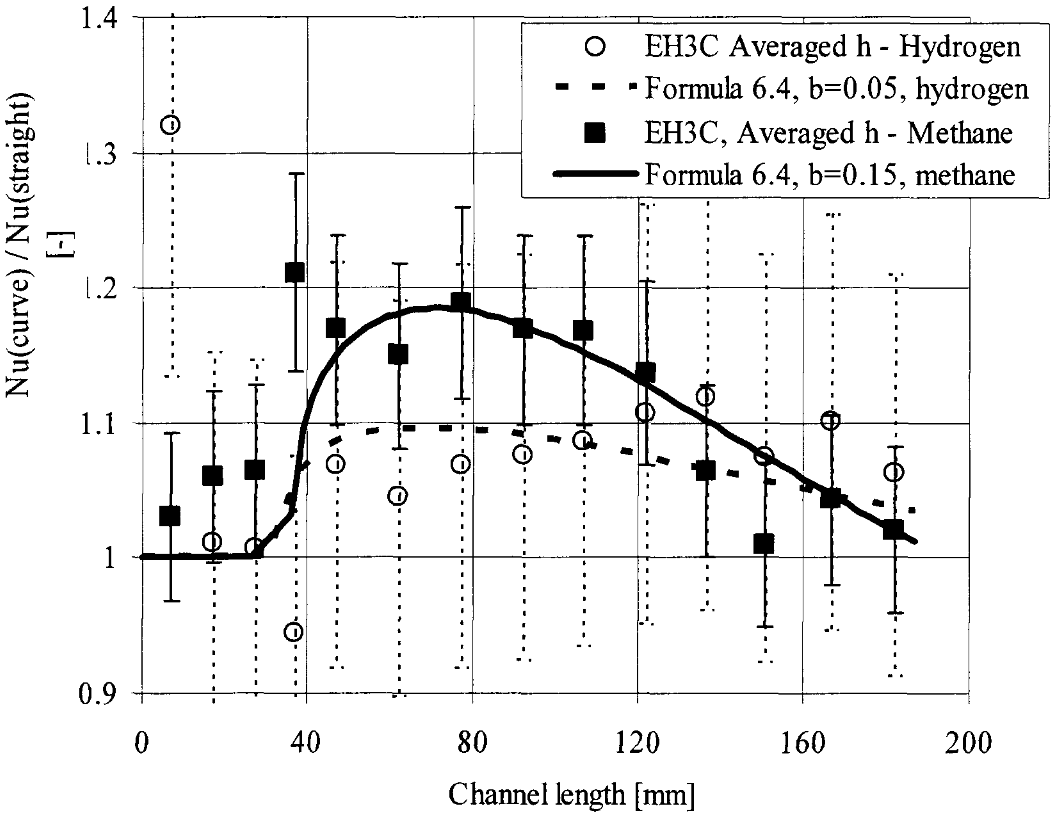

Figure 104 : Curved to straight heat transfer coefficient ratio for constant coefficient over the channel periphery with a new empirical correlation.

6.1.5. Comparison of the methane and hydrogen test cases

For the methane experimental case, the convective heat transfer coefficient ratio is higher than in the hydrogen case.

$$\left(\left. \frac{Nu_{curve}}{Nu_{straight}} \right|_{Averaged,CH4} \right)_{EXP} \approx 1.2 > \left(\left. \frac{Nu_{curve}}{Nu_{straight}} \right|_{Averaged,H2} \right)_{EXP} \approx 1.1 \qquad \textbf{(6.5)}$$

The Dean numbers were calculated for both test cases (see 3.1.2): the methane Dean Number (*1.6* 10^4) is twice as low as the hydrogen case. This behaviour is contradictory to the experimental results, as the methane test case indicates a higher influence of the curvature on the local heat transfer on the concave side. The value of the heat flux density could be the main reason for the divergence between the two test cases and explain this contradiction.

The edge vortices contain the Dean vortices far away from the concave side. With a highly asymmetrical heat flux density (*20 MW* m^{-2}), the edge vortices seem to be domminant in comparison to the Dean vortices (see 4.1.5) for the first half of the curvature. Later the Dean vortices grow until they have direct contact with the concave wall which increases the curved to straight heat transfer ratio. The experiment with highly asymmetrical heat flux (hydrogen case) does not elucidate the influence of the curvature at the concave side. Assuming this theory, the edge vortices could be dominant along the entire length of the curvature preventing the Dean vortices from joining the concave side. For the methane case with lower heat transfer (~ *3MW* m^{-2}), the edge vortices are negligible which allows the Dean vortices to effectively cool the concave side.

Further experiments and numerical simulations should be conducted to determine the validity of these assumtions (see 6.2).

6.1.6. Discussion of turbulence models and empirical correlations

The experiments of Neuner, which share the closest similarity to the EH3C test cases and to real rocket engine configurations, the concave heat transfer enhancement was better modelled by the empirical correlation of Kumakawa.

For the methane test case of the EH3C experiment, the numerical simulations were adapted to describe the heat flux enhancement due to the curvature at the concave side. Concerning the averaged heat transfer coefficient analysis, any existing empirical correlation can match perfectly the experimental results. For the hydrogen test case, all empirical models and numerical simulations overestimate the heat transfer coefficient enhancement in curvature. The RSM turbulence model seems to be the most appropriate to simulate fluids in curved rectangular channels under highly asymmetrical heat flux. RSM is the only numerical turbulence model which calculates edge vortices. A modified version of the Niino empirical correlation proposed in order to match the EH3C experimental results with hydrogen and methane.

6.2. Outlook

The role of curvature in heat transfer in cooling channels of rocket engine was investigated numerically and experimentally.

Concerning the experimental EH3C investigations, the measurement accuracy can be improved if the locations and the positions of the thermocouples are better identified. It has been shown that the uncertainty of the position of the temperature sensors is the main source of measurement error. The tomography method is one of the most precise non-destructive methods of analysing the dimensions of a mechanical structure. Tomography could be used on the EH3C channels to identify precisely the position of the sensors at the channel walls, in order to improve the experimental measurements. Moreover, the pressure sensors and thermocouples used to determine the calorimetric heat gain and the pressure losses need to be implemented directly after the inlet manifold and before the outlet manifold to calculate the real energy balance through the channel. Indeed, the data analysis from these inlet and outlet sensors has shown the high influence of the manifold on the fluid in terms of additional heat gain and pressure loss. Unfortunately, it is difficult to directly implement sensors in the channel flow, due to the restrictively small dimensions of the channels.

In order to continue the analyse work concerning the experimental and numerical results, it would be useful to conduct additional experiments with each coolant under identical heat fluxes. This concerns methane under cryogenic conditions and hydrogen under ambient temperature. This would provide the same experimental conditions for both coolants in order to compare directly the curvature influence on the heat transfer for the two media. With the knowledge gained during manufacture of the EH3C channels, it would possible to produce other test specimens with different geometrical parameters, for example sharper curvature, convex heating, aspect ratio change, etc. The investigation of phase change is another possibility for further study concerning the evaporation of fluid inside the cooling channels during the start up transient of the engine for expander cycles engine configuration.

Additional numerical simulations could be conducted to complete the investigation of the methane case, particularly with the RSM turbulence model. Moreover, different asymmetrical heat flux densities could be simulated to analyse the interference of the edge vortices with the Dean vortices which depends on the level of heat flux.

APPENDICES

Appendix 1: Physical background of CFD

- *Conservation equations for mass, momentum and energy*

All the equations presented in this study use the Einstein summation convention. The basic Navier-Stokes equations are presented here, as well as the energy conservation equation and the mass conservation:

Continuity equation:

$$\frac{\partial \rho}{\partial t}+\frac{\partial}{\partial x_i}(\rho U_i)=0 \qquad \textbf{(6.6)}$$

Momentum equation:

$$\rho\frac{DU_i}{Dt}=-\frac{\partial p}{\partial x_i}+\rho g_i+\frac{\partial \tau_{ij}}{\partial x_j} \qquad \textbf{(6.7)}$$

Energy equation:

$$\frac{D\rho e}{Dt}=\rho g_i U_i-\frac{\partial}{\partial x_i}(pU_i)+\frac{\partial}{\partial x_i}(\tau_{ij}U_j)-\frac{\partial q_i}{\partial x_i}+\left(\dot{Q}_v\right)_r \qquad \textbf{(6.8)}$$

Where e is the global internal energy per mass unit, q_i the correspondent conductive heat flux and $\left(\dot{Q}_v\right)_r$ the heat source per volume unit.

- *Turbulence Modelling*

To characterise the turbulence of a flow, the thermal and dynamical parameters are decomposed into time averaged component and temporal fluctuation component. Thus, the basic equations are time averaged. The Reynolds-averaged Navier-Stokes equations (RANS) are mostly used to treat turbulence flows, because of calculation time reduction and limited requirement of computing power. The cross products of turbulent velocities, temperature and pressure bring additional unknowns. Hence a turbulence model must enclose the equation system, bringing additional equations. The choice of the right turbulence model and the right wall treatment represents one of the most important challenges for any numerical application that is to represent the dynamic and the thermal behaviour close to reality. The turbulence can be RANS- modelled with a two-equation (k-ε, k-ω) closure equation system or a seven-equation model (Reynolds Stress Model).

The *2*-equations closure equation system of turbulence uses the Boussinesq assumption to calculate the Reynolds stress tensor, by bringing the concept of turbulent viscosity.

$$\tau_{ij}=\mu_t\left(\frac{\partial U_i}{\partial x_j}+\frac{\partial U_j}{\partial x_j}\right) \qquad \textbf{(6.9)}$$

The turbulent component (Eddy viscosity concept) of the viscosity is thus directly deduced from the *2* equations turbulence model:

- for the k-ε model $\mu_t=C_\mu \rho\frac{k^2}{\varepsilon}$ **(6.10)**

- for the k-ω model $\mu_t = \rho \dfrac{k}{\omega}$ **(6.11)**

The k-ω model seems to be well adapted to conjugate heat and mass transfers, [Wilcox, 1986]. Numerical simulations based on the k-ω turbulence resolution have shown a good approximation of dynamical behaviours in curvature [Song, 2000]. Nevertheless, the k-ω model would present strong sensitivity to free-stream conditions. That can be improved by the good compromise of an SST model (Shear Stress Transport). This SST- *2* equations turbulence model uses a blending function to apply the k-ε model in the bulk region and the k-ω inside the boundary layer [Menter, 1994].

The turbulence equations of the k-ε and the k-ω turbulence models are presented here:

k-ε turbulence model

$$\frac{\partial \rho k}{\partial t} + (\rho U_i k)_{,i} = (\tau_{ij} U_j)_{,i} - \rho\varepsilon + \left[(\mu + \mu_t) \frac{\partial k}{\partial x_i} \right]_{,i} \qquad \textbf{(6.12)}$$

$$\frac{\partial \rho \varepsilon}{\partial t} + (\rho U_i \varepsilon)_{,i} = c_{\tau 1} (\tau_{ij} U_j)_{,i} - c_{\tau 2} \rho \frac{\varepsilon^2}{k} + \left[\left(\mu + \frac{\mu_t}{\sigma_\tau} \right) \frac{\partial \varepsilon}{\partial x_i} \right]_{,i} \qquad \textbf{(6.13)}$$

c_μ	$c_{\tau 1}$	$c_{\tau 2}$	σ_k	σ_τ
0.09	1.45 → 1.55	1.92→2	1	1.3

k-ω Wilcox turbulence model

$$\frac{\partial \rho k}{\partial t} + (\rho U_i k)_{,i} = (\tau_{ij} U_j)_{,i} - \beta^* \rho k \omega + \left[\left(\mu + \frac{\mu_t}{\sigma_k} \right) \frac{\partial k}{\partial x_i} \right]_{,i} \qquad \textbf{(6.14)}$$

$$\frac{\partial \rho \omega}{\partial t} + (\rho U_i \omega)_{,i} = \alpha \frac{\omega}{k} (\tau_{ij} U_j)_{,i} - \beta \rho \omega^2 + \left[\left(\mu + \frac{\mu_t}{\sigma_\tau} \right) \frac{\partial \omega}{\partial x_i} \right]_{,i} \qquad \textbf{(6.15)}$$

α	β	$\beta*$	σ_k	σ_τ
5/9	0.075	0.09	2	2

Other kinds of closure models do not adopt the Boussinesq assumption and allow a non linear resolution of the Reynolds stress tensor. In some cases, the turbulence treatment is anisotropic and the turbulence resolution differs from spatial direction. This is quite well adapted to approach recirculation, high shear stress gradient regions and curvatures [Gretler, 2000] but needs a long computing time (Solving *7* equations instead *2*) and the convergence is not so stable as with *2*-equation models. Except from the resolution of the Reynolds stresses, the particular BSL RSM "Baseline Reynolds Stress Model" is based on an ω- equation, but integrating blending coefficients from the k-equation. As well as for the SST model, an interpolation is made between the near to wall regions (using an ω resolution) and the free stream region (using an ε resolution).

The BSL-RSM turbulence model is presented here, where six equations are used to solve the Reynolds stress tensor by an anisotropic way and the seventh equation corresponds to the ε or the ω resolution, depending on the location of the fluid cell. Only the ω equation is presented here because of automatic use of the ω equation in cooling channels (the distance to wall is so restricted that only the ω equation is used for the SST or the BSL-RSM turbulence models).

$$\frac{\partial(\rho\tau_{ij})}{\partial t}+\frac{\partial(U_k\rho\tau_{ij})}{\partial x_k}=-\rho P_{ij}+\frac{2}{3}\beta'\rho\omega k\delta_{ij}-\rho\Pi_{ij}+\frac{\partial}{\partial x_k}\left(\left(\mu+\frac{\mu_t}{\sigma^*}\right)\frac{\partial\tau_{ij}}{\partial x_k}\right) \qquad \textbf{(6.16)}$$

$$\frac{\partial(\rho\omega)}{\partial t}+\frac{\partial(U_k\rho\omega)}{\partial x_k}=\alpha\frac{\omega}{k}P_k-\beta\rho\omega^2+\frac{\partial}{\partial x_k}\left(\left(\mu+\frac{\mu_t}{\sigma}\right)\frac{\partial\omega}{\partial x_k}\right)+2(1-F_1)\rho\frac{1}{\sigma_2\omega}\frac{\partial k}{\partial x_k}\frac{\partial\omega}{\partial x_k} \qquad \textbf{(6.17)}$$

σ^*	σ	β	α	δ_{ij}	σ_2
1→2	0.856→2	0.075→0.0828	0.44→0.553	1 if i=j ; 0 else	0.856

$$\alpha=\frac{\beta}{\beta'}-\frac{0.41^2}{\sigma\sqrt{\beta'}} \qquad \textbf{(6.18)}$$

Π_{ij} is the pressure-strain correlation and P_{ij} is the production tensor of Reynolds Stress.

$$P_{ij}=\tau_{ik}\frac{\partial U_j}{\partial x_k}+\tau_{jk}\frac{\partial U_i}{\partial x_k} \qquad \textbf{(6.19)}$$

- *Wall treatment*

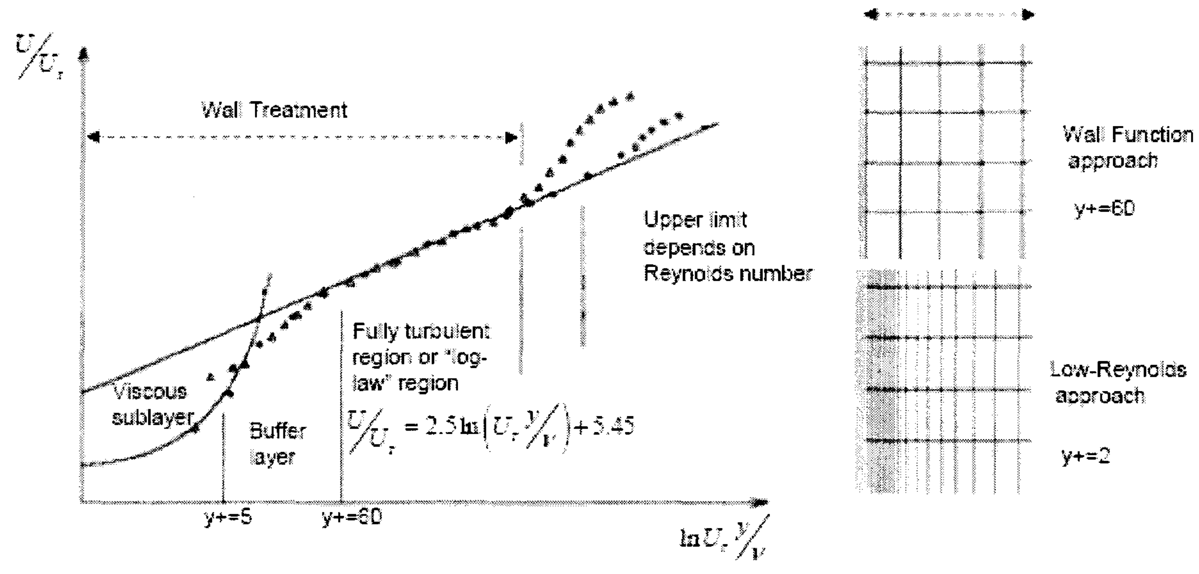

Figure 105 : Wall function/Low-Reynolds Model description.

There are two different approaches for the near-wall treatment. First, there are "logarithmic wall functions", in which the viscosity-affected inner region is not numerically calculated but replaced by semi-empirical e to bridge the viscosity-affected region between the wall and the fully-turbulent region. The other approach is called Low-Reynolds Model, in which the turbulence models are modified to enable the viscosity-affected region to be resolved with a fine mesh near the wall, including the dynamical resolution of the laminar viscous sublayer. This method is more precise than the logarithmic approximation but requires much more cells near the wall domains. These two approaches are depicted in Figure 105.

y+ represents the dimensionless distance to wall $y+ = \frac{U_\tau y}{\upsilon}$ and U_τ the main flow friction velocity $U_\tau = \sqrt{\frac{\tau_w}{\rho}}$.

Appendix 2: Manufacturing and Assembly

A straight channel (first EH3C-test specimen) and a curved channel with asymmetrical concave heating (second EH3C-test specimens) were machined, to study the concave curvature effects on asymmetrical heat transfer, see Figure 106. The following pictures (Figure 106) show the EH3C straight and concave curved channels.

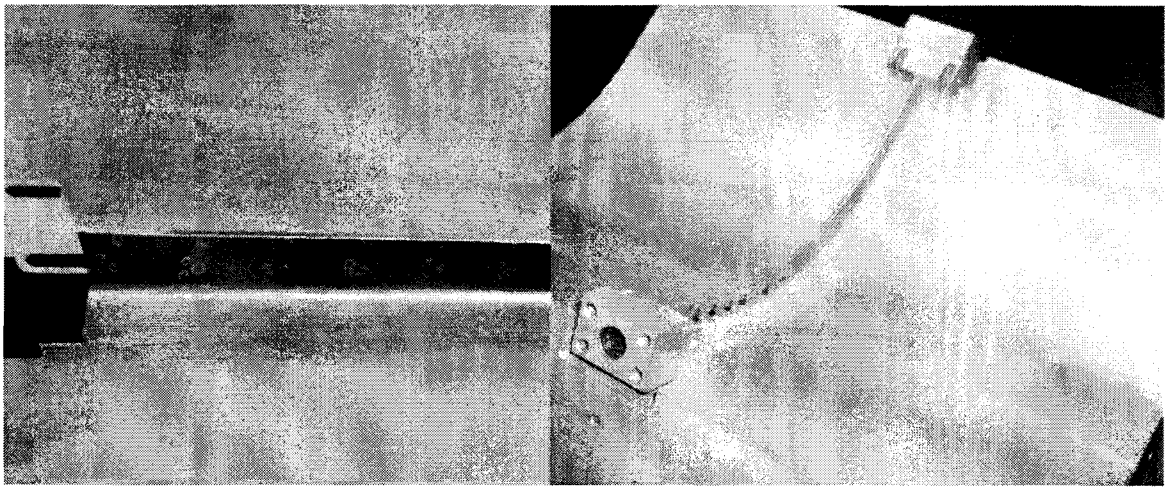

Figure 106 : Straight and curved EH3C channels.

A special copper alloy (Elbrodur G) was chosen as material, used to be the predilection material of the DLR combustion chambers. Elbrodur G has been already investigated and presents a good compromise between mechanical and thermal properties (high heat capacity and thermal conductivity for a consequent mechanical resistance). The thermal parameters of this copper alloy were investigated [Oschwald, 2004].

The fabrication process of the EH3C test specimen is briefly described:

- Machining of the thermal nozzle (block + channel walls), Figure 107a
- Milling of the micro-channel (milling cut of *0.5 mm* width) along the throat section of the thermal nozzle, Figure 107a
- Enclosure process (electro-deposition) with copper, Figure 107b
- Machining of the upper-wall profile of the channels, Figure 107b
- Drilling of micro holes for the sensors implementation, Figure 107b
- Nickel layering by chemical process to limit radiative losses and oxidation, Figure 107c
- Implementation of the convergent and divergent at the channel in- and outlet, Figure 107c
- Drilling of the electrical cartridges emplacements (Figure 107d)
- Installation of the sensors, of the maintaining system, of the spring system, Figure 107e

Concerning the sensors themselves, to ensure better thermal contact, the thermocouples are pressed on the channel wall with a spring system delivering a force up to *2 N* per sensor, as it is shown in Figure 107e. This mechanical force increases the contact surface and avoids change of the measured temperature during experiments due to vibrations, shocks or mechanical deformations.

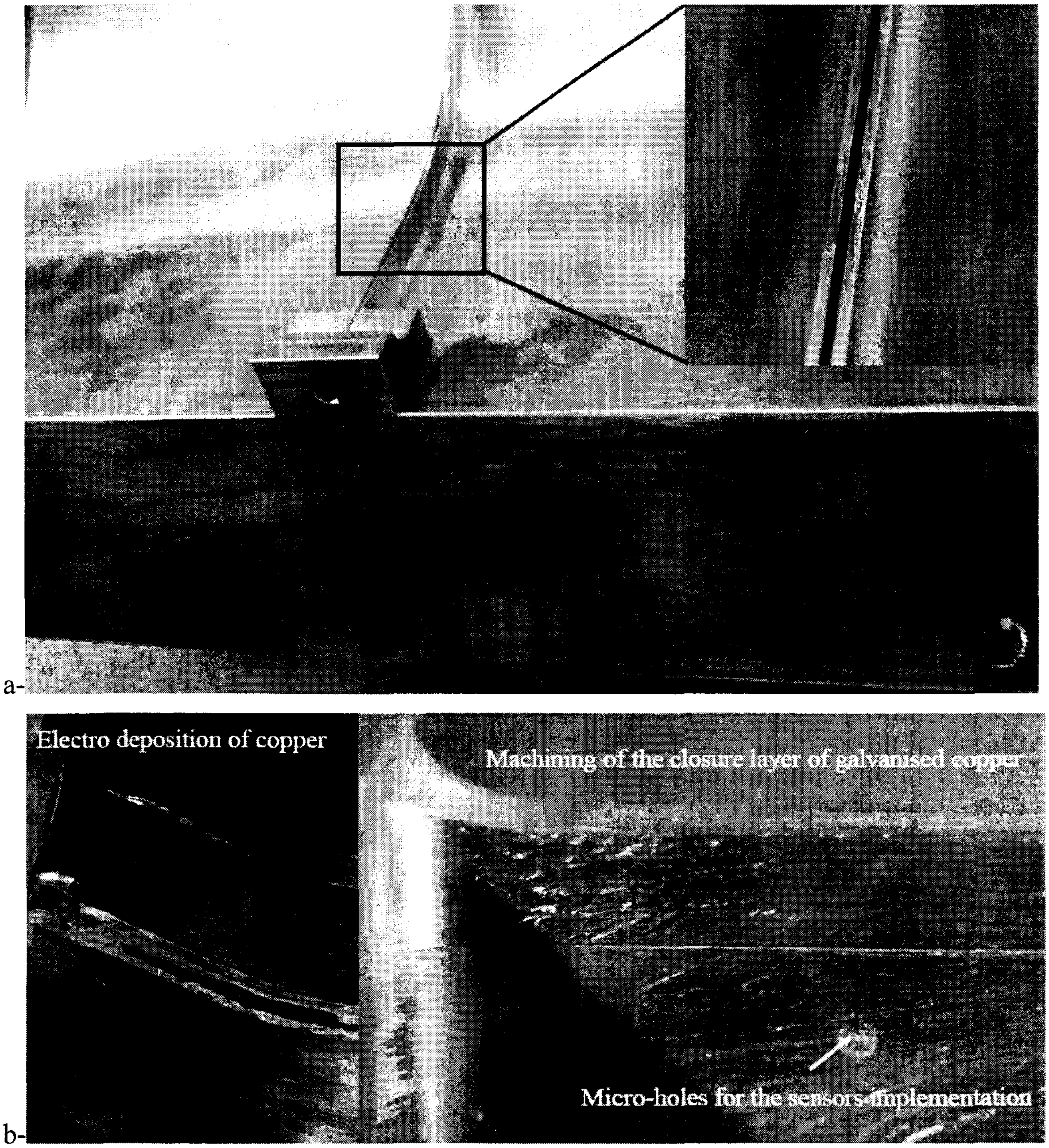

Figure 107 : Machining process of the EH3C test specimens a- and b-.

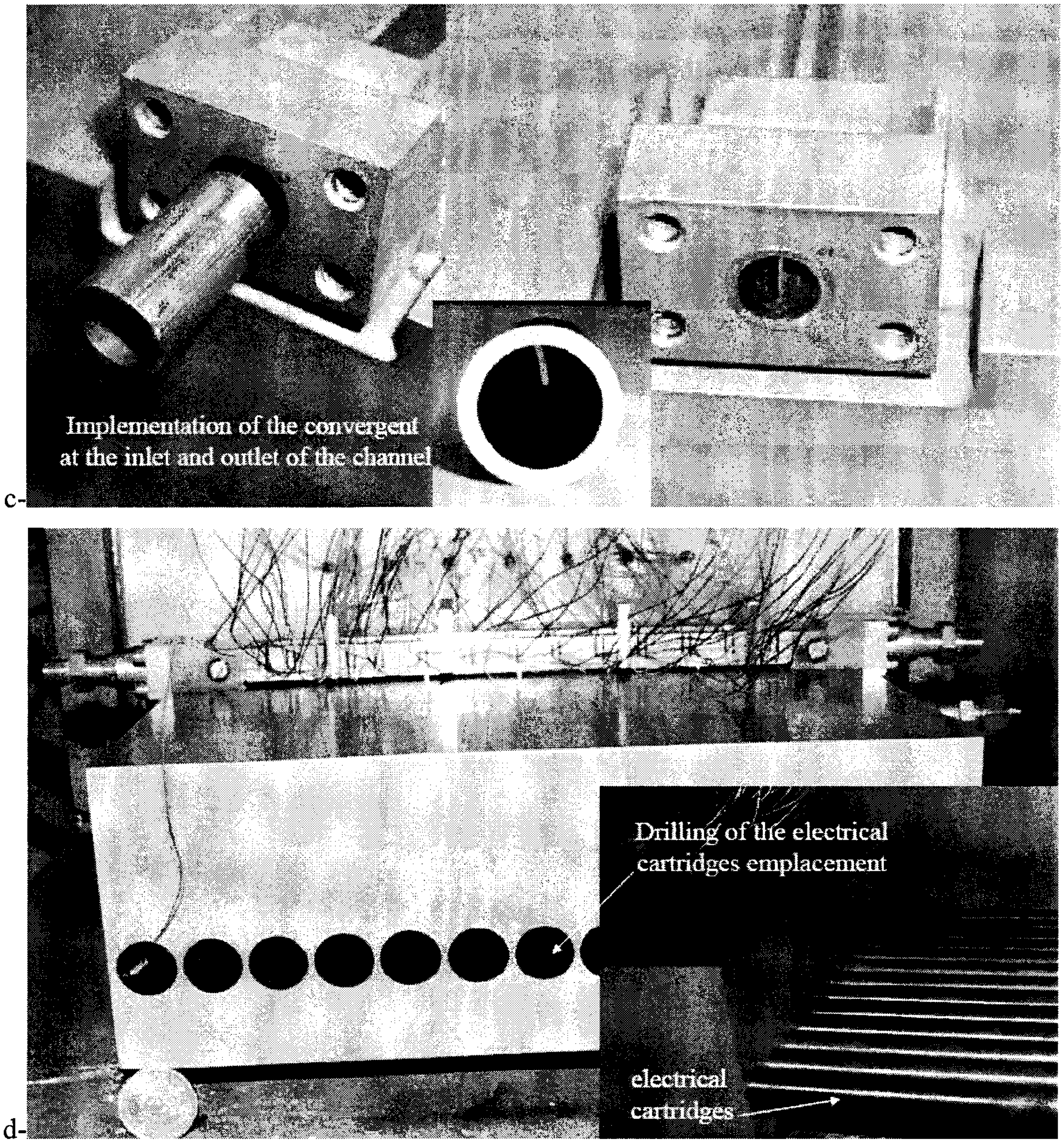

Figure 107 : Machining process of the EH3C test specimens c- and d-.

e-

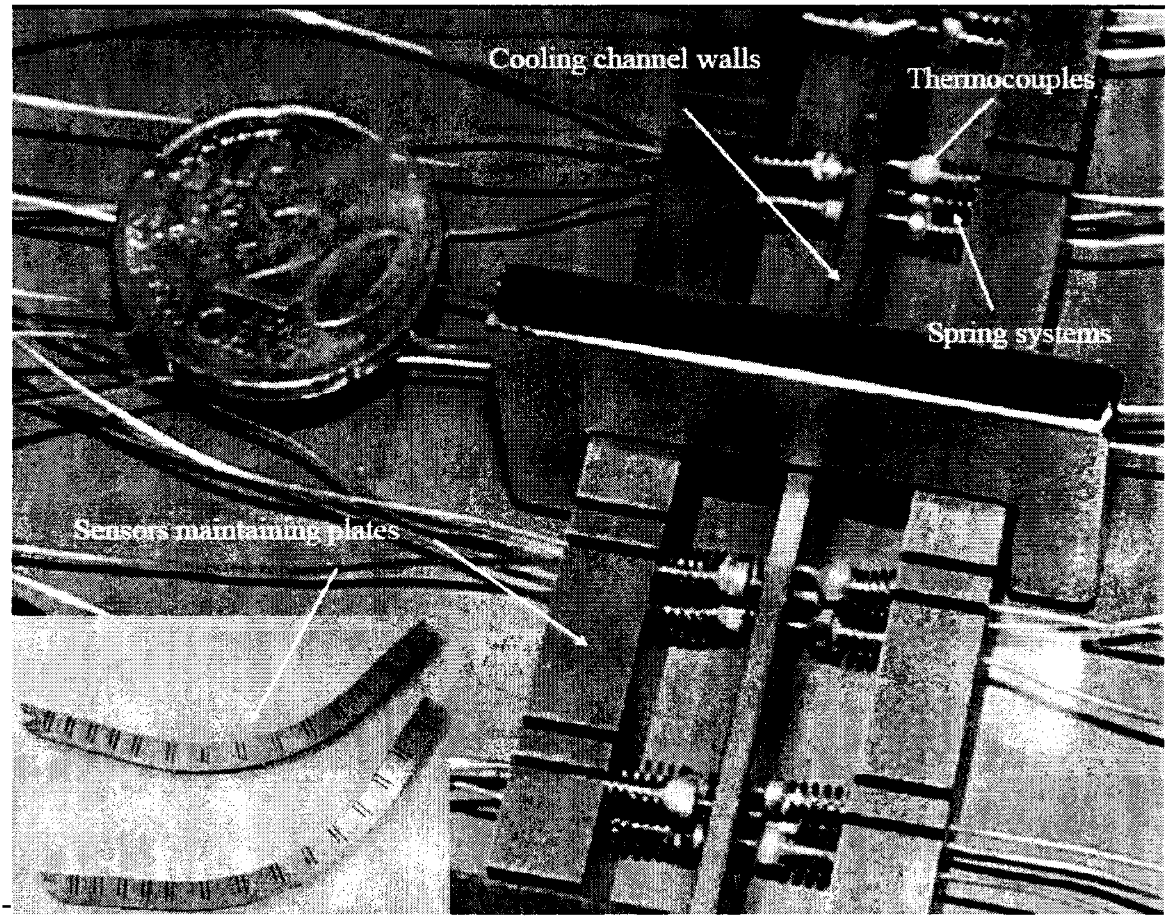

Figure 107 : Machining process of the EH3C test specimens e-.

Appendix 3: Electrical and heat transfer layout

Considering the probable heat losses between the test specimens and their environments through convection, conduction and radiation, the electrical power requirement was defined. The copper block is put in a containment box for security reasons on the one hand, and in a nitrogen bath on the other hand, avoiding oxidation of the heated specimens. The conduction process can be neglected with the ambient nitrogen because of very low conductivity of the gas, $\lambda_{N_2} \approx 0.032\,Wm^{-1}K^{-1}$.

$$\dot{Q}_{losses} = \dot{Q}_{convection} + \dot{Q}_{radiation} + \underbrace{\dot{Q}_{conduction}}_{neglected} \tag{6.20}$$

3D thermal numerical simulations were carried out with cylindrical locations for the cartridges in the block, as shown in Figure 108. The test specimen geometry was divided into two for symmetry reason. The fluid was modelled with a temperature of 80K and a heat transfer coefficient of $h = 50000\ W.m^{-2}.K^{1}$ through all channel walls. The heat cartridges provide a constant heat flux density over their cylindrical contact surface. This constant heat flux density was changed in order to reach the maximal temperature that the material in the copper block can withstand (about *750 K*). $\dot{q}_{heaters} = 5.8\ Wcm^{-2}$ was found to be an ideal heating system . Imposing a constant temperature at the cartridges periphery, the delivered value of the heat flux density through the heaters periphery has an averaged of the conclusion of the preceding simulation.

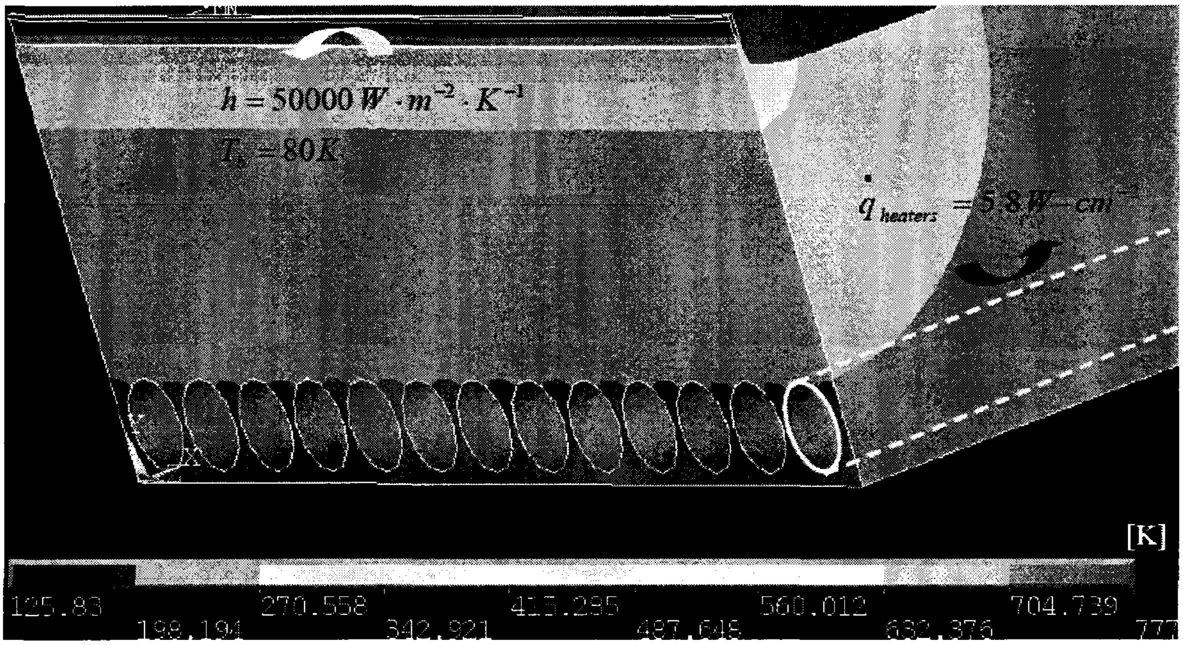

Figure 108 : 3D thermal numerical simulation of the straight EH3C test specimen.

The electrical need can be thus evaluated $P_{el} = \dot{q}_{heaters}\, S_{heaters} = 875W$ per electrical heaters, giving a need of *13* times this value (*13* cartridges giving about *12 kW*) for the straight test specimen and *16* times for the curved test specimen (about *14 kW*).

The following relation estimates the heat losses by radiation from the heated copper alloy to the containment walls, made in steel, in the curved channel configuration:

$$\dot{Q}_{radiation} = \frac{\sigma}{\dfrac{1}{\varepsilon_{copper}} + \dfrac{S_{copper}}{S_{steel}}\left(\dfrac{1}{\varepsilon_{steel}} - 1\right)} S_{copper}\left(T^4_{copper} - T^4_{steel}\right) \tag{6.21}$$

The emissivity factor depends on the copper and steel surfaces. Assuming that the emissivity of the steel is *0.3* (non-oxide steel), the radiation coefficient for the copper alloy contributes to the radiative heat losses in high proportion:

$$\begin{aligned}
\varepsilon_{copper-polish} &= 0.03 \rightarrow \dot{Q}_{copper\rightarrow steel} = 75W \\
\varepsilon_{copper-scrape} &= 0.07 \rightarrow \dot{Q}_{copper\rightarrow steel} = 173W \\
\varepsilon_{copper-oxidised} &= 0.8 \rightarrow \dot{Q}_{copper\rightarrow steel} = 1514W
\end{aligned} \tag{6.22}$$

The oxidation of Elbrodur must be prevented or thermal radiation will represent *10%* of the electrical need. A solution is to galvanize the surface with a nickel layer. Indeed, nickel does not oxidize and has a small emission coefficient $\varepsilon_{Ni}(700K) = 0.1$ that corresponds to a loss of *244 W* (*1.7%*) for the curved channel. Concerning the straight channel, this has a lower heated surface in its block, the radiative losses reach *180 W*.

To minimize natural convection heat losses, the experiments were carried out with vacuum containment. The vacuum level is unfortunately so bad (*10 mbar*) that humidity highly perturbs the thermocouples' location (by ice deposition in the cryogenic range on the upper part of the channels). Indeed, the repeatability tests provided under vacuum are not satisfactory. It has been experimentally shown that nitrogen environment really contains less humidity than the provided vacuum. With nitrogen in the containment, the measurements are no more perturbed by ice formation, but now the convective losses have to be taken into account (see the repeatability tests in the part 5.2.4).

The natural convection thermal losses were estimated, considering the experimental conditions: the containment contains nitrogen at *1.5 b*ar at a temperature of *400 K* during a test. The thermodynamic gas properties under these conditions can be derived from the Prandtl number and the Grashof number.

$$\begin{aligned}
\Pr &= \frac{\mu c_p}{\lambda} \sim \frac{2.2\cdot 10^{-5} \times 1045}{0.032} \sim 0.72 \\
Gr &= \frac{g {L_{base}}^3 \beta_d \Delta T}{\upsilon^2} \sim \frac{9.81 \times 0.2^3 \times 0.0025 \times 250}{\left(0.17\cdot 10^{-4}\right)^2} \sim 1.7\cdot 10^8
\end{aligned} \tag{6.23}$$

A standard dimensionless relation can deliver a Nusselt number of the natural convection around the containment (Gersten, 1992):

$$\begin{aligned}
Nu &= 0.8\left(Gr \Pr^2\right)^{1/4} \\
Nu &\sim 84 \rightarrow h = \frac{Nu\lambda}{L_{base}} \sim 13\ Wm^{-2}K^{-1}
\end{aligned} \tag{6.24}$$

With this value of heat transfer coefficient for natural convection and the heat losses were estimated for the two test configurations, the straight and the curved test specimen:

$$\dot{Q}_{convection} = h(T_{copper} - T_{N_2})S = 650\,W \tag{6.25}$$

The same calculation for the curved channel gives *870 W* and represents *6%* loss per natural convection.

Hence the upper part of the channel cannot be fully adiabatic. The very low temperature (under *230 K* in the upper part of the channel) can imply an additional heat transfer from the environment to the fluid which would minimise the asymmetrical heating and the fin effect.

$$\Pr = \frac{\mu c_p}{\lambda} \sim \frac{2.2 \cdot 10^{-5} \times 1045}{0.032} \sim 0.72$$
$$Gr = \frac{g L_{base}{}^3 \beta_d \Delta T}{\upsilon^2} \sim \frac{9.81 \times 0.0019^3 \times 0.0025 \times (400-250)}{\left(0.17 \cdot 10^{-4}\right)^2} \sim 87 \qquad \textbf{(6.26)}$$

$$Nu = 0.8\left(Gr \Pr^2\right)^{1/4}$$
$$Nu \sim 2.06 \rightarrow h = \frac{Nu\lambda}{L_{base}} \sim 34 W m^{-2} K^{-1} \qquad \textbf{(6.27)}$$

$$\dot{Q}_{up\_convection} = h_{up}(T_{N_2} - T_{up}) S_{up\_channel} < 1W \qquad \textbf{(6.28)}$$

This effect can be neglected.

Appendix 4: Flow requirements of the EH3C experiments

Concerning the hydrogen tests, the fluid properties were evaluated at the entrance of the channels, with the ideal gas model:

$\rho = 12.45\ kg\ m^{-3}$

$c_p = 12888\ J\ kg^{-1}\ K^{-1}$

$\lambda = 0.068\ W\ m^{-1}\ K^{-1}$

$\mu = 0.39\ 10^{-5}\ Pa\ s$

The surface of a section is noted S_c:

$$S_c = h_C\, w_C = 0.5 \cdot 10^{-3}\ \text{☺}\ 4.6 \cdot 10^{-3} = 2.3 \cdot 10^{-6}\ m^2 \qquad \textbf{(6.29)}$$

The mass flow rate through the channel was determined to still have supercritical and subsonic conditions at the channel outlet. The outlet pressure must stay greater than the critical pressure ($p_{outlet} > 13.15\ bar$) and the outlet velocity must remain below sound speed (the outlet Mach number $M_{outlet} < 1$). The mass flow rate was numerically estimated taking into account the compressibility effects, the high heat input along the channel and the pressure losses along the channel, see in the chapter 4. The mass flow rate of the hydrogen would reach $5\ g \cdot s^{-1}$.

Appendix 5: Structural layout and experimental qualification

The material is submitted to high thermal dilatation in the ground part (highest temperature) and not in the channel (lowest temperature) which creates high tensile stresses (up to *0.6%* as total deformation). To check the mechanical resistance of these test specimens, numerical studies were compared to literature [Popp, 1996] and to experimental results on test prototypes.

Coupled numerical simulations delivered a thermal field with mechanical load distribution. Numerical thermo-mechanical simulations were performed in order to evaluate the 3D thermal strain, as represented in Figure 109. The thermal stresses are really high (*350 MPa*) in the structure along the channel. Indeed, the hot massive copper block imposes its thermal dilatation to the channel walls.

The corresponding global (mechanical and thermal, elastic and plastic) strain reaches *0.6%* of global deformation.

The theoretical life cycle that corresponds to the level of this deformation indicates more than *100* life cycles.

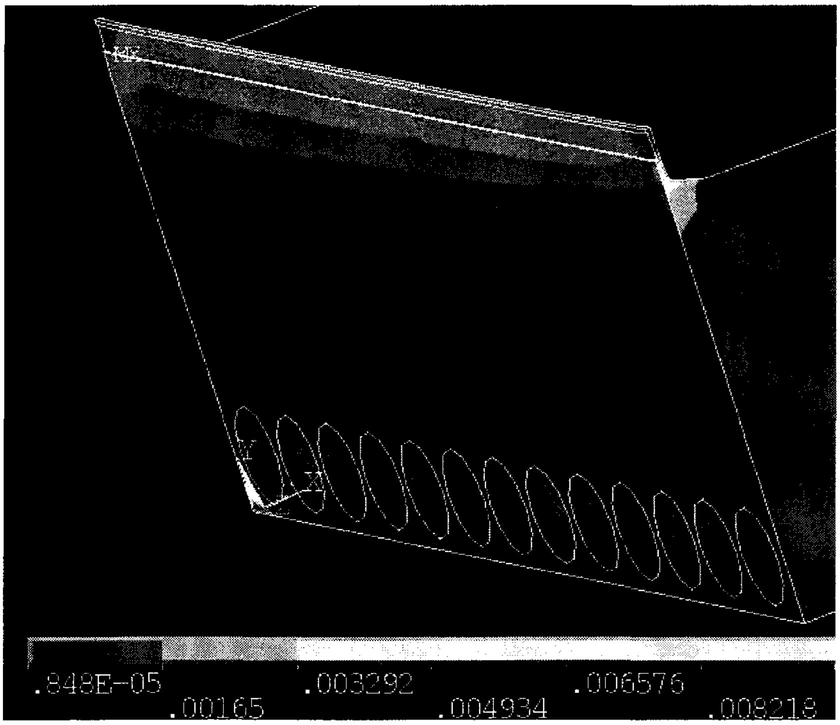

Figure 109 : Coupled thermo-mechanical simulation to estimate the total strain in the channel structure, scale represents total deformation.

Several prototypes were designed and tested by thermo-mechanical fatigue processes. These prototypes were manufactured under the geometrical requirements of the EH3C test specimen (see 3.1.2.1), without the block to reduce the need of material. The global manufacturing process of the EH3C test specimens were validated by the fabrication of two prototypes. The milling, cutting and electro-deposition processes were verified. The two prototypes were thermally loaded by introducing liquid nitrogen in the heated channel. This thermal gradient corresponds to an axial global strain of *0.4%*. This thermal loading was experimentally repeated several times in order to create thermal cycles.

Figure 110 illustrates the fatigue tests on these prototypes.

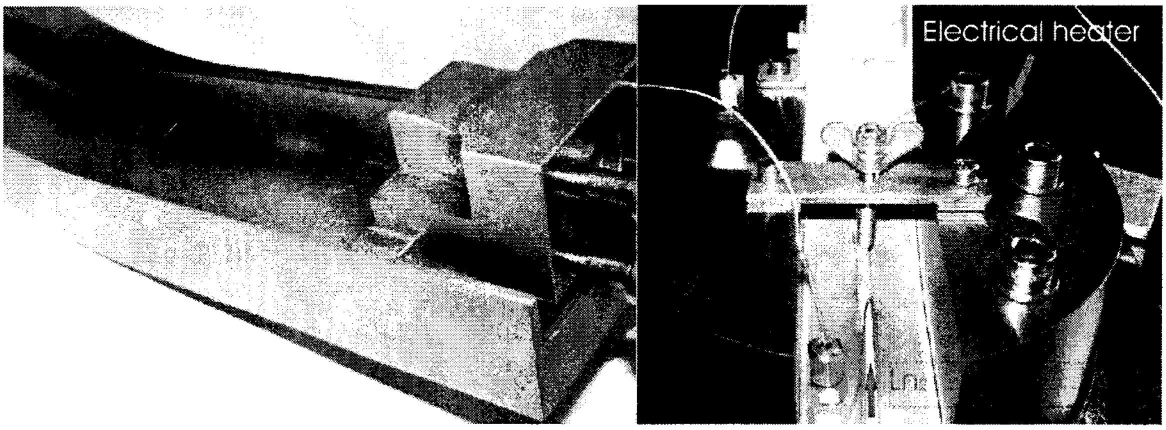

Figure 110 : Prototypes under thermal and mechanical load cycles.

Appendix 6: Test bench

A special test bench was designed and built up for “cold flow” experiments at DLR, including the EH3C experiments. The fluid supply system can provide a maximum pressure of *100 bar* for different media (nitrogen, hydrogen, methane, helium, oxygen…). A nitrogen cooling system was developed: a heat exchanger is submerged in a liquid nitrogen bath. Figure 111 proposes an overview of the simplified flow diagram. Figure 112 illustrates the test bench. The measurement and command systems were realised with the commercial interface software Labview. The mass flow is controlled by a measurement with a Coriolis mass flow meter and a cryogenic valve. An internal measurement panel of pressure and temperature sensors controls the enthalpy distribution along the experimental chain through the different components (inlet valve, nitrogen bath, Coriolis mass flow meter, valves, test specimen…).

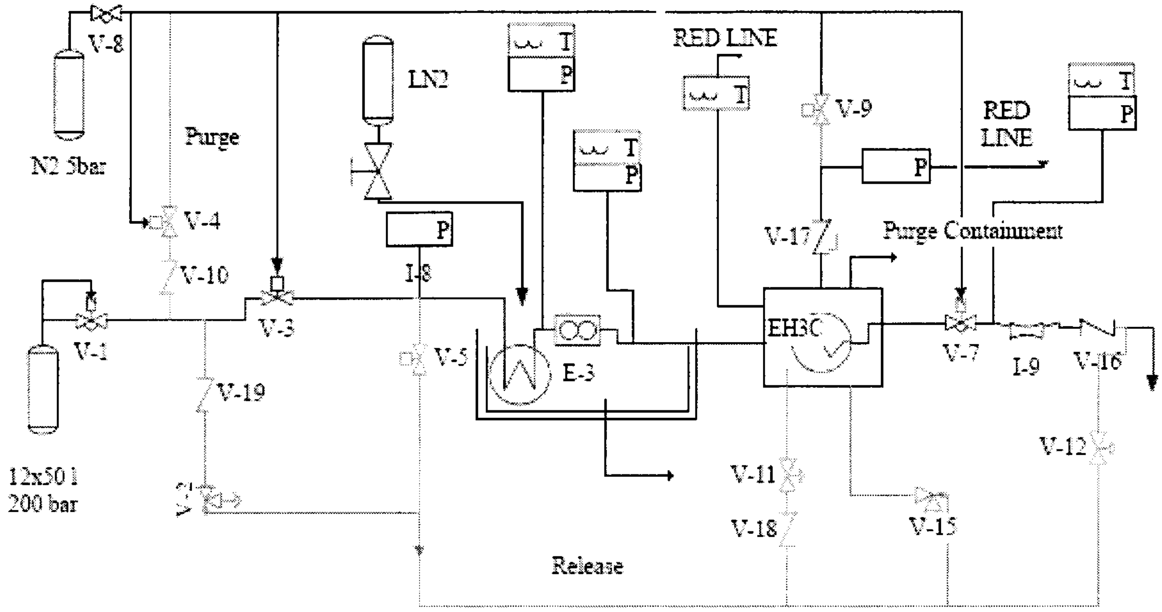

Figure 111 : Flow diagrams of the DLR M3.2 Test Bench.

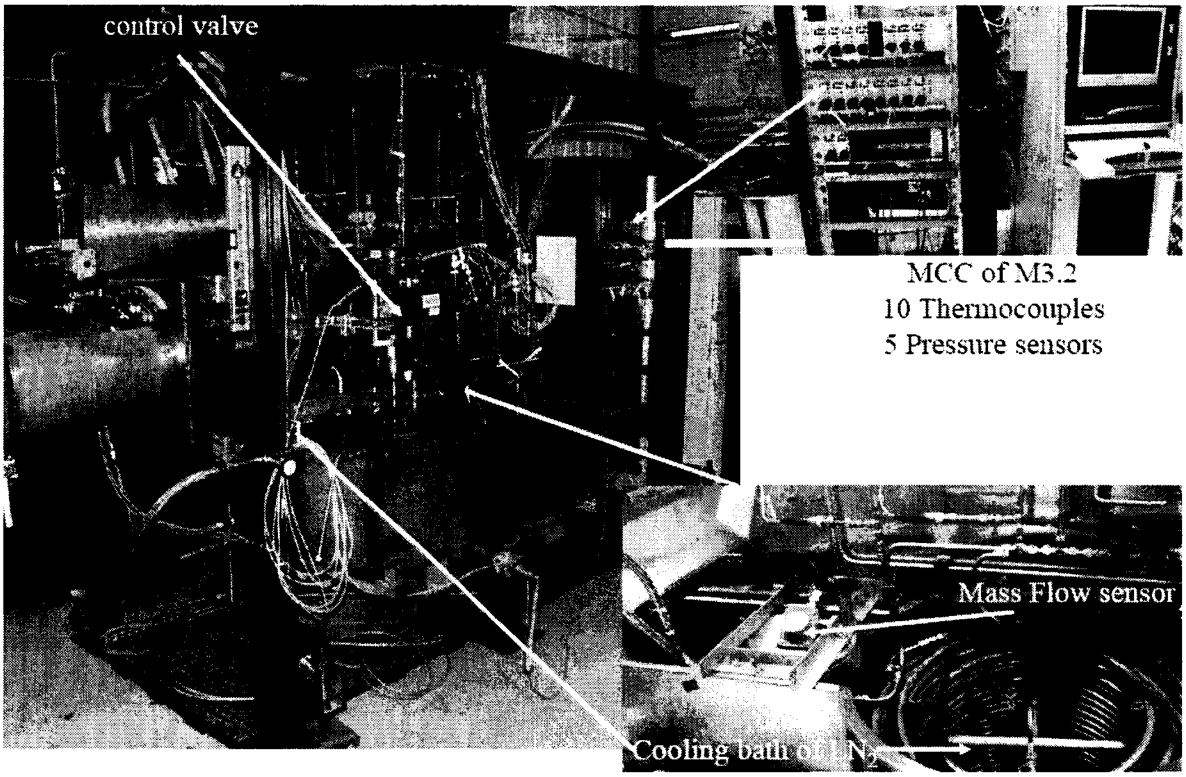

Figure 112 : Picture of the M3.2 test bench.

An external data acquisition system was developed to record the reading of more than *100* thermocouples with a sampling rate of *1 kHz*. The four electronic acquisition cards have a resolution of *16 bits* each.

Reference temperatures for the thermocouples (cold junction) are measured on the acquisition cards by Pt-100 sensors.

An electrical power supply system was built to deliver electrical power of up to *25 kW*. A panel of *20* PID regulators was integrated, in order to control the electrical power delivered into the test specimen. The electrical cartridges have an integrated thermocouple to directly regulate the dissipated power to obtain the desired temperature.

All the EH3C experiments had to follow the security norms preventing possible leakages of the galvanic upper layer of the channels. A containment was designed to ensure hermetic environment and security (security valves and explosion protected area), as shown in Figure 113.

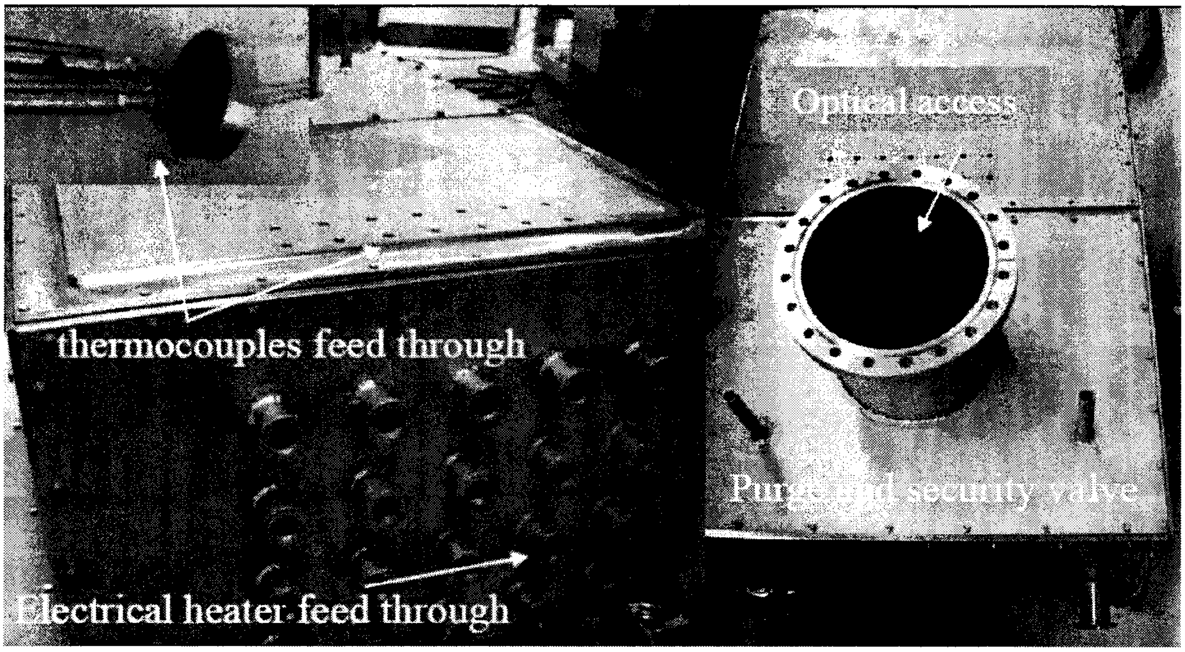

Figure 113 : Containment ensuring hermetic environment and explosion protection.

Appendix 7: Coordinates of the 98 EH3C-thermocouples locations

	Z	Y		Z	Y		Z	Y		Z	Y		Z	Y
$T_{14,1}$	183.3	-1.5	$T_{11,1}$	138.3	-1.5	$T_{8,1}$	93.3	-1.5	$T_{5,1}$	48.3	-1.5	$T_{2,1}$	18.3	-1.5
$T_{14,2}$	183.3	-0.8	$T_{11,2}$	138.3	-0.8	$T_{8,2}$	93.3	-0.8	$T_{5,2}$	48.3	-0.8	$T_{2,2}$	18.3	-0.8
$T_{14,3}$	180.7	-0.1	$T_{11,3}$	135.7	-0.1	$T_{8,3}$	90.7	-0.1	$T_{5,3}$	45.7	-0.1	$T_{2,3}$	15.7	-0.1
$T_{14,4}$	180.7	0.5	$T_{11,4}$	135.7	0.5	$T_{8,4}$	90.7	0.5	$T_{5,4}$	45.7	0.5	$T_{2,4}$	15.7	0.5
$T_{14,5}$	183.3	1.4	$T_{11,5}$	138.3	1.4	$T_{8,5}$	93.3	1.4	$T_{5,5}$	48.3	1.4	$T_{2,5}$	18.3	1.4
$T_{14,6}$	183.3	2.9	$T_{11,6}$	138.3	2.9	$T_{8,6}$	93.3	2.9	$T_{5,6}$	48.3	2.9	$T_{2,6}$	18.3	2.9
$T_{14,7}$	180.7	5.6	$T_{11,7}$	135.7	5.6	$T_{8,7}$	90.7	5.6	$T_{5,7}$	45.7	5.6	$T_{2,7}$	15.7	5.6
$T_{13,1}$	168.3	-1.5	$T_{10,1}$	123.3	-1.5	$T_{7,1}$	78.3	-1.5	$T_{4,1}$	38.3	-1.5	$T_{1,1}$	8.3	-1.5
$T_{13,2}$	168.3	-0.8	$T_{10,2}$	123.3	-0.8	$T_{7,2}$	78.3	-0.8	$T_{4,2}$	38.3	-0.8	$T_{1,2}$	8.3	-0.8
$T_{13,3}$	165.7	-0.1	$T_{10,3}$	120.7	-0.1	$T_{7,3}$	75.7	-0.1	$T_{4,3}$	35.7	-0.1	$T_{1,3}$	5.7	-0.1
$T_{13,4}$	165.7	0.5	$T_{10,4}$	120.7	0.5	$T_{7,4}$	75.7	0.5	$T_{4,4}$	35.7	0.5	$T_{1,4}$	5.7	0.5
$T_{13,5}$	168.3	1.4	$T_{10,5}$	123.3	1.4	$T_{7,5}$	78.3	1.4	$T_{4,5}$	38.3	1.4	$T_{1,5}$	8.3	1.4
$T_{13,6}$	168.3	2.9	$T_{10,6}$	123.3	2.9	$T_{7,6}$	78.3	2.9	$T_{4,6}$	38.3	2.9	$T_{1,6}$	8.3	2.9
$T_{13,7}$	165.7	5.6	$T_{10,7}$	120.7	5.6	$T_{7,7}$	75.7	5.6	$T_{4,7}$	35.7	5.6	$T_{1,7}$	5.7	5.6
$T_{12,1}$	153.3	-1.5	$T_{9,1}$	108.3	-1.5	$T_{6,1}$	63.3	-1.5	$T_{3,1}$	28.3	-1.5			
$T_{12,2}$	153.3	-0.8	$T_{9,2}$	108.3	-0.8	$T_{6,2}$	63.3	-0.8	$T_{3,2}$	28.3	-0.8			
$T_{12,3}$	150.7	-0.1	$T_{9,3}$	105.7	-0.1	$T_{6,3}$	60.7	-0.1	$T_{3,3}$	25.7	-0.1			
$T_{12,4}$	150.7	0.5	$T_{9,4}$	105.7	0.5	$T_{6,4}$	60.7	0.5	$T_{3,4}$	25.7	0.5			
$T_{12,5}$	153.3	1.4	$T_{9,5}$	108.3	1.4	$T_{6,5}$	63.3	1.4	$T_{3,5}$	28.3	1.4			
$T_{12,6}$	153.3	2.9	$T_{9,6}$	108.3	2.9	$T_{6,6}$	63.3	2.9	$T_{3,6}$	28.3	2.9			
$T_{12,7}$	150.7	5.6	$T_{9,7}$	105.7	5.6	$T_{6,7}$	60.7	5.6	$T_{3,7}$	25.7	5.6			

Appendix 8: Experimental Procedure

The thermal and the flow dynamical steady states were reached to begin the measurements. The steady states are considered to be reached when the following parameters are constant over the time: Inlet and outlet temperatures of the channel, mass flow rate and temperature of the block.

The mass flow rate was set up to obtain subsonic flow in the channel. The outlet pressure was thus restricted to the sonic limit value, insuring an outlet Mach number $M<1$.

In order to reduce the mechanical loads on the galvanic layer, closing the cooling channel, the thermal stresses have to be minimised. The thermal strains cannot be avoided but it can be useful to avoid thermal shocks. Indeed, if the channel is heated first (up to *400°C* for the hydrogen case), and afterwards the cold fluid enters the channel, the outlet of the channel still has high temperature. This induces additional axial thermal stresses during the transient and stabilizing phase. It was thus decided to let the coolant flow first through the channel and only afterwards heat the blocks. The galvanic layer will not reach high temperatures.

The test procedure can be summarised:

- Ensure leakage tests of the experimental feed lines with helium
- Purge of the experimental feed line with nitrogen
- Ensure vacuum and thus nitrogen overpressure in the containment
- Fill in the lines gradually with hydrogen/methane up to *40 bar*
- Fill in the bath with liquid nitrogen with the inlet valve open (only for the hydrogen experiment)
- Open the controlling valve to cool down the channel, and let a mass flow rate develop in the experimental chain and the channel
- Switch on the electrical heating
- Wait for thermal and dynamical steady states
- Store of data and change mass flow rate
- Switch off the electrical heating
- Fill out the nitrogen bath, while keeping a mass flow rate of cold propellant through the channel.
- Wait for ambient temperatures
- Purge the experimental chain with nitrogen.

Appendix 9: Inlet and outlet fluids properties

Under *38 bar* and *78 K*, hydrogen has the following properties, with the aid of the NIST program [Younglove, 1982]:

$c_p(H_2\,inlet) = 12730\ J\ kg^{-1}\ K^{-1}$

$\lambda(H_2\,inlet) = 0.0664\ W\ m^{-1}\ K^{-1}$

$\mu(H_2\,inlet) = 0.389 \cdot 10^{-5}\ Pa\ s$

Under *37 bar* and *296 K*, methane has the following properties:

$c_p(CH_4\,inlet) = 2472\ J\ kg^{-1}\ K^{-1}$

$\lambda(CH_4\,inlet) = 0.03676\ W\ m^{-1}\ K^{-1}$

$\mu(CH_4\,inlet) = 1.176\ 10^{-5}\ Pa\ s$

At the outlet of the straight channel, the fluid properties were estimated at the measured pressure and temperature conditions, with the aid of the NIST program:

Under 26 bar and 231 K, hydrogen has the following properties:

$c_p(H_2\,outlet) = 14016\ J\ kg^{-1}\ K^{-1}$

$\lambda(H_2\,outlet) = 0.15279\ W\ m^{-1}\ K^{-1}$

$\mu(H_2\,outlet) = 0.756 \cdot 10^{-5}\ Pa\ s$

Under 23 bar and 366 K, methane has the following properties:

$c_p(CH_4\,outlet) = 2499\ J\ kg^{-1}\ K^{-1}$

$\lambda(CH_4\,outlet) = 0.0457\ W\ m^{-1}\ K^{-1}$

$\mu(CH_4\,outlet) = 1.354\ 10^{-5}\ Pa\ s$

Moreover, the hydrogen properties were estimated with the Redlich-Kwong and the Younglove [Younglove, 1982, Redlich-Kwong, 1949] models along the center streamline of the straight channel, with the aid of the CFD calculations.

Figure 114 illustrates the heat capacity of hydrogen along the channel length.

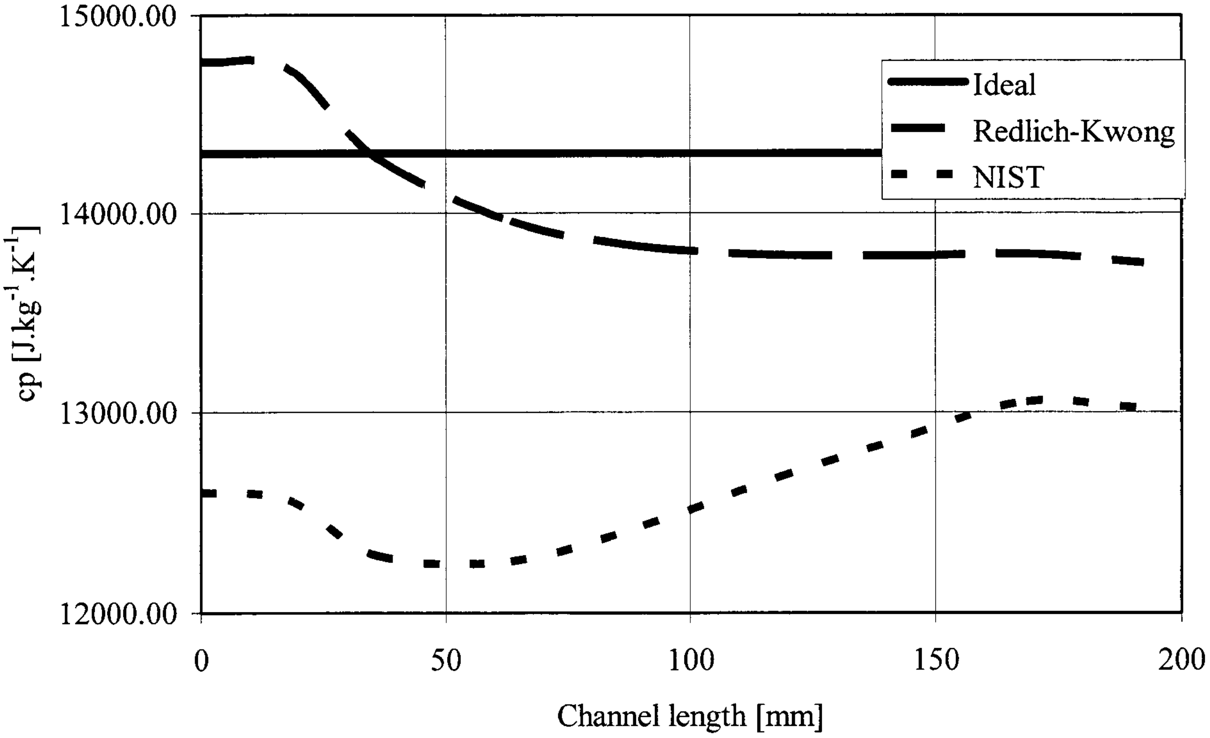

Figure 114 : Hydrogen heat capacity along the channel length, taken in the middle of the channel from numerical simulations.

BIBLIOGRAPHY

Adams, T., M., Abdel-Khalik, S., I., Jeter, S., M., Quresci, Z., H., An Experimental Investigation of Single-Phase Forced Convection in Microchannels, Int. J. Heat Mass Transfer, Vol. 41, Nos 6-7, pp.851-857, 1998

Adler, M., Strömung in gekrümmten Rohren, Zeitschrift für Angewandte Mathematik und Mechanik, Band 14, Heft 5, Kaiser Wilhelm Institut für Strömungsforschung, Göttingen, Oktober 1934.

Belfort, G., Mallubhotla, H., Edelstein, W., A., Early, T., A., Bifurcation and Application of Dean Vortex Flows, 12th International Couette-Taylor Workshop, September 6-8, 2001, Evanston, IL USA.

Berger, S.A., Talbot, L., Department of Mechanical engineering, University of California, Berkley, California 94720, Yao, L.-S., Department of Mechanical and Aerospace Engineering, Arizona State University, Tempe, Arizona 85281, *Flow in curved pipes* Am. Rev. Fluid Mech., 1983, 15: 461-512.

Blasius, H., Das Ähnlichkeitsgesetz bei Reibungsvorgängen, Physikalische Zeitschrift, Vol. 12, 1911, pp. 1175-1177, or refer to Schlichting, H., Boundary Layer Theory, pp. 560-566, McGraw-Hill, 1968.

Camci, C., Rizzo, D., H., Secondary flow and forced convection heat transfer near endwall boundary layer fences in a 90° turning duct, International Journal of Heat and Mass Transfer 45, pp. 831-843, 2002.

Carlile, J., Quentmeyer, R., An Experimental Investigation of High-Aspect-Ratio Cooling Passages, AIAA-92-3154, 28th Joint Propulsion Conference and Exhibits, July 1992, Nashville.

Choi, S., B., Barron, R., F., Warrington, R., O., Fluid Flow and Heat Transfer in Microtubes, DSC-Vol. 32, Department of Mechanical and Industrial Engineering, Louisiana Technical University, Ruston, Micromechanical Sensors, Actuators, and Systems, ASME 1991.

Dean, R., B., Reynolds Number Dependence of Skin Friction and Other Bulk Flow Variables in Two-Dimensional Rectangular Duct Flow, Journal of Fluids Engineering, June 1978, Vol. 100, pp. 215.

Dean, W.R., *Note on the Motion of Fluid in a Curved Pipe*, M.A., Imperial College of Science, Phil. Mag. iv. p. 208, 1927

Dean, W.R., *The stream-line Motion of Fluid in a Curved Pipe*, (second paper), M.A., Imperial College of Science, Phil. Mag. S7. Vol.5. No 30. April 1928.

Dejc, M.E., Technical gasdynamic, Energia, Moscow, 1974 (Дейч, М.Е., Техническая газодинамика, Энергия, Москва, 1974)

Dexter, C., E., et Al., AIAA Progress in Astronautics and Aeronautics, Liquid Rocket Thrust Chambers, Aspect of Modeling, Analysis, and Design, Vol. 200, Chapter 16, pp. 553-600, 2004.

Dipprey, D., F., Sabersky, R., H., Heat and Momentum Transfer in Smooth and Rough Tubes at Various Prandtl Numbers, International Journal of Heat and Mass Transfer, Vol. 6, pp. 329-353, 1962.

Dittus, F., W., Boetler, L., M., K., Univ. Of Calif. Pubs Engr, p. 443, 1930

Esch, T., Raumfahrtantriebe, Lehr- und Forschungsgebiet, Fahrbereich Luft- und Raumfahrttechnik, Fachhochschule Aachen, 4-3, Oktober 2003.

Finnemore, E., John, J., Franzini, B., “Fluid Mechanics: with engineering Applications”, Tenth Edition

Fröhlich, A., Immich, H., LeBail, F., Popp, M., Three-Dimensional Flow Analysis in a Rocket Engine Coolant Channel of High Depth/Width Ratio, AIAA 91-2183, 27th Joint Propulsion Conference, June 24-26, 1991, Sacramento, California, USA.

Fröhlich, A., Popp, M., Schmidt, G., Thlemann, D., Heat Transfer Characteristics of H2/O2 Combustion chambers, AIAA 93-1826, AIAA/SAE/ASME/ASEE Joint Propulsion Conference, 1993

Gessner, F., B., Jones, J., B., On some Aspect of fully-developed turbulent flow in rectangular channels, J. Fluid Mech. (1965), vol. 23, pp. 689-713.

Gersten, K., Herwig, H., Strömungsmechanik, Grundlagen und Fortschritte der Ingenieurwissenschaften, Vieweg, 1992

Gersten, K., Schlünder, E. U., Heat Exchanger Design Handbook, Vol. 2, Fluid Mechanics and Heat Transfer, VDI-Verlag, Düsseldorf, 1983, pp. 2.2.2-2 to 2,2.2-21

Girgis, I., G., Liu, J., T., C., Mixing enhancement via the release of strongly nonlinear longitudinal Görtler vortices and their secondary instabilities into the mixing region, F. Fluid Mech. Vol 468, pp. 29-75, 2002.

Gnielinski, V., New Equations for Heat and Mass Transfer in Turbulent Pipe and Channel Flow, Int. Chem. Eng., vol. 16, pp.359-368, 1976.

Görtler, H., Über eine Analogie zwischen den Instabilitäten laminarer Grenzschichtströmungen an konkaven Wänden und an erwärmten Wänden, Institut für Angewandte Mathematik, Universität Freiburg i. Br., Hebelstr. 40, XXVIII. Band 1959.

Görtler, H., Über eine dreidimensionale Instabilität laminarer Grenzschichten an konkaven Wänden, 2.Band. Nr.1., 1940, Nachrichten aus der Mathematik, Gesellschaft der Wissenschaft Göttigen.

Gretler, W., Baltl, M., Numerical calculation of fully developed turbulent flow in curved channel: An extended algebraic Reynolds-stress model, Forschung im Ingenieurwesen, vol. 66, pp. 138-146, 2000

Hartnett, J., P., Koh, J., C., Y., McComas, S., T., A Comparison of Predicted and Measured Friction Factors for Turbulent Flow Through Rectangular Ducts, ASME, Journal of Heat Transfer, February 1962, pp. 82-88.

Hausen, H., Neue Gleichungen für die Wärmeübertragung bei freier und erzwungener Strömung, Allg. Wärmetechnik 9, 75-79, 1959.

Herbetz, A., Systemanalytische, vergleichende Untersuchung von transpirativ- und regenerativ gekühlten Brennkammern eines Racktenmotors, DLR, SART, DGLR-2001-117.

Hess, H., L., Kunz, H., R., A Study of Forced Convection Heat Transfer to Supercritical Hydrogen, Journal of Heat Transfer, p. 41, February 1965.

Hofman, A.: Mitt. Hydraul. Inst. T.H. München

Idelchik, I., E., Handbook of Hydraulic Resistance, Jaico Publishing House, Juni 2005.

Immich, H., Mayer, M., Cryogenic Liquid Rocket Engine Technology Developments with the German National Technology Programme, 33rd Joint Propulsion Conference, July 6-9, 1997, Seattle, USA.

Ito, H., Friction Factors for Turbulent Flow in Curved Pipes, Institute of high speed mechanics, Tohoku University, Sendai, Japan, Journal of Basic Engineering, p. 123, June 1959.

Jayanti, S., Hewitt, G. F., A Numerical Study of Bifurcation in Laminar Flow in Curved Ducts, International Journal For Numerical Methods in Fluids, Vol. 14, 253-266, 1992.

Jeschke, P., Longitudinal vortices in laminar boundary layer flows and influence on heat transfer, Fortschritt-Berichte VDI,Reihe 7, Nr. 350, TU Darmstadt, 1998. [Jeschke, P., Längswirbel in laminaren Grenzschichtströmungen und deren Einfluss auf den Wäremeübergang, Fortschritt-Berichte VDI,Reihe 7, Nr. 350, TU Darmstadt, 1998.]

Jones Jr, O., C., An Improvement in the Calculation of Turbulent Friction in Rectangular Ducts, Journal of Fluids Engineering, pp. 173-181, June 1976

Kumakawa, A., Saski, M., Niino, M., Sakamoto, H., and Sekita, T., „Thermal Conduction Characteristics of an Electrically Heated Tube Modelled after the LE-7 Main Burner“, presented at the 30th Space Sciences and Technology Conference, October 15, 1986.

Kudriavzev, V., M., Fundamental principles and computation of liquid-fueled rocket engines, Moscow, Visshaia Shkola, 1993. [Кудрявцев В.М., Основы теории и расчета жидкостных ракетных двигателей, Москва, Высшая школа, 1993.]

Launder, B., E., Spalding, D. , B., Lectures in Mathematical Models of Turbulence, Academic Press, London, England, 1972.

Leutheuseer, H., J., Turbulent Flow in Rectangular Ducts, Journal of Hydraulics Division, Proceedings of the American Society of Civil Engineers, May 1963.

Ligrani, P., Flow visualisation and flow tracking as applied to turbine components in gas turbine engines, Meas. Sci. Technol. Vol. 11, pp. 992-1006, 2000

Locke, J., M., Landrum, D., B., Uncertainty Analyses of Heat Transfer to Supercritical Hydrogen in Cooling Channels, AIAA 2005-4303.

Loh, W., H., T., Jet, Rocket, Nuclear, Ion and Electric Propulsion: Theory and Design, Springer-Verlag, Berlin, 1968

Lopes, A., S., Piomelli, U., Palma, J.M.L.M., Large Eddy Simulation of the Flow in an S-Duct, AIAA 2003-0964.

Matsson, O. J. E., Alfredsson, P. H., Secondary Instability and Breakdown to Turbulence in Curved Channel Flow, Applied Scientific Research, Vol. 51, pp. 9-14, 1993

Mc Carty, R. D., Hord, J., Roder, H. M., Selected Properties of Hydrogen (Engineering Design Data), U.S. Department of Commerce, February 1981.

Mc Carty , R. D., Weber, L. A., "Thermophysical Properties of Parahydrogen from the freezing Liquid Line to 5000 R for Pressures to 10,000 Psia", NBS Technical Note 617, 1972.

McEligot, D., M., Jackson, J., D., "Deterioration " criteria for convective heat transfer in gas flow through non-circular ducts, Nuclear Engineering Design 232, 2004, pp. 327-333.

Menter, F. R., Multiscale model for turbulent flows, 24th Fluid Dynamics Conference, AIAA, 1993

F. R. Menter, Two-Equation Eddy-Viscosity Turbulence Models for Engineering Applications, AIAA *Journal,* 32(8):1598-1605, August 1994.

Meyer, M., Electrically Heated Tube Investigation of Cooling Channel Geometry Effects, AIAA-95-2500, 31st AIAA/ASME/SAE/ASEE Joint Propulsion Conference and Exhibit, 1995, San Diego, CA, NASA Lewis Research Center, Cleverland, OH, USA.

Meyer, M.L., The Effect of Cooling Passage Aspect Ratio on Curvature Heat Transfer Enhancement, NASA Technical Memorandum 107426, March 1997, Lewis research Center, Cleverland, Ohio, USA.

Moody, L.F., Friction Factors for Pipe Flow, J. Heat Transfer, vol. 66, pp.671-684, 1944

Moody chart, http://ce.metu.edu.tr/~ce374/images/moodychart.jpg

Mori, Y., Nakayama, W., Study on Forced Convective Heat Transfer in Curved Pipes, Int. J. Heat Mass Transfer, Vol. 10, pp. 37-59, Pergamon Press 1967.

Münch, C., Métais, O., Turbulence in Cooling Channels of Rocket Engines, Large Eddies Simulation, Comptes Rendu de Mécanique de l'Académie des Sciences 333 (2005) 574-579.

Naot, D., Shavit, A., Wolfshtein, M., Numerical Calculation of Reynolds Stresses in a Square Duct with Secondary Flow, Wärme- und Stoffübertragung 7 pp. 151-161, 1974.

Neuner, F., Preclik, D., Popp, M., Funke, M., Kluttig, H., Experimental and Analytical Investigation of Local Heat Transfer in High Aspect Ratio Cooling Channels, AIAA-98-3439, 34th AIAA/ASME/SAE/ASEE Joint Propulsion Conference & Exhibit, July 13-15, 1998 / Cleverland, OH, Daimler-Benz Aerospace AG, Space Infrastructure Propulsion, TU Dresden, Institute of Thermodynamics.

Neuner, F., Preclik, D., Zinner, W., Dittmann, A., Weiterentwicklung von Vorhersagenmethoden zur Beschreibung des Wärmeübergangs in Racketenbrennkammern, DGLR-JT-96-089, Daimler-Benz Aerospace AG, TU Dresden, Institute of Thermodynamics, 1996.

Niino, M., Kumakawa, A., Yatsuyanagi, N., Suzuki, A., Heat Transfer Characteristics of Liquid Hydrogen as a Coolant for LO_2/LH_2 Rocket Thrust Chamber with the Channel Wall Construction, National Aerospace Lab of Japan, Ohgawara, Miyagi, Japan. AIAA/SAE/ASME, 18th Joint Propulsion Conference, Cleverland, Ohio, June 21-23, 1982.

NIST, National Institute of Standards and technology, http://webbook.nist.gov/chemistry/fluid

Novotny, J., L., McComas, S., T., Sparrow, E., M., Eckert, E., R., G., Heat Transfer for Turbulent Flow in Rectangular Ducts with Two Heated and Two Unheated Walls, A.I.Ch.E Journal, p. 466, 1964.

Oschwald, M., Suslov, D., Woschnack, A., Einfluss der Temperaturabhängigkeit der Materialeigenschaften auf den Wärmeaushalt in regenerativ gekühlten Brennkammern, DGLR-2004-111

Peng, D.-Y., D.P., Robinson, A New Two-Constant Equation of State, In: Ind. Eng. Chem. Fundam., 15(1), S. 59-64, 1976

Petitjeans, P., Wesfreid, J.E., Deplano, V., Vlad, G., Effect of curvature on the velocity profile and boundary layer in flow through a curved channel, La recherche aérospatiale, 1995, n°2, 125-138, HMP de l'ESPCI, Paris, IMF, Marseille, SNECMA, Villaroche.

Petitjeans, P., Wesfreid, J.E., Spatial Evolution of Görtler Instability in a Curved Duct of High Curvature, AIAA Journal, Vol. 34, No 9, pp. 1793-1800, September 1996.

Petukhov, B., Kurganov, V., Gladuntsov, A., Heat Transfer in Turbulent Pipe Flow of Gases with Variable Properties, Heat Transfer Soviet Research, 1973, 5, pp. 109-116.

Popp, M., Schmidt, G., Rocket Engine Combustion Chamber Design Concepts for Enhanced Life, AIAA 96-3303, Joint Propulsion Conference, July 1-3, 1996, Lake Buena Vista, Fl, USA.

Quentmeyer, R., Carlile, J., An Experimental Investigation of High-Aspect-Ratio Cooling Passages, AIAA 92-3154, 28th Joint Propulsion Conference and Exhibit, July 6-8, 1992/ Nashville, USA.

Raynaud, M., Traité Génie Energétique, Le problème inverse de conduction de la chaleur, Techniques de l'ingénieur, France, 2000.

Redlich, O., Kwong, J.N.S., Chem Rev, 44 :233, 1949.

Saccadura, J. F., Initiation aux transferts thermiques, Lavoisier – Technique et documentation, pp. 38-39, 1980

Salinas Vazquez, M., Métais, O., Large-eddy simulation of the turbulent flow through a heated square duct, J. Fluid Mech., vol. 453, pp. 201-238, 2002.

Scaggs, W. F., Taylor, R. P., Coleman, H. W., Measurement and Prediction of Rough Wall Effects on Friction Factor – Uniform Roughness Results, Journal of Fluids Engineering, Vol. 110, pp. 385-391, December 1988.

Schlichting, H., Gersten, K., Grenzschicht-Theorie, Springer Verlag Berlin Heidelberg, 1968, edition 1997

Seban, R.A., McLaughlin, E.F., Heat Transfer in Coiled Tubes with Laminar and Turbulent Flow, International Journal of Heat and Mass Transfer 6, 1963, pp. 387-395.

Shah, R., K., Thermal entry length solutions for the circular tube and parallel plates, Proc. 3rd Natnl. Heat Mass Transfer Conference, Indian Inst, Technol Bombay, Vol. I, Paper HMT-11-75, 1975

Snieder Roel, *The role of non linearity in inverse problems*, IOP Publishing Ltd, UK, 1998

Song, B., Amano, R. S., Application of non-linear k-ω model to a turbulent flow inside a sharp U-bend, Computational Mechanics 26, pp. 344-351, 2000

So, R.M.C., Mellor, G.L., Experiment in convex curvatures effects in turbulent boundary layers, Department of Aerospace and Mechanical Sciences, Priceton University, New Jersey 08540, Journal of Fluid Mechanic, 1973, vol. 60, part1, pp. 43-62.

Song, B., Amano, R. S., Application of non-linear k-ω model to a turbulent flow inside a sharp U-bend, Computational Mechanics, vol. 26, pp. 344-351, 2000

Sparrow, E., M., Cur, N., Turbulent Heat Transfer in a Symmetrically or Asymmetrically Heated Flat Rectangular Duct With Flow Separation at Inlet, ASME, Vol. 104, pp. 82, 1982.

Sparrow, E., M., Lloyd, J., R., Hixon, C., W., Experiments on Turbulent Heat Transfer in Asymmetrically Heated Rectangular Duct, ASME, pp. 170, May 1966.

Sturgis, J.C., Mudawar, I., Single-phase Heat Transfer Enhancement in a Curved, rectangular Channel subjected to Concave Heating, International Journal of Heat and Mass Transfer 42 (1999), pp. 1255-1272, Purdue University, West Lafayette, USA.

Suslov, D., Torres, Y., Woschnak, A., Oschwald, M., Vorrichtung und Verfahren zur Erzeugung von Wärmeströmen definierter Wärmestromdichte, 2006-03-02, DLR, European Patent Office, DE102004042901.

Suslov, D., Woschnak. A., Sender, J., Oschwald, M., Test Specimen Design and Measurement Technique for Investigation of Heat Transfer Processes in Cooling Channels of Rocket Engine under Real Thermal Conditions, AIAA 2003-4613.

Suslov, D., Kopp, W., Oschwald, M. „Verfahren und Vorrichtung zur Temperaturbestimmung mittels eines Thermoelementes“, Patent N 102005058136, 2006

Tani, I., Production of Longitudinal Vortices in the Boundary Layer along a concave Wall, journal of Geophysical Research, Volume 67, N°8, July 1962, University of Tokyo, Japan.

Taylor, M.F., A Method of Predicting Heat Transfer Coefficients In The Cooling Passages Of Nerva and Phoebus-2 Rocket Nozzle, NASA Lewis Research Centre, Cleverland, Ohio, AIAA 68-608, 4th Propulsion Joint Specialist Conference, June 10-14, 1968

Taylor, M.F., Correlation of Local Heat-Transfer Coefficients for SinglePhase Tubulent Flow of Hydrogen in Tubes with Temperature Ratios to 23, NASA TN D-4332, Lewis Research Center, Cleverland, Ohio, September 27, 1967.

Torres, Y., Verification of measurement technique for investigation of heat transfer in cooling channels of rocket engines, DLR Report DLR-LA-WT-RP-005, Master Internship Report, August 2004, University of Valenciennes, France.

Torres, Y., Stefanini, L., Suslov, D., Influence of Curvature in Regenerative Cooling System of Rocket Engine, 2nd European Conference for Aerospace Science, EUCASS, Brussel, July 2007.

Tsai, S., F., Sheu, W., H., Numerical exploration of flow topology and vortex stability in a curved duct, International Journal for numerical methods in engineering, in press, 2006

VDI-Wärmeatlas, Db 34, 8. Auflage 1997

Wadel, M., F., Comparison of High Aspect Ratio Cooling Channel Designs For a Rocket Combustion Chamber, AIAA-97-2913, 33rd Joint Propulsion Conference & Exhibit, July 6-9, 1997, Seattle, USA.

Wadel, M., F., Meyer, M., L., Validation of High Aspect Ratio Cooling in a 89 kN (20,000 lb_f) Thrust Combustion Chamber, AIAA 96-2584, 32nd Joint Propulsion Conference, July 1-3, 1996, Lake Buena Vista, FL, USA.

White, C. M., Streamline Flow Through Curved Pipes, Proc. R. Soc. London, A123, pp. 645-663, 1929.

Wilcox, D.C, Multiscale model for turbulent flows, AIAA 24th Aerospace Sciences Meeting, 1986.

Woschnak, A., Oschwald, M., Thermo- and Fluid- mechanical Analysis of High Aspect Ratio Cooling Channels, DLR Lampoldshausen, Space Propulsion, 74239 Hardthausen, Germany, AIAA, 2001-3404, 37th AIAA/ASME/SAE/ASEE/ JPC, Conference and Exhibits, 8-11 July 2001, Salt Lake City, UT.

Woschnak, A., Suslov, D., Oschwald, M., Experimental and Numerical Investigations of Thermal Stratification Effects, AIAA 2003-4615, 39th AIAA/ASME/SAE/ASEE/JPC Conference and Exhibits.

Wenneberg, J., C., Anderson, W., E., Haberlen, P., A., Jung, H, Merkle, C., L., Supercritical Flows in High Aspect Ratio Cooling Channels, AIAA 2005-4302, 41st Joint Propulsion Conference & Exhibit, 10-13 July 2005, Tucson, US.

Wennerberg, J., C., Hogirl, J., Schuff, R., Anderson, W., E., Merkle, C., L., Study of Simulated Fuel Flows in High Aspect Ratio Cooling Channels, AIAA 2006-4708, 42nd Joint Propulsion Conference & Exhibit, 9-12 July 2006, Sacramento, US.

Yagley, J., Feng, J., Merkle, C., L., Lee, Y., T., The Effect of Aspect Ratio on the Effectiveness of Combustor Coolant Passages, AIAA-92-3153, 28th Joint Propulsion Conference and Exhibit, July 6-8, 1992, Nashville, USA.

Younglove, B. A., Thermophysical properties of fluids. I. Argon, ethylene, parahydrogen, nitrogen, nitrogen trifluoride, and oxygen, Journal of Physical and Chemical Reference Data, Vol. 11, 1982

Zhaoshung, Z., Weidong, H., Hua, S., Particle Tracking Method for Measurements of Turbulence Properties in a Curved Channel, Applied Scientific Research, Vol. 51, pp. 249-254, 1993

Zhang, J., Zhang, B., Jü, J., Fluid Flow in a rotating curved rectangular duct, Int. Journal of Heat and Fluid Flow 22, pp. 583-592, 2001.

Zucrow, M., J., Hoffman, J., D., Gas Dynamics, School of Mechanical Engineering Purdue University, 1976

Figures and Tables

▪ FIGURES

TABLES

Transferts énergétiques dans les canaux de refroidissement courbes de moteurs fusées

MOTS-CLEFS : Transferts de Chaleur Asymétriques, Transfert de masse, Tourbillons de Dean, Tourbillons de « coins », Canaux Courbes de refroidissement à haut facteurs de forme, Nombre de Nusselt, Moteurs fusées, Écoulements secondaires, Expérience en mécanique des fluides et en thermique, Mesures de températures, Simulations numériques CFD, Reynolds Stress Model (RSM), Hydrogène, Méthane, Cryogénique, DLR

Les matériaux de la chambre de combustion des moteurs fusées doivent supporter d'extrêmes contraintes mécaniques et thermiques de par les gradients considérables de pression et de température. L'optimisation des systèmes de refroidissement se révèle donc être un élément majeur lors du design des chambres de combustion. Concernant le système de refroidissement convectif dit « régénératif », les ergols circulent dans les canaux de refroidissement, qui sont usinés le long de la chambre de combustion. Les canaux doivent épouser le profile de la tuyère et ne sont donc pas rectilignes. Cela créé des écoulements secondaires dus aux forces centrifuges, les tourbillons de Dean. Ces écoulements secondaires viennent modifier l'écoulement principal et les transferts de chaleur des canaux de refroidissement.

Le projet expérimental EH3C (Electrical Heated Curved Cooling Channels) a été soutenu par l'institut allemand de propulsion spatiale DLR, dans le cadre de cette thèse. Deux prototypes expérimentaux ont été conçus, fabriqués et testés, reproduisant les canaux de refroidissement d'un moteur fusée dans lesquels circulent des ergols (hydrogène et méthane). Le premier prototype est un canal droit à haut facteur de forme, alors que le second reprend la même géométrie mais présente une courbure. Ces deux prototypes ont été testés au DLR dans des conditions expérimentales similaires avec pour objectif de mettre en valeur le rôle de la courbure sur le transfert de chaleur et les pertes de charges. Des simulations numériques ont aussi été réalisées pour modéliser ces expériences.

Heat and mass transfers in curved cooling channels of rockets engines

KEYWORDS: Heat Transfer, Flow Transfer, Curved flows Dean vortices, “Edges” vortices, Cooling Channel, Nusselt, Rocket Engine, Secondary Motions, Hydrogen, Methane, CFD, Reynolds Stress Model (RSM), Fluid Experiments, Temperatures measurement, Cryogenic, DLR

The materials of the combustion chamber wall of rocket engines have to withstand extreme thermal and mechanical loadings, which are managed by efficient cooling. For an optimal design of the cooling system, with minimal hydrodynamic losses, a precise knowledge of the heat transfer is required. The combustion chamber profile imposes curvatures to the cooling channel, because they follow the nozzle profile of the combustion chamber. These curvatures create secondary flows inside the channel and bring heat flux modifications through the chamber walls: the Dean vortices.

The experimental project EH3C (Electrical Heated Curved Cooling Channels) was supported by the german space propulsion center (DLR) in the scope of this PhD. Two test specimens were designed, manufactured and tested. The first specimen is a single straight cooling channel, presenting a high aspect ratio and the second one is curved, in order to enlighten the curvature effects on the heat transfer and the pressure loss. Numerical simulations were provided to model the experiments.

DISCIPLINE: Mécanique énergétique

INTITULE ET ADRESSE DE L'U.F.R. OU DU LABORATOIRE :

LME Laboratoire de mécanique énergétique, EA 2447, UVHC, Université de Valenciennes et du Hainaut-Cambrésis, Le Mont Houy, F-59313 Valenciennes Cedex 9

Bibliotheque..Universitaire..de..Valenciennes
00900546